

MEASUREMENT OF THE STANDARD MODEL BETA ASYMMETRY
PARAMETER, A_β , IN ^{37}K

A Dissertation

by

RICHARD SPENCER BEHLING

Submitted to the Office of Graduate and Professional Studies of
Texas A&M University
in partial fulfillment of the requirements for the degree of

DOCTOR OF PHILOSOPHY

Chair of Committee,	Sherry J. Yennello
Co-Chair of Committee,	Dan Melconian
Committee Members,	Charles M. Folden III
	John Hardy
	Joseph Natowitz
Head of Department,	François P. Gabbaï

May 2015

Major Subject: Chemistry

Copyright 2015 Richard Spencer Behling

ABSTRACT

Low energy nuclear β -decay experiments have been instrumental in shaping our understanding of the weak interaction and the development of the standard model. Today these experiments continue to help our understanding evolve by measuring the predictions of the standard model to even greater levels of accuracy. Recently an experiment to measure the standard model β -asymmetry correlation parameter, A_β , was carried out at TRIUMF.

This experiment is the first time that a measurement of A_β has been made in ^{37}K . Additionally it is the first time that A_β , in any isotope, has ever been measured making use of a source of cold atoms provided by a magneto-optical trap. The experiment was carried out by the TRINAT (TRIUMF neutral atom trap) collaboration.

In order to make this measurement the ^{37}K atoms had to be highly spin polarized and this was done via optical pumping. In the course of the data analysis a large difference between the response of the rate-equation model and the optical Bloch model to the presence of misaligned magnetic field was observed. The resolution of this model difference is ongoing and a well motivated approximate polarization of 0.99 ± 0.01 has been used as a place holder to allow the analysis to be carried through to completion.

Assuming this final number for the polarization for the atoms we find $A_\beta(0) = -0.5639 \pm 0.0094$, in agreement with the standard model predicted value of -0.5706 ± 0.0007 . If we do not assume the polarization number is correct our result will be $PA_\beta = -0.5583 \pm 0.0109$ This value of A_β corresponds to a ρ value of $\rho = 0.553_{-0.021}^{+0.034}$. Combining this measurement with measurements from other $T=1/2$ mirror transitions a value for $|V_{ud}| = 0.9723 \pm 0.0017$ is calculated. This measurement interpreted

in the framework of the manifest-left right symmetric model excludes masses of M_2 above 230 GeV at the 90% confidence level at $\zeta = 0$.

DEDICATION

For Jessica, Kingston, and Truman

ACKNOWLEDGEMENTS

Thanks to the people who made this dissertation possible. In particular I would like to acknowledge the hard work of Konstantin Olchanski, Alexandre Gorelov, John Behr and Dan Melconian. Without the hardwork of these four individuals this project never would have been completed.

I would also like to thank my wife Jessica and son Kingston who had to endure a miserable year living in a tiny basement in Vancouver instead of our nice house in Texas, and Truman who came along to join us at the end.

TABLE OF CONTENTS

	Page
ABSTRACT	ii
DEDICATION	iv
ACKNOWLEDGEMENTS	v
TABLE OF CONTENTS	vi
LIST OF FIGURES	ix
LIST OF TABLES	xiii
1. INTRODUCTION	1
1.1 Simple Physical Picture of Observable	2
1.2 Motivation	5
1.3 Physics of the Decay of ^{37}K	6
1.4 Simple Overview of the Experiment	10
1.5 The Author’s Contribution	14
2. THEORETICAL BACKGROUND	16
2.1 Jackson, Treiman, Wyld and the Standard Model	16
2.1.1 A Toy Beta Energy Spectrum	18
2.1.2 The Form of A_β Assuming the Standard Model	19
2.2 Interpreting a Measurement of A_β in the Context of the Standard Model	25
2.3 Modification to the Standard Model due to Right-Handed Currents .	27
2.3.1 The Manifest Left-Right Symmetric Model	29
2.3.2 The Non-Manifest Left-Right Symmetric Model	34
2.4 Model Constraints and Exclusion Plots	38
2.4.1 Exclusion Plot Construction	38
2.5 Other Constraints on Right-Handed Currents	41
2.5.1 Unitarity of the CKM Matrix	41
2.5.2 Unpolarized Longitudinal Polarization	42
2.5.3 Polarized Longitudinal Polarization	42
2.5.4 Muon decay	43
2.5.5 Expected Limits From ^{37}K	44

2.5.6	Limits in the Non-Manifest Model	45
3.	GEANT SIMULATIONS	47
3.1	GEANT4 Simulations of the Experiment	47
3.2	Kinematic Constraints and the Mandelstam Variables	47
3.3	Event Generator	50
3.4	Recoil-Order Effects	50
3.5	The Fermi Function	55
3.6	The Geometry Definiton	58
3.7	Experimental Cloud Input Into GEANT4	60
3.8	Testing With GEANT4	64
3.9	Multithreading in ^{37}K Simulations	67
3.10	Future Work with GEANT4	70
4.	EXPERIMENTAL SETUP	73
4.1	Design Against Major Systematics	73
4.2	Geometry Elements	74
4.2.1	The Chamber	74
4.2.2	Silicon Carbide Mirrors	76
4.2.3	Electrostatic Hoops	79
4.3	Detectors	84
4.3.1	Scintillator Detectors	84
4.3.2	Silicon Detectors	87
4.3.3	Shakeoff Electron MCP	93
4.3.4	Ion MCP	95
4.4	Timing	97
4.5	Data Acquisition	99
5.	POLARIZATION MEASUREMENT	106
5.1	Overview	106
5.2	Polarization Models	106
5.2.1	A Simple Polarization Calculation	107
5.2.2	Rate Equation Model	112
5.2.3	Optical Bloch Model	114
5.3	The Photoionization Data	117
5.4	Difference Between the Models	123
5.5	Polarization Experiments with ^{41}K	129
5.5.1	Effect of Temperature on Polarization	131
5.5.2	Summary of Offline Experiments	132
5.6	Final Value of the Polarization	132

6. DATA ANALYSIS	134
6.1 Cleaning and Preparing the Data	134
6.1.1 Equal Time In Each Polarization State	134
6.1.2 Energy Spectrum From Waveforms	136
6.1.3 Timestamp Mismatch	143
6.1.4 Energy Agreement Algorithm	151
6.1.5 Cleaning the MCP Time Signals	151
6.2 Asymmetries	154
6.2.1 The Super-Ratio	154
6.2.2 Super-Ratio Uncertainty	156
6.2.3 Why the Super-Ratio is Super	158
6.3 Asymmetry as a Function of Cycle Time	159
6.4 Timing Coincidence Between the Scintillators and the Electron MCP	161
6.5 Asymmetry as a Function of Angle	161
6.6 Asymmetry as a Function of β Energy	165
6.6.1 Systematic Uncertainties	171
6.6.2 The Final Result	178
7. FUTURE PROSPECTS AND SUMMARY OF RESULTS	183
7.1 Future Prospects	183
7.1.1 Size and Position Sensitivity of Electron MCP	183
7.1.2 Increase Polarization Diagnostics	184
7.1.3 Higher Electric Field	186
7.1.4 Improved GEANT4 Simulations	186
7.1.5 Blind Analysis	187
7.2 Summary	188
REFERENCES	191
APPENDIX A. STRIP DETECTOR CALIBRATIONS	206
APPENDIX B. SCINTILLATOR CALIBRATIONS	212
APPENDIX C. MIRROR SPECIFICATION	215

LIST OF FIGURES

FIGURE	Page
1.1 Polar β probability distribution	3
1.2 The dependence of decay rate on angle and energy for fixed A_β	4
1.3 Energy level diagram of ^{37}K	8
1.4 Map showing all of the sources from which the standard model prediction of A_β is derived	9
1.5 Model of experimental geometry	11
2.1 A simple kinematic β energy spectrum	19
2.2 Comparison of exclusion contours with published results	40
2.3 Predicted exclusion contour levels from ^{37}K compared with other experiments assuming the manifest left-right symmetric model	44
2.4 Predicted exclusion contour levels in non-manifest case	46
3.1 General interaction schematics	48
3.2 A schematic of the event generation algorithm in the GEANT4 code	51
3.3 Energy dependence of A_β due to recoil-order effects	52
3.4 Comparison of different Fermi functions	56
3.5 Nuclear radii in the area of ^{37}Ar	57
3.6 GEANT4 file size comparison	59
3.7 Scattering from mirror substrates	60
3.8 Experimental data showing the extent of the cloud	62
3.9 GEANT4 typical events	64
3.10 Sorted list of volume names that most strongly scatter positrons	66

3.11	Architecture of analyzer program	69
3.12	Comparison of electric fields	71
4.1	Two views of the experiment	75
4.2	Design considerations for different mirror angles	78
4.3	The hoop and ion micro channel plate assembly before installation in the chamber	81
4.4	Charge state time distributions	83
4.5	Scintillator design and testing	86
4.6	Detailed layout and axis choice for silicon detectors	88
4.7	Schematic showing the detector cabling	90
4.8	Strip detector information	92
4.9	The shakeoff electron micro channel plate	94
4.10	The ion micro channel plate with mask and delay line anode	96
4.11	Timing diagram of the experiment	98
4.12	NIMIO32 trigger firmware part 1	100
4.13	NIMIO32 trigger firmware part 2	101
4.14	NIMIO32 trigger firmware part 3	102
4.15	Electronics diagram	103
5.1	Schematic of photoionization process during optical pumping	108
5.2	Two level system to demonstrate the density matrix	115
5.3	Test of photoionization technique using ^{41}K	118
5.4	Relative timings of photoionization events	120
5.5	Photoionization timing shift after run 996	121
5.6	Photoionization events ordered by optical pumping time	123

5.7	Comparison of the the polarizations output from the rate equation model and the optical Bloch model for a varying value of misaligned magnetic field here referred to as B_{bad}	124
5.8	A typical fit of the optical pumping spectrum	125
5.9	The values of the polarization returned from the fits	127
5.10	Sublevel populations given by the two OP models	128
5.11	A schematic of the offline polarization measurement setup	130
5.12	A schematic of polarization light injection optics mounted on the 19.5° optical pumping arms	131
6.1	Fake asymmetry as a function of energy left in the scintillator produced by unequal time in each polarization state	135
6.2	The macroscopic timing filter applied to the data	136
6.3	Different views of waveform data	138
6.4	This is a typical waveform fit that was obtained using Eq. 6.1	139
6.5	A schematic view of different waveform energy extraction algorithms .	141
6.6	Spectrum differences between the digital charge integrating and peak sensing algorithms	142
6.7	Comparison of strip firing across detector	144
6.8	The effect of silicon detector coincidence condition on the scintillator energy spectrum before fixing the data stream mismatch	145
6.9	Silicon energy gated on scintillator energy before fixing the data stream mismatch	146
6.10	Comparison of the energy spectrum of ^{37}K with that of ^{90}Sr	147
6.11	Diagnosis of the timestamp mismatch	148
6.12	A schematic of the algorithm to correct the timestamp mismatch . . .	150
6.13	Ion - photodiode timing spectrum showing many poorly understood peaks broken out by hit number	153

6.14	Asymmetry between the scintillators as a function of cycle time . . .	160
6.15	Relative timing between the scintillator and the electron MCP	162
6.16	Simulated $\cos \theta$ distribution for silicon detectors	163
6.17	These are heatmaps of β hits on the bottom silicon detectors during polarized time	164
6.18	Asymmetry for two slices in $\cos \theta$	166
6.19	The scintillator energy spectrum.	167
6.20	Summary of A_β fitting procedure	170
6.21	Some asymmetry plots showing the effect of different systematic un- certainties considered	173
6.22	The effect of different conditions on the energy spectra and fits	176
6.23	Interpretation of our measurement of A_β in the framework of the stan- dard model and in the framework of right-handed current model. . . .	180
6.24	Projected limits from future experiments measuring the correlation parameters A_β and B_ν at the 0.1% level of precision.	181
A.1	This is a typical GEANT4 fit to a silicon strip spectrum	207
B.1	Upper scintillator calibration fit with GEANT4	213

LIST OF TABLES

TABLE	Page	
2.1	The standard model correlation coefficients that enter into experiments with polarized nuclei	20
2.2	Definition of manifest left-right symmetric model parameters for the neutron	31
3.1	All of the input values that are needed to calculate recoil order effects for ^{37}K	53
3.2	Trap position and movement by polarization state	63
4.1	Energy loss in scintillator wrapping materials tested	87
5.1	Some different coincidence peak timing cuts tried	121
6.1	Error budget	178
A.1	Strip detector calibration lower Y	208
A.2	Strip detector calibration lower X	209
A.3	Strip detector calibration upper Y	210
A.4	Strip detector calibration upper X	211
B.1	Scintillator calibrations	212

1. INTRODUCTION

Nuclear β -decay experiments played a critical role in the development of the standard model of particle physics (SM). In a classic paper on the subject of β -decay, Lee and Yang proposed that there was no evidence to support the assertion that parity was conserved in β -decay [1]. In the paper they also proposed several experiments that would definitively answer this question. Two of the proposed experiments were carried out, one by Wu [2] and the other by Garwin [3]. Both showed that parity is violated in β decay. Building on this foundation, modern experiments continue to make ever more precise measurements of parity violation in nuclear β -decay and continue to test SM predictions and provide constraints on physics beyond the SM [4, 5, 6, 7, 8, 9, 10, 11, 12, 13, 14].

At Canada's national laboratory for particle and nuclear physics (TRIUMF), the TRIUMF neutral atom trap collaboration (TRINAT) has a mature program to measure SM asymmetry parameters [15] from the beta decay of atoms confined in a magneto-optical trap (MOT). A MOT is an ideal source for radioactive decay experiments because the atoms are thermally cold (~ 1 mK) and spatially confined (~ 1 mm³) by the combined action of a magnetic field and laser light, eliminating scattering from any containing volume. In the research proposal submitted as part of my preliminary examination it is stated that the goal of this project is to make a $\sim 1\%$ measurement of the SM β -asymmetry parameter, A_β , of ^{37}K confined in a MOT and spin polarized by means of optical pumping (OP). At the 1% level of precision our measurement would be the third most precise measurement of A_β in any system. This project is meant to be a spring board to propel the TRINAT experimental program on to making the most precise measurement of A_β in any

system at the 0.1% level or beyond. In this work I will describe what was done to achieve this stated goal and report the result of our effort.

1.1 Simple Physical Picture of Observable

It is important that we connect the the concept of β -asymmetry to its physical interpretation. Intuitively, A_β can be understood to be a measure of the likelihood of a β -particle being emitted in a direction relative to the direction of the original nuclear spin. If we can develop an understanding of the simple physical picture it will greatly facilitate the understanding of all the rest of this work. The next equation is a simplified version of the decay rate of polarized atoms:

$$\text{differential decay rate} \sim 1 + A_\beta P \frac{v}{c} \cos \theta. \quad (1.1)$$

In this equation P is the average polarization vector that represents the expectation value of the nuclear spins projected on a common axis, v/c is a relativistic factor, and θ is the polar angle between the nuclear spin and the momentum vector of the emitted β . If we consider that β s with a few MeV of kinetic energy have $v/c \approx 1$ and assume for the sake of simplicity that $P = 1$, we can see that the decay rate in this case only depends on the value of A_β and the angle with respect to the polarization direction. Shown in Fig. 1.1 is a graphical representation of the probability of a β being emitted at some angle θ with respect to the original nuclear polarization axis while making the two previously stated assumptions. It is so important to understand the relationship between A_β and the observed β spectrum that I have included a second graphical representation of Eq. 1.1 as Fig 1.2. In this representation, instead of showing the probability, I show the change in decay rate from the rate at 90° and have not made the assumption that $v/c = 1$ so that we can see how the asymmetry changes with the energy of the emitted β .

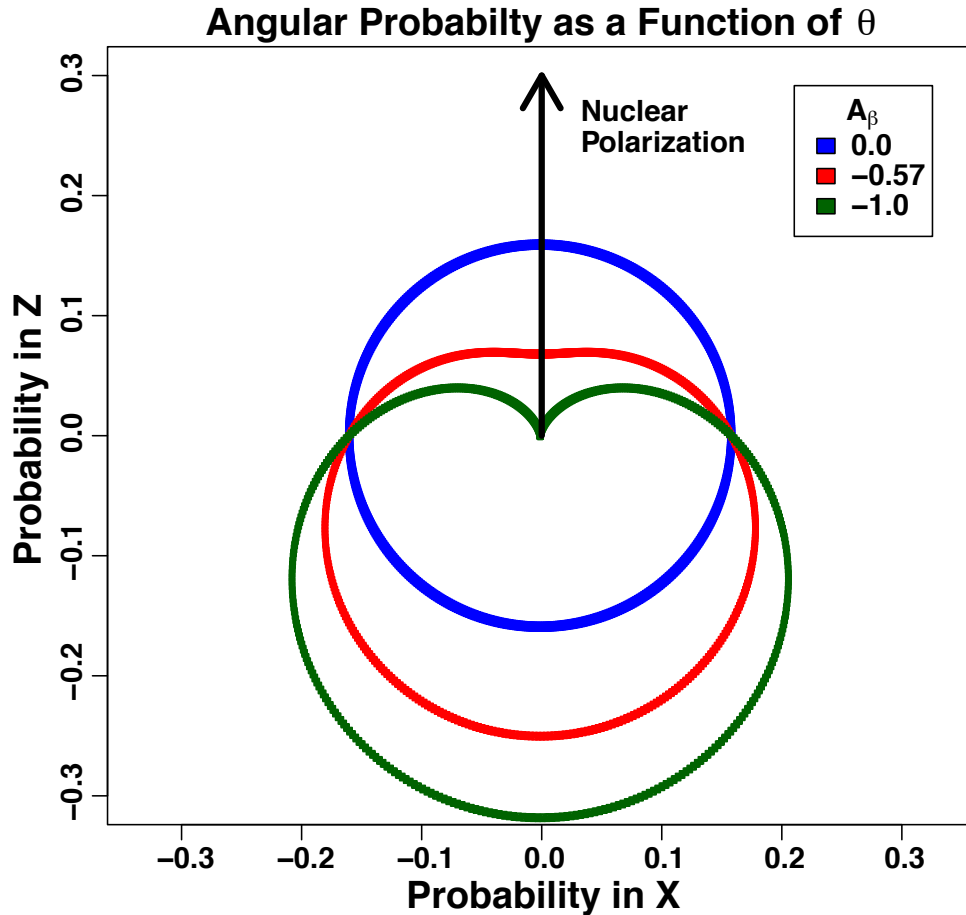


Figure 1.1: Polar β probability distribution. This is a polar probability distribution plot in the polar angle, θ , for β particles emitted in a given decay with respect to the zenith direction defined by the nuclear polarization vector so that the distance from the origin at each point is the probability of a β being emitted at that angle θ . A_β does not affect the azimuthal, ϕ , distribution of decay products and in ϕ the angular distribution is symmetric. For $A_\beta = 0$ the decay is isotropic in θ and there is no angular preference for the β . In the case of $A_\beta = -1$ the probability that a β will be emitted in the direction of the nuclear polarization goes to zero. A positive sign of A_β would reflect the plots across the “probability in $Z = 0$ ” line so that the β s would prefer to go in the direction of the nuclear polarization instead of against it.

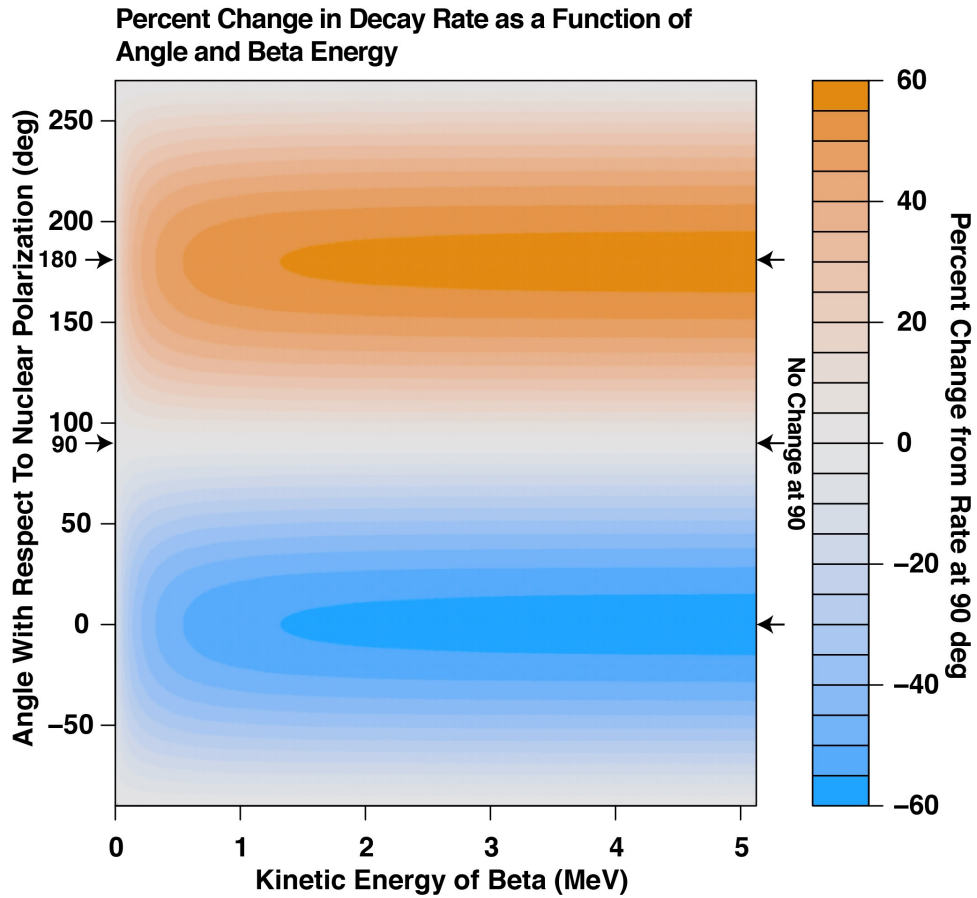


Figure 1.2: The dependence of decay rate on angle and energy for fixed A_β . The β distribution at 90° does not change with A_β as seen in Fig. 1.1. Therefore it is a useful reference point to look at the percent change in the likelihood of observing a β particle for different angles and energies. This plot has been specialized to ^{37}K where the endpoint energy is 5.1 MeV and the SM value of $A_\beta = -0.570$.

1.2 Motivation

A measurement of A_β can be interpreted in a couple of different contexts to gain access to different physics questions. The first question to answer is if the experimentally measured value match the SM predicted value. As the SM has been rigorously tested in so many areas we expect the answer to this question to be yes. If a deviation from the SM predicted value was observed it could be a sign of new physics. Finding a single deviation from the standard model would be exciting but would need to be validated. At the level of precision that we were aiming for in this experiment we are not going to approach the 5σ deviation limit needed to claim a discovery. To get to that limit we would need to make at least a $\sim 0.01\%$ measurement of A_β . Two orders of magnitude better than the current experiment.

Until we reach that level of precision there are other useful ways to interpret our results. One way to do this would be to combine our result with results from a similar set of nuclei in such a way that systematic errors in one result get washed out by averaging over the set while at the same time increasing the signal to noise ratio of the physics signature. Recently it was shown that an evaluation of $|V_{ud}|$ could be carried out for a set of $T = 1/2$ mirror transitions, including ^{37}K [16], that would be complimentary to the much more precise evaluation done using superallowed $0^+ \rightarrow 0^+$ [17] decays.

It is not necessary to assume the framework of the SM when interpreting our measurement of A_β . In this case another model can be assumed. One example of another model that could be used is a left-right symmetric model in which right-handed currents can exist. In this case our measurement of A_β will be able to place constraints on the parameters of this model.

1.3 Physics of the Decay of ^{37}K

Before drilling down to the particular physics in question it would be beneficial to review some basic β -decay terminology. A similar review of the material presented here can be found in any nuclear physics textbook with the author consulting these [18, 19, 20, 21] in the preparation of this manuscript. One of the first important things to know is how to classify a particular transition as either Fermi, Gamow-Teller, or mixed Fermi/Gamow-Teller. Before we mention the selection rules it is important to know why being able to classify a given transition is helpful. If we know that a given transition is pure Gamow-Teller, for instance, then we know that there is no vector component in the interaction, and this makes calculating the SM correlation parameters trivial as will be shown later on. Additionally if we know that a given transition is mixed, then the calculation is more work and requires additional input. There are some other important things to keep in mind about the terminology. The first is that all three of the previously mentioned classes – namely Fermi, Gamow-Teller, or mixed Fermi/Gamow-Teller – are the three types of β -decays that make up the set known as “allowed decays”. Allowed decays are those for which the change in nuclear spin from the initial to the final state denoted as, ΔJ , is equal to 0 or ± 1 and there is no change in parity from the initial to final nuclear state. All other beta decays are termed forbidden and there are degrees of forbiddenness. In this context forbidden does not mean that a transition cannot occur, but instead that it will simply occur more slowly. Another aspect that must be considered when classifying decays is the change in the isospin, ΔT , between the parent and daughter. We are now prepared to learn the selection rule for classifying a decay as Fermi, Gamow-Teller, or mixed Fermi/Gamow-Teller. A Fermi decay is

distinguished by,

$$\Delta J = 0, \Delta T = 0, \text{ and no parity change.} \quad (1.2)$$

Alternatively a Gamow-Teller decay is distinguished by,

$$\Delta J = 0, \pm 1, \Delta T = 0, \pm 1, \text{ excluding } J = 0 \rightarrow 0, \text{ and no parity change.} \quad (1.3)$$

The third classification mixed Fermi/Gamow-Teller are simply the decays that satisfy both Eq. 1.2 and Eq. 1.3 simultaneously.

The main 97.89% branch of the β^+ decay of ^{37}K to ^{37}Ar is $J = 3/2^+ \rightarrow J' = 3/2^+$ [22]. An energy level diagram from ^{37}K is shown in Fig. 1.3. Both parent and daughter state have $T = 1/2$. From the aforementioned selection rules we can see that it is a mixed Fermi/Gamow-Teller transition. At this point it is also worth mentioning that the decay $^{37}\text{K} \rightarrow ^{37}\text{Ar}$ is a mirror transition. Mirror nuclei are isobaric nuclei that have their number of protons and neutrons interchanged. For example ^{22}Ne ^{22}Na ^{22}Mg are isobars, but ^{22}Ne and ^{22}Mg are mirrors of one another. Mirror nuclei are special in that their level schemes should be identical except for modifications due to the presence of isospin non-conserving forces, such as the Coulomb interaction [24] and this is a reflection of the underlying symmetry in the nuclear structure. The whole point in mentioning this is to point out that from a theoretical point of view corrections for mirror nuclei can be more easily calculated because of the simpler nuclear structure.

A good reference that shows explicitly how the SM correlation parameters are calculated for a set of $T = 1/2$ mirror transitions is given by Ref. [25] along with details about the theoretical corrections. A simple schematic diagram summarizing

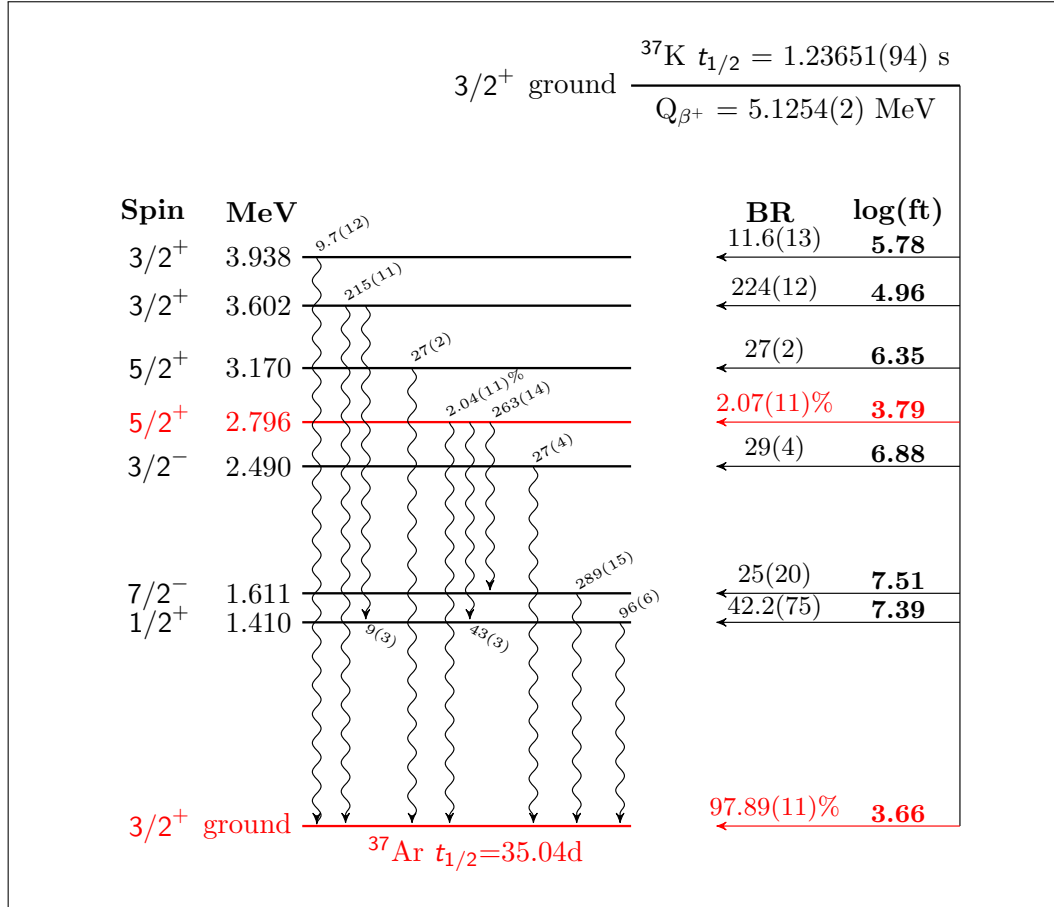


Figure 1.3: Energy level diagram of ^{37}K . Unless denoted by a percent sign the units for the β and γ branching ratios are given in parts per million. The two levels highlighted in red are the levels that we are interested in. The main branch that we will measure is to the ground state of ^{37}Ar . It is a mixed transition and to make a standard model prediction we need to have a value of ρ . The 2% branch is a pure Gamow-Teller transition therefore does not need a value of ρ to make a standard model prediction of $A_\beta = -0.6$. The half-life of potassium ^{37}K was taken from our group's recent measurement [23]. The branching ratios, spins, and energies were taken from [22]. Our group recently undertook an experiment to update the branching ratio measurements but the results were not ready for publication at this time.

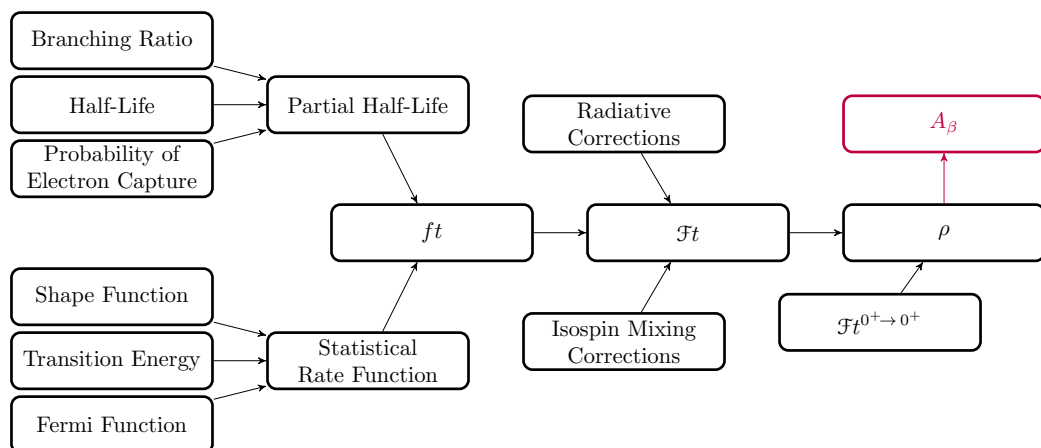


Figure 1.4: Map showing all of the sources from which the standard model prediction of A_β is derived. Until recently the largest uncertainty in the SM model prediction of A_β for ^{37}K was derived from the contribution of the uncertainty from the half-life [25]. For this reason a more precise measurement of the half-life was made at the Texas A&M University Cyclotron Institute [23].

their technique and showing all of the dependencies of the SM prediction of A_β is shown in Fig. 1.4. For β^+ mirror transitions the expression for A_β in the limit of zero momentum transfer is:

$$A_\beta = \frac{\rho^2 - 2\rho\sqrt{J(J+1)}}{(1 + \rho^2)(J + 1)}, \quad (1.4)$$

where J is the nuclear spin, and the value ρ is defined as,

$$\rho \equiv C_A M_{GT} / C_V M_F. \quad (1.5)$$

C_A (C_V) are the axial-vector (vector) coupling constants and M_{GT} (M_F) the Gamow-Teller (Fermi) matrix elements. Eq. 1.4 is sufficiently complete in terms of the physics that it encapsulates to be referred to as the SM prediction of A_β at zero β kinetic energy. We will see in Chapter 3 that there are also small corrections called recoil-order

effects that modify the value of A_β as a function of the kinetic energy of the emitted β .

1.4 Simple Overview of the Experiment

Not all isotopes are equal. Some are more interesting to study because they present enhanced sensitivity to certain physics. Others are more often studied because they are easier to make and work with. Here is a summary of the most important points about ^{37}K that make it both an interesting and practical case to study.

Isobaric Analog Decay Recoil-order corrections can be computed.

97.89% Branching Ratio Small background from decays to non-analog states.

1.2365 s Halflife Can be made and transported effectively. Reasonable count rates.

Low losses from the trap.

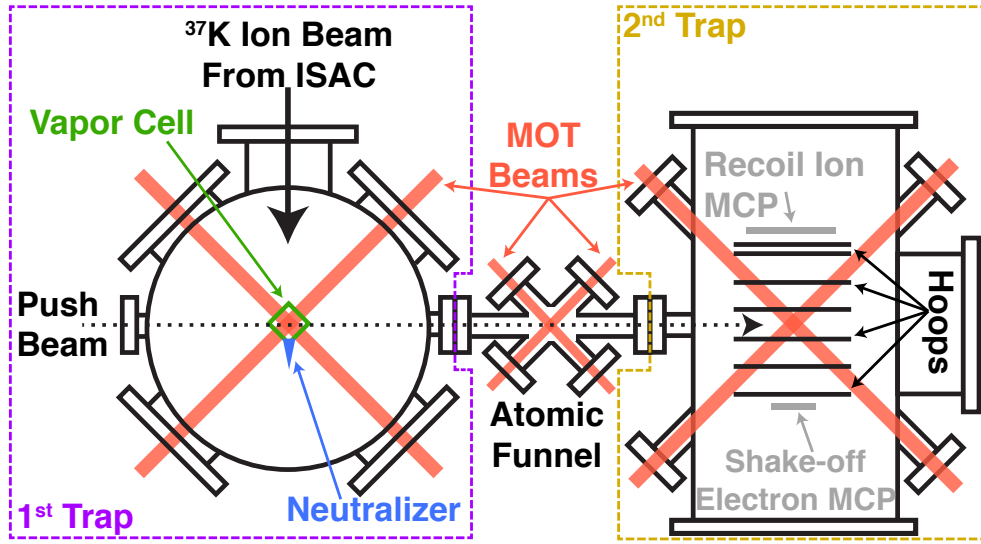
A_β Never Measured Adding another case to SM test.

B_ν Previously Measured Allows for consistency checks.

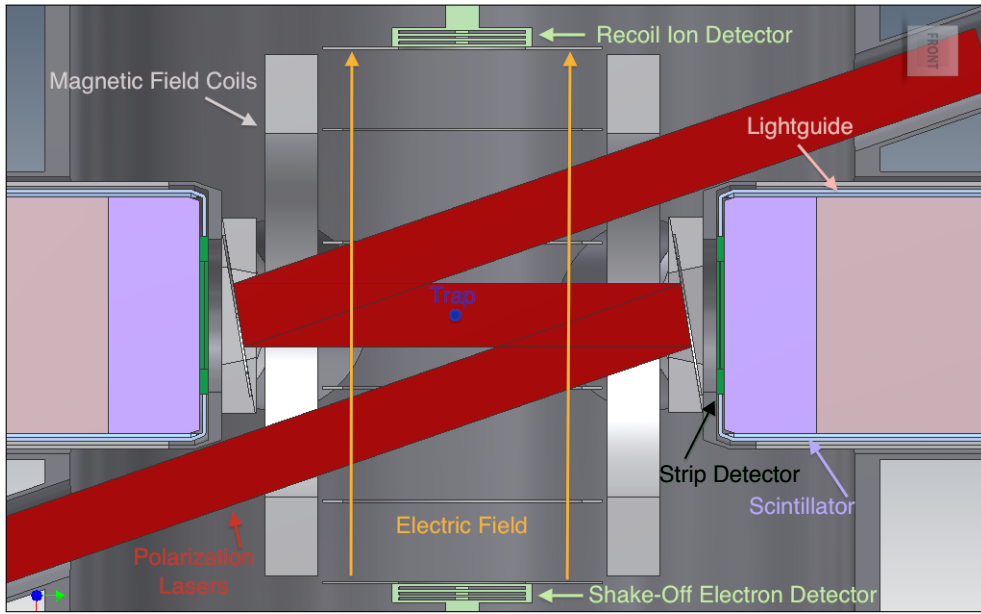
Alkali Metal Electronic structure suitable for trapping in a MOT.

Hyperfine structure similar to ^{41}K Trap development can be done offline.

The experiment was carried out at the ISAC facility at TRIUMF. ^{37}K was produced by bombarding a TiC target with 40 μA of 500 MeV protons from the TRIUMF main cyclotron and up to 3.8×10^7 $^{37}\text{K}/\text{s}$ [26] were extracted and transported at 60 keV to the TRINAT end station where it was neutralized and confined using a double-MOT system. In order to understand how the experiment works it is necessary to understand the geometry of the experimental setup. A simplified version of this is shown in Fig. 1.5b. Initially the radioactive atoms are confined and cooled in the center of the large vacuum volume by the combined action of AC-MOT lasers [28] (not shown) and an oscillating 1 kHz magnetic field produced by the magnetic field



(a) Schematic of the TRINAT two MOT system



(b) Schematic of geometry elements in the 2nd trap.

Figure 1.5: Model of experimental geometry. Fig. 1.5a is a schematic of the two MOT system [27]. The incoming ion beam is stopped in a neutralizer. A very small fraction of the neutral ^{37}K is trapped in a 1st trap and these atoms after cooling are pushed over the the 2nd trap where the experiment takes place. Fig. 1.5b is a cut away view with important parts of the 2nd trap geometry labeled. To give a sense of scale the laser beams are 2.4 cm in diameter. The polarization axis is defined by the propagation direction of the laser beams because of this the strip detectors and scintillators which together comprise the β detectors are placed along this axis. The direction of the polarization vector, right or left, along the polarization axis is controlled by the circular polarity of the laser light.

coils. Then the atoms are released from the confining field and are polarized through the action of the optical pumping laser, shown in Fig. 1.5b, and a static 2.5 G magnetic field produced by the same coils that produced the MOT field. After $\approx 100 \mu\text{s}$ of optical pumping, the nuclear spins of the ensemble of atoms are almost perfectly aligned with the β -detection axis. This is when we start counting. The polarization of the atoms can be flipped by changing the polarity of the OP light and is done every 16 s. The β -detection axis is defined by the propagation direction of the laser beams and for this reason our detectors, silicon strip detectors backed by plastic scintillators, are placed along this axis as shown in Fig. 1.5b.

An experiment was performed earlier by the TRINAT collaboration to measure A_β in ^{37}K . However, the experiment suffered from a large background: atoms escaped from the trap and adhered to surfaces inside the chamber, and would depolarize before decaying. This large background of valid – albeit unpolarized – β decays reduced the asymmetry signal from the polarized atoms in the trap. To reduce this background a shakeoff electron detector, pioneered at Berkeley [29] and tested in a previous TRINAT experiment, was added as a coincidence condition that allowed us to trigger off of events that originated in the trap and exclude most of the unpolarized background. Shakeoff electrons from a decay were swept by the 350V/cm field onto an MCP and its time was recorded. The MCP used for this task was only 40 mm in diameter. This means that most electrons originating from places other than the trap cannot reach it and in this manner we can exclude most of the unpolarized background.

In Eq. 1.1 we saw a simplified decay rate, ω , for the ^{37}K atoms. In the simplified context that we are working under we will make an assumption to further our conceptual understanding of the experiment: The assumption is that $\cos \theta = \cos(0)$ for the detector pointed to by the angular momentum vector of the nuclei and $\cos \theta = \cos(\pi)$

for the other detector. In this case A_β can be extracted from the observed asymmetry in the two detectors for a given polarization direction:

$$A_\beta \approx \frac{\omega^+ - \omega^-}{\omega^+ + \omega^-} \left(\frac{c}{v}\right) \left(\frac{1}{P}\right). \quad (1.6)$$

Where ω^\pm is the rate of β s observed in the detector that is in the direction of (+) or opposite (-) the direction pointed to by the original nuclear spin vector. The reason for showing Eq. 1.6 was to point out that to measure A_β we need three things. First, we need a measurement of the polarization of the atoms, P . Second, we need a measurement of the kinetic energy of the β to obtain v/c . Third, we need the observed asymmetry as seen by our detectors. There are other terms that make a non-negligible contribution (for example, the alignment term will sum in the denominator), but they will be accounted for in the final data analysis and are not shown here for the sake of simplicity. In addition, our final analysis will use the super-ratio instead of the naive asymmetry shown in Eq. 1.6. The super-ratio can be thought of as a ratio of ratios and is shown in detail in Section 6.2.1. The asymmetry computed via the super-ratio uses not only information from both detectors but uses the additional information gained by changing the spin direction. The reason for using the super-ratio is that more sources of systematic uncertainty cancel out; such an analysis was used recently in extracting A_β from the decay of ultra-cold neutrons [30].

In experiments of this type, knowledge of the polarization is the most critical aspect because it enters into the final decay rate multiplied by, A_β , the quantity that we are trying to measure. It is possible to measure *in situ* the polarization of the atoms independent of the asymmetry by selectively ionizing valence electron from the excited state in the optical pumping transition. This technique was successfully

used in this experiment to measure photoions. When fitting this data a large model dependent systematic uncertainty was observed. This subject is covered in depth in chapter 5.

1.5 The Author's Contribution

My first contribution to this project was to engineer a new experimental chamber. Much consideration was given to every aspect of the of its design. The chamber that had been in place at TRINAT had served well for many years but was initially optimized for an experiment with ^{38m}K that had neither optical pumping lasers nor optical pumping aligned beta detectors. Additionally because of its small size, the old chamber would have limited us to detectors of very small solid angle coverage. In addition to these mechanical limitations, trapping technology has progressed and the newly designed chamber allowed us to take advantage of some of those advances, specifically an AC-MOT [28]. This redesign was therefore a crucial step to allow the TRINAT collaboration to move into a new era of precision measurements.

The second major contribution that I made to the project was the development of a realistic **GEANT4** model of the experimental setup. The **GEANT4** simulations were used in all phases of the experiment. They were used in the design phase to make choices about construction materials and distances. They have also been used in the final analysis to fit the experimental results in order to extract our physics result.

The third major contribution that I made to the experiment was the development of the data acquisition system along with the commissioning of the detectors. This included optimizing the scintillator signal by determining the optimal length of the lightguides and determining which wrapping material to use, and how much μ -metal shielding was needed. It also included testing the silicon detectors and debugging the position-sensitive readout and implementing the algorithms to deter-

mine the energy from the digitized waveforms. It also involved the creation of a fast field programmable gate array (FPGA) trigger and the mechanical alignment of the detectors.

The fourth major contribution was in the analysis of the collected data. From the beginning of this project a follow-up had been planned. The analysis of this data set allowed us to learn about the major systematic errors that we need to correct and mitigate in the follow-up experiment in order to make a truly precision measurement.

2. THEORETICAL BACKGROUND

Discoveries in β -decay theory have been instrumental in the creation and development of the SM. It will not be possible in the present work to give a complete review of the entire history of β -decay or an extensive review of the SM. I will limit my discussion in this section to the part of the SM and some of the most common extensions of the SM as they pertain to a measurement of A_β .

2.1 Jackson, Treiman, Wyld and the Standard Model

One of the classic papers in the field of beta decay was written by Jackson, Treiman, Wyld in 1957 [31] and built off of the groundbreaking work of Lee and Yang from the previous year [1]. In it the authors considered a number of possible experiments and wrote down decay rates for them considering all of the possible Lorentz-invariant forms of the weak interaction in allowed β decay, namely vector, axial-vector, scalar, and tensor. The authors give decay rates for different experiments considering the possible presence of all of these interactions.

One of the decay rates that they give is for an experiment using what they called “oriented” nuclei. Throughout this work I will use almost exclusively the similar but not exactly equivalent term “polarized”, the distinction being that an atom can have its spin aligned along the polarization axis in one of two possible ways. Polarization is the expectation value of the spin directions projected on a given axis. In our case this axis is defined by the optical pumping laser beams. It is possible that if 50% of the atoms have their spins aligned along this axis in one direction and the other 50% have their spins pointed along the axis in the other direction, the alignment or orientation of the atoms would be 100% but the polarization would be 0%. On the other hand if 100% of the atoms have their spins pointed in the same direction along

this axis then the polarization would be 100% and this also implies the orientation would still be 100%. The decay rate as given in Jackson's paper for experiments involving polarized nuclei is,

$$\begin{aligned} \omega(\langle J \rangle | E_e, \Omega_e, \Omega_\nu) dE_e d\Omega_e d\Omega_\nu &= \frac{1}{(2\pi)^5} |\vec{p}_e| E_e (E_e^0 - E_e)^2 dE_e d\Omega_e d\Omega_\nu \xi \left\{ 1 + a_{\beta\nu} \frac{\vec{p}_e \cdot \vec{p}_\nu}{E_e E_\nu} \right. \\ &+ b_{\text{Fierz}} \frac{m_e}{E_e} + c_{\text{align}} \left[\frac{\vec{p}_e \cdot \vec{p}_\nu}{3E_e E_\nu} - \frac{(\vec{p}_e \cdot \hat{j})(\vec{p}_\nu \cdot \hat{j})}{E_e E_\nu} \right] \left[\frac{J(J+1) - 3\langle (\vec{J} \cdot \hat{j})^2 \rangle}{J(2J-1)} \right] \\ &\left. + \frac{\langle \vec{J} \rangle}{J} \cdot \left[A_\beta \frac{\vec{p}_e}{E_e} + B_\nu \frac{\vec{p}_\nu}{E_\nu} + D \frac{\vec{p}_e \times \vec{p}_\nu}{E_e E_\nu} \right] \right\}. \end{aligned} \quad (2.1)$$

Let us start the process by identifying all of the terms in the equation. ω is the decay rate of the polarized atoms. The $dE_e d\Omega_e d\Omega_\nu$ multiplied by ω means that this is a differential decay rate, or in other words that to determine the rate itself we must integrate over some area of the electron energy spectrum and some piece of solid angle. This rate is for polarized atoms, where $\langle \vec{J} \rangle$ denotes the expectation value of nuclear spin vector and \hat{j} is a unit vector in the direction of $\langle \vec{J} \rangle$. Along these same lines also notice that in the equation there are terms for the magnitude of the nuclear spin J and vector values for the nuclear spin \vec{J} . In later chapters when we talk about measuring the polarization of the atoms, the number that we are trying to measure corresponds to $\langle \vec{J} \rangle / J$. As mentioned in the previous paragraph there is a distinction between polarization and alignment. The term,

$$\left[\frac{J(J+1) - 3\langle (\vec{J} \cdot \hat{j})^2 \rangle}{J(2J-1)} \right], \quad (2.2)$$

is the alignment. The vectors \vec{p}_e and \vec{p}_ν are the electron and neutrino 3-momentum and E_e and E_ν are their total energies. The value denoted E_e^0 is the endpoint energy

of the β particle. The other terms ξ , $a_{\beta\nu}$, b_{Fierz} , c_{align} , A_β , B_ν , and D are all special values that are defined in the paper. These parameters describe in a general way the β -decay mediated by the weak interaction. Since the authors went out of their way to allow for all possible interactions, when we invoke the standard model assumptions some of these terms are identically zero. The rest were incorporated into the standard model and have definite predictions for their values. We will see in the next section how to calculate such a prediction in an effort to understand what we are assuming when we do so. A table showing the SM predicted values for these values is shown in Table 2.1.

2.1.1 A Toy Beta Energy Spectrum

At this point it will be profitable to take a look at a smaller more manageable piece of Eq. 2.1 and connect back to something that should be familiar to us. The first piece includes the kinematic terms that come at the beginning of the equation:

$$\omega_0 = \frac{1}{(2\pi)^5} |\vec{p}_e| E_e (E_e^0 - E_e)^2. \quad (2.3)$$

The easiest way to understand what this function does will be to rearrange it in terms of the kinetic energy of the emitted beta (T_e) and to plot the result. The rearranged equation is,

$$\omega_0(T_e) = \frac{1}{(2\pi)^5} (T_e + m_e) (T_e^0 - T_e)^2 \sqrt{(T_e + m_e)^2 - m_e^2}, \quad (2.4)$$

and the plot showing the result using the value of $T_e^0 = 5.125461$ MeV for ^{37}K is shown in Fig. 2.1. Looking at the plot we see the familiar shape of a β energy spectrum. It is worth noting here that this is not the whole story about the β energy spectrum. There is one important contribution to the shape of the β spectrum

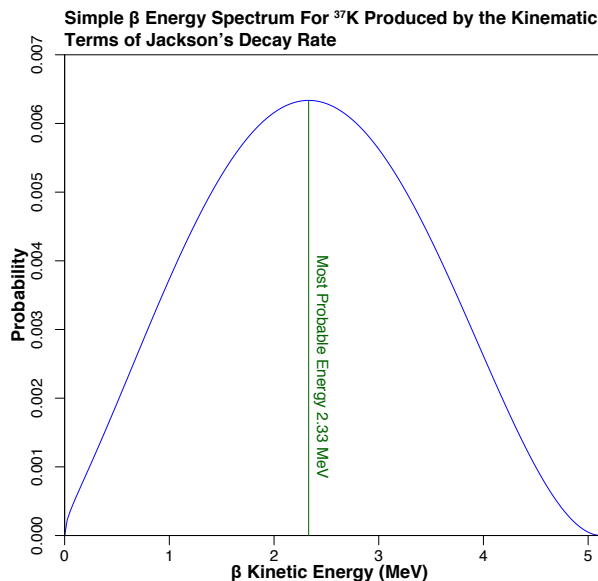


Figure 2.1: A simple kinematic β energy spectrum. From this simple beta spectrum we can learn useful information such as the most probably beta energy that can be found by taking the first derivative of Eq. 2.4 and setting it equal to zero and solving for T_e . The result of this operation is shown in Ref. [32] as equation A8 and A9.

that does not appear in Eq. 2.1: the Fermi function, $F(Z, E)$. The Fermi function modifies the simple beta spectrum shown in Fig. 2.1 to include the attractive or repulsive Coulomb force experienced by β^- and β^+ respectively in the presence of the charged daughter nucleus. Further discussion about the Fermi function appears in Section 3.5, where we will explore how to actually calculate it. Meanwhile it is sufficient to say that Eq. 2.3 is the beta energy spectrum and that Eq. 2.1 extends this simple spectrum to also include information about the angle of the emitted beta and neutrino.

2.1.2 The Form of A_β Assuming the Standard Model

We will now return to Jackson's polarized decay rate, shown in Eq. 2.1 and examine the correlation coefficients. In this section we will focus on A_β because that was the focus of our experiment, but this section will serve as an archetype for

Definitions From Jackson <i>et al.</i> Assuming the Standard Model		
Correlation Coefficient	SM definition	$^{37}\text{K } J = 3/2$
	$J' = J; \beta^+ \text{ decay}$	$\rho = 0.5766 \pm 0.0021$
$a_{\beta\nu}$	$\frac{1 - \rho^2/3}{1 + \rho^2}$	0.667 ± 0.002
b_{Fierz}	0	0
c_{align}	$\frac{\rho^2(2J - 1)}{(1 + \rho^2)(J + 1)}$	0.199 ± 0.001
A_β	$\frac{\rho^2 - 2\rho\sqrt{J(J + 1)}}{(1 + \rho^2)(J + 1)}$	-0.5706 ± 0.0007
B_ν	$\frac{-\rho^2 + 2\rho\sqrt{J(J + 1)}}{(1 + \rho^2)(J + 1)}$	-0.770 ± 0.002
D	0	0

Table 2.1: The standard model correlation coefficients that enter into experiments with polarized nuclei. Also shown are their standard model predictions and values for ^{37}K . The value of ρ shown here was calculated using the input values given in Ref. [25] except for the lifetime of ^{37}K that was taken from Ref. [23].

how the SM predictions of all of the correlation coefficients could be derived. If we examine a current paper on the topic of beta decay such as Ref. [16], we can find an expression for A_β that looks like this,

$$A_\beta = \frac{\rho^2 - 2\rho\sqrt{J(J+1)}}{(1+\rho^2)(J+1)}. \quad (2.5)$$

Our goal by the end of this section is to get back to Eq. 2.5. We will begin with Jackson's equation A3 for ξ [31],

$$\xi = |M_F|^2(|C_S|^2 + |C_V|^2 + |C'_S|^2 + |C'_V|^2) + |M_{GT}|^2(|C_T|^2 + |C_A|^2 + |C'_T|^2 + |C'_A|^2). \quad (2.6)$$

The reason for starting here is that Jackson only gives an expression for A_ξ so to arrive at A we will need to divide by ξ . To understand what we are doing we need to identify the terms. M_F and M_{GT} are the Fermi and Gamow-Teller matrix elements. The C_i s are the coupling constants for the different types of interactions with $i = S$ (scalar), V (vector), T (tensor), and A (axial-vector). There also exists the possibility of pseudo-scalar contributions that would appear in Eq. 2.6, but only if, as Jackson points out, the assumption that the recoiling ion can be treated non-relativistically does not hold. Jackson further explains the primed coefficients arise from the parity-nonconserving interactions introduced by Lee and Yang [33]. We will now apply our first SM assumption namely that vector and axial-vector currents exist and that tensor and scalar currents do not [34, 35]. The mathematical translation of this assumption is to set $C_T = C'_T = C_S = C'_S = 0$. Doing this allows us to simplify ξ :

$$\xi = |M_F|^2(|C_V|^2 + |C'_V|^2) + |M_{GT}|^2(|C_A|^2 + |C'_A|^2). \quad (2.7)$$

The second assumption that we will make is that neutrinos are massless and travel at the speed of light. In recent years the discovery of neutrino mass has meant that we now know that this is not true. It is good to keep in mind that it is an assumption made by the standard model and actually a very good one because the neutrino mass is so small. For a spin $1/2$ massless particle traveling at the speed of light there are two possible helicity states: ± 1 . Where helicity is defined as m_s/s with the spin projection axis being chosen as the direction of travel of the particle. We will call something right-handed with helicity = $+1$ if the spin points in the direction of travel $m_s = 1/2$ and we will call something left-handed with helicity = -1 if the spin points against the direction of travel $m_s = -1/2$. We will now go one step further and make the assumption that all neutrinos are left-handed and all anti-neutrinos are right-handed. This assumption is what we mean when we say that parity is maximally violated [36, 20]. It is worth noting here that saying neutrinos are massless and travel at the speed of light does not imply that they are all left-handed. Saying that they are all left-handed however does imply that they are massless and do travel at the speed of light. Helicity is only a Lorentz-invariant quantity if the particles are massless and traveling at the speed of light. This is how we know that the assumptions we made here are not 100% correct because neutrinos do have mass and that means helicity is no longer a Lorentz-invariant quantity. Putting that aside, in terms of the equation that we are currently examining, the mathematical translation of our assumption is $C_V = C'_V$ and $C_A = C'_A$.

There are some other sign conventions that have been used by various authors. Notably as pointed out in Appendix A of Ref. [37] authors such as Herczeg follow the γ matrix convention of [38]. This convention differs from that used by Jackson and can mean that the signs of each operation needs to be kept track of carefully if comparing between authors. Following through the steps shown here with an

alternate formalization such as $-C'_i = C_i$ would lead to the wrong sign for A_β . In the case of ξ it does not matter because of the absolute values, but in the case of $A_\beta\xi$ it does. Applying our constraint with the appropriate sign for our situation to ξ we arrive at the simplified version that we will use,

$$\xi = 2(|M_F|^2|C_V|^2 + |M_{GT}|^2|C_A|^2). \quad (2.8)$$

We will now follow a similar procedure starting from Jackson's equation A7 in Ref. [39] for $A_\beta\xi$ given as,

$$\begin{aligned} A_\beta\xi = 2 \left[\pm|M_{GT}|^2\lambda_{J'J} \left[\text{Re}(C_T C'_T{}^* - C_A C'_A{}^*) \right. \right. \\ \left. \left. + \frac{\alpha Z m_e}{p_e} \text{Im}(C_T C'_A{}^* + C'_T C_A{}^*) \right] \right. \\ \left. + \delta_{J'J} M_F M_{GT} \sqrt{\frac{J}{J+1}} \left[\text{Re}(C_S C'_T{}^* + C'_S C_T{}^* - C_V C'_A{}^* - C'_V C_A{}^*) \right. \right. \\ \left. \left. \pm \frac{\alpha Z m_e}{p_e} \text{Im}(C_S C'_A{}^* + C'_S C_A{}^* - C_V C'_T{}^* - C'_V C_T{}^*) \right] \right]. \quad (2.9) \end{aligned}$$

The \pm is to distinguish between electron decay (upper) and positron decay (lower). α is the fine structure constant and Z is the charge of the daughter nucleus. The lower sign applies to the positron decay of ^{37}K . $\lambda_{J'J}$ is a spin dependent function defined as equation A1 in Ref. [39] and $\delta_{J'J}$ is the Kronecker delta function. We will make the same assumption about tensor and scalar currents as above: namely $C_T = C'_T = C_S = C'_S = 0$

$$A_\beta\xi = 2\Re \left[-|M_{GT}|^2\lambda_{J'J}(-C_A C'_A{}^*) + \delta_{J'J} M_F M_{GT} \sqrt{\frac{J}{J+1}} (-C_V C'_A{}^* - C'_V C_A{}^*) \right]. \quad (2.10)$$

We will also make the same assumption of maximal parity violation , $C_V = C'_V$ and $C_A = C'_A$. We will now invoke our third assumption that time reversal symmetry is not violated. Mathematically this is the same thing as saying that the coupling constants C_i are all real and we can therefore drop the complex conjugates

$$A_\beta \xi = 2 \left[|M_{GT}|^2 \lambda_{J'J} |C_A|^2 - 2\delta_{J'J} M_F M_{GT} \sqrt{\frac{J}{J+1}} (C_V C_A) \right]. \quad (2.11)$$

In order to find A_β we divide Eq. (2.11) by Eq. (2.8) to get

$$\frac{A_\beta \xi}{\xi} = \frac{2 \left[|M_{GT}|^2 \lambda_{J'J} |C_A|^2 - 2\delta_{J'J} M_F M_{GT} \sqrt{\frac{J}{J+1}} (C_V C_A) \right]}{2(|M_F|^2 |C_V|^2 + |M_{GT}|^2 |C_A|^2)}. \quad (2.12)$$

Dividing the numerator and denominator by $|C_V|^2 |M_F|^2$ we obtain

$$A_\beta = \frac{\frac{|M_{GT}|^2 |C_A|^2}{|M_F|^2 |C_V|^2} \lambda_{J'J} - 2\delta_{J'J} \sqrt{\frac{J}{J+1}} \frac{M_{GT} C_A}{M_F C_V}}{1 + \frac{|M_{GT}|^2 |C_A|^2}{|M_F|^2 |C_V|^2}}. \quad (2.13)$$

We will now invoke the definition of ρ given in Eq. 1.5 to arrive at,

$$A_\beta = \frac{\rho^2 \lambda_{J'J} - 2\delta_{J'J} \sqrt{\frac{J}{J+1}} \rho}{1 + \rho^2}. \quad (2.14)$$

Now for the case of all of the mirror transitions considered in [16] $J' = J$. Therefore we can write $\lambda_{J'J}$ as $1/(J+1)$ and the value of Kronecker delta as 1 giving,

$$A_\beta = \frac{\rho^2 \frac{1}{J+1} - 2\sqrt{\frac{J}{J+1}} \rho}{1 + \rho^2},$$

$$A_\beta = \frac{\rho^2 - 2\rho\sqrt{J(J+1)}}{(1 + \rho^2)(J+1)}. \quad (2.15)$$

which agrees with Eq. 2.5.

2.2 Interpreting a Measurement of A_β in the Context of the Standard Model

In the last section we examined the assumptions that we make when using the SM to calculate predictions of the correlation coefficients of polarized ^{37}K . In this section we will take a step back and look at how our measurement could be combined with others to form a different test of the SM. One way to test the SM is to test the unitarity condition of the Cabibbo-Kobayashi-Maskawa (CKM) quark mixing matrix, which transforms quark mass eigenstates into quark weak eigenstates. The formulation of this test can be written down using the elements of the first row of the CKM matrix [40]:

$$|V_{ud}|^2 + |V_{us}|^2 + |V_{ub}|^2 = 1. \quad (2.16)$$

The test is most sensitive to the dominant terms $|V_{ud}|$ and $|V_{us}|$ and their uncertainties. The first term $|V_{ud}|$ is obtained by study of weak decays involving the lightest quarks, and $|V_{us}|$ from the decay of K-mesons. Much work has been done over many years to measure $|V_{ud}|$ to a fantastic level of precision. Currently the strictest limit placed on $|V_{ud}|$ comes from evaluation of the set of nuclear superallowed $0^+ \rightarrow 0^+$, pure Fermi transitions [17]. Recently it was shown that a complimentary evaluation could be carried out for a set of $T = 1/2$ mirror transitions, including ^{37}K [16]. In this evaluation, exactly like the mixed decay of the neutron, it is necessary to have an independent measurement of the $\mathcal{F}t$ for the transition and of one of the SM correlation parameters. Despite appearing in the review, ^{37}K did not contribute significantly to the final result because of the large 3% error in the neutrino asymmetry parameter, B_ν [15], used in the calculation. A 1% measurement of A_β would be a timely addition to the body of data used to calculate $|V_{ud}|$ in this manner as it can

be used in conjunction with the value of B_ν in the calculation and the value from ^{37}K would contribute more meaningfully to the overall result.

The way that this is done is described in [16] for a set of $T=1/2$ mirror nuclei and recently carried out specifically for the case of ^{37}K in [23]. The first step of the procedure is to define $\mathcal{F}t_0$ as follows

$$\mathcal{F}t_0 = \mathcal{F}t C_V^2 |M_F^0|^2 \left(1 + \left(\frac{f_A}{f_V} \right) \rho^2 \right). \quad (2.17)$$

In this equation $\mathcal{F}t$ is the corrected ft value and includes corrections for radiative and isospin-symmetry-breaking effects. M_F^0 is the isospin symmetry limit of the Fermi matrix element and has a value of 1 for $T = 1/2$ mirror transitions. Additionally f_A and f_V are the statistical rate functions for the axial and vector parts of the interaction. The vector coupling constant, C_V , has been introduced previously along with ρ . If the vector current is conserved and the correction terms are valid, $\mathcal{F}t_0$ should be the same across the whole set of $T = 1/2$ transitions. In order to use our measurement of A_β to extract the ρ we need to invert Eq. 2.15. During this inversion we need choose the appropriate sign from the quadratic formula giving

$$\rho = \frac{-\sqrt{J(J+1)} + \sqrt{J(J+1) + (J+1)A_\beta - (J+1)^2 A_\beta^2}}{-1 + (J+1)A_\beta}. \quad (2.18)$$

For each isotope in the set we calculate $\mathcal{F}t_0$; then we will find the weighted average of these and call this value $\overline{\mathcal{F}t_0}$ [16]. This quantity will be related to V_{ud} in the following manner:

$$V_{ud}^2 = \frac{K}{\overline{\mathcal{F}t_0} G_F^2 (1 + \Delta_R^V)} \quad (2.19)$$

where $K/(\hbar c)^6 = 2\pi^3 \ln 2\hbar/(m_e c^2)^5 = 8120.278(4) \times 10^{-10} \text{ GeV}^{-4}\text{s}$ [23], the Fermi constant $G_F/(\hbar c)^3 = 1.16637(1) \times 10^{-5} \text{ GeV}^{-2}$ [41], and Δ_R^V is a radiative correction calculated for the vector current. At the conclusion of this work, Sec. 6.6.2, these equations are used with the value of A_β that we measured to extract a value for $|V_{ud}|$ from the set of $T = 1/2$ mirror transitions given in Ref. [16].

2.3 Modification to the Standard Model due to Right-Handed Currents

Let us suppose that the SM is not correct. In that case its predictions would fail. Through the years experiments have sought to test the SM predictions to a high degree of accuracy to see if the measured values and the calculated values agree. If the agreement is good between the SM and experimentally measured values then this restricts the validity of other models that produce a prediction in disagreement with the measured values.

β -decay observables are no exception to this general pattern of prediction and measurement and model refinement. In section 2.1.2 we saw some of the assumptions that were made in constructing our SM predictions of the β -decay correlation parameters. It is possible to construct other models where these same assumptions are relaxed or simply do not apply. For example, what if we relaxed the assumption that all neutrinos are left-handed and all anti-neutrinos are right-handed? What effect would this have on β -decay? Mathematically this would mean that the value of $C_V \neq C'_V$ since their equality implies maximal parity violation. The expression for A_β using the same definition of ρ from Eq. 2.13 and making the assumption that $C_V \neq C'_V$ is

$$A_\beta = \frac{\rho^2 \lambda_{J,J} (1 + \frac{|C'_A|^2}{|C_A|^2}) - 2\delta_{J,J} \rho \sqrt{\frac{J}{J+1}} (\frac{C'_A}{C_A} + \frac{C'_V}{C_V})}{(1 + \frac{|C'_V|^2}{|C_V|^2}) + \rho^2 (1 + \frac{|C'_A|^2}{|C_A|^2})}. \quad (2.20)$$

We will be looking at this equation in more detail in the following sections. It is important to understand some of the theory behind this equation and some of the other theoretical consequences of this relaxation of the standard model assumptions. One way of constructing such a model would be to extend the $SU(2)_L \otimes U_1$ gauge group of the electroweak sector of the SM to $SU(2)_R \otimes SU(2)_L \otimes U_1$ [42, 32, 43, 44]. Extending the SM in this manner would mean that there are at least three new gauge bosons W_R^\pm and Z' . The W_R and the W_L , its standard model counterpart, are the mediators of charged weak processes. These weak eigenstates are a superposition of the the W mass eigenstates, W_1^\pm and W_2^\pm . Following the notation of Herczeg [45],

$$\begin{aligned} W_L &= W_1 \cos \zeta + W_2 \sin \zeta \\ W_R &= -W_1 \sin \zeta + W_2 \cos \zeta, \end{aligned} \tag{2.21}$$

where ζ is the mixing angle and we will define $\delta \equiv m_1^2/m_2^2$.

In the literature there is a class of models known as manifest left-right symmetric[46, 47, 48]. Such models assume that the details of the two different sectors are the same: *viz.* the quark mixing matrix elements $V_{ud}^L = V_{ud}^R$, and the couplings of the interactions $g_L = g_R$, and additionally they ignore any CP violation that would arise from complex phases in the mixing. The difference in the decay rates under this model arises from the mass difference between W_1 and W_2 and the degree of mixing ζ . Historically such manifest left-right symmetric models were parameterized in terms of two quantities x and y or r_V and r_A . I will explain these parameterizations in detail in the next section.

Following the same pattern of increasing complexity followed to this point we will further discuss another set of models that relax the assumptions that are made in the manifest case and have $V_{ud}^L \neq V_{ud}^R$, $g_L \neq g_R$, and they also include the possibility

of CP violating phases [32, 45, 49]. Luckily for us these models use the same C_i s that were introduced in Eq. 2.1 for their entry point and are thus more clear to how right handed currents affect the measured observables in light of what has already been shown here. In the next two sections I will lay out these two types of models and show how they relate to one another.

2.3.1 *The Manifest Left-Right Symmetric Model*

One of the most concise and accessible explanations of the manifest left-right symmetric model, specifically as it applies to the β -decay of free neutrons was written by Abele [46]. The neutron is a good place to for us to start when looking at decay observables because it is a mixed transition just like ^{37}K . This means that in the equations a λ will be present that will act as a place holder for our value ρ . This similarity means that anything that we learn from neutron decay will be immediately applicable to ^{37}K after changing signs from e^- to e^+ decay and changing any spin functions for $J = 1/2$ to use $J = 3/2$. In the paper Abele lays out expressions for the decay observables in the neutron including A_β , and B_ν and how they would be modified in the presence of right-handed currents. This is good because for ^{37}K we have a previous measure of B_ν and are currently trying to make a measurement of A_β . The major difficulty that I encountered when using this paper was that most of the equations written in the paper contain typographical errors or are simply wrong.

One of the goals of this chapter is to be able to write code to make exclusion plots of the right-handed current model parameters based on currently available experimental input. To give us confidence that our code is working correctly we will need to be able to compare its results to published limits. In Abele's paper there is an exclusion plot of the parameters δ and ζ (see Eq. 2.21 and following). If I try to reproduce his figure using the expressions listed in the paper it does not work.

In order to reproduce his figure I had to make the corrections listed in Table 2.2 to his equations. I have listed references where appropriate to justify making these changes. Before I show any of the results from the program I will show in detail one of the correction exercises that I performed because we will use the result from this section in the next section for comparison to non-manifest models and thus it is critical to use the right expression for the comparison.

Abele, as shown in Table 2.2, uses the notation of Bég [47] who was the first author to publish a paper about the right-handed current models applied to nuclear β -decay. His notation uses r_A , and r_V . As mentioned earlier, other authors use x and y , where $r_A = y$, and $r_V = x$. This notation was introduced the same year by Holstein [48]. Throughout this section we will use the r_V and r_A notation from Bég because it is easier to connect back to the vector and axial vector nature of the interaction.

The correction that I intend to show is the expansion of r_V and r_A in terms of δ , the mass ratio, and ζ , the mixing angle given. The expansion origin of the expansion is Ref. [48]. We will show here how these expressions were derived. In the process we will come up with a change in minus signs from what is shown in the reference. The correct expressions that we will derive for r_V and r_A are

$$\begin{aligned} r_V &= \frac{\delta(1 + \tan \zeta) - \tan \zeta(1 - \tan \zeta)}{\delta \tan \zeta(1 + \tan \zeta) + (1 - \tan \zeta)}, \\ r_A &= \frac{\delta(1 - \tan \zeta) + \tan \zeta(1 + \tan \zeta)}{-\delta \tan \zeta(1 - \tan \zeta) + (1 + \tan \zeta)}. \end{aligned} \tag{2.22}$$

To show that my expressions are correct I will start at the beginning and lay out explicitly everything that we need to now in order to arrive at Eq. 2.22. If one

Definition	Citation for Correction
$\epsilon = \frac{1 + \tan \zeta}{1 - \tan \zeta}$	
$r_V = \frac{1 + \eta_{VA}}{1 - \eta_{VA}},$	
$r_A = \frac{\eta_{AA} + \eta_{VA}}{\eta_{AA} - \eta_{VA}}$	
$\eta_{AA} = \frac{\epsilon^2 + \delta^2}{\epsilon^2 \delta + 1}$	
$\eta_{VA} = \frac{\epsilon \delta - \epsilon}{\epsilon^2 \delta + 1}$	[47]
$A_\beta = \frac{-2(\lambda^2(1 - r_A^2) + \lambda(1 - r_A r_V))}{\epsilon^2 \delta + 1}$	[50, 32]
$B_\nu = \frac{2(\lambda^2(1 - r_A^2) - \lambda(1 - r_A r_V))}{\epsilon^2 \delta + 1}$	Symmetry with A_β
$\frac{ft^{0^+ \rightarrow 0^+}}{f^R \tau_{\text{neutron}} \ln 2} = \frac{(1 + r_V^2) + 3\lambda^2(1 + r_A^2)}{2(1 + r_V^2)}$	Algebra Error

Table 2.2: Definition of manifest left-right symmetric model parameters for the neutron. The table also list citations for corrections to the expressions if they differ from what is listed by Abele [46].

examines [48] one sees that r_V and r_A are defined as follows,

$$\begin{aligned} r_V &= \frac{1 + \eta_{VA}}{1 - \eta_{VA}}, \\ r_A &= \frac{\eta_{AA} + \eta_{VA}}{\eta_{AA} - \eta_{VA}}. \end{aligned} \tag{2.23}$$

It should be noted that sometimes in the paper Holstein writes η_{VA} and at other times η_{AV} to mean the same thing. I believe the source of this confusion comes from the fact that this paper is a comment on Bég's paper where η_{AV} was defined. I will use the Holstein notation. Since Holstein was only commenting on a previously published paper he never defines the η s in his paper and one is forced to look at the Bég paper to discover their definitions:

$$\begin{aligned} \eta_{AA} &= \frac{\epsilon^2 m_2^2 + m_1^2}{\epsilon^2 m_1^2 + m_2^2}, \\ \eta_{VA} &= \frac{-\epsilon(m_2^2 - m_1^2)}{\epsilon^2 m_1^2 + m_2^2}, \end{aligned} \tag{2.24}$$

where ϵ is defined to be

$$\epsilon = \frac{1 + \tan \zeta}{1 - \tan \zeta}. \tag{2.25}$$

Having all of the definitions in hand we will now begin the not too tedious process of showing that Eqs. 2.23 are the same as Eqs. 2.22. We will start by dividing the numerators and denominators of Eqs. 2.24 by m_2^2 and employing the definition that $\delta \equiv m_1^2/m_2^2$

$$\begin{aligned} \eta_{AA} &= \frac{\epsilon^2 + \delta}{\epsilon^2 \delta + 1}, \\ \eta_{VA} &= \frac{\epsilon \delta - \epsilon}{\epsilon^2 \delta + 1}. \end{aligned} \tag{2.26}$$

We will now insert the values from Eqs. 2.26 into Eqs. 2.23:

$$r_V = \frac{1 + \frac{\epsilon\delta - \epsilon}{\epsilon^2\delta + 1}}{1 - \frac{\epsilon\delta - \epsilon}{\epsilon^2\delta + 1}}, \quad (2.27)$$

$$r_A = \frac{\frac{\epsilon^2 + \delta}{\epsilon^2\delta + 1} + \frac{\epsilon\delta - \epsilon}{\epsilon^2\delta + 1}}{\frac{\epsilon^2 + \delta}{\epsilon^2\delta + 1} - \frac{\epsilon\delta - \epsilon}{\epsilon^2\delta + 1}}.$$

Multiplying the numerators and denominators by $\epsilon^2\delta + 1$, we come to something that is beginning to take a familiar form

$$r_V = \frac{\epsilon^2\delta + 1 + \epsilon\delta - \epsilon}{\epsilon^2\delta + 1 - \epsilon\delta + \epsilon}, \quad (2.28)$$

$$r_A = \frac{\epsilon^2 + \delta + \epsilon\delta - \epsilon}{\epsilon^2 + \delta - \epsilon\delta + \epsilon}. \quad (2.29)$$

For brevity, we will only finish the exercise for r_V since the reduction of the expression for r_A is similar. We start by inserting the values of ϵ from Eq. 2.25,

$$r_V = \frac{\left(\frac{1+\tan\zeta}{1-\tan\zeta}\right)^2\delta + 1 + \left(\frac{1+\tan\zeta}{1-\tan\zeta}\right)\delta - \left(\frac{1+\tan\zeta}{1-\tan\zeta}\right)}{\left(\frac{1+\tan\zeta}{1-\tan\zeta}\right)^2\delta + 1 - \left(\frac{1+\tan\zeta}{1-\tan\zeta}\right)\delta + \left(\frac{1+\tan\zeta}{1-\tan\zeta}\right)}. \quad (2.30)$$

and then multiply the numerator and denominator by $(1 - \tan\zeta)^2$:

$$r_V = \frac{(1 + \tan\zeta)^2\delta + (1 - \tan\zeta)^2 + (1 - \tan\zeta)(1 + \tan\zeta)\delta - (1 - \tan\zeta)(1 + \tan\zeta)}{(1 + \tan\zeta)^2\delta + (1 - \tan\zeta)^2 - (1 - \tan\zeta)(1 + \tan\zeta)\delta + (1 - \tan\zeta)(1 + \tan\zeta)}. \quad (2.31)$$

For the sake of completeness I will do the rest of the algebra: first

$$r_V = \frac{\delta + 2\delta\tan\zeta + \delta\tan^2\zeta + \delta - \delta\tan^2\zeta - 1 + \tan^2\zeta + 1 - 2\tan\zeta + \tan^2\zeta}{\delta + 2\delta\tan\zeta + \delta\tan^2\zeta - \delta + \delta\tan^2\zeta + 1 - \tan^2\zeta + 1 - 2\tan\zeta + \tan^2\zeta},$$

and then, combining terms, we come to the final result:

$$r_V = \frac{\delta + \delta \tan \zeta + \tan^2 \zeta - \tan \zeta}{\delta \tan^2 \zeta + \delta \tan \zeta - \tan \zeta + 1}. \quad (2.32)$$

A similar treatment given to r_A yields a similar result:

$$r_A = \frac{\delta - \delta \tan \zeta + \tan^2 \zeta + \tan \zeta}{\delta \tan^2 \zeta - \delta \tan \zeta + \tan \zeta + 1}. \quad (2.33)$$

It is apparent that the two parts of Eq. 2.22 perfectly match Eq. 2.32 and Eq. 2.33 and we have established that indeed these are valid representations of r_V and r_A now with the minus signs in the correct places.

2.3.2 The Non-Manifest Left-Right Symmetric Model

We will now examine the non-manifest models and try to understand how they relate to the manifest model and to the SM. I used as a starting point the equations found in Herczeg [49]. Combining Herczeg's equations directly with those from Jackson gives the wrong sign for A_β and B_ν . The problem as Severijns [37] explains is the different choice of γ matrices. Consequently the equations that I will use will follow γ matrix convention of Jackson and Severijns so there will be slight differences to Herczeg's equations. The thing that makes Herczeg's approach so valuable is that as a starting point for his work he begins by giving expressions for the coupling constants given originally in Jackson [31]. This helps us to make the connection back to what we saw in Sec. 2.1.2.

In order to tie everything together I will show that by enforcing the assumptions made in the manifest model that the non-manifest model will collapse to the same thing. Using this knowledge and the explicit connection to Eq. 2.1 written down by Herczeg we will then be armed with the knowledge that we will need to be able to

write down equations for how the SM correlation parameters would be affected by the presence of right handed currents.

Starting with Herczeg's equations for the SM coupling constants:

$$\begin{aligned}
C_V &= g_V(a_{LL} + a_{LR} + a_{RR} + a_{RL}), \\
C'_V &= g_V(a_{LL} + a_{LR} - a_{RR} - a_{RL}), \\
C_A &= g_A(a_{LL} - a_{LR} + a_{RR} - a_{RL}), \\
C'_A &= g_A(a_{LL} - a_{LR} - a_{RR} + a_{RL}).
\end{aligned} \tag{2.34}$$

Herczeg does not give explicit definitions for a_{LL} , a_{LR} , a_{RR} , and a_{RL} in his 2001 paper [49] but he does in his 1986 paper [45]. In this paper Herczeg gives the definitions in two parts. We will combine them here for the sake of simplicity,

$$\begin{aligned}
a_{LL} &= \left[\frac{g_L^2}{8m_1^2} \cos^2 \zeta + \frac{g_L^2}{8m_2^2} \sin^2 \zeta \right] \cos \theta_1^L, \\
a_{LR} &= \left[-\frac{g_L g_R}{8m_1^2} + \frac{g_L g_R}{8m_2^2} \right] \cos \zeta \sin \zeta e^{i(\alpha+\omega)} \cos \theta_1^R, \\
a_{RR} &= \left[\frac{g_R^2}{8m_1^2} \sin^2 \zeta + \frac{g_R^2}{8m_2^2} \cos^2 \zeta \right] e^{i\alpha} \cos \theta_1^R, \\
a_{RL} &= \left[-\frac{g_L g_R}{8m_1^2} + \frac{g_L g_R}{8m_2^2} \right] \cos \zeta \sin \zeta e^{-i\omega} \cos \theta_1^L.
\end{aligned} \tag{2.35}$$

These expressions involve two CP violating phases ω and α . In principle, CP violation could exist in this sector. However, our current object is to show the equivalence of the two models under a specific set of assumptions and, since the manifest model assumes no CP violation, we set both ω and α to zero here. We will also rewrite $\cos \theta_1^{(L/R)}$ as $V_{ud}^{(L/R)}$ following the example of [17]. We rewrite Eq. 2.35

using these modifications, which yields

$$a_{LL} = \left[\frac{g_L^2}{8m_1^2} \cos^2 \zeta + \frac{g_L^2}{8m_2^2} \sin^2 \zeta \right] V_{ud}^L, \quad (2.36)$$

$$a_{LR} = \left[-\frac{g_L g_R}{8m_1^2} + \frac{g_L g_R}{8m_2^2} \right] \cos \zeta \sin \zeta V_{ud}^R, \quad (2.37)$$

$$a_{RR} = \left[\frac{g_R^2}{8m_1^2} \sin^2 \zeta + \frac{g_R^2}{8m_2^2} \cos^2 \zeta \right] V_{ud}^R, \quad (2.38)$$

$$a_{RL} = \left[-\frac{g_L g_R}{8m_1^2} + \frac{g_L g_R}{8m_2^2} \right] \cos \zeta \sin \zeta V_{ud}^L. \quad (2.39)$$

Since our present intent is to check the consistency between the manifest and non-manifest models it is useful to put them into the same form. We do this by using the r_V and r_A notation that we used in the last section. We find a definition for constructing r_V and r_A in terms of Eq. 2.35 in [51]:

$$r_V = \frac{a_{RR} + a_{RL}}{a_{LL} + a_{LR}}, \quad (2.40)$$

$$r_A = \frac{a_{RR} - a_{RL}}{a_{LL} - a_{LR}}. \quad (2.41)$$

Expanding all of the definitions of a_{LL} , a_{LR} , a_{RR} , and a_{RL} in Eq. 2.40 - 2.41 we come to,

$$r_V = \frac{\left[\frac{g_R^2}{8m_1^2} \sin^2 \zeta + \frac{g_R^2}{8m_2^2} \cos^2 \zeta \right] V_{ud}^R + \left[-\frac{g_L g_R}{8m_1^2} + \frac{g_L g_R}{8m_2^2} \right] \cos \zeta \sin \zeta V_{ud}^L}{\left[\frac{g_L^2}{8m_1^2} \cos^2 \zeta + \frac{g_L^2}{8m_2^2} \sin^2 \zeta \right] V_{ud}^L + \left[-\frac{g_L g_R}{8m_1^2} + \frac{g_L g_R}{8m_2^2} \right] \cos \zeta \sin \zeta V_{ud}^R}, \quad (2.42)$$

$$r_A = \frac{\left[\frac{g_R^2}{8m_1^2} \sin^2 \zeta + \frac{g_R^2}{8m_2^2} \cos^2 \zeta \right] V_{ud}^R - \left[-\frac{g_L g_R}{8m_1^2} + \frac{g_L g_R}{8m_2^2} \right] \cos \zeta \sin \zeta V_{ud}^L}{\left[\frac{g_L^2}{8m_1^2} \cos^2 \zeta + \frac{g_L^2}{8m_2^2} \sin^2 \zeta \right] V_{ud}^L - \left[-\frac{g_L g_R}{8m_1^2} + \frac{g_L g_R}{8m_2^2} \right] \cos \zeta \sin \zeta V_{ud}^R}.$$

We now continue to apply more of the assumptions of the manifest left-right model; viz. $V_{ud}^R = V_{ud}^L = V_{ud}$ and $g_L = g_R = g$. Applying these conditions allows for the cancellation of many extra terms,

$$\begin{aligned}
r_V &= \frac{\left[\frac{1}{m_1^2} \sin^2 \zeta + \frac{1}{m_2^2} \cos^2 \zeta \right] + \left[-\frac{1}{m_1^2} + \frac{1}{m_2^2} \right] \cos \zeta \sin \zeta}{\left[\frac{1}{m_1^2} \cos^2 \zeta + \frac{1}{m_2^2} \sin^2 \zeta \right] + \left[-\frac{1}{m_1^2} + \frac{1}{m_2^2} \right] \cos \zeta \sin \zeta}, \\
r_A &= \frac{\left[\frac{1}{m_1^2} \sin^2 \zeta + \frac{1}{m_2^2} \cos^2 \zeta \right] - \left[-\frac{1}{m_1^2} + \frac{1}{m_2^2} \right] \cos \zeta \sin \zeta}{\left[\frac{1}{m_1^2} \cos^2 \zeta + \frac{1}{m_2^2} \sin^2 \zeta \right] - \left[-\frac{1}{m_1^2} + \frac{1}{m_2^2} \right] \cos \zeta \sin \zeta}.
\end{aligned} \tag{2.43}$$

From here on out the process is simple algebra. So we multiply by m_1^2/m_1^2 and rearrange to come up with,

$$\begin{aligned}
r_V &= \frac{\sin^2 \zeta + \delta \cos^2 \zeta - \cos \zeta \sin \zeta + \delta \cos \zeta \sin \zeta}{\cos^2 \zeta + \delta \sin^2 \zeta - \cos \zeta \sin \zeta + \delta \cos \zeta \sin \zeta}, \\
r_A &= \frac{\sin^2 \zeta + \delta \cos^2 \zeta + \cos \zeta \sin \zeta - \delta \cos \zeta \sin \zeta}{\cos^2 \zeta + \delta \sin^2 \zeta + \cos \zeta \sin \zeta - \delta \cos \zeta \sin \zeta}.
\end{aligned} \tag{2.44}$$

Finally we divide the numerators and denominators by $\cos^2 \zeta$ and use the relation that $(\sin \zeta)/(\cos \zeta) = \tan \zeta$ to come to our final result,

$$r_V = \frac{\tan^2 \zeta + \delta - \tan \zeta + \delta \tan \zeta}{1 + \delta \tan^2 \zeta - \tan \zeta + \delta \tan \zeta}, \tag{2.45}$$

$$r_A = \frac{\tan^2 \zeta + \delta + \tan \zeta - \delta \tan \zeta}{1 + \delta \tan^2 \zeta + \tan \zeta - \delta \tan \zeta}. \tag{2.46}$$

These expressions are exactly the same as those given in Eq. 2.32 and Eq. 2.33. We therefore conclude that, if this model framework is used and the assumptions of the manifest left-right symmetric model are applied, that Herczeg's more general

expressions collapse to those derived by Holstein and Bég.

We have now shown that the manifest left-right symmetric model is a subset of the more general non-manifest models. Knowing how the coupling constants change in the presence of right handed currents, Eq. 2.34, we could plug these equations into Eq. 2.20 to come up with a value of A_β in the presence of right-handed currents. We could also plug these coupling constants into the equations given by Jackson [31] and follow the procedure in Sec. 2.1.2 to show how any of the correlation coefficients would be modified. In the next section we use what we have learned here to make a program that will make exclusion plots for the right-handed current parameters δ and ζ , by comparing experimentally measured values to the predictions returned by these models.

2.4 Model Constraints and Exclusion Plots

In this section we will use the math that we saw in the last section to make visual representations of the current status of experiments. We will not just look at the expected constraints coming from our experiment with ^{37}K but we also want to compare with other experiments in different systems.

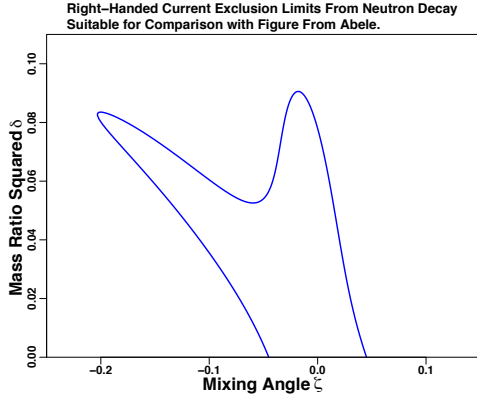
2.4.1 Exclusion Plot Construction

As mentioned earlier in Sec. 2.3.1 Abele [46] used all of the available measurements from neutron β -decay at the time of publication to produce an exclusion plot showing the phase space for δ and ζ that could be ruled out by the measurements at the level of precision of the available measurements.

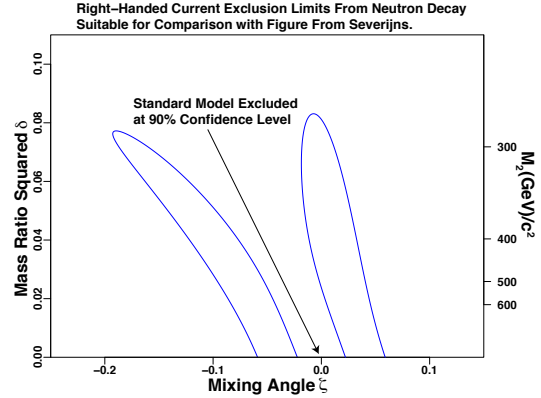
How are such graphs made? The algorithm that is listed here is for the case of a mixed transition where you have a ρ value that will also change as a function of δ and ζ . Not all of the other limits have a ρ dependence and in that case the minimization step can be skipped.

1. Make a grid of δ and ζ values.
2. Choose a pair of δ and ζ .
3. Calculate the right-handed current modified values of A_β , B_ν and any other observable that you have a measure of, using your best guess for ρ .
4. Check the χ^2 value defined as $\sum_{\text{observables}} \frac{(\text{Value}_{\text{experimental}} - \text{Value}_{\text{Calculated}})^2}{\sigma_{\text{experimental}}^2}$.
5. Minimize the the χ^2 by varying ρ .
6. Record ρ value for the δ , ζ pair.
7. If more δ , ζ pairs remain unused go to 2.
8. Find minimum χ^2 for all points sampled.
9. Find confidence interval contours by adding the appropriate amount to the minimum value found in 8.

In an effort to validate the program I tried to recreate the exclusion plot of right-handed current parameters appearing in Abele's paper. In my first attempt I simply used the expressions listed in his paper. That did not work. This disagreement is what led me to the further investigation that ultimately produced the expressions that I have listed in Table 2.2. Using these equations the figure was successfully reproduced. The second step in the validation process was then to use the more general non-manifest expressions given in Herczeg that we discussed in the last section. I set the starting conditions such that my program would use the same manifest left-right symmetric model assumptions with the more general equations. As we showed in the last section, the two answers should be the same and this was a pure software test to try and test for bugs. In this case I also successfully produced Abele's figure. These



(a) Using neutron values given in Abele



(b) Using more recent PDG values for neutron [53]. This plot should be compared with that given by Severijns.

Figure 2.2: Comparison of exclusion contours with published results. The lines on the plots are the contours that correspond to exclusion at the 90% confidence levels. The purpose of making these figures is to gain confidence that our program is working correctly by reproducing published results. Fig. 2.2a should be compared with Fig. 2 of [46] and Fig. 2.2b should be compared with Fig. 2 of [52]. By eye both figures are identical to their corresponding reference. It is interesting that using the recent neutron numbers excludes the standard model. As explained in Ref. [52] this is due to conflict over the neutron lifetime.

tests however were all suspect because as shown I had reason to disbelieve some of Abele's equations and this also meant that I had to suspect his figure also. Therefore the next step in the validation process was to find more published examples and to compare with them. Along with limits arising from other sources, Severijns, in a recent review, [52] published similar exclusion plots. Those produced by my program agree with his. See Fig. 2.2 for two example comparison cases.

Having made successful comparisons to published results we are now satisfied that we have both the physics and programming right. We can now return to what we would really like to do and that is estimate the exclusion intervals that we can expect by successfully making a measurement of A_β in ^{37}K . We will also see how our

measurement compares with limits set by other experiments.

2.5 Other Constraints on Right-Handed Currents

In the proceeding sections a great amount of time was spent getting into the details of the story to be able to fully appreciate the assumptions that went into each of the calculations. This was a useful exercise because, now that we have developed some understanding about how the equations work and how to manipulate them, I will write down some equations for other constraints on right handed currents and we will be able to understand them in the proper context.

In a recent review article, N. Severijns has organized the limits on right handed currents in the framework of a manifest left-right symmetric model arising from nuclear β decay [52]. I will attempt to build on his work here and additionally show the constraints arising from muon decay and the expected results from this experiment.

2.5.1 Unitarity of the CKM Matrix

In addition to what we have already seen of Herczeg's work in Eq. 41 of his paper [49] he gives an expression for the elements of the first row of the CKM matrix,

$$|V_{ui}|_{\text{expt}}^2 \simeq |V_{ui}|^2(1 + 2\text{Re } \bar{a}'_{LL}) \quad (i = d, s, b). \quad (2.47)$$

This allows us to place a constraint on the presence of right handed currents if we have a measure of these elements. John Hardy and Ian Towner have provided us with the necessary information to make such a constraint, see Equation 36 and 37 of [17], and the constraint is,

$$0.99995 \pm 0.00061 = 1 + 2\text{Re } \bar{a}_{LR}. \quad (2.48)$$

What is the effect of the constraint from Eq. 2.48? A visualization is shown as the pink lines in Fig. 2.3. This constraint is by far the tightest on the mixing angle, ζ . However this constraint is not sensitive to the mass ratio, δ .

2.5.2 Unpolarized Longitudinal Polarization

It is possible to put constraints on the presence of right-handed currents by looking at the ratio of longitudinal polarizations of the β s emitted in a pure Fermi decay relative to a pure Gamow Teller decay. The limit generating equation in the manifest left-right symmetric case is given by [52] as,

$$\frac{P_F}{P_{GT}} = 1 - 8\delta\zeta. \quad (2.49)$$

The two most precise measurements of this type are for $P(^{26m}\text{Al})/P(^{30}\text{P}) = 1.003(4)$ [54] and $P(^{14}\text{O})/P(^{11}\text{C}) = 0.9996(37)$ [55]. They can be combined together to form the limit $\delta\zeta = (1.3 \pm 3.4)10^{-4}$ [56]. This constraint is shown in Fig. 2.3 as the red lines. Like the unitarity condition at $\zeta = 0$ it places no constraint on δ .

2.5.3 Polarized Longitudinal Polarization

It was suggested by Quin that longitudinal polarization measurements could be made more sensitive to the mass ratio δ by performing the experiments with polarized nuclei [57]. The measurements would still take advantage of a ratio between isotopes that cancels out some systematic uncertainties. Four such measurements have been carried out, using ^{12}N and ^{107}In [58, 59, 60]. In these measurements one determines either the $R^+ = P^-/P^+$, where P is the longitudinal polarization in the the direction of the nuclear polarization vector (+), or against it (-). It is also possible to draw conclusions from other ratios such as $R^0 = P^-/P^0$ where the ratio is formed by the longitudinal polarization of the positrons emitted against the nuclear polarization

direction over the longitudinal polarization for positrons emitted from unpolarized atoms. The combined result of all four measurements is $(\delta + \zeta)^2 = 0.0004(26)$ [32]. This constraint is shown in Fig. 2.3 as the dark blue lines. It is still the best limit to date on δ from nuclear β decay.

2.5.4 Muon decay

The whole focus of Herczeg's 1986 [45] paper was to explain the limits arising from muon decay in left-right symmetric models. He lays out how the the Michel parameters and the muon polarization would change in the presence of right handed currents. Some of the parameters are much less sensitive than others. The combination of ξP_μ is the most sensitive in the case of manifest model so we will use it here. The equations that we will need are for the muon polarization,

$$P_\mu = \frac{|1 - \eta_{LR}|^2 - |\eta_{RR} - \eta_{RL}|^2}{|1 - \eta_{LR}|^2 + |\eta_{RR} - \eta_{RL}|^2}$$

$$\eta_{ik} = a_{ik}/a_{LL} \quad (ik = RR, LR, RL), \quad (2.50)$$

where the a_{ii} functions are listed in Eqs. 2.36 – 2.39. Before we can write down ξ we need to define $c_{ii} = a_{ii}/V_{ud}^{R,L}$ ($ik = LL, RR, LR, RL$), where $V_{ud}^{R,L}$ is the corresponding V_{ud} value listed in Eqs. 2.36 – 2.39 for a given a_{ii} . With this definition we can now write down how ξ would change in the presence of right-handed currents,

$$\xi = \frac{1 - |\kappa_{RR}|^2 + 3(|\kappa_{LR}|^2 - |\kappa_{RL}|^2)}{1 + |\kappa_{RR}|^2 + |\kappa_{LR}|^2 + |\kappa_{RL}|^2}$$

$$\kappa_{ik} = c_{ik}/c_{LL} \quad (ik = RR, LR, RL). \quad (2.51)$$

Knowing these equations we will be able to find a limit if we have a measurement of the value ξP_μ . The measurement was provided by the TWIST collaboration and is

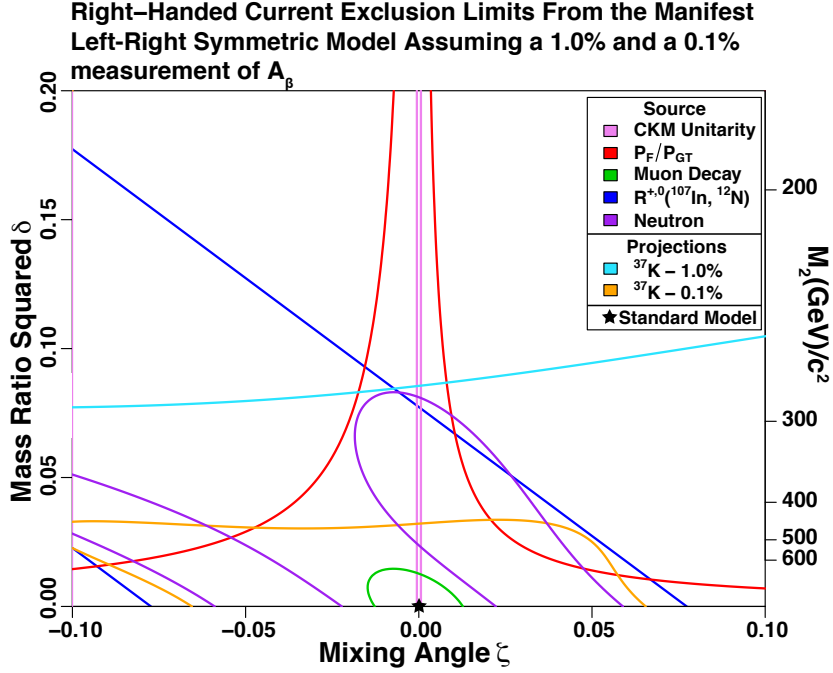


Figure 2.3: Predicted exclusion contour levels from ^{37}K compared with other experiments assuming the manifest left-right symmetric model. This plot shows the limits placed on the right-handed current model parameters, δ and ζ originating from various experiments. Also shown on the plot are projected limits originating from ^{37}K using the current value of B_ν and the ft value and assuming a measurement of A_β at the standard model value with a precision of 1% and 0.1%. A precision of 1% is what we expect from the current data set so is not an unrealistic representation of the impact of the current experiment. In order to cut down on available phase space then we need to pursue precision measurements at least an order of magnitude more precise than the current generation as shown by the 0.1% exclusion interval.

$\xi P_\mu = 1.00084 \left({}^{+170}_{-69} \right)$ [61, 62]. This constraint is shown in Fig. 2.3 as the green line. It is the best limit to date on δ from any source. The neutron constraints, purple line, produce tight yet inconsistent limits but as mentioned earlier there exists a problem with the neutron lifetime so the neutron limits are suspect.

2.5.5 Expected Limits From ^{37}K

Now that we have something to compare with we will add in what we expect to see from this experiment. As mentioned earlier we have a measurement of the neutrino

asymmetry parameter, $B_\nu = 0.755 \pm 0.024$, for ^{37}K [15]. To make our limits we will use this value and $ft = 4605(8)$ s [23] along with $ft^{0^+ \rightarrow 0^+} = 3071.81 \pm 0.83$ s [17]. For the purpose of this exercise we will assume that we have made a measurement of A_β in ^{37}K at exactly its SM value with a precision of 1% of its value and 0.1% of its value. The constraints on right-handed current that we expect from these two measurements are shown in Fig. 2.3 as the light blue (1%) and gold line (0.1%). We can see that if we achieve a precision of 1%, the goal for the current experiment, that our constraint will be competitive with that coming from the longitudinal polarization of β s from polarized sources, the current best limit on δ from nuclear β decay. This project was never meant to be the stopping point but the program goal is to achieve a precision level of 0.1% or beyond, and at that level of precision our experiment becomes competitive with other limits.

2.5.6 Limits in the Non-Manifest Model

We saw in Fig. 2.3 how our experiment stacks up with others in the case of the manifest left right symmetric model. This is just one possible model. As we saw in the section on the non-manifest left-right symmetric models, Sec. 2.3.2, it is the more general case and there are many more parameters. The difficulty is that with so many parameters to be varied, creating meaningful visualizations becomes more difficult. To investigate the effect of some of these parameters I have left everything with the value that it would have in the manifest case and then let only one value vary within some range. In Fig. 2.4 is a visualization, which follows this procedure, for the case of A_β measured in ^{37}K to 0.1%, the same previously assumed, in the last section. We can see some interesting things in the figure. The presence of the CP violation phase α only effects our knowledge of the mixing angle ζ and does not destroy our sensitivity to the mass ratio, δ . The real problem is with the relative

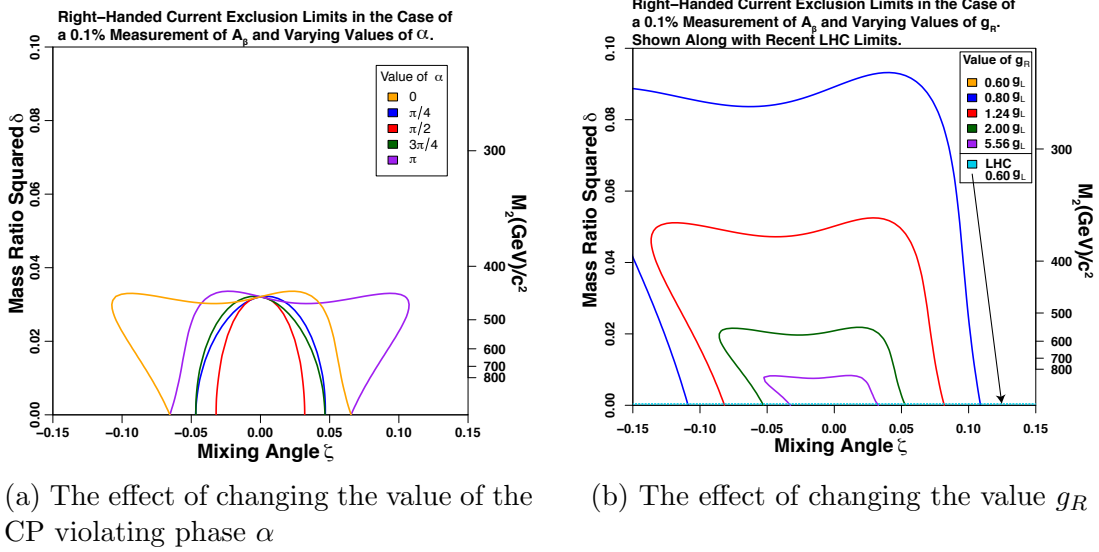


Figure 2.4: Predicted exclusion contour levels in non-manifest case. Both of these figures show the same 0.1% exclusion level as shown in Fig. 2.3 for ^{37}K but in this case the assumptions of the manifest left-right symmetric model have been relaxed and in the case of Fig. 2.4a the CP violating phase α has been allowed to vary. In the case of Fig. 2.4b the value of g_R has been allowed to vary.

strength of this interaction. As seen in Fig. 2.4b if $g_R \ll g_L$ then the level of precision needed to put constraints on δ , and ζ significantly increases. With so many unknown parameters it will be difficult to make progress in this area. There are limits from the LHC that are able to give us some guidance.

In a recent paper Heikinheimo [63] discusses the implications of a 2.8σ deviation from the SM in the $pp \rightarrow 2j + ee$ channel observed by CMS in a dedicated search for right-handed currents. As he explains, the observed signal strength excludes a W_R with $g_L = g_R$ and matches better with a $g_R \approx 0.6g_L$ keeping $\text{CKM}_R = \text{CKM}_L$. Using this value of g_R the mass limit that can be generated is 2 TeV. This limit is shown Fig. 2.4b where it can be compared with limits from A_β generated with various values of g_R .

3. GEANT SIMULATIONS

3.1 GEANT4 Simulations of the Experiment

In order to successfully simulate a β -decay experiment it is necessary to construct a proper model of β -decay. A good starting place for such a model is to impose the kinematic limits that originate from energy and momentum conservation. A convenient way to express these limits is through the use of the Mandelstam variables. After applying the correct kinematic limits, we will introduce the standard model framework. This means that we will generate a configuration that satisfies energy and momentum conservation and then use a Monte Carlo acceptance-rejection step using the decay rate for polarized atoms, Eq. 2.1, as our decision making criterion. The last step is to use the libraries provided as part of the **GEANT4** package to simulate the passage of the β and other particles through the simulated materials of the detector. The results of tracking and energy loss are then aggregated and read out as a “.root” file suitable for comparison with our experimental data.

In this chapter it will be impossible to give all the details of the code and how it works. A general description will be given here. The code itself is available at <https://code.google.com/p/potassium-thirty-seven-simulation/source/checkout>.

3.2 Kinematic Constraints and the Mandelstam Variables

The Mandelstam variables are a very general way of expressing energy and momentum conservation in a Lorentz-invariant way. Let us consider the interactions shown in Fig. 3.1a. It should be noted that the \mathbf{K} s represent the 4-momentum of the particles. We need to be careful about Lorentz-invariance because the β particles and neutrinos will need to be treated relativistically. The recoiling daughter could

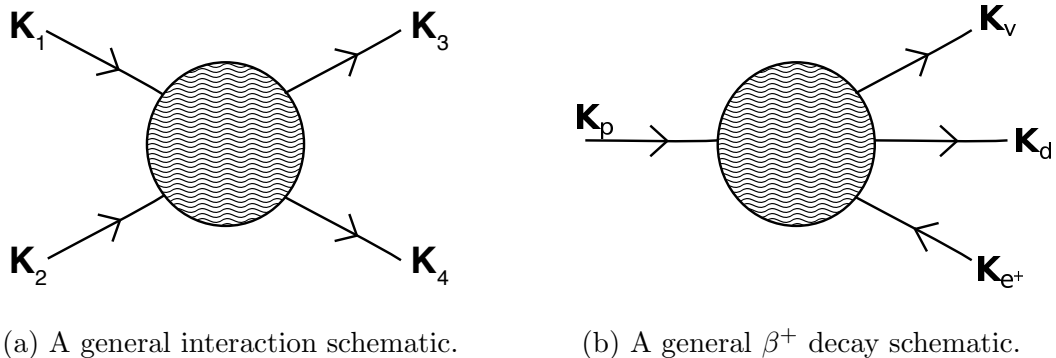


Figure 3.1: General interaction schematics. One important point to remember is that if we write down the Mandelstam variables for the interaction shown in Fig. 3.1a then the Mandelstam variables for the interaction in Fig. 3.1b are the same except for a minus sign introduced in front of \mathbf{K}_2 . The origin of this minus sign becomes more clear when we consider Fig. 3.1b and that the move from the left to the right also involves a change from particle to antiparticle.

be treated classically but will receive the full treatment also since it will not hurt to do it properly. For the general process shown in Fig. 3.1a, the Mandelstam variables [64] can be defined as:

$$\begin{aligned}
 s &= (\mathbf{K}_1 + \mathbf{K}_2)^2 = (\mathbf{K}_3 + \mathbf{K}_4)^2, \\
 t &= (\mathbf{K}_1 - \mathbf{K}_3)^2 = (\mathbf{K}_2 - \mathbf{K}_4)^2, \\
 u &= (\mathbf{K}_1 - \mathbf{K}_4)^2 = (\mathbf{K}_2 - \mathbf{K}_3)^2.
 \end{aligned}
 \tag{3.1}$$

We will now begin to specialize the general treatment into the case that we are interested in. We consider the decay of a parent (^{37}K) into three particles in the final state: the recoiling daughter (^{37}Ar), a positron, and an electron neutrino. This is shown in Fig. 3.1b. We will let \mathbf{P} represent the normal 3-vector momentum of the particles. As mentioned in the caption of Fig. 3.1, when we move a line from the left of the figure to the right, we need to add in a minus sign. Knowing this, we can

write down the Mandelstam variables for a positron decay,

$$\begin{aligned}
s &= (\mathbf{K}_p - \mathbf{K}_\nu)^2 = (\mathbf{K}_d + \mathbf{K}_{e^+})^2, \\
t &= (\mathbf{K}_p - \mathbf{K}_d)^2 = (\mathbf{K}_\nu + \mathbf{K}_{e^+})^2, \\
u &= (\mathbf{K}_p - \mathbf{K}_{e^+})^2 = (\mathbf{K}_d + \mathbf{K}_\nu)^2.
\end{aligned} \tag{3.2}$$

I will go through the expansion of the variable s to show what constraints on the kinematics we can derive from it. The treatment for the other two is similar and only the results will be shown:

$$s = (\mathbf{K}_p - \mathbf{K}_\nu)^2 = (\mathbf{K}_d + \mathbf{K}_{e^+})^2, \tag{3.3}$$

$$M_p^2 + 2|\mathbf{P}_p||\mathbf{P}_\nu| \cos \theta_{p\nu} - 2E_p E_\nu + M_\nu^2 = M_d^2 - 2|\mathbf{P}_d||\mathbf{P}_{e^+}| \cos \theta_{de^+} + 2E_d E_{e^+} + M_{e^+}^2.$$

If we choose to look at the decay from the rest frame of the parent, then $\mathbf{P}_p = 0$ and $E_p = M_p$ and Eq. 3.3 simplifies to,

$$M_p^2 - 2M_p E_\nu + M_\nu^2 = M_d^2 - 2|\mathbf{P}_d||\mathbf{P}_{e^+}| \cos \theta_{de^+} + 2E_d E_{e^+} + M_{e^+}^2. \tag{3.4}$$

We now observe that kinematically the highest possible energy that the neutrino can achieve would be when $|\mathbf{P}_d| = 0$, $E_d = M_d$, $|\mathbf{P}_{e^+}| = 0$, and $E_{e^+} = M_{e^+}$. Making these substitutions we arrive at the final result

$$\begin{aligned}
M_p^2 - 2M_p E_\nu^{\max} + M_\nu^2 &= M_d^2 + 2M_d M_{e^+} + M_{e^+}^2, \\
-2M_p E_\nu^{\max} &= M_d^2 + 2M_d M_{e^+} + M_{e^+}^2 - M_p^2 - M_\nu^2, \\
E_\nu^{\max} &= \frac{M_p^2 + M_\nu^2 - (M_d + M_{e^+})^2}{2M_p}.
\end{aligned} \tag{3.5}$$

The logic to work out the other two cases is exactly the same and the results are,

$$E_d^{\max} = \frac{M_p^2 + M_d^2 - (M_\nu + M_{e^+})^2}{2M_p}, \quad (3.6)$$

$$E_{e^+}^{\max} = \frac{M_p^2 + M_{e^+}^2 - (M_d + M_\nu)^2}{2M_p}. \quad (3.7)$$

In the experiments at hand, the mass of the neutrino can safely be ignored and indeed it is set to zero in the simulation, but I have chosen to leave it in so that we can be aware that it will contribute slightly.

3.3 Event Generator

In this section I give an overview of how the events are made in `GEANT4`. A schematic of the algorithm is shown in Fig. 3.2. There are two main parts to the algorithm that should be pointed out. In Fig. 3.2 everything above the “SM decay rate Monte Carlo (MC)” decision block is kinematics. The algorithm ensures that both energy and momentum are conserved and that the limits introduced by Eq. 3.5–3.7 are obeyed. The SM decay rate MC step inserts the recently chosen kinematics into the decay rate for polarized atoms, Eq. 2.1, and then goes through an acceptance/rejection step in which a random number is drawn between 0 and the maximum value that the polarized decay rate can reach. The event is accepted if the computed decay rate is less than this random number and it is rejected otherwise and another set of kinematics is generated.

3.4 Recoil-Order Effects

Recoil-order effects are the small differences in the correlation parameters that we see when we do not make the assumption, that we have implicitly made until now, that the nucleus is infinitely heavy [65, 66, 67]. In order to reproduce the β spectrum at the 0.5% level of precision in ^{37}K recoil order-effects must be taken into account.

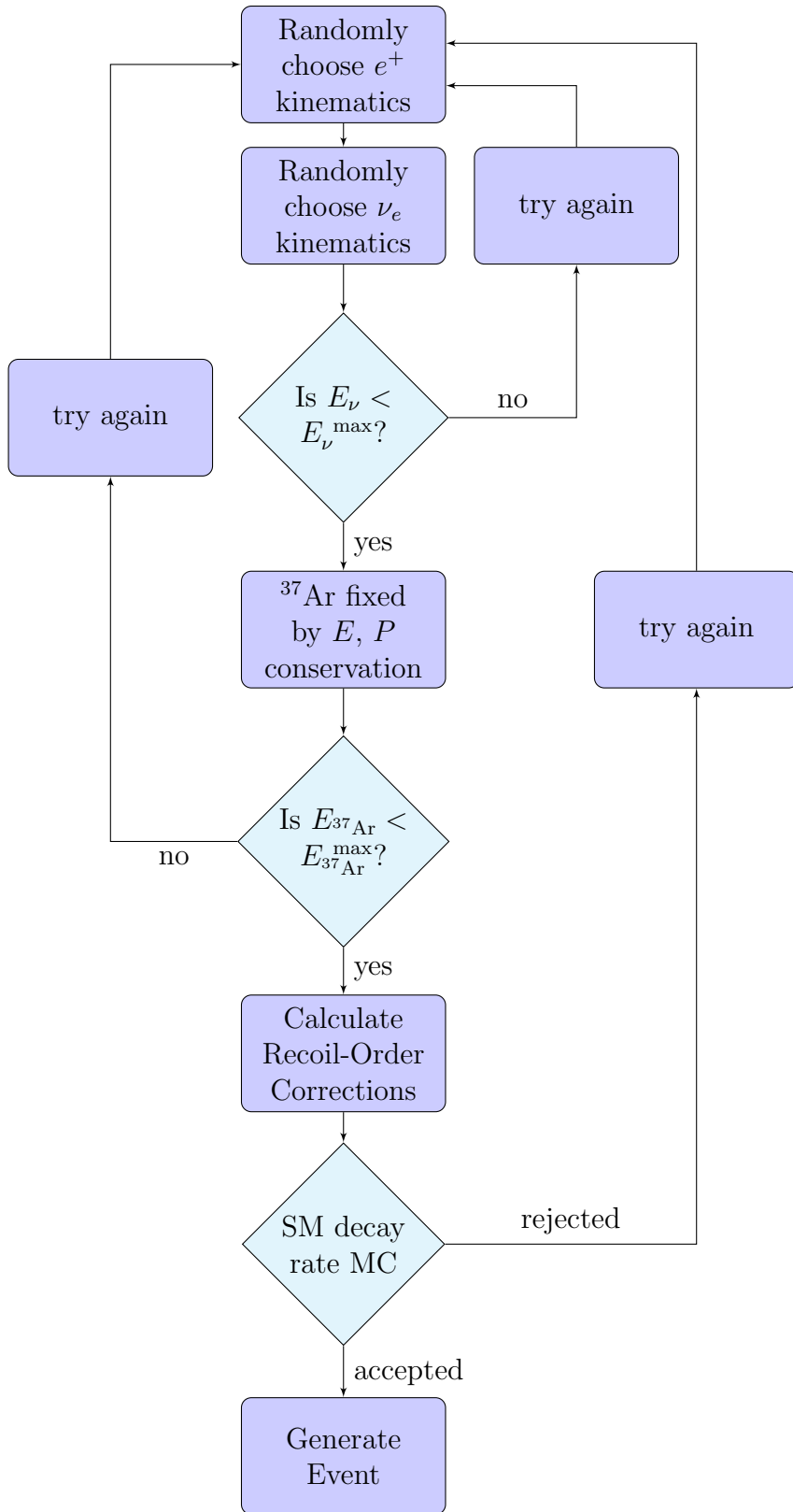


Figure 3.2: A schematic of the event generation algorithm in the GEANT4 code.

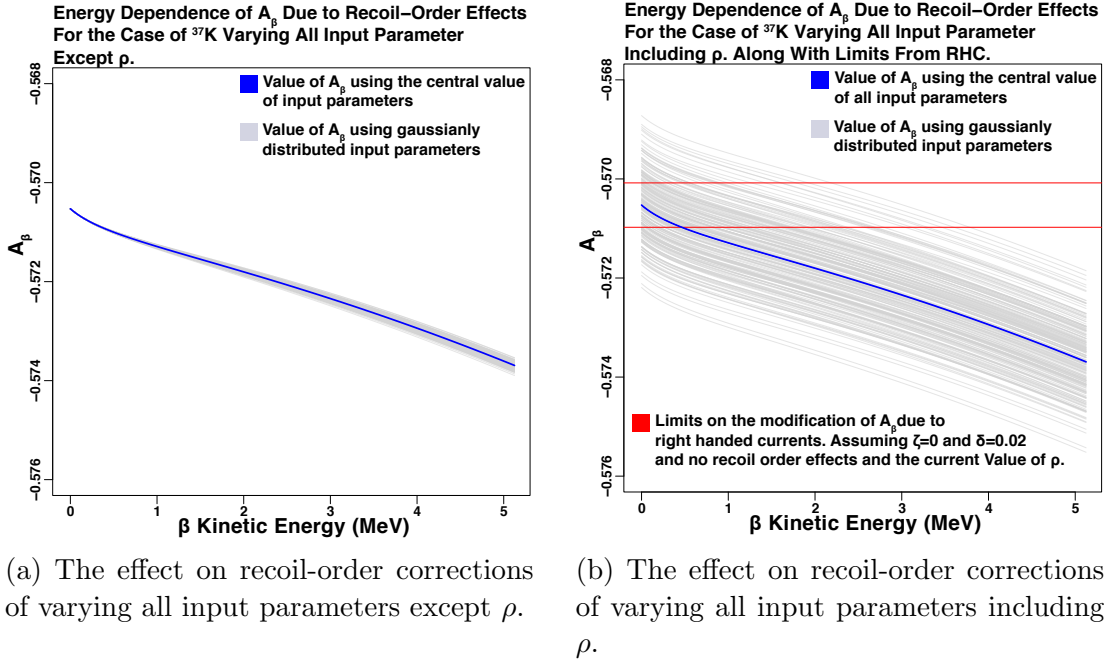


Figure 3.3: Energy dependence of A_β due to recoil-order effects. These plots show us that as we move to higher β energy that we will see a larger observed asymmetry. The equations that go into calculating the recoil-order effects are extremely complicated and take a large amount of input values listed in Table ???. Rather than trying to calculate all of the partial derivatives to calculate the uncertainty I assumed that the input parameters are all Gaussian variables with mean equal to their central value and σ equal to their stated uncertainty and calculate many times A_β as a function of energy each time drawing new input values from the Gaussian distributions. A sample of 200 of these Monte Carlo simulation is what is shown in grey. These two plots together tell us that recoil-order effects affect most strongly the slope of $A_\beta(E)$, Fig. 3.3a, and that the value of ρ most strongly affects its intercept, Fig. 3.3b.

They are not explicitly shown in the decay rate for polarized atoms, Eq. 2.1, but can be added in. For allowed beta decay the recoil-order corrections are calculable with some further input both experimental and from shell model calculations. All of the inputs needed to calculate the recoil-order corrections for the main branch of ^{37}K are shown in Table ??.

The major consequence of taking into account recoil-order corrections is that

Recoil-Order Corrections Input		
Property	Value	Source
Branching Ratio	$97.99 \pm 0.14\%$	[22]
Probability Electron Capture	0.080%	[25]
$t_{1/2}[s]$	1.23651 ± 0.00094	[23]
Statistical Rate Function	3623.9 ± 0.7	[25]
f_A/f_V	1.00456 ± 0.0009	[25]
δ'_R	$1.431 \pm 0.039\%$	[25]
$\delta_C^V - \delta_{NS}^V$	$0.79 \pm 0.06\%$	[25]
$\mathcal{F}t^{0^+ \rightarrow 0^+}[s]$	3071.4 ± 0.8	[17]
Sign of Rho	+	[25]
Average Mass ^{37}K and ^{37}Ar [amu]	36.97007611(12)	[16]
^{37}K Magnetic Moment [μ_N]	0.20321 ± 0.00006	[68]
^{37}Ar Magnetic Moment [μ_N]	1.146 ± 0.001	[69]
^{37}K Quadrupole Moment [$e \cdot \text{fm}^2$]	10.6 ± 0.4	[70]
^{37}Ar Quadrupole Moment [$e \cdot \text{fm}^2$]	7.6 ± 0.9	[71]
Mass of ^{37}K [amu]	36.973375889	[72]
Mass of ^{37}Ar [amu]	36.966776331	[72]
Average Kinetic Energy β [MeV]	2.307002	[25]
$R[\hbar c^2/\text{MeV}]$	4.637	[73]
M_F	1.0000	[73]
M_{GT}	-0.62376	[73]
$M_{r,2}[\hbar c^2]$	12.899	[73]
$M_{\sigma r,2}[\hbar c^2]$	-8.0455	[73]
$M_Q[\hbar c^2]$	-0.827	[73]
$M_{r,p}[\hbar c^2]$	0	[73]
M_L	1.4158	[73]
$M_{\sigma L}$	0	[73]
$M_{1Y}[\hbar c^2]$	-10.105	[73]
$M_{2Y}[\hbar c^2]$	0.00000064	[73]
$M_{3Y}[\hbar c^2]$	2.052	[73]
$M_{\sigma rp}[\hbar c]$	0	[73]
g_V	1.0000	[73]
g_A	0.92438	[73]
g_M	4.2196	[73]
g_P	0	[73]
g_S	0	[73]
g_{II}	0	[73]

Table 3.1: All of the input values that are needed to calculate recoil order effects for ^{37}K .

all of the SM correlation coefficients are no longer simply numbers, as shown in Table 2.1, but are now functions of the kinetic energy of the β . Recoil-order effects will have a small ($\lesssim 0.2\%$) effect on the SM predictions for the correlation coefficients, and in particular induce a stronger energy-dependence to their values. This energy dependence for A_β is shown in Fig. 3.3. A_β could also acquire an energy dependence if we did away with the two SM assumptions that tensor and scalar currents do not exist and that time reversal symmetry is not violated. This can be seen by examining Eq. 2.9. The energy dependence from recoil-order effects does not require us to violate any of the SM assumptions. Following the notation of Holstein [65], the values of the correlation coefficients as derived by Dan Melconian and Praveen Shidling are,

$$\begin{aligned}
a_{\beta\nu}(T_e) &= \frac{f_2(T_e)}{f_1(T_e)}, \\
c_{\text{align}}(T_e) &= \frac{-f_{12}(T_e)(2J-1)}{f_1(T_e)(J+1)}, \\
A_\beta(T_e) &= \frac{f_4(T_e) + f_7(T_e)/3}{f_1(T_e)}, \\
B_\nu(T_e) &= \frac{f_6(T_e) + f_5(T_e)/3}{f_1(T_e)}, \\
\xi(T_e) &= 2f_1(T_e).
\end{aligned} \tag{3.8}$$

The definitions of the f_x functions can be found in [65]. It should be noted that these equations using Holstein's formalization have been compared by Dan Melconian with Ian Towner's calculations [73] using his shell model and the independent formalization of Behrens and Bühring [66, 67] and they agree well. This comparison using a completely different calculation framework gives us confidence that our equations are correct. In the **GEANT4** simulation once a set of kinematic conditions is chosen as described in the previous section then the recoil-order effects to all of the correlation

parameters are calculated at that energy. This this configuration with corrections is then sent on to the Monte Carlo acceptance/rejection step.

3.5 The Fermi Function

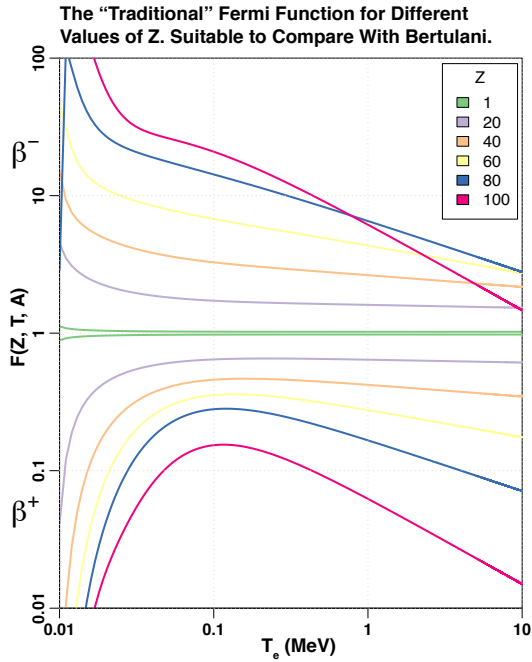
As mentioned in Sec. 2.1.1, to properly evaluate Eq. 2.1 it is necessary to have an expression for the Fermi Function [74, 75, 76]. We use the form given by Fermi, reworked here slightly to be in terms of the kinetic energy of the electron, T_e ,

$$F(T_e, Z', R') = 2(S + 1) \left(2R' \sqrt{\left(\frac{T_e}{m_e} + 1\right)^2 - 1} \right)^{2(S-1)} e^{\pi\eta} \frac{|\Gamma_c(S + i\eta)|^2}{|\Gamma_r(2S + 1)|^2},$$

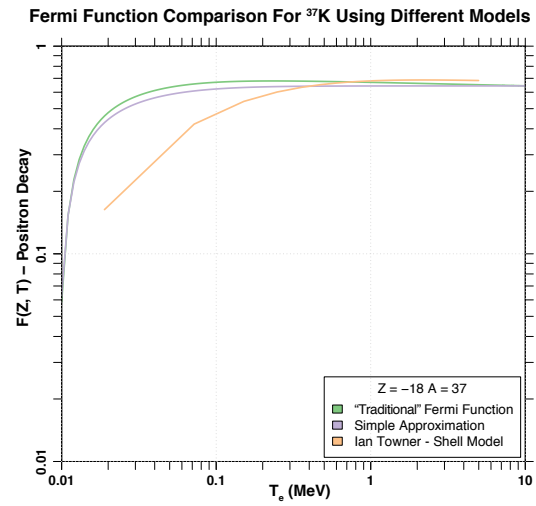
$$\text{with } \eta = \frac{\frac{T_e}{m_e} + 1}{\sqrt{\left(\frac{T_e}{m_e} + 1\right)^2 - 1}} \text{ and } S = \sqrt{1 - \alpha^2 Z'^2} \quad (3.9)$$

This equation in the literature has come to be known as the “traditional” Fermi function. It should be noted that the values Z' and R' are the charge and the radius of the daughter nuclei because the Fermi function is essentially the solution to the Dirac equation for the β moving in the electric field produced by the daughter nucleus. Traditionally what has made using Eq. 3.9 hard is the evaluation of the complex gamma function. I only know of one commonly available implementation in C with a permissive software license, the exceptional GNU scientific library [78]. In the case that the radius of the nucleus has not been measured, the expression $R = R_0 A^{1/3}$ could be used. For the case of ^{37}Ar the root mean square charge radius (R_{RMS}) has been measured to be 3.3903 ± 0.0022 fm [79]. We will make the assumption that the charge is uniformly distributed within the spherical nuclear volume so the radius that we use is related to R_{RMS} by the following expression.

$$R = \sqrt{\frac{5}{3}} R_{\text{RMS}}^2 \quad (3.10)$$



(a) The “traditional” Fermi Function.



(b) Comparison of ^{37}K Fermi function calculated using the shell model

Figure 3.4: Comparison of different Fermi functions. The value of the “traditional” Fermi function shown in Fig. 3.1a for different Z values. The purpose in making this plot was to compare with the Fermi Function plots shown in Ref. [18] to verify that my implementation of Eq. 3.9 was correct. In Fig. 3.1b we see a comparison of the “traditional” Fermi function, a simple non-relativistic approximation from [18], and a version from Ian Towner [77] that takes in account screening from the atomic electrons and no longer treats the nucleus as spherical. The deviation between the models becomes large below the rest mass of the electron.

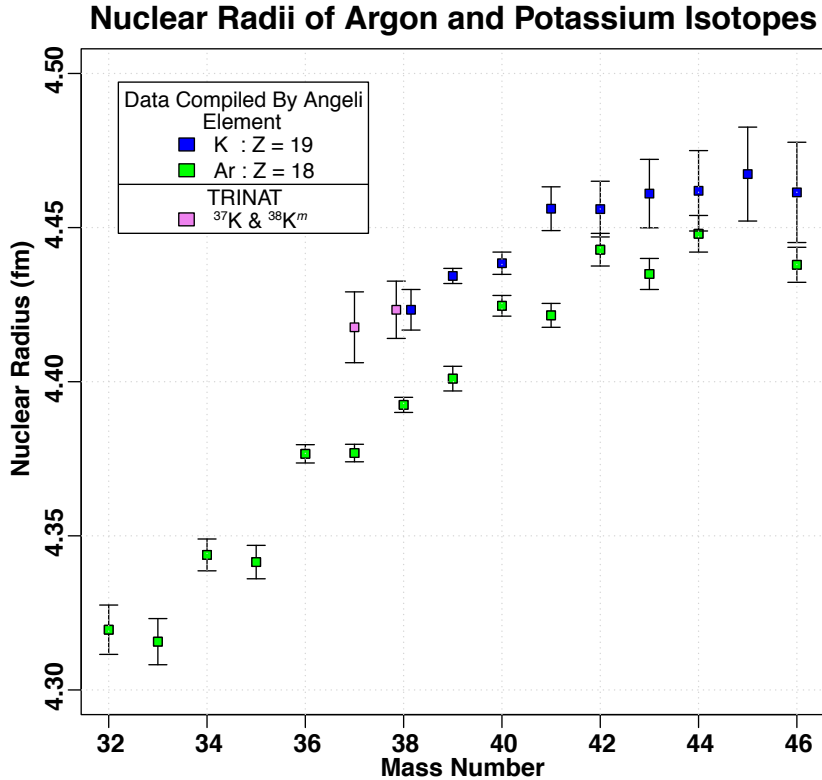


Figure 3.5: Nuclear radii in the area of ^{37}Ar . An isotope shift measurement between ^{37}K and $^{38}\text{K}^m$ against a ^{39}K reference has recently been done by TRINAT [80], but this is only a relative measurement that has to be combined with the absolute measurement of the charge radius of ^{39}K . An absolute measurement can be obtained by examining x-rays from normal and muonic atoms and has been done for ^{39}K [81]. The resulting radius for ^{37}K , 4.42 ± 0.01 fm, is plotted alongside the compiled data from Angeli [79] for comparison.

A distribution of the measured nuclear radii near ^{37}Ar is shown in Fig. 3.5. This includes the measurement of the charge radius of ^{37}K made by TRINAT. This version of the Fermi function takes into account the relativistic nature of the electron but does assume a uniform spherical charge distribution. There are more sophisticated models now that take into account the deformed nature of different nuclei.

Ian Towner, taking into account effects such as screening from atomic electrons and the shape of ^{37}K has calculated the value of the Fermi function for ^{37}K at various

points along the β energy spectrum. A comparison between the “traditional” Fermi function and what was calculated by Ian Towner is shown in Fig. 3.1b. It was found that the difference from the “traditional” form, shown in Eq. 3.9, was small for the case of β kinetic energy greater than its rest mass. Since this is the region of the spectrum that we are most interested in we decided that the “traditional Fermi function” would be sufficient for use in simulation for this experiment.

3.6 The Geometry Definition

The geometry definition is one of the most time consuming and arduous processes involved in creating a successful simulation. The **GEANT4** collaboration has still not been able to make the import process from CAD programs reliable and so each detector element needs to be specified by hand. This is not too bad for trivial setups but becomes a large challenge for real world detectors. To give an indication of the size of the task for our experiment we can use file size as a measure of complexity and compare all of the files in the **GEANT4** project. The results are shown in Fig 3.6. While designing the experimental apparatus we used **GEANT4** simulations to guide some of the decisions about materials to use and the placement of different detector elements. For example, inside the chamber there are two mirrors from which both a MOT laser and an optical pumping laser beam have to reflect. Since these mirrors define the polarization axis of the ^{37}K it is necessary that they be placed directly in front of the β detectors so the β s will have to pass through them before being detected. There are only a few materials available that can be made into large three inch mirrors and are also low enough Z to suppress β scattering. I simulated the scattering effects that different mirrors would have and the results can be seen in Fig. 3.7. In the end we decided to make the mirrors from silicon carbide because such mirrors can be made extremely thin. Thus the scattering from it was the smallest

Sorted List of the Largest Files in the Geant4 Simulation
Total Lines of Code in the Repository: 10364

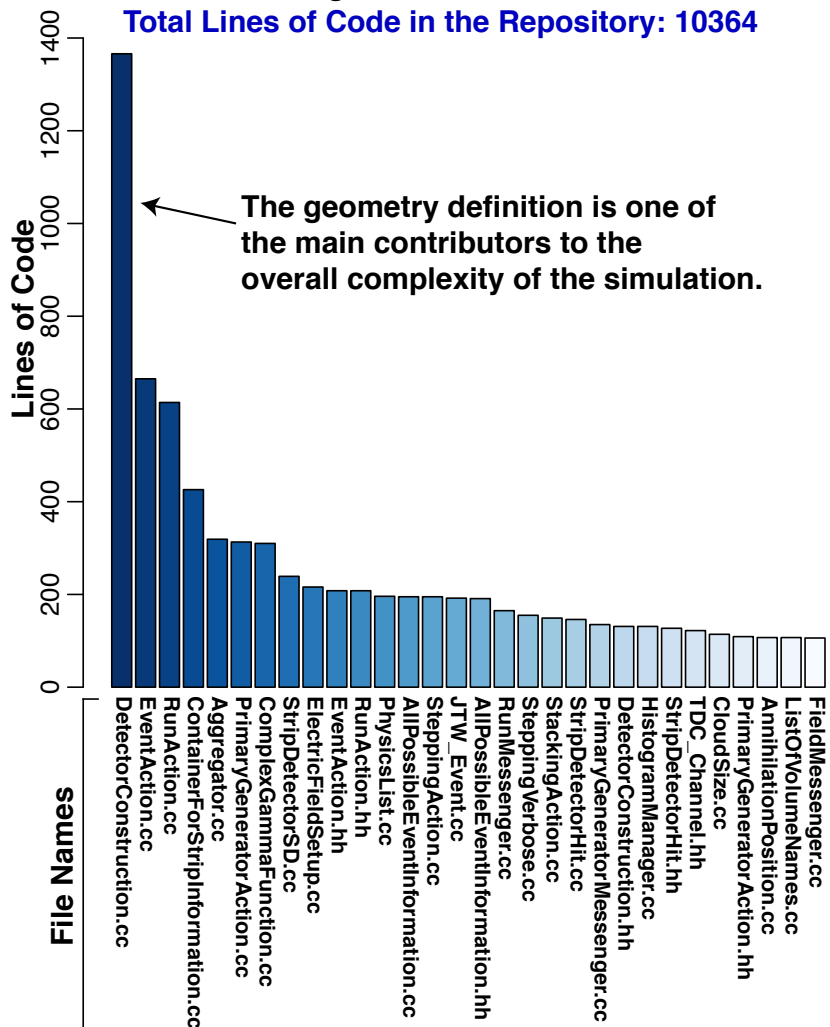


Figure 3.6: GEANT4 file size comparison. File size is not a perfect measure of complexity in software development because often similar code is copied and pasted. In the case of DetectorConstruction.cc this is not the case. The dimensions, placement, and rotation of every piece of detector hardware are hard coded.

observed.

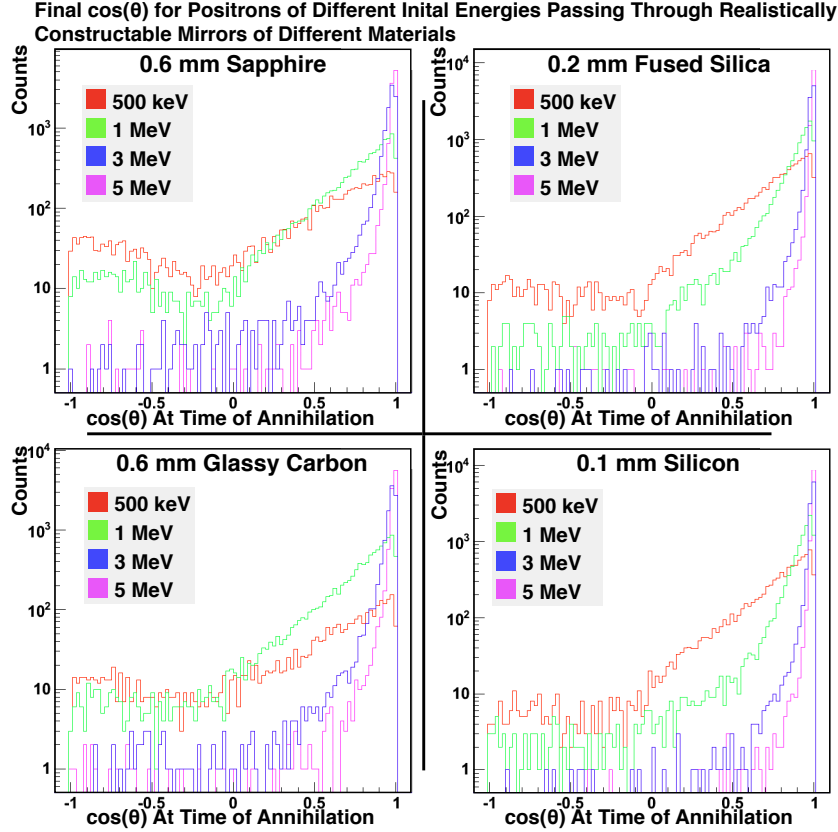


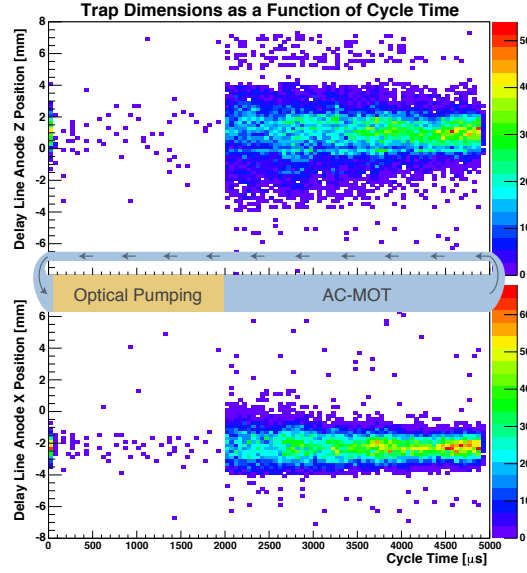
Figure 3.7: Scattering from mirror substrates. In the simulation, a divergentless beam of monoenergetic positrons were sent through the experimental geometry with while changing only the materials and dimensions of the mirrors. The reason that both variables were simultaneously changed is that for a real mirror of a given diameter there exists a lower limit on the thickness that a mirror could be made from for each type of material. The positrons all started off with a $\cos \theta = 1$ deviation from this value at the time of annihilation is due to scattering.

3.7 Experimental Cloud Input Into GEANT4

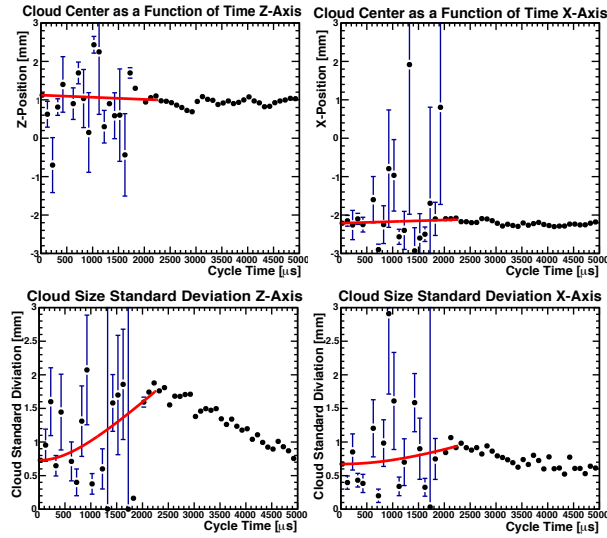
In order to make the simulation realistic we will need to use some experimentally measured input parameters dealing with the trap size and movement during the

optical pumping time. Using these numbers means that the event generator can produce events drawn from the same statistical distribution in space and initial velocity as the ^{37}K in the experiment.

In two of three dimensions the trap is imaged directly by photoions from the trap hitting the ion micro channel plate (MCP) that is backed by a position sensitive delay line anode. A view showing the extent of these photoions coming from the trap in the X and the Z directions throughout the cycle time is shown in Fig. 3.8a. “Cycle time” refers to the fact that we are constantly collecting ^{37}K polarizing them counting decays and then repeating. To see the details of this cycle timing see Sec. 4.4. Fit values for all of the relevant information necessary to model the cloud dynamics in `GEANT4` is listed in Table 3.2. There are some anomalous measurements on listed on the table, namely the Z temperature and the change in Z width. These numbers are an order of magnitude larger than the equivalent numbers in the other two directions. In this dimension the trap was observed to be slightly bimodal. The larger final width is due to the evolution of two displaced gaussian populations instead of just one in the other dimensions. This final state will be larger and hence the fit temperature will also be larger. The basic assumption that we operate under is that none of the statistics listed there should be affected by polarization state. Using the numbers listed in the table it is possible to start checking systematic uncertainties in the asymmetry measurement. To do this all of the numbers are set to the average values for the two polarization states except for the value that you are trying to vary. Simulations are then run with this value set to the average of the two polarization states and with that value set to the central values for the two polarization states. The difference in the returned value of the asymmetries of these two simulations is then taken to be a systematic uncertainty on the final measurement.



(a) Photoions as a function of optical pumping time

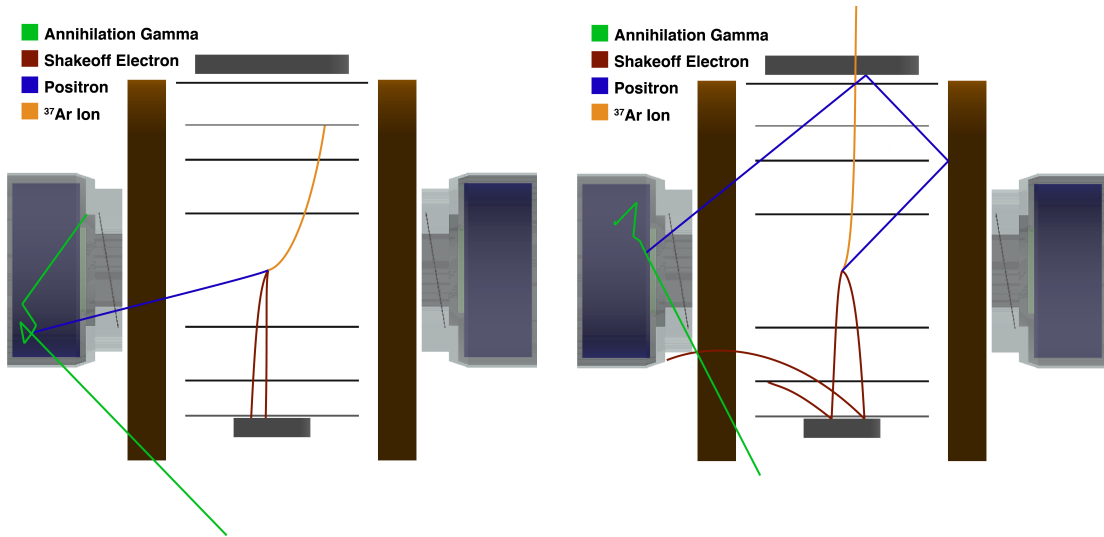


(b) Fits of the trap position and width

Figure 3.8: Experimental data showing the extent of the cloud. The trap position was fairly constant throughout the run. In Fig. 3.8a you can see the trap condense during the MOT times from 2000 – 5000 μs . The time from 250 – 2000 μs is the optical pumping time and we don't expect to see many photoions during this time because there are few atoms in the excited state. Fits for the cloud movement and the size of the cloud are shown in Fig. 3.8b the values from all of the fits for the two polarization states are shown in Table 3.2. What is not shown here is the trap position in the Y dimension. This dimension is much more difficult because it relies on the MCP timing signal and is hard to disentangle from the electric field. Mellisa Anholm at TRIUMF disentangled this as part of her analysis. The numbers from all of the fits appear in Table 3.2.

Trap Position and Movement					
Data Type	Units	σ^-		σ^+	
		Fit Value	Fit Error	Fit Value	Fit Error
X Position at t_0	mm	-2.20	0.06	-2.22	0.04
X Position t_{final}	mm	-2.108	0.002	-2.164	0.002
X Width σt_0	mm	0.79	0.04	0.49	0.03
X Width σt_{final}	mm	0.965	0.001	0.901	0.001
X Group Velocity	mm/ μs	4.8×10^{-5}	2×10^{-5}	2.8×10^{-5}	2×10^{-5}
X Temperature	mK	0.37	0.07	0.62	0.03
Z Position at t_0	mm	1.11	0.06	1.13	0.06
Z Position t_{final}	mm	0.99	0.01	1.040	0.007
Z Width σt_0	mm	0.76	0.04	0.68	0.03
Z Width σt_{final}	mm	1.716	0.003	1.821	0.004
Z Group Velocity	mm/ μs	-6.4×10^{-5}	3×10^{-5}	-4.4×10^{-5}	3×10^{-5}
Z Temperature	mK	2.56	0.07	3.08	0.06
Y Position at t_0	mm	1.51	0.05	1.60	0.06
Y Position t_{final}	mm	1.29	0.01	1.53	0.01
Y Width σt_0	mm	0.69	0.04	0.67	0.04
Y Width σt_{final}	mm	0.846	0.006	0.811	0.006
Y Group Velocity	mm/ μs	-9.0×10^{-6}	2×10^{-5}	-3.1×10^{-5}	3×10^{-5}
Y Temperature	mK	0.28	0.05	0.22	0.06

Table 3.2: Trap position and movement by polarization state. These numbers are from fits of the photoions during different times in the optical pumping cycle. The data to produce these numbers is shown in Fig. 3.8.



(a) The β goes directly into the detector. $\cos(\theta)_{\text{observed}} = \cos(\theta)_{\text{actual}}$
 (b) The β scatters into the detector. $\cos(\theta)_{\text{observed}} \neq \cos(\theta)_{\text{actual}}$

Figure 3.9: GEANT4 typical events. In Fig. 3.9a the e^+ (blue) goes directly through the strip detector and into the scintillator where it annihilates producing two gammas (green). The recoiling $^{37}\text{Ar}^-$ (orange) is swept by the electric field onto one of the electrostatic hoops. The shake-off electrons (red) are swept onto the electron MCP. This represents the type of events that we are trying to look for. In contrast to this ideal situation is the event shown in Fig. 3.9b. This event would most likely be accepted by the β asymmetry cuts because it left energy in both the strip detector and scintillator. Only in simulations can we tell that the β started off traveling in a direction opposite from what we observe with our detectors.

3.8 Testing With GEANT4

After completing the mechanical design phase the whole experimental apparatus was implemented in GEANT4 so that experimental physics results could be compared directly with the results of the simulation. One of the reasons for doing this is because with simulations it is possible to find out how often some types of bad events occur which, strictly from the readout of the various detectors, would be impossible to distinguish from good events. An example of such an event is shown in Fig. 3.9.

Using the GEANT4 model I was able to identify hot spots in the geometry for β

scattering that would lead to these types of bad events. The way that I did this was to keep track of all of the volumes that the positron entered for all events in **GEANT4**. Then I went through and sorted them by the events that would pass our experimental filter. I then made histograms of number of times that these accepted events entered the different volumes in the **GEANT4** simulation and sorted this histogram in descending order. The result of this procedure is shown in Fig. 3.10. On the bottom of each histogram are the names of the volumes that were entered. The volumes on the left hand side of each list are the names of the volumes that we expect. We expect in each ideal detected event that the β will have at least passed through the world volume \rightarrow a mirror \rightarrow a beryllium foil \rightarrow some air \rightarrow the silicon detector \rightarrow some teflon wrapping \rightarrow and finally the scintillator. Some of these volumes are not listed at 100% because gammas can reach the scintillators through other paths and still fulfill the requirements to pass as an accepted event. Highlighted in red is the first volume that is not part of the ideal event. In all cases it is the mirror mount in front of each scintillator. This volume is the largest source of scatter for all states.

We know that effects such as the finite cloud size and temperature as well as backscattering in the chamber will cause the observed asymmetry to be slightly less than the asymmetry of the generated events. This offset we will call the “asymmetry damping” and it will be denoted A_d . Using **GEANT4** data A_d was measured by comparing the asymmetry observed in the detectors, A_{obs} , with the asymmetry of generated events, A_{gen} . The generated asymmetry, A_{gen} , is simply equal to the SM value of $A_\beta = -0.5706(7)$. The observed asymmetry is then given by,

$$A_{obs} = A_{gen} - A_d. \tag{3.11}$$

The asymmetry damping factor calculated in this way is $A_d = -3(1) \times 10^{-3}$. The

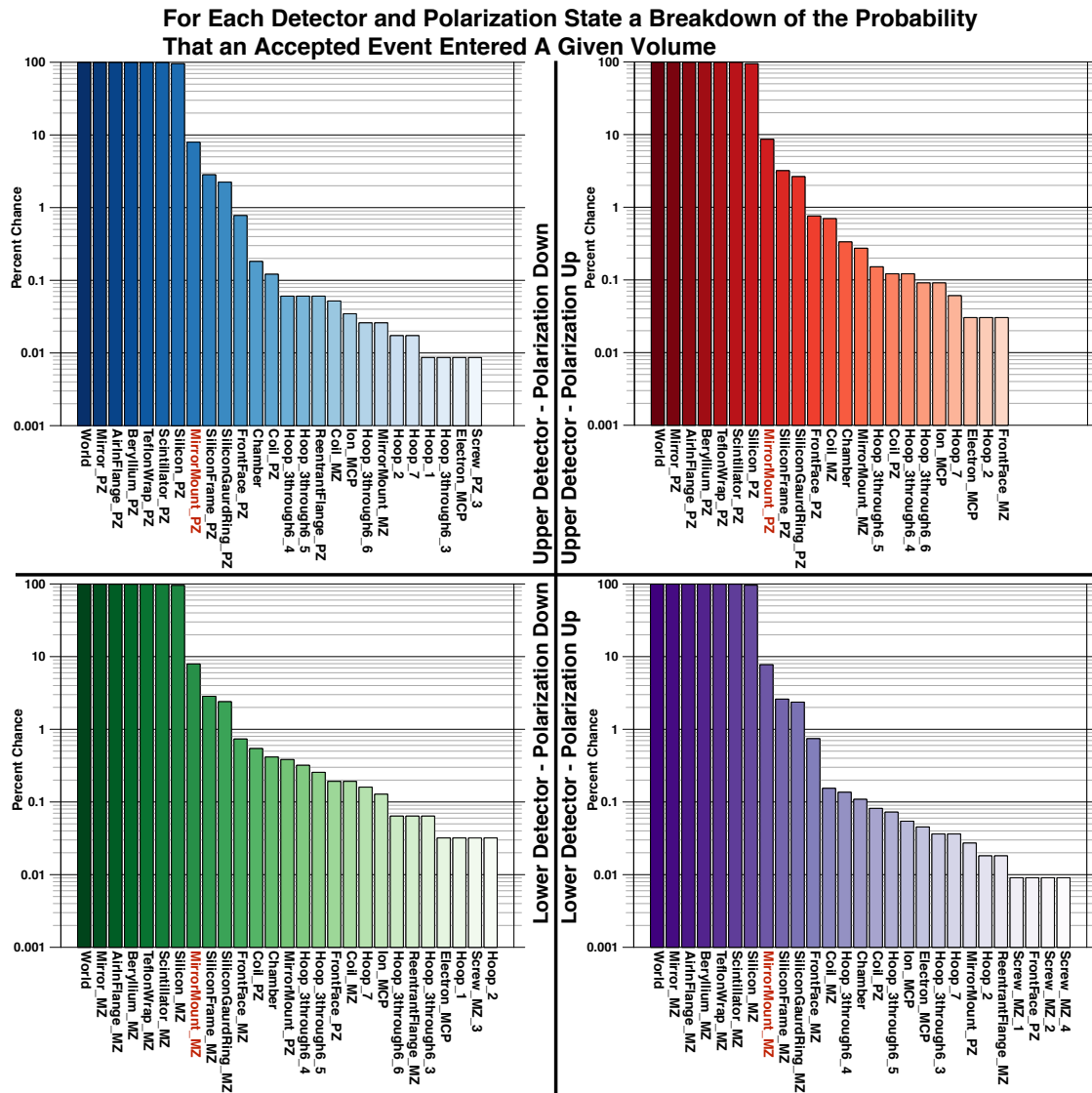


Figure 3.10: Sorted list of volume names that most strongly scatter positrons. This is a breakdown of the most common volumes for a positron to enter on its way to becoming a detected event. The plot is broken up by polarization state and by detector. The reason for doing this is to try and see what the effects are from having an off center trap and to try and see how things change with the rate. Remember that the rates for particles going with or against the polarization direction are very different and the backscatter fraction in the two different states is also different. Note that for a volume name to appear in a list it had to have at least one event enter that volume during the simulation so the number of volumes in each list can change between states.

presence of this asymmetry damping is the reason that we fit our experimentally observed asymmetry with the observed asymmetry from **GEANT4** so that all of the above mentioned effects that damp the asymmetry will be taken into account.

One of the last steps that we need to take with our **GEANT4** simulation is to implement some test to build our confidence that it is working the way that we think that it should. One such test that we can do is to measure beta events that scatter from one silicon detector back out and into the other. We will define the backscatter fraction, F_{bs} , as the number of events where both silicon detectors fired, $N_{1\&2}$, over the number of events where one of the detectors fired, $N_{1|2}$.

$$F_{bs} = \frac{N_{1\&2}}{N_{1|2}}. \quad (3.12)$$

When calculating this number we will also require there be only one pixel in each detector firing. The top X-odd strips from the **GEANT4** data are excluded as they are in the experimental data. A 17 keV energy agreement is required between the X and Y strips of each detector. We also require that one of the scintillators fired but exclude events where both did. When we calculate this fraction from **GEANT4** data we find $F_{bs}^{Sim} = 28(3) \times 10^{-6}$. Extracting this fraction from the experimental data we find $F_{bs}^{Exp} = 48(24) \times 10^{-6}$ in agreement with the simulation.

3.9 Multithreading in ^{37}K Simulations

In December 2013 the **GEANT4** collaboration released **GEANT4.10.0** with support for multithreaded event level parallelization. I performed work to investigate if it would be possible to migrate our existing code base to take advantage of the speed boost that could come with fine grained parallelization. What I found was disappointing. To make sure that parity existed between the experimental data and the **GEANT4** simulation data we had decided upon a unified file format. This greatly

improved our ability to write analysis code that could operate without modification on experimental or simulated data. The code necessary to preserve this parity of formats is incompatible with the multi-threading model of `GEANT4`.

In the experiment we used a multi-hit TDC. This means that in our output file there would be a variable number of times recorded for each channel. This situation is nicely represented by a C++ object `std::vector` that is a variable length array. The file format that we decided to use was a root `TFile` object with a root `TTree` object embedded in it. A `TTree` is essentially a two dimensional spreadsheet with columns representing the different input data sources, such as event time and scintillator peak height, and the rows of the `TTree` represent each event. `TTrees` can have columns of `std::vectors` thereby adding a third dimension to the analogy of the spreadsheet. For the experimental data this was an easy and natural choice for the representation of the data because the acquisition system was built to produce histograms saved in a `.root` files.

After I arrived back in Texas after the completion of the experiment in Vancouver a bug was found in the event loop of the data acquisition software. More will be said in Sec. 6.1.3 about how this bug was found. The effect of this was that the program had to be modified to buffer all of the event data and sync them by timestamp before writing a row in the `TTree`. Rewriting the analysis software to do this was a large undertaking as the main event loop of the data acquisition code had not been written by myself but by Konstantin Olchanski, from the data acquisition group at TRIUMF. The difficulty arose in that, like any piece of software that communicates with hardware over a serial bus, it was extremely dense. This programming effort is relevant in our present discussion of `GEANT4` because the software class that I wrote to accomplish this syncing, known as the Aggregator, was sufficiently general and had so few dependencies that it could be dropped into the `GEANT4.9` single-threaded code

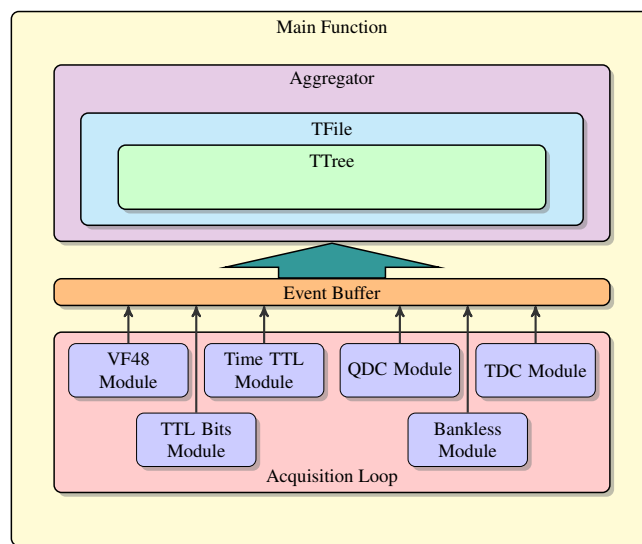


Figure 3.11: Architecture of analyzer program. In the December 2012 run the online data analysis program became unwieldy because there was no software architectural plan or style guidelines. In early 2013 the software was restructured to fit the design pattern shown here. As it turned out this same architecture was also well suited to the **GEANT4** event loop and the same software could be reused. This software reuse made it an easy job to produce identical output for both the experimental and simulation data.

without modification and serve the purpose of controlling communication with the TFile object the same as it does in the data acquisition code. The Aggregator class is the common point between the **GEANT4** code and the experimental data acquisition code. The design architecture of this class, shown in Fig. 3.11, and its accompanying application programming interface (API) are what make it easy for us to maintain the parity of file formats between the two systems.

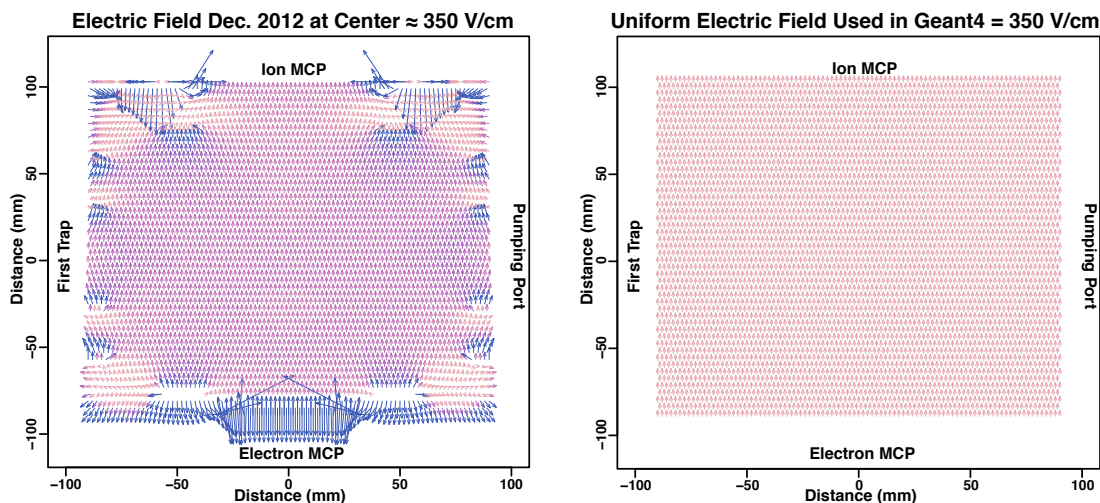
With the advent of multi-threading in **GEANT4.10.0** I attempted to have each worker thread create its own TFile and its own TTree and then they could each independently write data without interfering with each other – at least, that was the premise that I operated on. As it turns out ROOT was never designed to be

thread safe and lots of its functionality is based on taking advantage of function side effects through the manipulation of global state variables. In the world of concurrent programming “function side effects” and “global state” strike fear into the heart of programmers. It did not take much effort on my part to get to a place that I realized that using ROOT in this way would not work without a major rewrite of the Aggregator class. I searched through the GEANT4 documentation and found that the native GEANT4 analysis tools support a TTree like construct. This construct is both thread safe and can be easily transformed into a root TTree so that we could maintain the parity of file formats. The GEANT4 analysis tools version of TTree only supports C++ language built in types like int, float, and double, not std::vector. I submitted a feature request to the GEANT4 collaboration but to date this feature has not been implemented and until it is we will be forced to use GEANT4.9.6 as the last release before the switch to multithreading if we want to maintain the parity of the file format between the experimental and simulation data.

3.10 Future Work with GEANT4

GEANT4 is a wonderful tool because, depending on the amount of time and effort spent developing the simulation, it is possible to develop incredibly detailed simulations of all aspects of the experimental setup. In this section I will mention a few of the things that we wish to model in GEANT4 would like to have modeled in completely in GEANT4 but that until this point have been simplified or ignored because they would have required too much development time and the payback would not have merited the development cost.

The first item that we have put some effort into, but have not fully realized, is to incorporate the real electric field into GEANT4. Until this point we have been assuming that the electric field applied by the electrostatic hoops is a perfectly uniform



(a) A realistic field calculated using COMSOL (b) The homogeneous field used in GEANT4

Figure 3.12: Comparison of electric fields. The electric field shown in Fig. 3.12a is the field that we had assuming the potentials the we used in December 2012 computed by Alexandre Gorelov using COMSOL. The colors are the total field strength and the arrows represent the field vectors in only the two dimensions shown. This view is at $z = 0$ or in other words at the center of the chamber. The picture in Fig. 3.12a narrows at the top compared to Fig. 3.12b this effect is created by the rotation of the the arrow heads going from bottom to top.

350 V/cm. We know that this is not really the case but in the region of the trap we believe that this is a good assumption. A view of the difference between the two fields can be seen in Fig. 3.12. This is one area where we can leverage the development from other experiments. Praveen Shidling who has started the development of GEANT4 simulations for the TAMUTRAP experiment has successfully applied a custom magnetic field map in his work. To port this work over to our simulations would require a week for an experienced GEANT4 programmer.

The second item that we would like to implement in our GEANT4 model is detector response. Sherry Yennello's group, also at the Cyclotron Institute, has recently begun using the Aggregator class (written by me for our data acquisition and GEANT4

code) to start simulating the response of scintillator detectors. We are interested in using a similar setup to more closely model the effects of noise on the asymmetry measurements.

4. EXPERIMENTAL SETUP

This section will describe the experimental setup and what we did to collect the data analyzed in the present work. The TRINAT experimental apparatus that was in place during previous TRINAT experiments [15, 82, 83] was significantly upgraded before this experiment. The type and justification for some of the improvements that were made to the system were laid out in chapter six of Dan Melconian's PhD Dissertation [51]. Other improvements were made because trapping technology has progressed since the previous system was built. In this chapter I will outline the design and implementation process that we went through and highlight the improvements that were made in the current system.

4.1 Design Against Major Systematics

One of the major systematic errors encountered in the previous SM correlation parameter measurement experiment was caused by atoms that escaped from the trap and depolarized before decaying. There was no way to distinguish these unpolarized background events from polarized decays of interest that occurred in the trap. The design of the new chamber had to address this problem.

The measurement of B_ν in ^{37}K was a statistics limited measurement. The geometry for that experiment was slightly different than we require for A_β but we wanted to try and avoid its limitations by making the solid angle of our detectors larger. This way for a reasonably expected production rate of ^{37}K our measurement of A_β would not be statistics limited. In order to reduce, both statistical and systematic uncertainties, we decided upon a couple of different design principles that would guide our decision making. These design principles are:

1. Use a shakeoff electron detector to tag events coming from the trap [29, 84, 85],

2. Avoid pushing the trap during optical pumping by better balancing the power in each beam,
3. Cool the atoms more by moving closer to resonance after they are trapped [86],
4. Use a novel AC-MOT design to increase counting time by reducing the away time for eddy currents [28],
5. Make the solid angle of the detectors as large as possible.

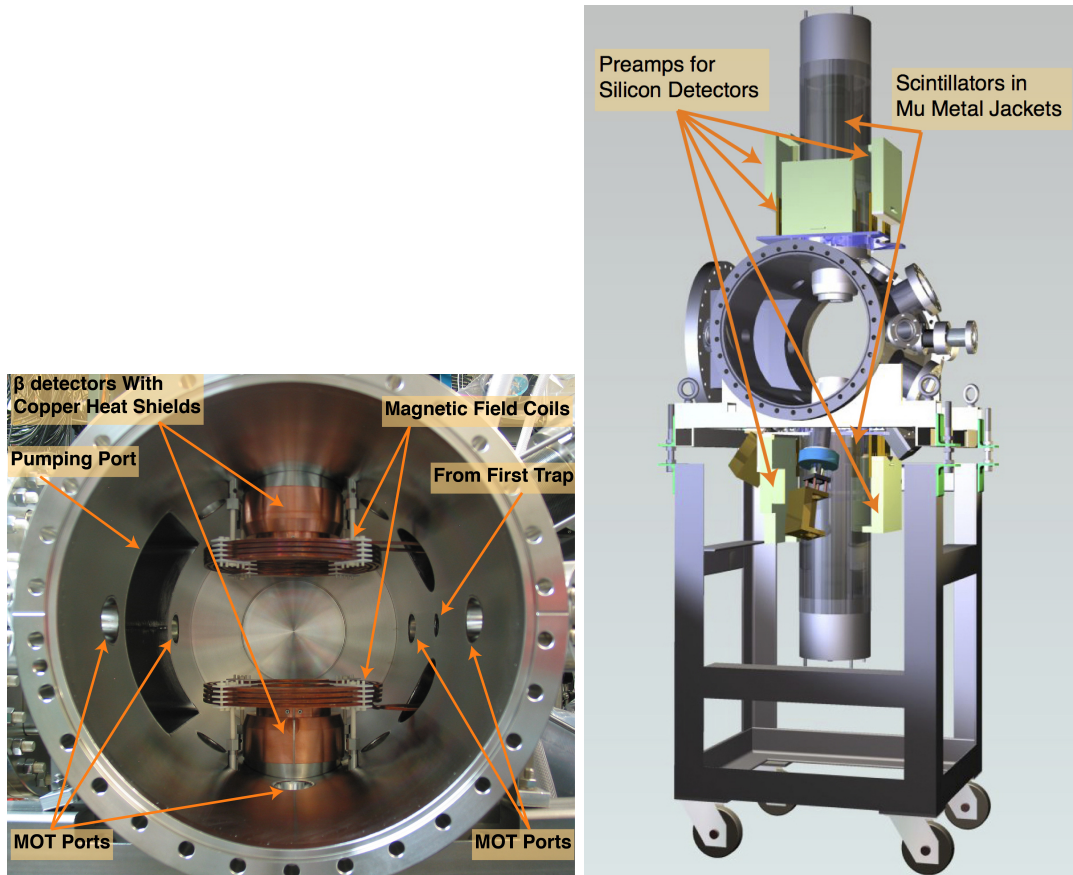
In the next section I will walk through the chamber design process and show how the strategies listed above influenced our design choices.

4.2 Geometry Elements

There are a number of pieces of the experimental setup that, although critical to the overall success of the experiment, are not directly involved in detecting the β s. This section is about some of these less exciting but very functional pieces of the experiment.

4.2.1 *The Chamber*

The vacuum chamber is the largest and most complicated pieces of the experimental setup. The design of the chamber is tied up with other factors such as the design of the mirrors and the need to provide optical access to the trap. One of the main guidelines that drove the design was to make it as large as possible. The reasons for this are threefold. First, in order to make the electric field near the trap as uniform as possible, the boundary effects of the chamber wall should be as far away as possible. Second, atoms that escape from the trap will eventually migrate to the walls where they will depolarize before decaying. We use the two MCP detectors to discriminate against this unpolarized background. If the walls are sufficiently far



(a) View Inside Chamber with β detectors installed. (b) Autodesk Rendering of the chamber.

Figure 4.1: Two views of the experiment. These views represent the progression of the experiment from conceptual design to engineering drawings to physical installation of the detectors.

away then neither the shakoff electron nor the recoiling daughter could reach their respective MCP. Third, a large number of optical access ports had to be incorporated into the design. If the chamber was too small then these ports would begin to overlap, significantly increasing the design complexity and price of the chamber. We decided to go with a chamber that used 14 inch conflat flanges as the main entrance ports. On these ports would be mounted the electrostatic hoops and MCP detectors.

Two other important considerations that were taken into account when designing the chamber were the electrical conductivity and the magnetic properties of the material. In the experiment the magnetic field from the MOT needs to be turned off before the atoms are optically pumped. The presence of stray magnetic fields is a depolarizing mechanism. If the material is extremely conductive, eddy currents induced in the material could continue to produce small magnetic fields for a long time. If the material is more resistive, the eddy currents die away quicker as they are dispersed as heat in the material. Also, the inherent magnetic response of the material has to be considered. We considered two materials for the chamber: titanium and stainless steel. Titanium's natural magnetism is extremely low but stainless steel has a higher electrical resistance. In the end 316L stainless steel was chosen because it was much cheaper and easier to machine than titanium. The flanges of the chamber are made from 316LN steel, which has even lower natural magnetism than 316L. The chamber was manufactured by the TRIUMF machine shop.

4.2.2 Silicon Carbide Mirrors

In order to measure A_β it is first necessary to prepare a sample of ^{37}K in a polarized state and then to have a way of measuring the β s that come from the decay and to know what the angle is between the β -detection axis and the polarization axis. For convenience in doing the data analysis it is simplest if the detection axis and the polarization axis are the same because the asymmetry maximized in this configuration (see Fig. 1.1). Since the polarization of the atoms is done through optical pumping, the direction of the magnetic field of the laser beams is what defines the polarization direction. In the previous setup the laser beam was sent into the chamber, where it reflected from an angled mirror and then through the trap, then reflected again from the flat mirror in front of the detector and exited back along the

path that it came in on. This setup worked well from the standpoint of alignment because only one mirror needed to be precisely aligned in the vacuum. So by maximizing the power returning along the same path as the incoming beam it was easy to optimize. The drawback to such a setup is that the two counter propagating beams, when they intersect with the trap, will always be asymmetric in power because of the extra reflection off of the flat mirror. This asymmetry in power would lead to the atoms absorbing more photons from one direction than the other. The effect of this is that the cloud would be pushed during the optical pumping time. Another aspect to consider is that, because the mirrors are placed asymmetrically, the β scattering will be different for each.

To overcome these problems it was decided that two counter propagating beams should be sent through the cloud, and reflect from identically angled mirrors. Then the power in each beam could be adjusted so that the power in each matches. Having matched power in both beams would eliminate laser induced trap movement. The downside to doing this is that the effort required is at least doubled. Now there needs to be two angled mirrors precisely aligned in the vacuum. The tune up becomes more complicated because there is no guarantee, the two beams are properly overlapped.

Once it was decided that two laser beams would be used, the next question that was asked was the angle at which the incident beam should enter the chamber. The reason why this is an important question is that it affects how close the detectors could be to the atom cloud. For a visual representation of why having a steeper mirror angle allows for detectors of greater solid angle see Fig. 4.2. Geometry is not the only design constraint in this case and some other important facts needed to be considered before choosing a mirror angle. First the dielectric mirror coatings used in polarization maintaining mirrors work better at shallower angles. Second since the β particles have to go through this mirror before hitting the detector it is should

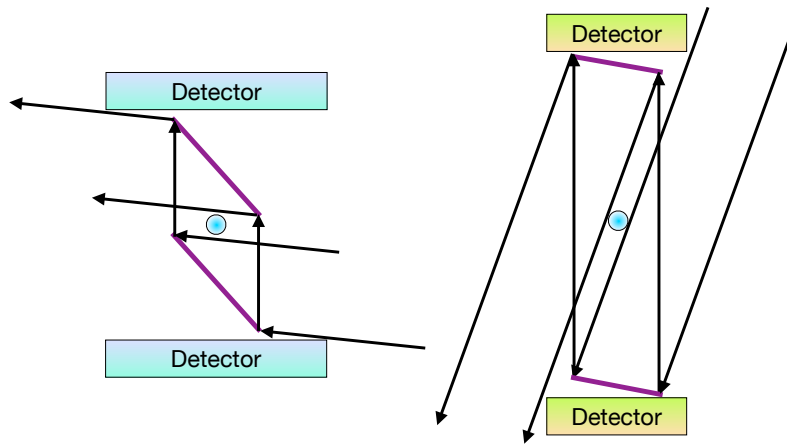


Figure 4.2: Design considerations for different mirror angles. This is a view of two hypothetical geometries that could be used in the optical pumping scheme of our experiment. The black arrows represent the outer dimensions of the optical pumping laser beam. The blue cloud in the middle represents the cloud of atoms and the purple lines represents the mirrors that would have to be placed in vacuum. Referring back to the design goals enumerated at the beginning of this chapter we can see by comparing the designs on the left hand side with steep mirror angles and those on the right with shallower mirror angles that increasing the mirror angle allows for designs with detectors of greater solid angle because the detectors can be both larger and closer. From the viewpoint of the mirror manufacturer shallower angles are preferred because of polarization minting dielectric coating. In the end the mirror that we got was a balance between these competing considerations.

be made out of a low Z material and should be extremely thin to prevent scattering. Third since the MOT laser beams have to travel along this same path and are fixed at one inch diameter, the diameter of the mirror needed grows like $1 \text{ in.} / \cos \theta$ to contain the laser beams. For all materials the larger the diameter of the mirror the thicker it needs to be to preserve the needed rigidity to maintain optical flatness across its surface.

After considering a few options with both experiment and Monte Carlo (see Fig. 3.7) we decided on a design with the mirrors placed at 19.5° and displaced from the trap center by 90 mm. This angle was chosen because it was the largest angle that we could use without compromising the polarization maintaining abilities of the mirrors, which fell off sharply above 20° . The mirror itself was made out of 0.25 mm-thick silicon carbide. Silicon carbide has a Young's modulus of 450 GPa, one of the largest known, so this allowed us to make a very large thin mirror from it.

4.2.3 *Electrostatic Hoops*

Once the location of the detectors was chosen and the direction of travel for the laser beams was established we could begin to think about the system that would be used to create the electric field that would sweep the recoiling daughter ions onto the the one MCP and the shakeoff electrons onto the other. The system would be comprised of a series of electrostatic hoops that would be set to appropriate voltages to produce an electric field that would be as uniform as possible for ions and electrons originating from the trap. It was decided early on that the hoops would be manufactured from glassy carbon. The reasoning behind this choice is that it is the lowest reasonable Z choice possible besides beryllium. One advantage that glassy carbon has over beryllium is that it is a semiconductor which means that it will not suffer from induced eddy currents the way that beryllium would.

The placement of the hoops was chosen in such a way as to allow the laser beams to pass through the gaps so that the hoops could be manufactured in simple shapes. In Fig. 4.3 is a view of the fully assembled hoop system along with the ion MCP. A rectangular design was chosen over a more symmetric circular hoop design because it allowed us to avoid collisions between the hoops and beta detectors during installation. With proper tuning of the electric potentials on the hoops it is possible to produce an electric field that is almost as uniform as the case of circular hoops. See Fig. 3.12a for a view of the electric field that was achieved in the plane of the trap. The design specification for the system was to produce a uniform field of 1000 V/cm along the MCP-axis.

The realization of such a system was more complicated than anticipated. Glassy carbon is an interesting material. It is jet black and has mirror surfaces. It has the acoustic quality of fine crystal and will ring if lightly tapped. It is very hard but extremely brittle. The way that parts are normally manufactured from glassy carbon is to machine the polymer resin into the desired shape before the carbonization process that transforms the polymer into glassy carbon. The deformation that occurs to the part during carbonization is well understood by the manufacturer and can be accounted for in the original design. Since we had so many custom parts, this process would have been prohibitively expensive so instead we decided to form the parts from cheaper bulk glassy carbon. What we learned along the way will be helpful to anyone trying to make parts from this material. The first approach that we tried was to machine the hoops from glassy carbon. It is possible to machine with diamond tipped tools at extremely high speed but the material is so brittle that sometimes the part unexpectedly shatters due to vibrations. Cutting and drilling were more successful than milling and all of the sleeves that additionally acted as spacers between the hoops, see Fig. 4.3, were made in this way.

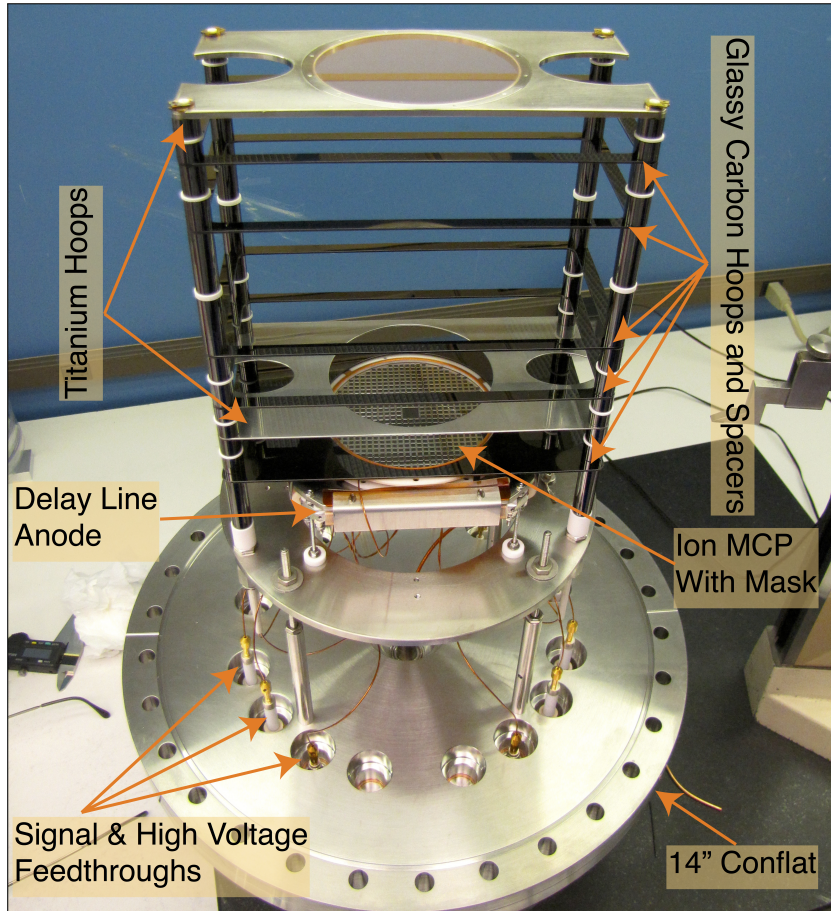


Figure 4.3: The hoop and ion micro channel plate assembly before installation in the chamber. This view shows the electrostatic hoops and the ion MCP detector. The mask on the ion detector is clearly visible. It is also possible to clearly distinguish the titanium hoops that replaced the glassy carbon ones that were broken in the manufacturing process. This whole assembly is mounted on a 14 inch conflat flange and is inserted fully assembled into the main chamber.

Because of the problems with traditional machining a second technique was tried, which was "wire fed" electrical discharge machining (EDM). This technique involves making a cutting jig and placing the glassy carbon in the jig. Then both are lowered into a water bath where a charged wire is moved through and when it comes sufficiently close to the part, the arc from the wire will ablate a small amount of the surface. The problem that we encountered with this technique was that our cutting jig was made out of aluminum and under the conditions just described the aluminum and glassy carbon would chemically react. Aluminum oxide would plate on the glassy carbon surface.

The last and most successful manufacturing technique that we tried, and the one that was ultimately employed to manufacture the hoops, was traditional EDM. Copper electrodes in the negative shape of each hoop were made at the TRIUMF machine shop and then on very slow speed without any cutting jigs and under heavy oil the arc from the electrode would burn cleanly through the glassy carbon at a rate of 0.4 mm per hour.

Having spent a lot of time and effort manufacturing the hoops we were disappointed when afterward we broke two of the seven. This led us to try to epoxy the broken pieces back together. We were again disappointed because we were unable to find an epoxy capable of adhering to the ultra smooth glasslike surface of the breaks. With beam time approaching we choose to manufacture two replacement hoops from grade 4 titanium instead of trying to replace the two broken hoops because the lead time for more glassy carbon was too long. We made the decision to use titanium because it is non-magnetic, has a relatively high electrical resistance for a metal to reduce eddy currents, and was light enough to be supported by the existing ceramic support structure. Grade 4 titanium is harder than other alloys allowing it to be polished to a finer finish. I polished each of these hoops by hand on a granite ta-

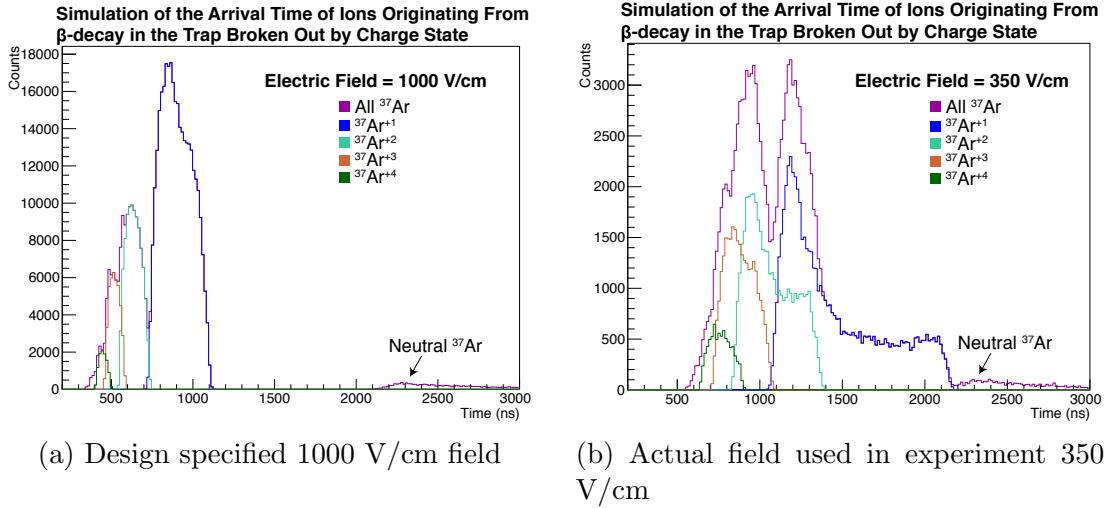


Figure 4.4: Charge state time distributions. At the design specified 1000 V/cm field the charge states 1+ and 2+ are cleanly separated from each other and from the neutral atoms that come in at around 2300 ns. The neutral atom time-of-flight is important in determining the trap position along the MCP-axis because it is independent from the electric field. As you can see in Fig. 4.4b at the achieved field of 350 V/cm none of the charge states are separated well and even the rising edge of the neutrals is not clean.

ble up to 3200 grit to avoid sparking. A week before the experiment was slated to begin, while conditioning the hoops, with the hoops at voltage producing a field of 850 V/cm, a spark occurred in the system. After this spark event occurred, two of the hoops became shorted together and we were not able to reliably apply a field of no more than 350 V/cm. This last minute change in field greatly reduced our ability to separate the recoiling atom charge states, and hence our ability to locate the trap spatially along the MCP-axis. Fig. 4.8 shows the simulated separation of charge states that could be expected with a 350 V/cm field and a 1000 V/cm field. This is not a critical problem in the case of measuring A_β but would be disastrous for trying to measure the other correlation parameters such as $a_{\beta\nu}$.

4.3 Detectors

A major part of the setup for this experiment was building up the β -detectors and implementing the data acquisition scheme for them. In addition to the β -detectors there are two MCP detectors that provide crucial information to us like tagging events from the trap and diagnostics about the trap size. This section will describe these detectors.

4.3.1 Scintillator Detectors

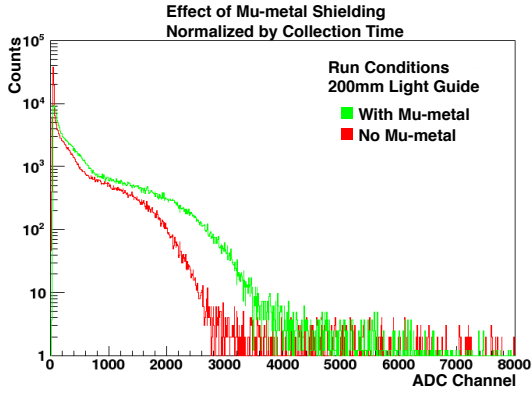
The scintillators were the first detectors that we bought and this meant that we also had the most experience using them. They are made of BC-408 plastic from Saint-Gobain Crystals. The scintillators are glued to a lightguide and PMT. The PMTs are 5" model 9823B tubes from ET Enterprises. They are blue-green sensitive and have 14 BeCu dynodes. The custom transistorized bases also supplied by ET Enterprises provide the anode and final dynode signals as output so that one of the signals could be used from timing measurements and the other for energy measurements.

Originally we tested the scintillators together with a Caen V1740 digitizer. This digitizer was a candidate module that would be used for the read out of these detectors. This digitizer lacks the timing resolution necessary to cleanly digitize the raw signals from the PMT but could be used following the example of the DEAP experiment at SNOLAB that stretches their raw scintillator signals in time and then uses an equivalent V1720 module to capture the waveforms from their detectors [87]. It was decided that this technique would not work for us and the scintillator signals during the experiment would not be digitized but instead recorded with a Caen V792 QDC.

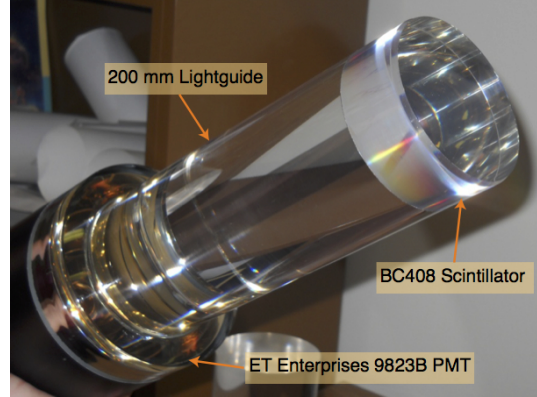
In order to design the full detector assembly one of the first things that needed

to be decided was the length of the light guides used to connect the scintillators to the PMTs. This is important because near the trap there are magnetic fields that can affect the efficiency of the PMT. This happens because a magnetic field can steer electrons away from the dynodes. The effect is largest between the photocathode and the first dynode because no multiplication has yet occurred and the electrons are at low energy [88]. One way that this problem can be mitigated is by wrapping the PMT in μ -metal. μ -metal is an alloy with high magnetic permeability that allows a path of least resistance for magnetic field lines around the shielded object. This technique works best when the μ -metal extends well in front on the photocathode. The increased signal that we see by shielding the photocathode with μ -metal is opposed by signal loss due to light scattering in the light guide. In order to test what the optimal lightguide length was we bought lightguides of three different sizes and tested each with μ -metal to decide which gave the best response. A comparison of the response of the detector for the three different lightguides tested is shown in Fig. 4.5c. The figure of merit for comparison of μ -metal shielding is the distance from the photocathode to the open end of the shield divided by the diameter of the μ -metal, L/d . For the 200 mm light guide that was selected in the final geometry the $L/d = 120 \text{ mm}/152.4 \text{ mm} = 0.79$.

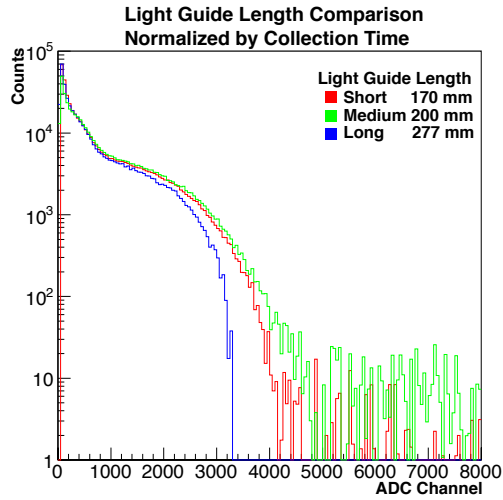
Another important question that we had about the scintillators was what sort of wrapping scheme would work best to optimize the response function. We tried different wrappings around the side of the scintillator including diffuse reflectors such as paper and teflon specular reflectors such as 3M-ESRTM and Al-mylar. The 3M-ESRTM allowed us to collect the greatest amount of scintillation light. The wrapping on the front face of the detector is important because not only does it aid in light collection but the β s also have to travel through this material before entering the scintillator. For this reason we wanted to make sure that the energy loss was going



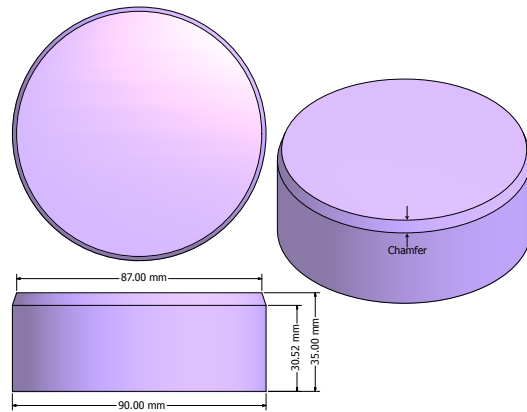
(a) Effect of Mu Metal Wrapping



(b) View of the Assembled Scintillator



(c) Comparison of Light Guide Lengths



(d) Scintillator Design Drawing

Figure 4.5: Scintillator design and testing. The scintillator dimensions (Fig. 4.5d) were chosen, using simulations from *GEANT4*, to stop a 5 MeV β . There is a chamfer cut on the front that allows the wires from the strip detector to bend around it more easily. The light guide length was chosen to be 200 mm because it allowed for the PMT to be pulled back further from the trap and allowed the μ -metal shielding (see Fig. 4.5a) to extend the furthest in front of the photocathode without hurting the response function in the way that the 277 mm light guide did (see Fig. 4.5c). The final assembly was glued together by the TRIUMF scintillator shop (see Fig. 4.5b).

Measured Energy Loss In Material	
Material	Energy Loss (keV) per Layer
3M-ESR TM	13.3
Teflon Tape	4.59
3 μ m Al Mylar	0.474
35 μ m Al Mylar	5.55

Table 4.1: Energy loss in scintillator wrapping materials tested. These are the materials that we measured both the energy loss and the effect on the scintillator spectrum. We decided to use teflon tape on the front face of the detector because it struck the best balance between the two competing variables.

to be low through this material. We measured the energy loss with a β source and a silicon detector along with measuring the signal response of the scintillator. A table of the measured energy losses is shown in Table 4.1. We selected one layer of teflon tape because it offered the best compromise between increased gain of the scintillator signal while still having a small enough energy loss.

4.3.2 Silicon Detectors

The silicon detectors are more complicated to work with than scintillators but they proved remarkably resilient in the experiment, even though we abused them. The detectors were manufactured by Micron and are 300 micron thick silicon with 40 parallel strips per side, with the strip direction on the two sides being orthogonal. The detectors were biased to +70 V during the experiment with +40 V being the nominal full depletion voltage. The voltage was supplied to the X strips and the Y strips were grounded. For a schematic layout of the detectors and the axis label assignments see Fig. 4.6. The bias was supplied through the preamps. The preamps were custom designed by Leonid Kurchaninov at TRIUMF to match the measured capacitance of the detectors supplied by Micron. Each preamp read off the signals from either the odd or the even set of twenty strips that were read off for a given detector plane.

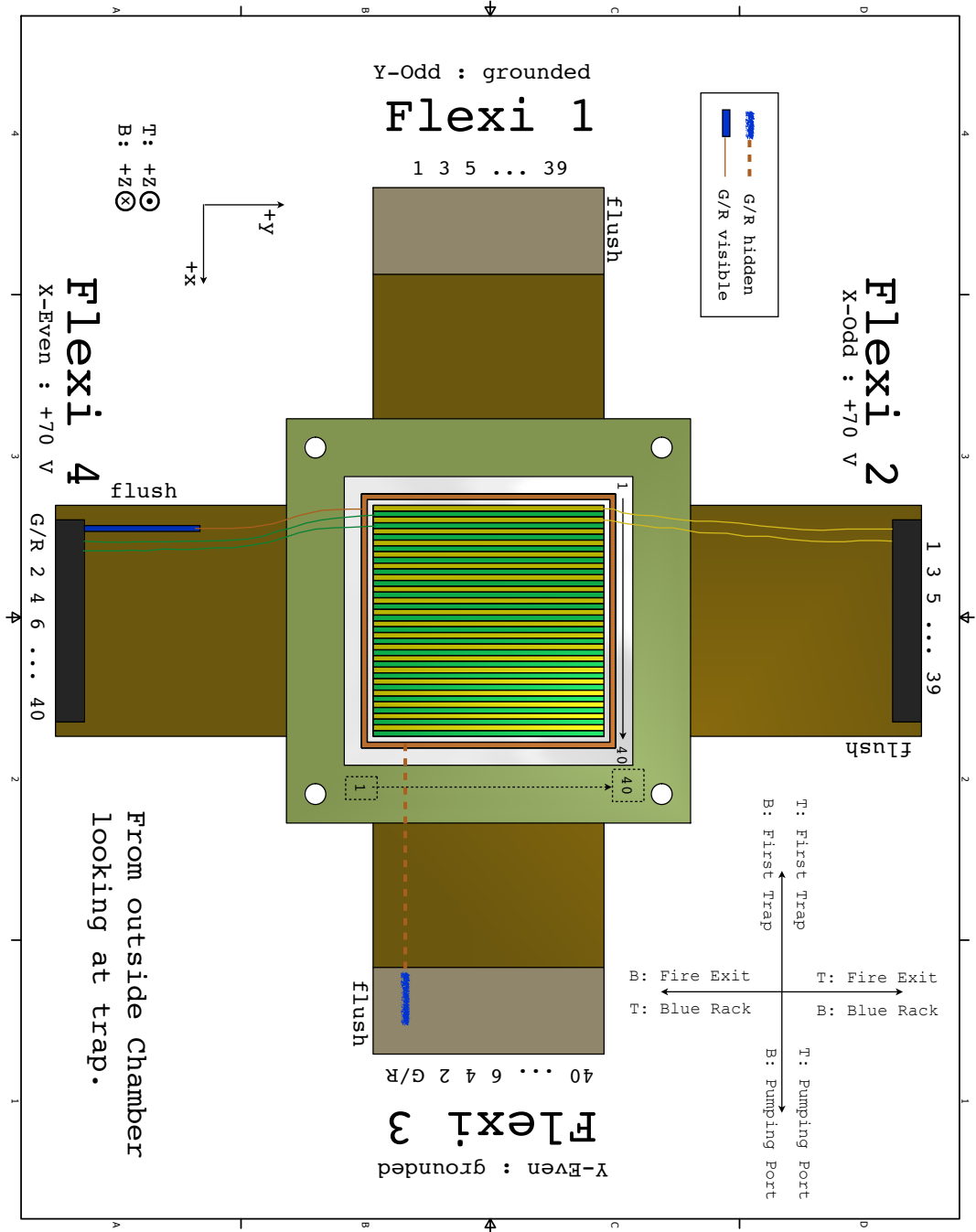


Figure 4.6: Detailed layout and axis choice for silicon detectors. The strip detectors are chiral with respect to inversion. This becomes important for hooking up the preamps in the case of the flexi 2 and 4 where the optical pumping ports dictate the way that the wires can bend.

Fig. 4.8c shows how the signals coming out from the detectors propagate through the preamps. These twenty channels were then broken apart and recombined into VF48 digitizer modules. A schematic showing how the signals were transported from the preamps to the VF48s is shown in Fig. 4.7. Each of the detectors, due to the presence of a guard ring to sink current, is chiral and has a definite handedness. This being the case the two detectors top and bottom cannot be installed in the exact same configuration. Fig. 4.6 shows the choice that I made to rotate around the x-axis when installing the detectors.

In addition to the physical strip numbering shown in Fig. 4.6 there are additional numbering schemes that need to be kept track of for these detectors. The second set of numbers come from the preamp channels. This is shown in Fig. 4.8c. The third set of numbers then comes from plugging the combined signals from the two preamps of a detector plane into a single VF48 module as shown in Fig. 4.7. The last set is then how the modules are read into the software. The full set of routings can be found in the configuration files for the analyzer and can be checked out from the git repository using the tag Dec2012Data.

One thing that was important to consider when we were designing the system was that we needed to balance the desire to put the detectors as close to the trap as possible while optimizing the detector performance. In the case of the strip detectors this meant that we had to consider how close we could reasonably get the preamps to the detectors. We originally planned to have the preamps inside of the reentrant flange touching the silicon detector. Calculations done by Leonid Kurchaninov showed that the preamps for a full detector would dissipate 70 W of heat. This was unacceptable in the very confined space of the reentrant flange and made us consider bringing them outside the mu-metal. By measuring the capacitance of the detector (36 pF) and the cables (24 pF) that would be used to bring the signal out, and using

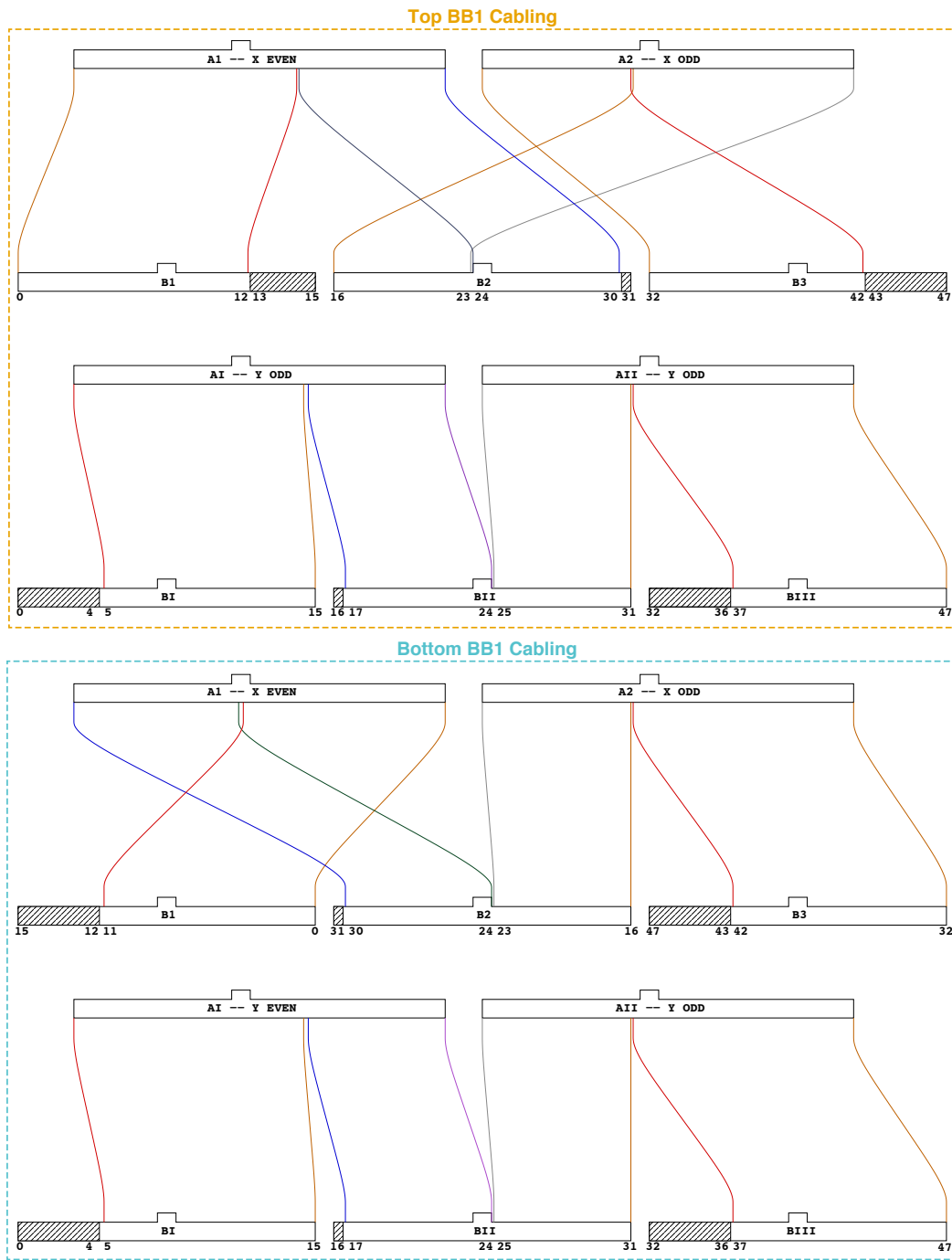


Figure 4.7: Schematic showing the detector cabling. This figure shows how the channel numbers get changed up on the way from the preamps to the VF48 modules.

some simulations to find the number of charge carriers that would be created by a minimally ionizing β , we were able to estimate that we would see a 2.6 keV increase in the noise by using longer cables.

During the experiment the strip detectors took a lot of abuse from an unexpected source. When we decided to use the AC-MOT, we knew that we would be able to damp eddy currents in the chamber by dissipating them as heat. We did not consider this to be a problem to the chamber as a whole because the walls are 1/2 inch thick and are air cooled everywhere except at the reentrant flanges. The reentrant flanges on the vacuum side are the closest object to the magnetic field coils, which means that they get the brunt of this heating. Additionally, because they are packed tightly with the silicon detectors and scintillators on the air side, they do not get much air cooling. This meant that in the experiment they heated up and, as they heated up, the leakage current on the silicon detectors rose. The nominal operating leakage current for the detectors is 300 nA. During the experiment once the apparatus had reached its equilibrium temperature the leakage current on the detectors was 7 μ A. With some success we directed the output of an air conditioning unit onto the outside of the chamber near the reentrant flanges. Nevertheless the leakage current remained high.

It was found during the experiment that the β spectrum was not separated from the noise peak for the X-odd strips of the top detector. This was disconcerting as they had all previously been shown to work as shown in Fig. 4.8a. As all of these strips were read out by the same preamp board, this board was the suspected culprit. This preamp board was replaced with the only available spare. This replacement board also proved to be broken and in the end we were not able to use any of the X-odd strips on the top detector for data analysis.

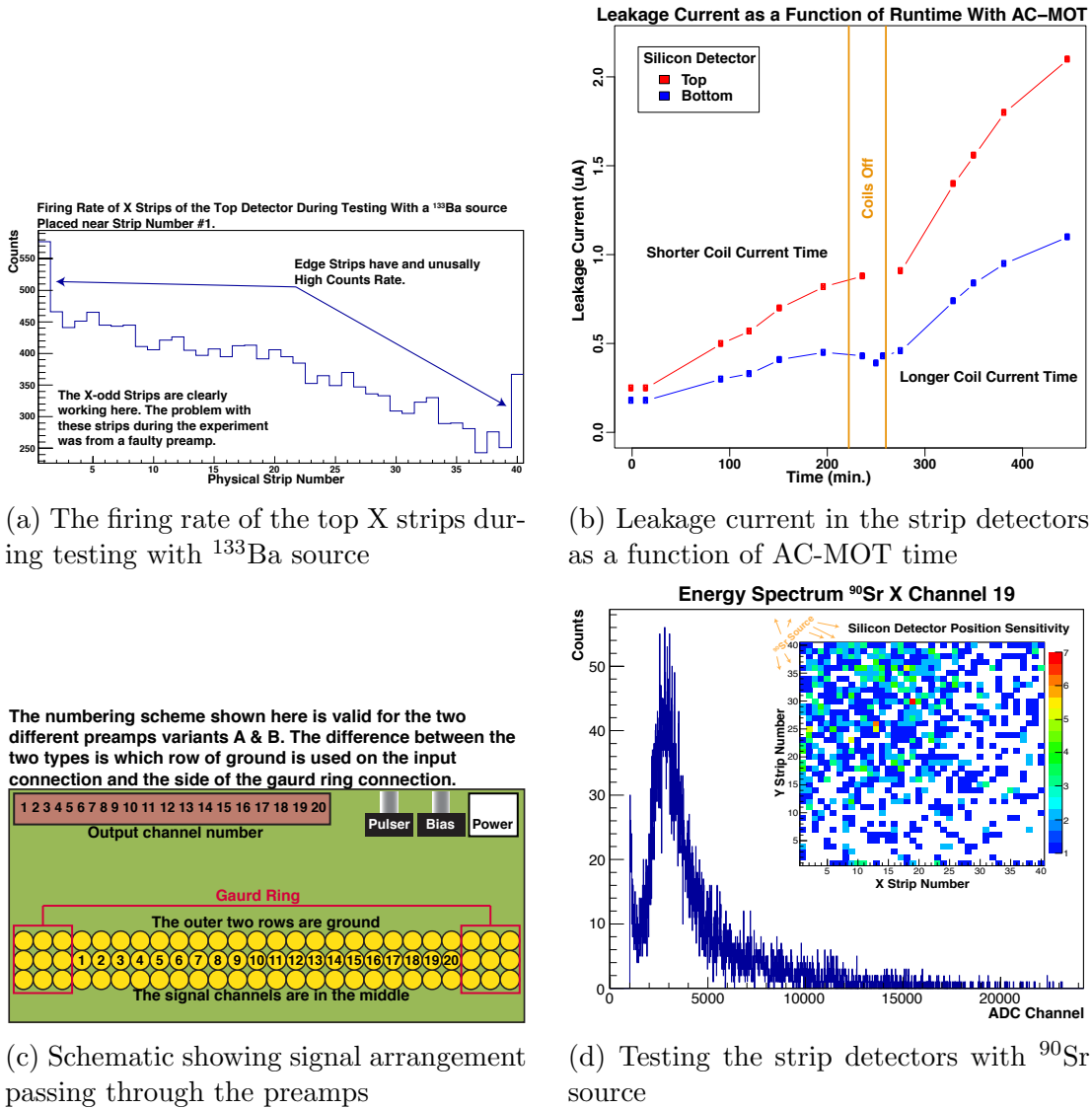
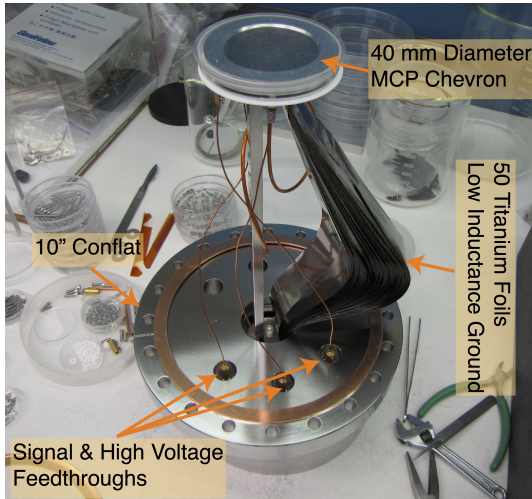


Figure 4.8: Strip detector information. The reason that we choose to use a strip detector was so that we could also get some position information about the β s as they passed through on the way to the scintillator. The energy spectrum for the strips and the position test were done with ^{90}Sr ^{133}Ba sources as shown in Fig. 4.8d and 4.8d. The strip detectors were not tested for high temperature operation like what is shown in Fig. 4.8b until the experiment when the action of the AC-MOT heated the flanges where they are located. There are two different varieties of preamp as shown by the schematic in Fig. 4.8c that need need to be planned for when bending the signal wires out of the μ -metal jacket.

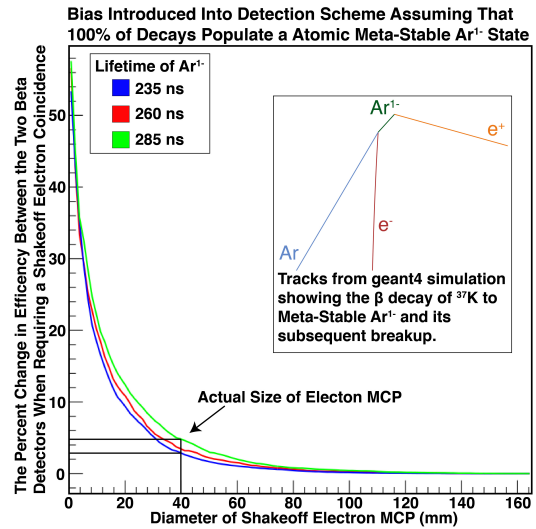
4.3.3 Shakeoff Electron MCP

The shakeoff electron MCP was the simplest detector that we used. It consisted of a simple stack of 40 mm diameter MCP plates in a chevron configuration. The holder and anode were designed and manufactured by Alexandre Gorelov. The signal was read out from a metal stainless steel anode. One thing that was unique about this particular detector was that it required a low inductance ground to optimize its signal. To accomplish this, fifty titanium foils were hand cut and attached so that they would hang in a splayed-out fashion. A picture of the detector can be seen before assembly in Fig. 4.9a. The low inductance ground did help but the signal from this detector suffered from reflections due to poorly matched impedance.

This detector was replaced after this experiment with a RoentDek 80mm diameter MCP backed by a Hex75 delay line anode. One of the purposes for this upgrade was to check that the 40mm plates that we used in this experiment were large enough to contain all of the shakeoff electrons from the β decay. One mechanism that could lead to a loss of electrons would be if the β decay of ^{37}K populated a short lived Ar^- state that would fly some distance before shedding its extra electron, which would then miss the MCP. This effect was simulated in **GEANT4**, shown in Fig. 4.9b, and under a worst case – albeit unrealistic – assumption that every ^{37}K decay populates this state, a bias as large as 4% could have been introduced into the asymmetry. In the follow-up experiment using the larger position sensitive MCP, it was shown that at an applied field of 350 V/cm, the same used in this experiment, all of the shakeoff electrons from the β decay of ^{37}K were contained in an area less than 40 mm in diameter. Also by measuring the “tail” of the electron timing spectrum an upper limit of 4% can be placed on the number of decays that can feed this excited state which implies the largest efficiency shift that could be observed is 0.2%



(a) Assembled electron MCP before installation



(b) Travel distance of Ar^{1-}

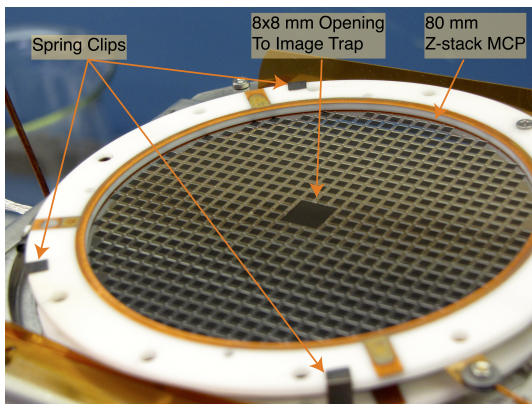
Figure 4.9: The shakeoff electron micro channel plate. As shown in Fig. 4.9b the detector mounts on a ten inch conflat flange. The titanium foils for the low inductance ground are clearly visible. This detectors only purpose was to provide a timing signal for the arrival of shakeoff or photoionization electrons and is therefore very spartan in its design. Due to its relatively small size we were concerned that electrons could miss the MCP if a metastable Ar^{1-} state was populated by the β decay or if the shakeoff energy spectrum was higher than predicted. Fig. 4.9b shows the results of a GEANT4 simulation where we assume that all decays populate this excited state. In this case a 4% change in efficiency between the two β detectors would be introduced by requiring a shakeoff electron coincidence. By measuring the “tail” of the electron timing spectrum we can place an upper limit of 4% on the number of decays that can feed this excited state which implies the largest efficiency shift that could be observed is 0.2%.

4.3.4 Ion MCP

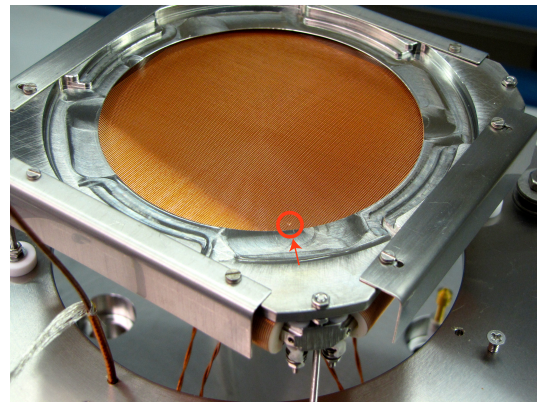
The ion MCP detector was the detector that allowed us to measure some of the properties of the atom cloud. It is a stack of three micro channel plates backed by a delay line anode, RoentDek DLD80. The electronics to supply high voltage to this detector and to decouple the signals from the high voltage were built at TRIUMF by Alexandre Gorolov and Leonid Kurchaninov.

The delay line anode provides position information by reading the signal on both ends of a long coil of wire and taking the time difference between the arrival of the two signals to determine where along the wire the signal originated. The response of the delay line anode is nonlinear across its entire length. This means that in order to get good position resolution out of it, it needs to be calibrated with a mask and that a transform needs to be applied to the data. A picture of the mask and the delay line anode are shown in Fig. 4.10. This process of calibrating the mask was done before the experiment by using 266 nm light to illuminate the inside of the chamber. Light of this wavelength has a high efficiency for firing the detectors.

During the calibration phase and continuing into the experiment there was a problem observed in the signals from the delay line anode. We were not receiving signals from the top 5 mm of the detector. Only after the experiment when the apparatus was disassembled were we able to discover that the spring clamps that held the detector in place had failed and that the detector had slipped down by 5 mm. This slipping did not affect the position knowledge because we had left the mask in place during the experiment, meaning that the calibration procedure could be redone with any data set.



(a) Assembled ion MCP before installation



(b) The delay line anode

Figure 4.10: The ion micro channel plate with mask and delay line anode. In this picture Fig. 4.10a we can see the Ion MCP with the mask installed with the large opening cut in the center to image the atom cloud. Also visible around the edge of the ceramic are the vendor supplied spring clamps that are intended to keep the detector in place. It was the failure of one of these springs that caused the detector to slip down. In picture Fig. 4.10b we can see the delay line anode. Circled in red is a defect on one of the wires that we found before assembling the device. It turned out not to be a problem.

4.4 Timing

Timing for the experiment was provide by a mixed set of devices. The gross timing for the experiment was provide by a computer running Windows 98 that will subsequently be referred to as the “trapping commuter”. The computer had a digital to analog converter (DAC) card installed in it. This card allowed it to send either digital or analog pulses out through a Bayonet Neill-Concelman (BNC) cable. This computer would send signals to the acousto optical modulator (AOM) that controlled when push beam came on and turned the MOT light on and off during the cycle. This is achieved by steering the correct frequency of light into the beamline at the correct time. At all other times the light is steered by the AOM into a beam dump. The purpose of the push beam was to move atoms that were confined in the first MOT into the second MOT which is where the nuclear detectors were located. TThe push beam would come about once a second and the polarity of the light was changed every 16 seconds. This computer also controlled the camera that would take a picture of the MOT while the polarization change happened. A timing diagram appears in Fig. 4.11. The timing accuracy of these signals was on the order of milliseconds. The logic level of these timing signals were recorded by the NIMO32 module for every recorded event. In addition to the level at trigger time the event following a change in the level of any of these signals would also be read out with a timestamp corresponding to the time that the signal level changed. This computer was running a non-real-time operating system and employed blocking input/output operations in its communications with the camera, there could be variability. This means that no guarantees can be made on any of the timings controlled by this computer. This variability leads to the time blocks in Fig. 4.11 labeled as “varies”. Since the timings were recorded with the events we could still order everything in

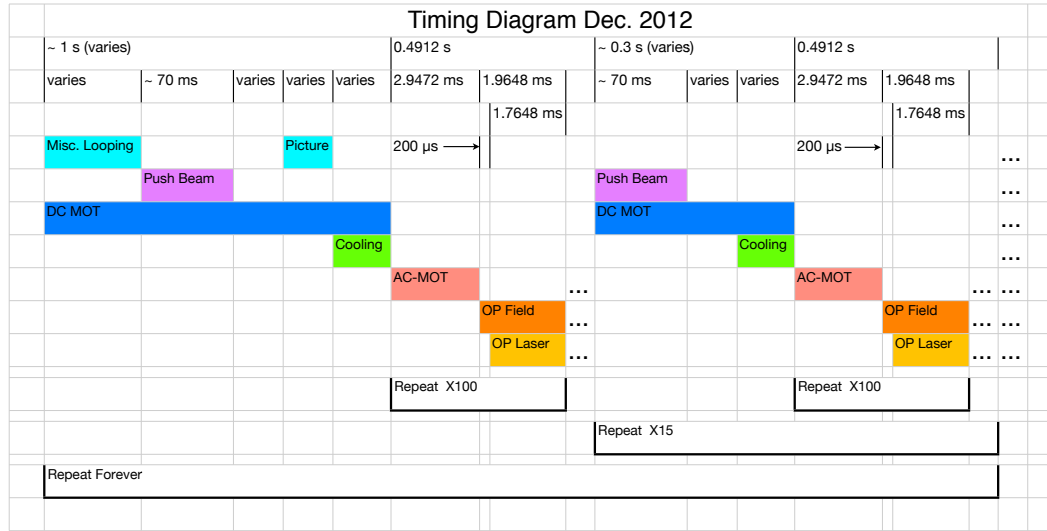


Figure 4.11: Timing diagram of the experiment.

time even if there was variability.

For the part of the experiment that required precision realtime control, the computer would hand off control to an arbitrary waveform generator. This generator was programmed to output a control sequence that would control the power supplies connected to the coils that generated the time varying magnetic field that was necessary during AC-MOT and optical pumping time. The arbitrary waveform generator also drives the electro-optic modulator (EOM) that varies the circular polarity of the MOT light in time with the changing magnetic field. The EOM does not change the polarization of the optical pumping light because it is not as precise as the liquid crystal variable retorter, but it is much faster and can handle the higher power of the MOT beams. These time scales are much smaller than those given to the computer to handle and a complete cycle of trapping/cooling optical pumping/counting would be repeated 100 times per second. The logic levels and level change timestamps were recorded from the signals originating from the waveform generator in the

same way that they were for the signal from the trapping computer. After this set of 100, control would be passed back to the computer to initiate the next push beam. The timing accuracy of the waveform generator is ~ 1 ns per 2 sec. cycle.

4.5 Data Acquisition

One of the largest contributions that I made to this experiment was the implementation of the data acquisition software. This was a major undertaking and was one of the principal reasons for my relocation to Vancouver. There are three parts of the data acquisition system that are of some interest. They are: first, the waveform readout from the silicon detectors; second, the fast FPGA trigger; and third, the event timestamps to count events compared to laser timings. The implementation of the data acquisition system was concurrent with the physical setup and testing of the detector. A simplified schematic showing the physical connection of the detectors with the data acquisition system is shown in Fig. 4.15.

The first area of interest that I will discuss is the waveform readout from the strip detectors. For each triggered event the waveforms for all 160 silicon strips was recorded. In chapter 6 we will see some of the recorded waveforms and what was done with them. The digitized signal was read out by the TRIUMF-developed VF48 digitizer modules [89]. Each module has a set of 6 fast 10-bit ADCs coupled to an Altera Cyclone EPC12 FPGA. Each ADC-FPGA pair manages 8 channels of input. Each waveform is sampled by this module at 60 MSPS.

Arguably the most critical piece of software in the experiment was the firmware trigger burned onto the FPGA of one of the NIMIO32 boards [90]. Each NIMIO32 module is equipped with an Altera Cyclone 1 EP1C6Q240C6N FPGA. The firmware for each board can be changed at any time to change its functionality. Some of the functionality that this module provided for us were: 16 32-bit scalars, a 20 MHz

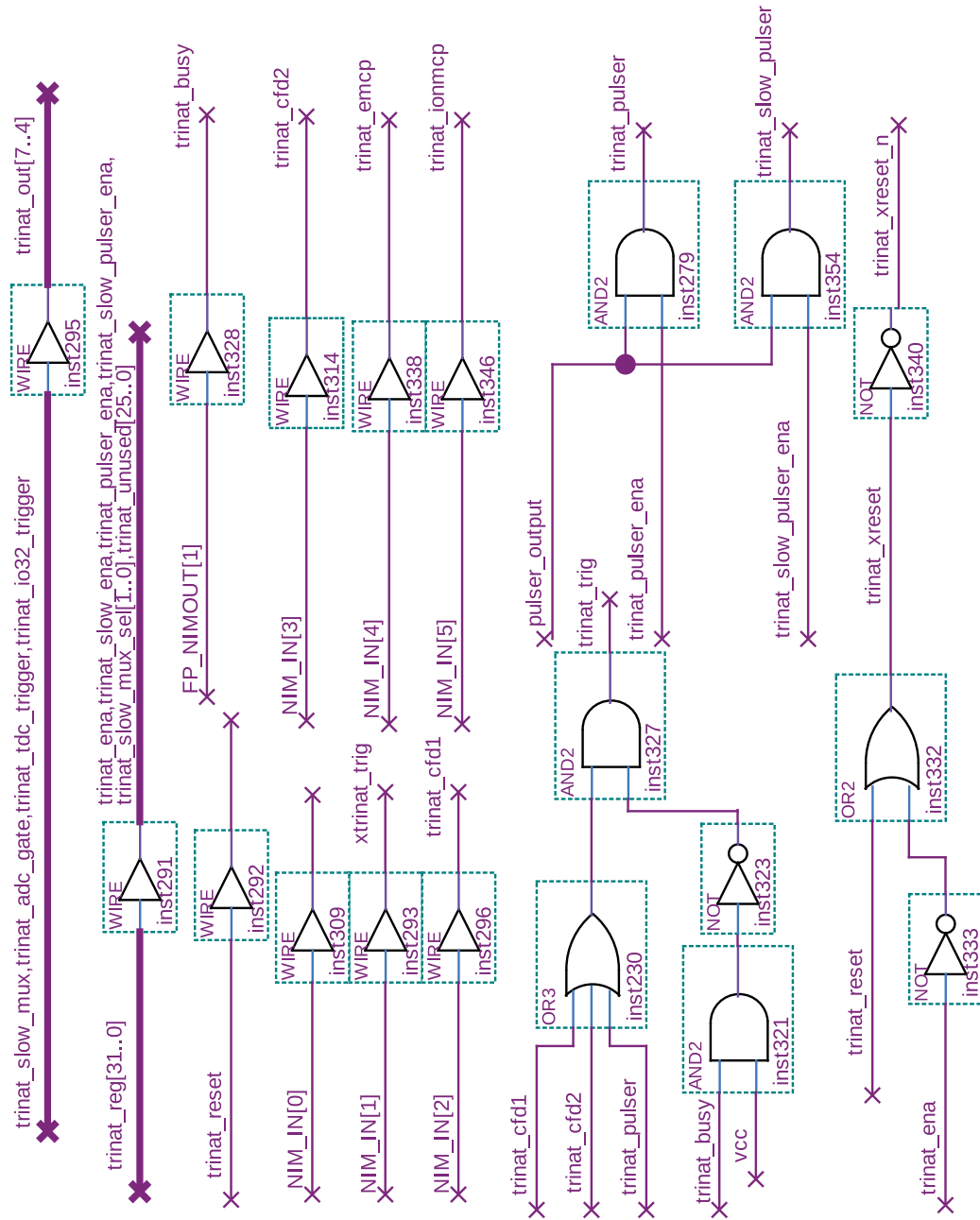


Figure 4.12: NIMIO32 trigger firmware part 1. Fig. 4.12, 4.13, 4.14 are a three part series of schematic representations of the VHDL code for trigger that was burned onto the FPGA for the Dec. 2012 experiment. There is much more to the firmware file such as the pulser definition and the interface with the VME crate but this is the part of the file that has been specialized to the TRINAT event trigger. Briefly, the trigger was an “or” between the electron MCP detector and the hardware coincidence between the scintillators. (See Fig 4.15) It was plugged into what is labeled here as trinat_cfd2. The busy signal is also generated by this module because it knows when an event has finished reading out on the VME bus. It appears here as trinat_busy.

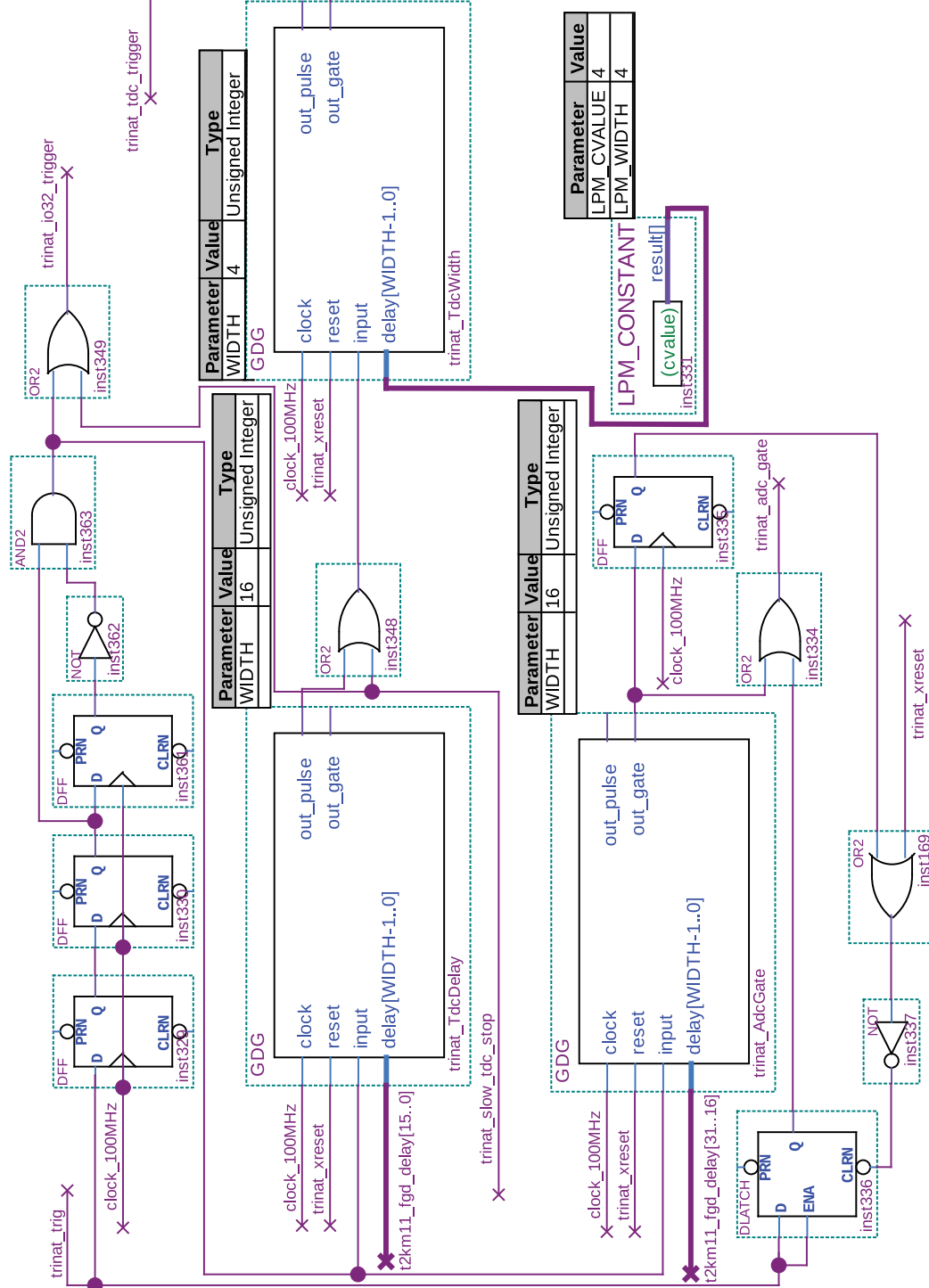


Figure 4.13: NIMIO32 trigger firmware part 2.

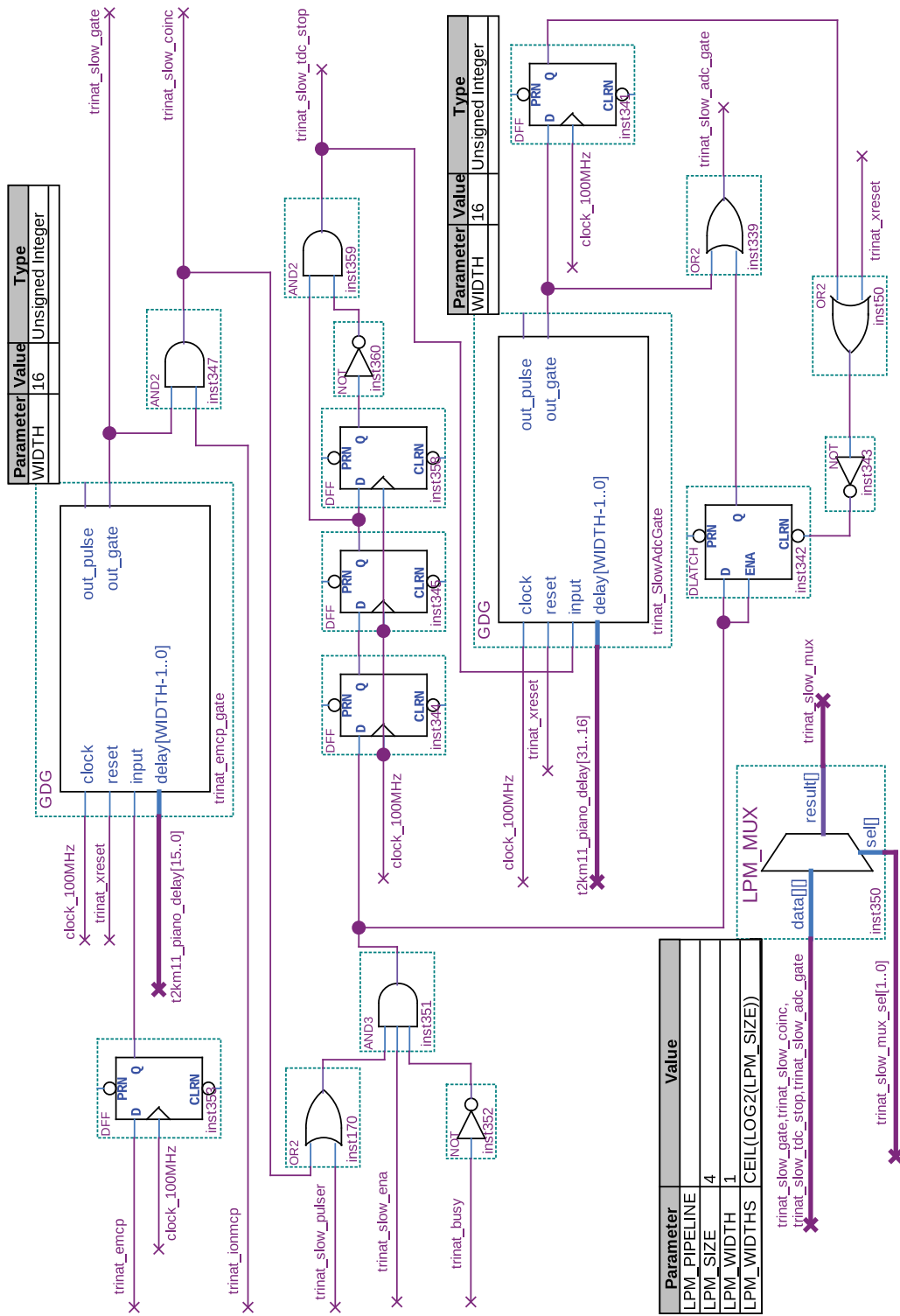


Figure 4.14: NIMIO32 trigger firmware part 3.

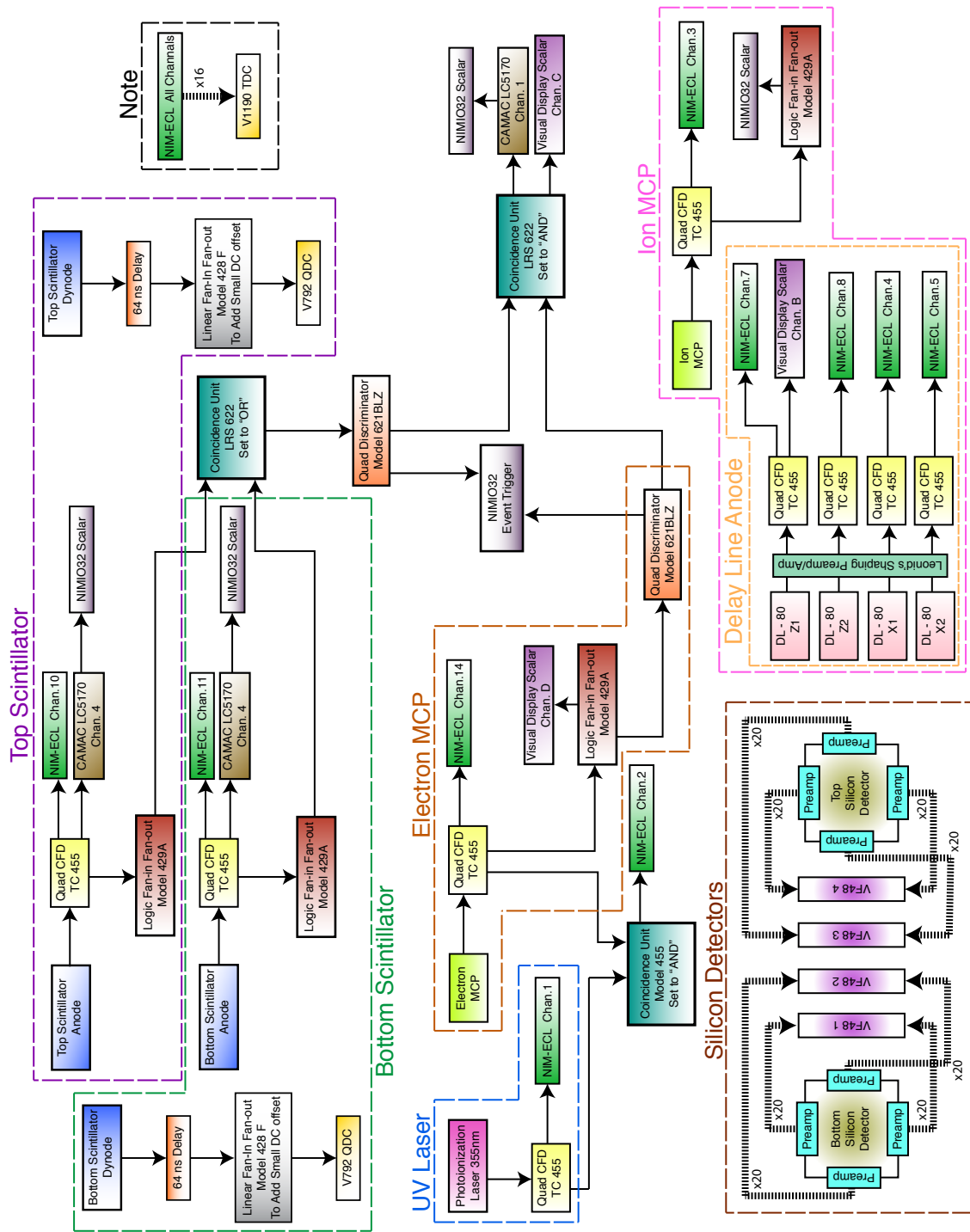


Figure 4.15: Electronics diagram. This is a simplified schematic of the most important connections to between the detectors and the data acquisition system. The event triggers were generated by the block labeled here as “NIMIO32 Event Trigger” which is documented separately in Fig. 4.12.

clock to sync the VF48 modules clock, a 40 MHz clock to sync the Caen V1190 clock, and 4 channels of 20 MHz timestamp registers, along with the global event trigger. This trigger was written in VHDL mostly by Konstantin Olchanski at TRIUMF with only a little modification done by me. A schematic representation of the trigger code is shown in Fig. 4.12 – 4.14. The goal of this trigger was to decide within about 10 ns of a detector firing whether to read out the data acquisition modules or not. When the trigger condition was satisfied, a busy signal would be sent that would block further incoming pulses. Simultaneously signals would be sent to each of the other modules to begin the readout procedure. The trigger scheme that we used during most of the experiment can be represented with C boolean logic symbols as $(ElectronMCP) \&\& (TopScintillator || BottomScintillator)$. This logic could of course also have been produced in analog electronics but the FPGA offered several advantages. First, if changes were made to the trigger logic no wires needed to be switched. Second, since the busy signal and gates for the ADCs were all produced by the FPGA less modules were needed reducing expense. Lastly, the FPGA affixed timestamps to the events and synced the clocks of the VF48s a necessary job that would be difficult to achieve with any other type of module.

The third interesting thing that our data acquisition system did was to record time stamps for each event as they were read out. These timestamps were supplied by the FPGAs on the NIMIO32 boards and the VF48 modules. The timestamps were synced with a 100 MHz clock and thus are subject to 10 ns jitter. This timing uncertainty is acceptable because the optical pumping signal that we were looking for with these timestamps comes on a much longer timescale and could tolerate clock jitter up to 1 μ s. In order to organize the events in time with respect to the slow laser control system, operating on the trapping computer, we relied on the time difference between the event timestamps, applied by the NIMIO32 modules to each triggered

event, and the timestamps originating from the change in logic level of timing pulses broadcast from the trapping computer. The ordering of detector signals in time within each event was done with the much faster time to digital converter (TDC) with a clock jitter of 20 ps.

5. POLARIZATION MEASUREMENT

5.1 Overview

This experiment allows for an *in situ* measurement of the polarization of the atoms in the cloud independent of the asymmetry measurement. This is important because A_β and the polarization are multiplied together in the decay rate (see Eq. 1.1). This means that the uncertainty from one is hard to disentangle from the other. We will begin this section by first developing a simple model for the polarization of the atoms. The development of this model will be useful to us because we will be able to understand the types of things that need to be considered and the assumptions that we need to make in order to construct such a model. We will then examine the photoionization technique that was used to measure the polarization of the atoms during the experiment, and give a description of some supporting experiments that were done offline after the experiment, which give a complementary picture of our knowledge of the polarization.

5.2 Polarization Models

When interpreting physics results, we often need to create a model of the data that helps us to understand the underlying effects and distinguish between background and real events. We often need to compare the results returned from various models to try and estimate systematic uncertainty that could be introduced by using a particular model. In this section I will introduce one calculation and two models for the observed polarization signal and apply them to our data in an effort to come to a definite answer to the question: “What was the polarization of the atoms in the Dec. 2012 data set?”

5.2.1 A Simple Polarization Calculation

To begin we will examine what is known as the “tail-to-peak ratio calculation.” It was developed by Daniel Roberge and documented in his master’s thesis [91]. We will step through the process of applying this calculation to ^{37}K and along the way gain some understanding of how it works. Fig. 5.1 shows the energy level structure of ^{37}K ’s valence electrons for the optical pumping transition that is used. The things that are important to note are that in a low magnetic field (in our case 2 Gauss), the spin of the atomic electrons, denoted as I , will couple to the spin of the nucleus, denoted as J . Due to this coupling these quantum numbers are no longer good by themselves but the combination F is, where $\vec{F} = \vec{I} + \vec{J}$. Also note that m_F ranges between -2 and $+2$. Finally note that there are a total of 8 possible states within $4S_{1/2}$ level.

We begin by making our first assumption, that all of the atoms which are not in the fully stretched ($m_F = 2$ or -2) state are in the next-to-stretched state $m_F = m_F^{max} - 1 = 1$ or -1 . We will also define x , to be the fraction of atoms not in the fully stretched state with, $x = (7/8)r$, where r is the “tail” to “peak” ratio. With the “tail” being the number of counts after the atoms have come to a steady state after being exposed to the optical pumping light for a long time and the “peak” being the number of counts in the initial burst of fluorescence that occurs when the light is first turned on. The $7/8$ comes from the fact that there are 8 possible states and that one of them is the fully stretched and seven are not. There are at least two ways that the polarization can be monitored during this process. The first is by looking at the number of de-excitation photons directly as a function of time. This works well with a large number on atoms in the trap a condition easily satisfied when using ^{41}K . An alternative approach that can be used with a low number of atoms in

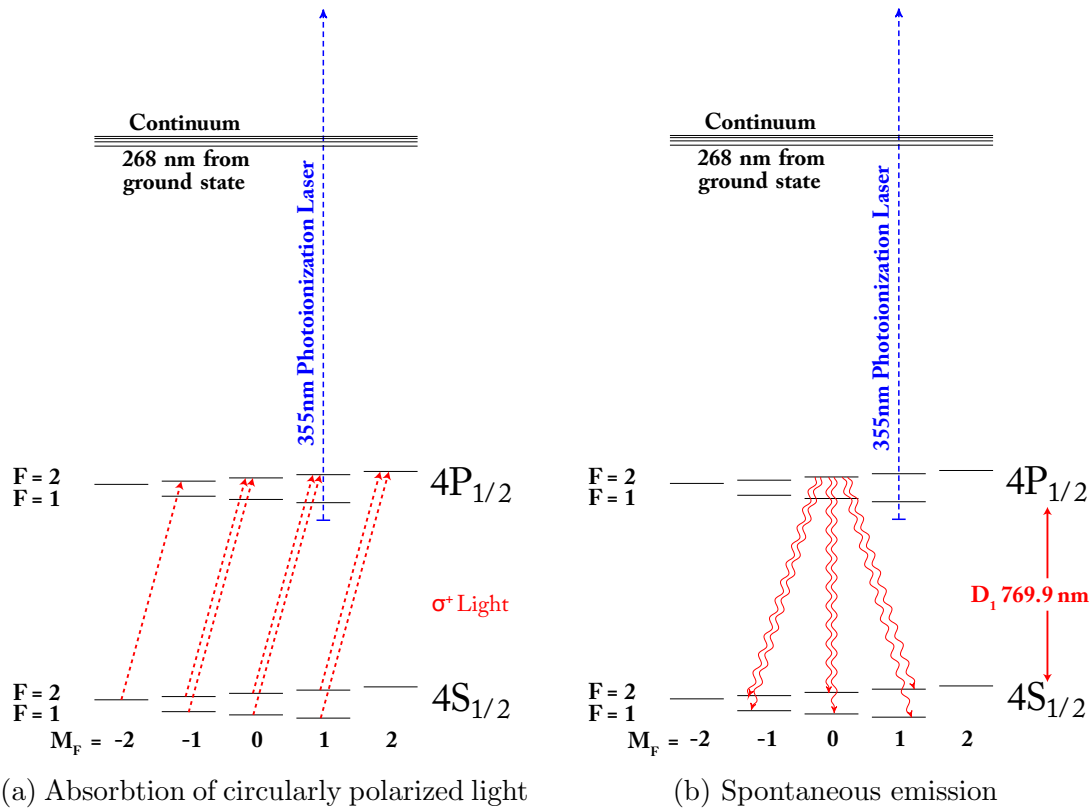


Figure 5.1: Schematic of photoionization process during optical pumping. The placement of the major levels, $4S_{1/2}$, $4P_{1/2}$, and the continuum along with the photoionization laser are to scale. The inter level splitting by m_F is approximate. As shown in Fig. 5.1a during the optical pumping process we will use photons to excite the atoms from the $4S_{1/2}$ to the $4P_{1/2}$ excited state. There are actually two separate collinear beams used in the process. One is called the pump and it is tuned to the $4S_{1/2}, F = 2 \rightarrow 4P_{1/2}, F = 2$ transition and the second called the repump is tuned to the $4S_{1/2}, F = 1 \rightarrow 4P_{1/2}, F = 2$ transition. Since the photons are circularly polarized they carry a unit of angular momentum with them and the absorption of such a photon will change the m_F state of the atom by ± 1 based on the circular polarity of the light. In the de-excitation process shown in Fig. 5.1b the photon might or might not carry away angular momentum and there are selection rules that govern which one of the transitions shown is most likely but all of the red lines are possible de-excitations. The atoms experience a biased random walk towards one of the extremes in m_F 2 or -2 ground states based on the input circular polarization being either σ^+ or σ^- . For atoms not in the presence of misaligned magnetic fields the absorption/radiation cycle is repeated on average 10 times before the atoms arrive in the $m_F = |2|$ state. Once in this state, not having a corresponding $m_F = |3|$ state in the $4P_{1/2}$ level to move into, the atom will no longer absorb photons.

that trap, such as when using ^{37}K , would be to use a laser that photoionizes from the excited state but not the ground state. In our case we use a laser with a wavelength of 355 nm and measure the number of photoions created by this process again as a function of time. In both cases we see a signal that has a sharp peak when the light is turned on and this signal falls to a value determined by any depolarizing mechanisms such as imperfect circular polarization of the light or misaligned magnetic fields.

Since we made the assumption that atoms not in the fully-stretched state are in the next-to-stretched state we need to define the wavefunctions $|F = 2, m_F = 1\rangle$ and $|F = 1, m_F = 1\rangle$. We look just at the case of σ^+ since σ^- will be identical. For each state the polarization is calculated as, $P = \langle \psi | J_Z | \psi \rangle$. Using the Clebsch-Gordan coefficients we come up with the following wavefunctions, at $B_{\text{misaligned}} = 0$, in the J_Z, I_Z basis set:

$$\begin{aligned} \psi_{2,1} = |F = 2, m_F = 1\rangle &= \frac{1}{2} \left| J_Z = \frac{3}{2}, I_Z = -\frac{1}{2} \right\rangle + \frac{\sqrt{3}}{2} \left| J_Z = \frac{1}{2}, I_Z = \frac{1}{2} \right\rangle, \\ \psi_{1,1} = |F = 1, m_F = 1\rangle &= \frac{\sqrt{3}}{2} \left| J_Z = \frac{3}{2}, I_Z = -\frac{1}{2} \right\rangle - \frac{1}{2} \left| J_Z = \frac{1}{2}, I_Z = \frac{1}{2} \right\rangle. \end{aligned} \quad (5.1)$$

The use of these wavefunctions can be justified because at the 2.5 G applied magnetic field that is used in the experiment the mixing in $P_{1/2}$ state is less than 0.2% and the energy shifts are less than 20 MHz. Using these definitions we can calculate what the polarization should be for our two states,

$$P(\psi_{2,1}) = \frac{1}{2}, \quad P(\psi_{1,1}) = \frac{5}{6}. \quad (5.2)$$

The next assumption that we have to make is that we expect these two states to be

populated in proportion to the transition rates feeding them,

$$\frac{|4P_{1/2}, m_F = 1\rangle \rightarrow |\psi_{2,1}\rangle}{|4P_{1/2}, m_F = 1\rangle \rightarrow |\psi_{1,1}\rangle} = \frac{1}{3}. \quad (5.3)$$

Implicit in this assumption is that the depolarizing mechanism is from poor circular polarization of the light because that is the only way an atom could make the transition $|4S_{1/2}, m_F = 2\rangle \rightarrow |4P_{1/2}, m_F = 1\rangle$. The degree to which the light is circularly polarized can be quantified by the Stokes parameter S_3 . Circularly polarized light can be thought of as a mixture of two states left and right handed polarized. For light of all right handed polarization the value of S_3 is 1 and -1 for all left handed polarization. The values in-between these extremes represent linear combinations of left and right polarization. Experimentally S_3 is measured by using a quarter wave plate to change the circularly polarized light into plane polarized light. Then a polarizer is placed in the beam and the intensity of light coming through this polarizer we will call I_1 . Then the polarizer is rotated 90° around the beam axis and the intensity is then remeasured. This intensity we will call I_2 . S_3 is then calculated as $S_3 = (I_1 - I_2)/(I_1 + I_2)$.

The other depolarizing mechanism misaligned magnetic field can move population between m_F states where $m_{F'} = m_F \pm 1$ without changing the other quantum numbers. In addition to moving populations between states having a misaligned magnetic field would also mean that we would need to come up with a new set of wavefunctions. Since we are assuming that our depolarizing mechanism is from imperfectly polarized light this is not needed.

Using this ratio of populations it is now possible to calculate the polarization that we would expect from the atoms in the non-stretched state as the sum of the two polarizations weighted by the population in each state giving, $P_{\text{non-stretched}} = 3/4$.

The last piece now is to combine this with the fraction of atoms that are in the fully stretched state for the total polarization of the entire population and make it a function of our observable r ,

$$P_{\text{total}} = (1 - x) + xP_{\text{non-stretched}} = 1 - \frac{7}{32}r. \quad (5.4)$$

Understanding how to calculate the polarization in this way is useful in that it has highlighted some of the points that need to be addressed in order to develop more sophisticated models. The first shortcoming of our simple calculation is that it does not produce a curve, but it is still useful because it is so easy to calculate. We use the long time value of the “tail” and the short time values from the “peak” and lump the information together to produce one number for the polarization. Since we start with a count spectrum as a function of time we would like to be able to produce a curve that can be fit to the data. The second shortcoming is that we had to make an assumption about which state the “non-stretched” atoms were in. Ideally we would like only to have to make an assumption about the initial states that the atoms are in and that the final distribution would be the result of the application of the model to that initial state. The final shortcoming was that we needed to make a choice about depolarizing mechanisms. Since they feed the “non-stretched” states differently we will come out with different numbers for the overall polarization depending on which states we choose to feed. This is a shortcoming that all of our models suffer from. The best that we can do is try to make careful measurements of one or the other of our depolarizing mechanisms and then fix the value of at least one and let the other one vary as a fit parameter.

5.2.2 Rate Equation Model

One model that addresses some of the shortcomings of our simple calculation from the previous section is known as the “rate equation model”. The rate equation model does a much better job at capturing the physics that we are interested in. A good reference that describes in detail the development of a rate equation model for cesium is Ref. [92]. The first assumption that we will make when using rate equation model is that the atoms at the beginning of the optical pumping time are in a uniform distribution in all eight states in the $4S_{1/2}$ levels. This is an assumption because just previous to the optical pumping time the MOT was on and this will populate all of the sublevels but not necessarily equally. It is possible to construct other configurations that hurt the final polarization. Using these other configurations will affect our peak height and shape. We know from experience that the fit is dominated by the long time “tail” because it is more statistically significant. This gives comparative freedom to the peak size and shape. According to the calculations done by Dan Melconian a worst case scenario of having an initial population of 50% in the $M_F = 2$ state and the 50% in the $M_F = -2$ would lead to 1% change in the the measured polarization of the atoms. Since we have no data to guide us on what the distribution of the atoms is after the MOT time we will continue with this assumption that the atoms are distributed equally in all the states. Then we will simulate the absorption of photons by each of these populations according to the input laser power and the emission of the photons from the excited state as spontaneous emission. As pointed out in Ref. [93], rate equation models are only valid in the region where absorption and stimulated emissions are small compared to spontaneous emission rates, and that because modern semiconductor lasers have sufficiently narrow line widths and have sufficient power that the assumptions implicit in rate equation models can break

down. At each time step in the process, the absorption or emission of photons is governed by the selection rules for each transition. The excited state emission lifetime of ^{37}K has not been measured directly but we can substitute the lifetime of the $4P_{1/2}$ excited state of ^{39}K , which is 26.72(5) ns [94], because they have similar hyperfine structure. If we simulate with time steps smaller than this time scale, then we are able to build up a smooth picture of the sublevel populations and hence polarization as a function of time. A model constructed only of the rate of incoming photons and the relative transition strengths is referred to as a rate equation model. The situation is analogous to the concentration of a daughter isotope in the decay chain from a parent sample. The concentration of the daughter changes as a function of time and can be calculated by knowing all of the transition rates along the entire chain and the initial amount of parent material.

This model employs quantized energy levels but lacks quantum coherent effects. As opposed to our simple tail-to-peak ratio calculation, the rate equation model is able to account for both depolarizing mechanisms: $S_3 < \pm 1$ and/or misaligned magnetic fields. The depolarization of the atoms due to poor S_3 is accounted for by introducing a rate for the atoms to absorb photons of the wrong angular momentum. The implementation of the effect of misaligned magnetic field is more involved. In this case the new magnetic field direction is defined to be the vector sum of the misaligned and aligned fields. The atom now is characterized by new quantum states, F' and $m_{F'}$. These new states are constructed as a linear combination of the previously aligned F and m_F states. Because our detectors have not moved we still need to know how things look along this original axis. The effect of making these new states a linear combination of the old ones is that populations of neighboring states get mixed. The Larmor precession around the new field axis will redistribute the population in these new F' states.

There have been a number of individuals within the TRINAT collaboration that have written code for rate equation models over the years. Throughout this work I used a fortran version that was written by John Behr, which included effects such as the measured rise time of the acousto optical modulator controlling the light going into the chamber and the ability to add in a time varying misaligned magnetic field. This feature was not used in fitting the fluorescence data because we believed that the magnetic field had come to a steady state by the time that we turned on the optical pumping light. In what comes after I refer to this particular implementation of the the rate equation model as the “rate equation model code”.

5.2.3 *Optical Bloch Model*

This bring us to the last model that we will examine, the optical Bloch model. It tries to overcome the deficiencies of the rate-equation models by introducing optical, hyperfine, and Zeeman coherent effects. These effects are introduced through a density operator formalization. A good reference to look at to learn about this model is by Tremblay and Jacques [93]. These authors treat the atom as a fully quantum mechanical system. This is a big step up from the rate equation models because it allows us to simulate purely quantum mechanical phenomena such as coherent population trapping. Coherent population trapping is where a significant portion of the atoms can become trapped in a superposition state in which they no longer absorb optical pumping photons. The polarization of the atoms in this dark state can be very different from what we would expect looking at the problem from a classical point of view [95]. Additionally because the atoms are no longer absorbing photons they will not be in the excited state to be photoionized. This means that in the “tail” region we will have fewer photoions and this will lead to a measurement of the polarization that is too high. For this reason we set our laser detunings far

The diagram illustrates a two-level system. At the top, two horizontal lines represent energy levels, labeled $|2\rangle$ (higher) and $|1\rangle$ (lower). Below these, a purple shaded box contains the wavefunction $|\psi\rangle = \begin{pmatrix} C_1 \\ C_2 \end{pmatrix}$ and its bra $\langle\psi| = (C_1^* \quad C_2^*)$. Below the purple box, the density matrix ρ is defined as the outer product $\rho = |\psi\rangle\langle\psi|$, which is shown to be equal to the matrix $\begin{pmatrix} C_1 C_1^* & C_1 C_2^* \\ C_2 C_1^* & C_2 C_2^* \end{pmatrix}$.

Figure 5.2: Two level system to demonstrate the density matrix. Imagine that we have the simple two level system shown here. Then we write the wavefunction as a simple linear combination of the two states. The density matrix is then the outer product of our wavefunction. The elements of the matrix then represent, ρ_{11} the probability of being in $|1\rangle$, ρ_{22} the probability of being in $|2\rangle$, and ρ_{12} and ρ_{21} the probability of being in a coherent superposition of the two. Recalling from undergraduate quantum mechanics that the expectation value for an operator is $\langle A \rangle = \langle\psi| A |\psi\rangle$ the equivalent relation for the density matrix is $\langle A \rangle = \text{Tr}(\rho A)$.

from the coherent population trapping resonance in this experiment. The connection between the two models is that the rate equation model uses just the populations of the states that are the diagonal elements of the density matrix whereas an optical Bloch model will additionally use the other off diagonal terms that are the quantum superposition of states.

Fig. 5.2 shows how the density matrix would be formed for a simple two level system. In the case of ^{37}K we will have a 16x16 matrix instead of the 2x2 one that we have in the figure, but the principle of how it is constructed remains the same.

At each time step in the simulation the change in the the density matrix is given by,

$$\dot{\rho} = -\frac{i}{\hbar}[H, \rho], \quad (5.5)$$

where H is the Hamiltonian for the interaction and the brackets in normal quantum mechanical notation are the commutator. The hard part of using Eq. 5.5 to simulate optical pumping is knowing the Hamiltonian. This was the major contribution of Ref. [93] in which the authors wrote out the Hamiltonian for an atom interacting with two collinear propagating beams, in our case the pump and repump, each of finite line width (10 MHz) and frequency (see Fig. 5.7).

Using this formalization it is much easier to introduce a misaligned magnetic field if we know what the Hamiltonian is. Again the hard work has been done for us by Renzoni [96]. This new interaction term can be added to the Tremblay Hamiltonian [93] in the usual quantum mechanical fashion. The effect of this misaligned magnetic field Hamiltonian is that it mixes neighboring states. This is what we also said about the rate equation model. In that case however the mixing was introduced in a non-rigorous way. A misaligned field does not mix any of the diagonal elements of ρ directly but mixes them through the off-diagonal elements which are not present in the rate equation model. This means the rate equation model is not going to be able to simulate the effect of misaligned fields without making some assumptions about the way that this off-diagonal mixing translates into mixing between the diagonal elements that it does simulate. Since this mixing is a truly quantum mechanical effect it can lead to coherent resonances such as the Bright resonance studied by Renzoni. Simulating the misaligned magnetic field is much cleaner in the optical Bloch model because no assumptions have to be made about the coupling between the diagonal elements of the density matrix the way that the rate equation model

does.

For all of the things that the optical Bloch model does right it is not perfect. Tremblay does not treat the laser light totally quantum mechanically the way he does the atom. This is because a full quantum treatment of the light is a very difficult QED problem and all of the models on the market today treat the light semi classically. The C++ implementation of the optical Bloch model for our system was written by Ben Fenker as part of his master’s degree. In what follows if I refer to this particular implementation as the “optical Bloch model code”.

5.3 The Photoionization Data

Now that we have an idea about the models that will be used to fit the data we need some data to fit. As mentioned in the caption to Fig. 5.1, one of the possible ways that we could probe the polarization is by looking at the photoions or the photoelectrons that come from the photoionization of atoms in the $4P_{1/2}$ excited state. The light needed for the photoionization comes from a JDS Uniphase NV-00211-100 355 nm optically switched diode laser that fires 0.5 ns pulses with 8.5 mWatt of power at 10 kHz with its clock independent of all others in the experiment. That means that it will randomly sample all times during the experiment, as shown in Fig. 4.11. This signal should be small because the photoionization cross section is very low and the atoms are optically pumped for about $\sim 2000 \mu\text{s}$ per cycle and there are 100 cycles per second. That means only about 20% of events come in the right time.

To help us get an idea of the type of signal that we expect to see, we can look at some data that we took the day before the run, using ^{41}K . At the time that we took the data we did not know if the system was working and this was truly a proof-of-principle test for us. We loaded the trap with millions of ^{41}K atoms and

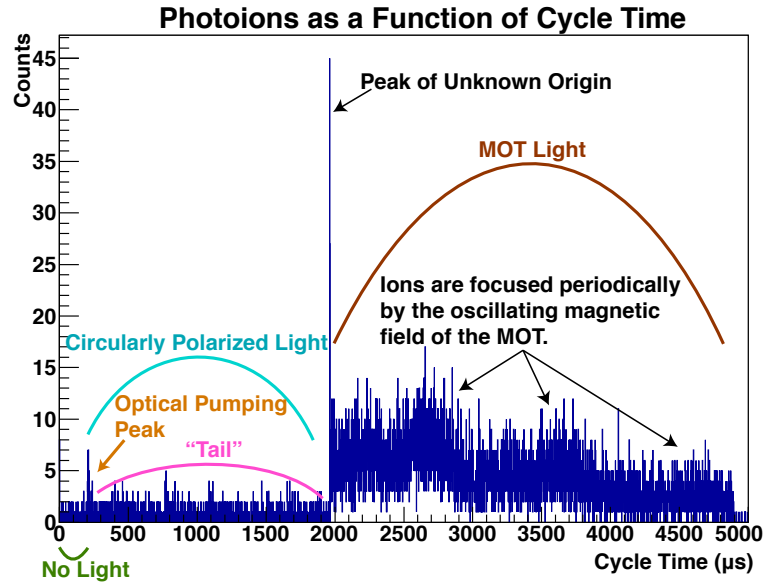


Figure 5.3: Test of photoionization technique using ^{41}K . This data comes from a test of the polarization measurement scheme using ^{41}K the day before the start of the experiment. Because we were using stable potassium we were able to load the trap with orders of magnitude more atoms than in the case of ^{37}K and it was possible to collect enough data to see the optical pumping peak in about one hour instead of the 7 days of beam time that went into Fig. 5.6 for ^{37}K .

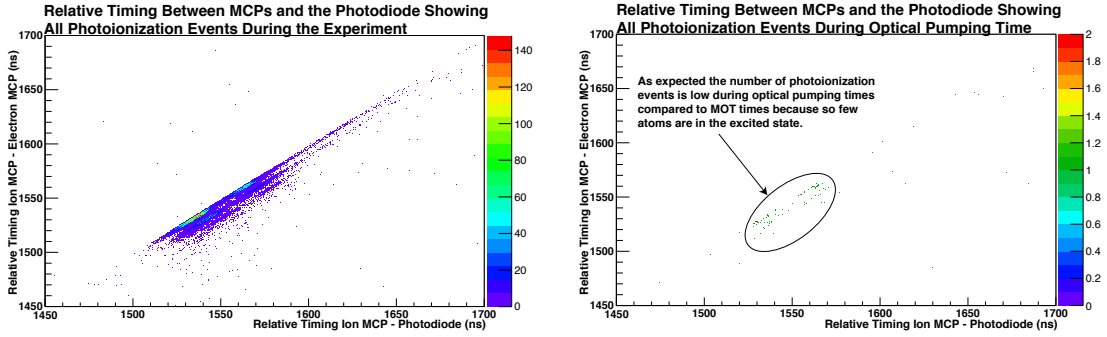
optical pumped the same way that we did during the experiment. The result of this is shown in Fig. 5.3. After an hour of counting we were able to see the formation of the optical pumping peak at the time that we expected it. This was a good proof-of-principle test and at the time it signaled to us that things were working. We have no reason to believe that it did not continue to work in the same fashion throughout the experiment because further polarization measurements using ^{41}K were done immediately after the experiment. These experiments are described at the end of this chapter.

We knew from the outset that the photoionization signal would be small because we would not be able to load the trap with as much ^{37}K as ^{41}K , but the signal should still be very clean. The reason that this signal should be so clean is that each time

the laser fired we have a signal from a photodiode that was monitoring the laser recorded on the TDC. If we look at the ion times recorded on the TDC with respect to the photo diode times we get at peak at about 1500 ns which is the time that it would take a singly charged $^{37}\text{K}^+$ ion starting from rest to move from the center of the chamber over to the detector in the electric field. A schematic view of these events is given in Fig. 5.4c. This technique works nicely for the photoions because they are separated so far in time, $1.5 \mu\text{s}$, from the laser pulse that also has a small chance of firing the MCP directly. Trying to do the same thing with the electron detector is harder because the electron time-of-flight is $\sim 3 \text{ ns}$ and it is harder to tell the difference between photoelectrons and the laser firing the plate directly. Instead we use the relative timing between the ion MCP and the electron MCP. Using the triple coincidence between the photodiode, the ion MCP, and electron MCP, we get the purity that we need to cleanly select photoionization events.

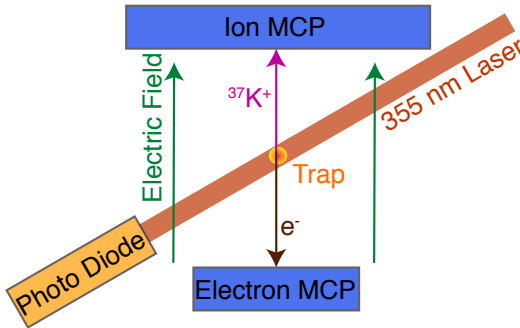
To start looking at the data we can make a 2D histogram of two of these relative timings like what is shown in Fig. 5.4. Plots like this are great for exploratory data analysis. We can see for example that there appear to be some stripes in Fig. 5.4a. These stripes are caused by the fact that during the experiment the electric field was changed along with thresholds on the constant fraction discriminators for the delay line anode in between run 995 and 996. This shift in electric field meant that the timing conditions that we applied for photoions are different before run 996 and after. To get an idea of the magnitude of the shift see Fig. 5.5. For each of these peaks, timing cuts were made by finding the mean and making cuts such that 95% and 99% of the peak area was encompassed. These cuts are shown in Table 5.1.

In addition to the timing cuts it is also possible to make a position cut on the photoions that hit the ion MCP. The position is provided to us via the delay-line anode that backs the ion MCP. The photoions start off with essentially zero mo-



(a) All photoionization events

(b) Photoionization events in optically pumping time



(c) Schematic of of photoionization event

Figure 5.4: Relative timings of photoionization events. Shown in Fig. 5.4c is a schematic view of a photoionization event. The relative timing between the detectors shown in this schematic are what make up the axis of the data plots shown in Fig. 5.4a and Fig. 5.4b. By comparing the data plots we see that there are many more photoionization events that occur outside of the optical pumping time than in the optical pumping time. There are two reasons for this. First, the amount of experimental time spent in the optical pumping phase is only a fraction of the total time. The second bigger effect comes from the fact that because the photoionization occurs from the excited state it is much more likely to occur during MOT times than during optical pumping when most of the atoms are fully polarized the ground state.

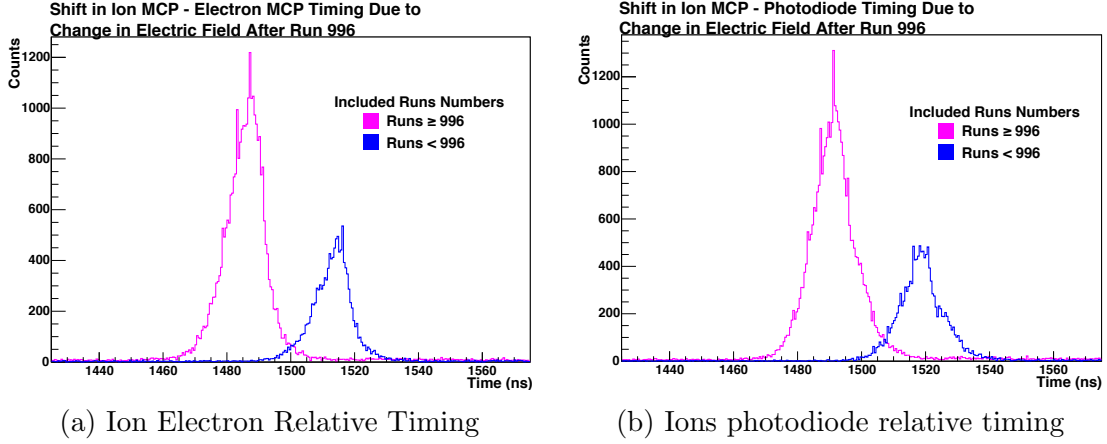


Figure 5.5: Photoionization timing shift after run 996. Due to the change in electric field after run 996 the photo ion/electron timing peak shifted. This shift means that we need separate timing conditions for the two different sets of data.

Photo Event Time Cuts				
Condition	I – E lower	I – E upper	I – P upper	I – P upper
Run < 996 95%	1502.0	1520.0	1508.4	1550.4
Run ≥ 996 95%	1468.1	1498.1	1479.91	1522.09
Run < 996 99%	1496.0	1526.0	1494.4	1564.4
Run ≥ 996 99%	1458.1	1508.1	1465.85	1536.15

Table 5.1: Some different coincidence peak timing cuts tried. All of the values shown are in ns. I – E stands for Ion MCP – Electron MCP timing as recorded on the TDC. Only the first hits were considered. I – P stands for Ion MCP – Photodiode timing as recorded on the TDC. Again this only considers the first hit. To change the result that is returned from the subtraction into ns one must multiply by 0.0976562 the TDC chips timing frequency and subtract 9.868 a constant offset that centers the zero time peaks.

momentum and are drawn by the electric field over to the plate. The distribution of ion hits on the plate is determined by the physical location of the trap, its extent, the temperature of the atoms, and the electric field. The reason for the changes to threshold settings and electric field after run 996 was because we believed that we were missing photoion events on the delay line anode. This turned out to be true. For the four pre-996 peak events that pass the timing coincidence shown in Table 5.1, none of them have position information recorded on the delay line anode because the threshold was set too high. For the eight post-996 peak events that passed the timing cuts all of them had position information. In the end we decided to use the position information only if it was available for a given event. The position cuts that we made on the delay line anode positions are $-5.56 \text{ mm} < x < 1.14 \text{ mm}$ and $-2.4 \text{ mm} < z < 4.66 \text{ mm}$.

Using the events that pass all of these cuts we can project onto a separate axis the time in the optical pumping cycle. This is ultimately the spectrum that we are interested in and the results of this projection are shown in Fig. 5.6. Using this spectrum we are now able to fit with our models to find out what the polarization is. One of the first things that we have to do is estimate the background on this plot. We can do this by using the counts in the time bins from 100 to 250 μs because the optical pumping light is not on during this time. Fitting this region with a flat line using a binned likelihood method gives 0.23 ± 0.12 . Where we place this background level will have a big impact on our final answer for the polarization so we will fix the background at the central value and fit for the polarization. This process will then be repeated for background levels fixed at plus and minus its uncertainty. We will then use the central value of the polarization that was found as our best answer and use the spread in the other two as a measure of the systematic uncertainty connected with our choice of background. We now have in hand a spectrum that we can try to

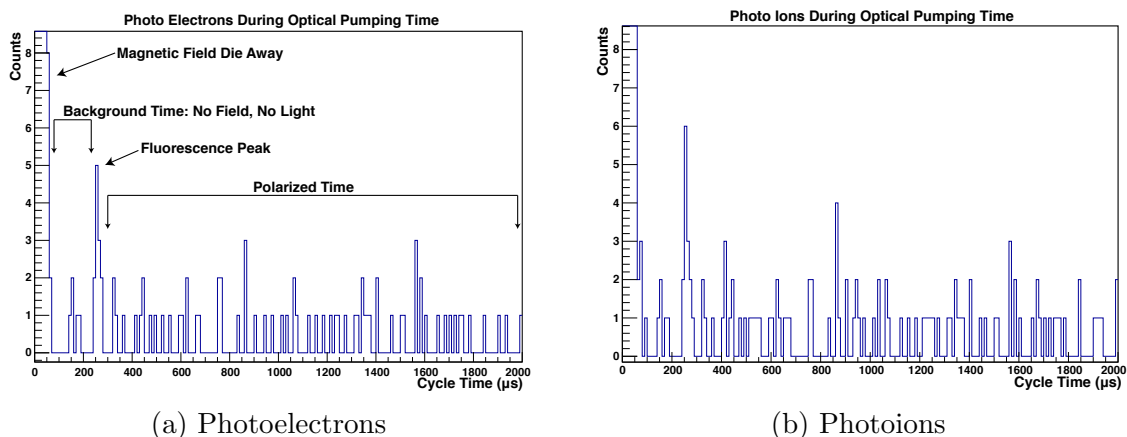


Figure 5.6: Photoionization events ordered by optical pumping time. In both cases we can see that there is a small peak at $250 \mu\text{s}$ on the plots. That is the time when the optical pumping light comes on and where we would expect a peak. We know that this technique works because we have used it with ^{41}K and in another experiment with ^{37}K . In that experiment the rates were an order of magnitude higher than in this experiment the same device unmodified found a clear peak. The only problem with this data is that the statistics are low.

fit with our three different models.

5.4 Difference Between the Models

We can quickly apply the simple tail-to-peak ratio calculation that we developed in Sec. 5.2.1. Doing this we come up with a polarization of 0.989 ± 0.004 . This is a useful number to keep in mind because it is close to what is expected, but there are a number of problems with this model and it should not be taken too seriously. For a better answer we will move onto fitting the spectrum.

To do this properly I developed a program that used ROOT's built-in binned likelihood fitting routines and at each step of the fit it calls via shell scripts an instance of either the optical Bloch model or the rate equation model code. When doing this it became clear to me that there is a major differences between the two codes. The expected result of fitting using the two models is that they should return very similar

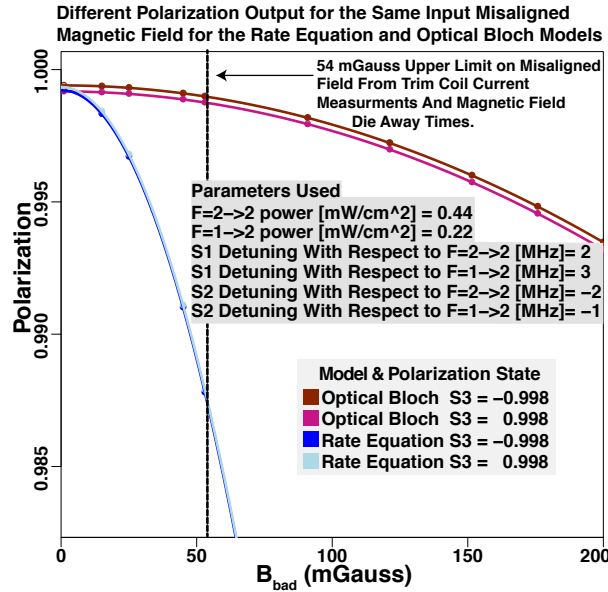


Figure 5.7: Comparison of the the polarizations output from the rate equation model and the optical Bloch model for a varying value of misaligned magnetic field here referred to as B_{bad} . It is clear from the plot that the two codes have very different polarization responses to misaligned magnetic field. However it was not obvious if, after fitting the fluorescence, the returned value for the polarization would be different even if the fits converged to considerably different B_{bad} .

results. There should be small differences because of the different physics included in each model. It was observed that the difference of the polarization returned by the two models was larger than expected. The difference arises when misaligned magnetic fields are included in the fit. To diagnose the problem I started by looking at the response of the code to the initial input of a different value of the misaligned field strength. The response of the two models is shown in the Fig. 5.7. From looking at this figure we see that the response of the model changes to the input value of the misaligned magnetic field, B_{bad} , but the question still remained: “After the fit would the value of the returned polarization be the same?”

The result of one of these fit procedures is shown in the Fig. 5.8. There are three fit lines on the plot that are for three different values for the background level that

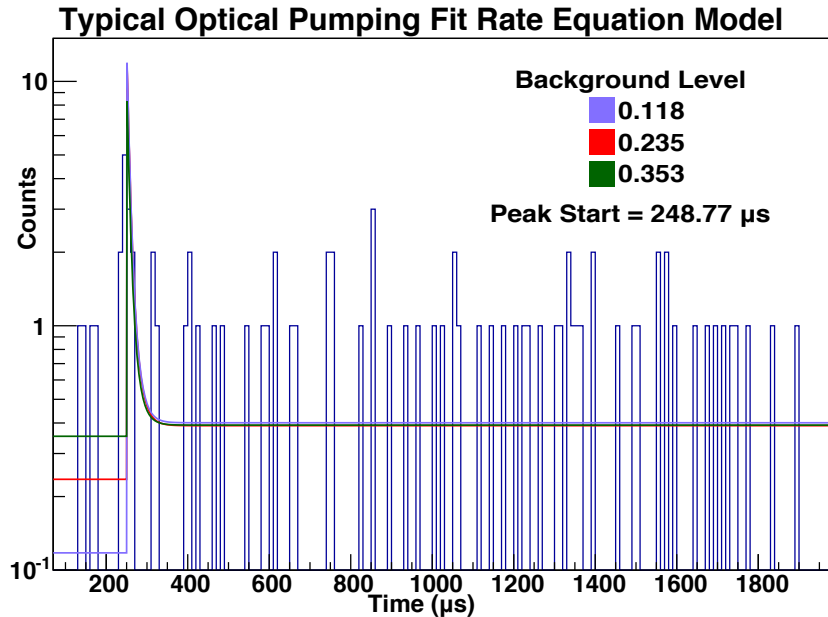


Figure 5.8: A typical fit of the optical pumping spectrum. The three different lines are for the three choices of background level. To see the returned polarization from the fits see Fig. 5.9.

were mentioned earlier. With this very low-count data, the background level that we choose will have a large impact on the fit polarization since it directly affects the “tail” level. The second parameter that needs to be fixed was the time that the light came on. The way that I decided on this time was to fix the “on” time originally at $245 \mu\text{s}$ and the background value to 0.235 then I let B_{bad} vary. After the program converged, I then fixed B_{bad} at its best fit value and let the start time vary to improve the fit. The value that I came up with was $248.77 \mu\text{s}$ and for the rest of the fits the start time was fixed at this value. The reason that they could not be simultaneously minimized is that the correlation between them was too large to allow the fit to converge.

The returned polarization from fits using the two models are shown in Fig. 5.9. Fig. 5.9a shows the case when letting the value of the misaligned magnetic field vary

while holding constant the value of S_3 at 0.98 as measured during the experiment. Using the technique described earlier. Fig. 5.9b shows the effect of fixing the value of the misaligned field to 0 and letting the value of S_3 vary.

We learn some interesting things from these plots. First we learned that with $B_{bad} = 0$ and S_3 free to vary, the two codes give basically the same answer. This is because the physics that governs this process is just an additional rate for absorbing photons of the wrong circular polarity and is easy to implement in both models. This similarity between the output polarization is what we expected to see from looking at the response of the two codes to a misaligned magnetic field (see Fig. 5.7). As B_{bad} approaches zero the polarization returned from the two codes converge to the same answer. The second thing we see is that the final polarization is independent of the depolarization mechanism in the rate equation model whereas the optical Bloch model is not. The presence of a misaligned magnetic field has a much larger effect in the optical Bloch model than a poor S_3 on the returned polarization.

To try and understand the difference that we were seeing between these two models, we looked at the sublevel populations returned by them. These populations are shown in Fig. 5.10 for each code at the best value of B_{bad} for the central value of the background. We see in the figure that the sublevel populations are similar but slightly different. This is what we expect. The sublevel populations give us no clues about which model to believe in terms of the physics and do not shed light onto why the returned misaligned field parameters are so different. The effort is ongoing to try and have the two models come to a consensus on what the polarization of the atoms was, and to place limits on both of the free parameters, S_3 and B_{bad} .

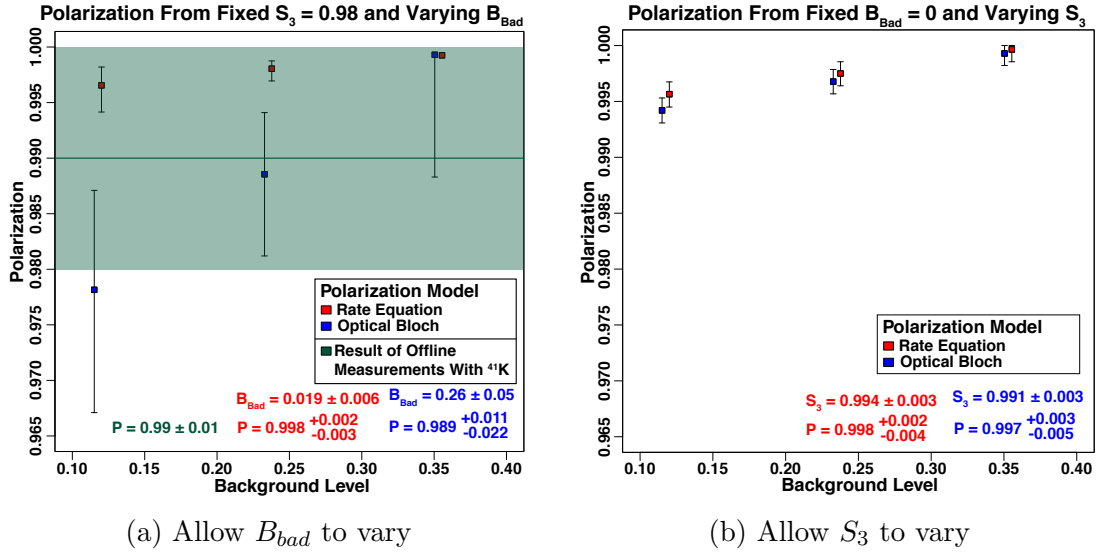
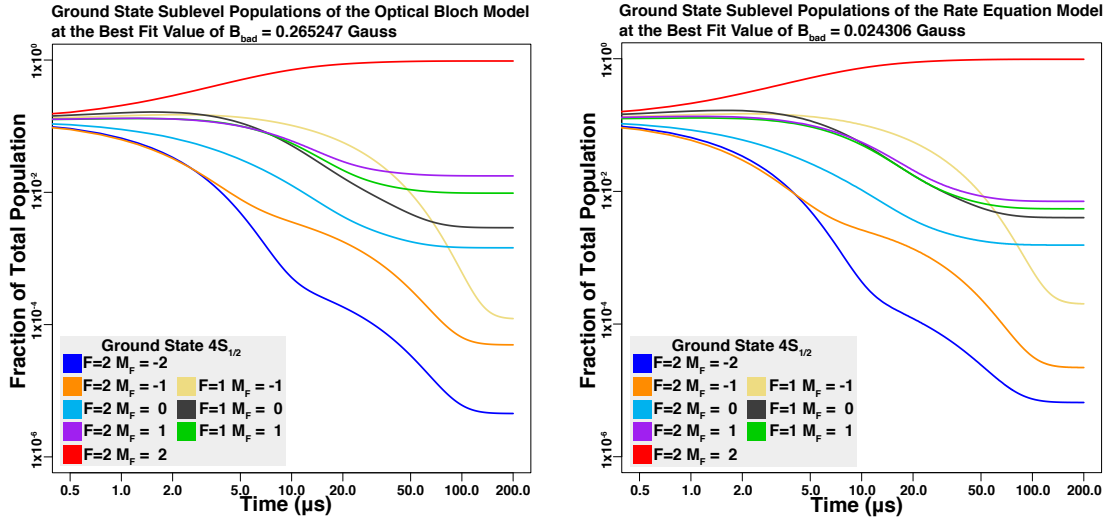
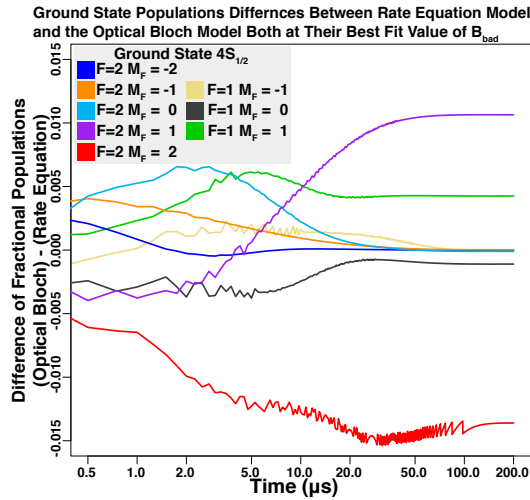


Figure 5.9: The values of the polarization returned from the fits. In Fig. 5.9a the experimental spectrum was fit with the value of S_3 was fixed at 0.98, the value measured during the experiment. Also shown in green on this plot is the value of the polarization as measured offline after the experiment using ^{41}K . In Fig. 5.9b the value of misaligned field was set to 0 to check that the two codes agreed at a place where the underlying physics should be the most similar, and they do. The final numbers reported at the bottom of each plot are the central value for the fit at background level 0.25. With the errors being the error from the fit at that background level added in quadrature with the difference in central value from the fits at the other two background values. Trying to fit the S_3 and misaligned field simultaneously does not work because the parameters are too highly correlated.



(a) Ground state populations from fit using the optical Bloch model.

(b) Ground state populations from fit using the rate equation model.



(c) The difference in the ground state populations from the two models.

Figure 5.10: Sublevel populations given by the two OP models. The spectrum shown in Fig. 5.8 was fit using the two models with a fixed value for S_3 and allowing the value of the misaligned field, B_{bad} , to vary. These are the sublevel populations returned at the best fit values for each model. The actual values of the B_{bad} returned from the fit differ by an order of magnitude, but the sublevel populations look very similar. As shown in Fig. 5.10c there are high frequency differences between the models. These high frequency differences are probably from the way that the differential equation algorithms work and not from quantum coherences in the optical Bloch model which would give smoother oscillations. In either case they die away after $\sim 100 \mu\text{s}$ and the model differences reach a steady state.

5.5 Polarization Experiments with ^{41}K

^{41}K is stable and has a 6% abundance in naturally occurring potassium. After the experiment was over a number of experiments were performed by other members of the collaboration in Vancouver with ^{41}K . The goal of these experiments was to load the trap with ^{41}K and measure the achieved polarization while simulating the conditions of the experiment. ^{41}K is a good candidate for these test as the hyperfine structure is very similar to that of ^{37}K , it is stable, and it is readily available. This means that orders of magnitude more atoms can be loaded in the trap compared to ^{37}K and the polarization can be measured by directly measuring the de-excitation photons, thus simplifying, and speeding up each experiment. What follows in the next sections is a summary of work done by our collaborators in Vancouver after the A_β experiment. It is summarized here because the information is complementary to what was described in the previous section. For a fuller description of these experiments refer to Ioana Craiciu's co-op term report [97].

As mentioned previously the signal that was used to monitor the polarization was the fluorescence photon signal of atoms returning to the ground state after having been excited by the optical pumping laser beam (see Fig. 5.1). If atoms reach the fully stretched $m_F = 2$ or -2 state there does not exist a suitable state in the $4P_{1/2}$ level that they can be pumped into and, because they can no longer be excited, they will also stop fluorescing. This signal is very similar to the photoion signal that was discussed in the previous section and will have the same shape. Because it is easy to implement online, the simple tail-to-peak calculation from Eq. 5.4 was used to monitor the experiments in progress. Later the data were fit with the rate equation model and optical Bloch model code. A schematic diagram of the setup used to collect the data is shown in Fig. 5.11.

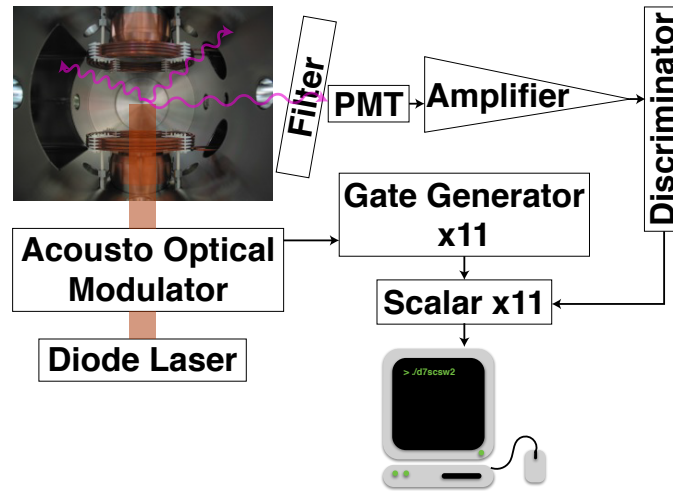


Figure 5.11: A schematic of the offline polarization measurement setup. The optical pumping signal falls off exponentially so the gate widths to the scalars increase roughly exponentially so that each scalar ends up with about the same number of counts in it. Another item of importance not shown on this schematic is the angle dependent filter between the PMT and the chamber that allows the optical pumping and fluorescence light through, but blocks the MOT light.

The trap was loaded and the atoms allowed to cool. Then for 16 cycles the data collection alternated between fluorescence and background counting. Then the polarization was flipped and there would be another 16 cycles alternating between fluorescence and background. The AOM that allowed the optical pumping light into the chamber sent a start signal to the the gate generators that reset the scalars and initiated the counting pattern. This group of 16 and 16 was repeated 8 times and then for each pair of signal and background spectra the background was subtracted and the data summed. This scheme for background subtraction was chosen to try to reduce the systematic error that results from variations in the number of atoms in the trap and in drifts in laser power.

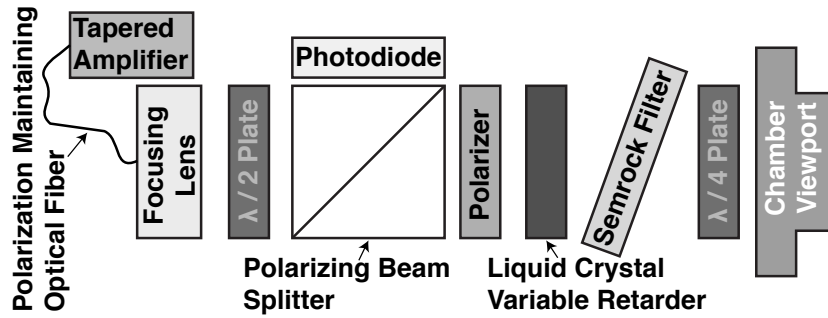


Figure 5.12: A schematic of polarization light injection optics mounted on the 19.5° optical pumping arms. The liquid crystal variable retarder is the element that is responsible for circularly polarizing the optical pumping light. Its performance is sensitive to its temperature.

5.5.1 *Effect of Temperature on Polarization*

In the December 2012 experiment, it was found that, because of the action of the AC-MOT, the temperature of the strip detectors was rising. As the temperature rose so did the leakage current of the silicon detectors. To avoid damaging the detectors a portable air conditioning unit and ducts were set up that would blow cold air on to the flanges where the strip detectors were situated. Other elements of the experimental setup were also affected by this cooling one of them being the liquid crystal variable retarder (LCVR) that was part of the polarization control elements mounted on the 19.5° arms of the chamber (see Fig. 5.12). The experiments that I have just been describing identified the cooling of the LCVR as the dominant systematic error in trying to simulate the December 2012 run conditions. As we did not record the temperature of the LCVR during the run it could not be reproduced accurately. What we do know is that the LCVR on the lower optical pumping port was cooled more than the LCVR on the top and that this caused an asymmetry in power between the upward and downward propagating beams. A limit on the negative effect that this could have on the polarization was estimated by offline

experiments to be 0.002 ± 0.008 .

5.5.2 Summary of Offline Experiments

The final result of these experiments as reported to the collaboration are that the polarization of the atoms as measured by the offline experiments was 0.992 ± 0.006 . This number is already taking into account the small change in S_3 from offline to online experiments and the change in the current applied to the trim Helmholtz coils that are loaded on the frames in the push beam direction. This number also is an average of the two polarization states. The final step is to apply the 0.002 ± 0.008 that comes from the loss in power of the upward going beam due to the cooling of the lower LCVR to arrive at 0.99 ± 0.01 as the final number for the polarization from these offline experiments. All of these polarization numbers were produced by fitting with the rate equation code and so suffer from the same uncertainty about the presence of misaligned magnetic fields that we have discussed in this chapter. This model uncertainty is not included in the quoted uncertainty.

5.6 Final Value of the Polarization

At this time, because of the ongoing efforts to try to diagnose the problem with the models with respect to the presence of misaligned magnetic fields, we cannot report a better number for the polarization than the systematic limited 0.99 ± 0.01 found from offline measurements. This number also suffers from the same problem of misaligned field versus poor S_3 but the presence of other large systematic errors such as the effect of temperature on the LCVR in this measurement lessen the relative importance of this uncertainty. This can be seen by comparing to the polarization fits shown in Fig. 5.9 where it can be seen that 0.99 ± 0.01 encompasses or overlaps all of the fit values. Along with the polarization it is also important to know the alignment of the atoms to simulate the full decay rate. In the polarization region between 0.98

and 1, the polarization and the alignment of the atoms have a linear relationship and a polarization 0.99 ± 0.01 corresponds to an alignment of 0.99 ± 0.01 . Below a polarization of 0.9 this relationship breaks down and the two quantities diverge nonlinearly.

Since approximate results are more helpful than no results, and we need a number for the polarization and its uncertainty in order to finish the analysis of A_β , I will proceed using this number knowing that in the future, when the model differences have been resolved, it will be superseded by a fit value from the online data.

6. DATA ANALYSIS

6.1 Cleaning and Preparing the Data

The raw data that we stored on the harddrives of our data acquisition computer represented a multi year effort devoted to simulation, design, fabrication, assembly, and testing of a large experimental setup. Like all experiments, not all of the data is useful. The first part of this chapter will deal with the data filtering that had to take place before the physics analysis could happen. The second part of this chapter will detail what was done to extract A_β from the data.

6.1.1 Equal Time In Each Polarization State

One of the easiest to understand details that we need to pay attention to is to make sure that there was an equal amount of time spent in each polarization state. If more time were spent in one polarization state than the other, this would produce a false asymmetry. It is possible to show this with `GEANT4` data that started with equal times in both states and was filtered to remove randomly a portion of time from one state and not the other. The results of this filter are shown in Fig 6.1. As can be seen, this leads to an asymmetry that we would be unable to distinguish from the asymmetry coming from A_β . In order to avoid this type of bias, a filter was applied to the experimental data which excluded the data that were collected at the beginning and end of each run, and only accepted the data that were part of the complete 32 second set. Since the polarization was flipped every 16 seconds, this filter ensured that equal time was spent in both polarizations states. A graphical representation of this filter is shown in Fig. 6.2.

Another similar bias to the time asymmetry would be an asymmetry in the number of atoms in the trap between the two polarization states. This bias was checked

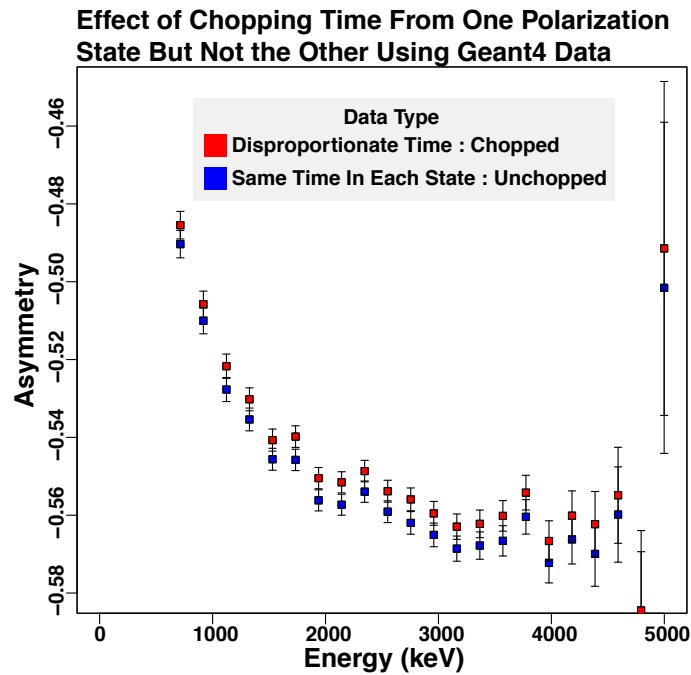


Figure 6.1: Fake asymmetry as a function of energy left in the scintillator produced by unequal time in each polarization state. The size of the fake asymmetry is proportional to the amount of time spent in one state versus the other and assuming a constant count rate would produce an effect of $\Delta A_\beta = 0.15(\% \text{time difference between states})$.

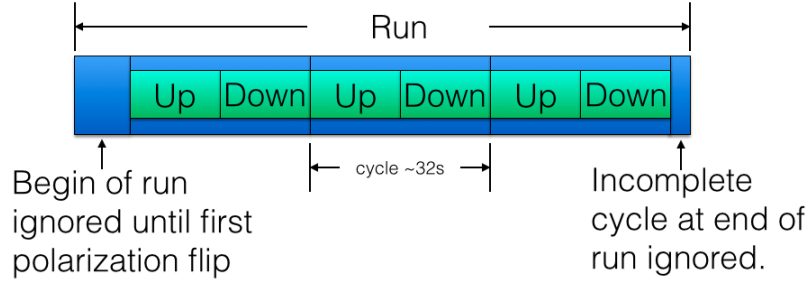


Figure 6.2: The macroscopic timing filter applied to the data. The data acquisition computer and the atomic control computer did not share a common clock. The effect of this was at the start of each run the atoms could be in either polarization state. To ensure that no bias was introduced by preferentially starting or ending runs in one polarization state everything up to the first polarization flip and then again at the end of each run was ignored.

by looking at the difference in the number of shakeoff electrons, ions, and summed scintillator signals between the polarization states. As expected these signals on a cycle-by-cycle basis were Gaussianly distributed around zero difference between states. This means that over the course of the entire experiment that this asymmetry will average to zero. To verify this a check was made by vetoing the 5% of cycles where this count asymmetry was largest and seeing the effect on the final answer. This is included in the error budget.

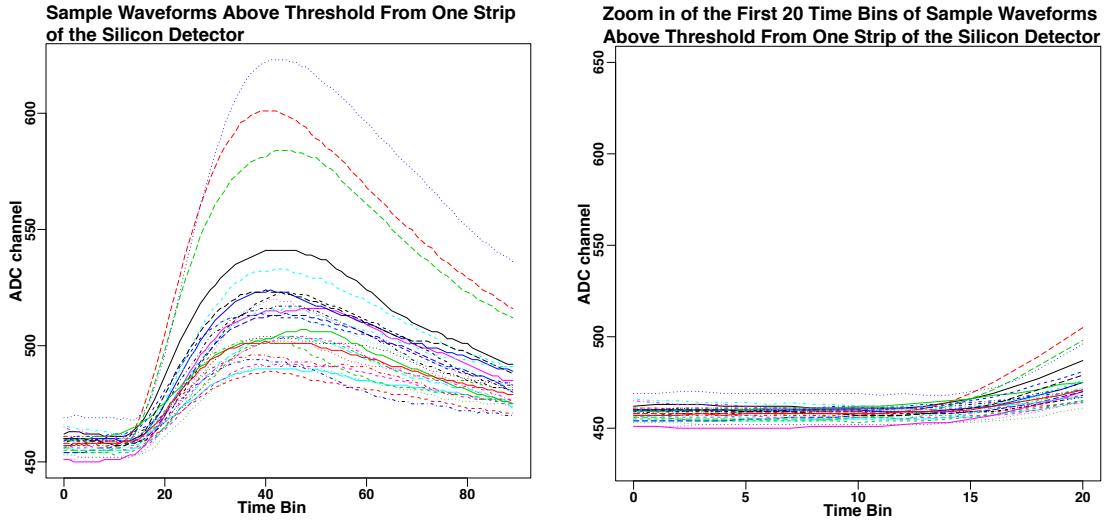
6.1.2 Energy Spectrum From Waveforms

The silicon detectors along with the preamps that we used produced signals that were much slower than the scintillators and MCPs. A typical decay time of a pulse in the silicon detector is about $3 \mu\text{s}$ whereas a signal in the PMT is about 15 ns. It would be possible to use the PMT signal to generate a gate for a peak-sensing ADC and collect the energy spectrum from the silicon in this manner. However in the future we want to be able to put the silicon detectors into the event trigger and it would be cost prohibitive to buy constant fraction discriminators (CFD) for all 160 channels

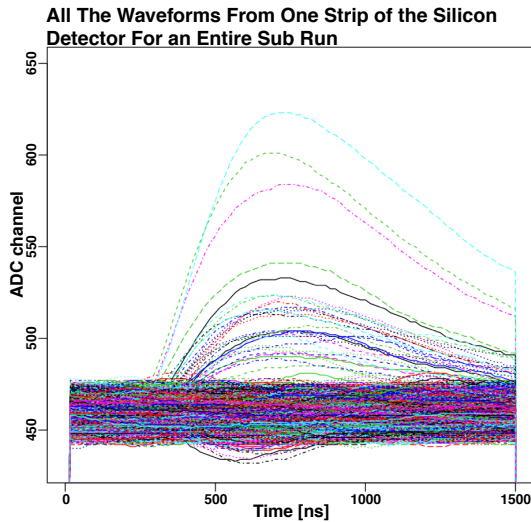
of silicon. For this reason it was decided to use digitizers for the silicon detectors. The silicon detectors were not put into the trigger for this experiment because to do so would require that the signals from the PMTs and MCPs be digitized as well. A firmware trigger would also have to be developed that would determine how far back in time each detector would need to be read back, depending on what signal came in first.

To initiate the waveform readout from these modules we used a signal provided by the NIMO32 that was the “OR” of the scintillator and electron MCP signals. Reading out all of the waveforms is a slow operation and deadtime could become an issue at high count rates. However, at the 300 Hz peak count rate that we were operating at, it was not a problem. We tested this by doubling the readout time of the waveforms and it did not affect our count rates. The waveforms from one strip for an entire subrun are plotted in Fig. 6.3c. The signals that we are interested in extracting look like those shown in Fig. 6.3a. The difference being, from what is shown, is that we would like to use something more sophisticated than a simple threshold for finding them so that we could find small peaks that are buried in the noise band shown in Fig. 6.3c. Crucial to our effort to find those events is the event-by-event correction for the DC-offset. This DC-offset can be found by averaging the the first 10 time bins of each waveform shown in Fig. 6.3b.

In order to use the waveform data for physics we needed a way to make an energy spectrum from the raw waveforms. This is the job that could be done with a CFD, a gate generator and an ADC. This problem can be broken into two smaller problems; first, classify each waveform as a real or background event and second, extract an energy value for each waveform. The first thing we did to try to solve the energy extraction problem was to fit each of the waveforms with an analytic function. Then we could solve the classification problem based on the results of the fit. The fitting



(a) The pulses from Fig. 6.3c that pass a simple threshold. (b) A zoomed in view of first 20 time channels from Fig.6.3a.



(c) All of the waveforms from one channel for an entire subrun

Figure 6.3: Different views of waveform data. There are some important features to take note of when looking at these waveforms. The first point is that because of the external trigger that all of the pulses from real β events should start at the same time, see Fig 6.3b. Another important point is that because the baseline drifts it is important that event-by-event to subtract this off. We can also see that for large pulses the falling edge gets cut off. This will provide nonlinear energy dependence to the spectrum if we integrate the peaks. Also we see in Fig. 6.3b some negative going peaks from image charges that occur when an adjacent strip fires.

Scilicon Detector Waveform Fit With Analytic Function

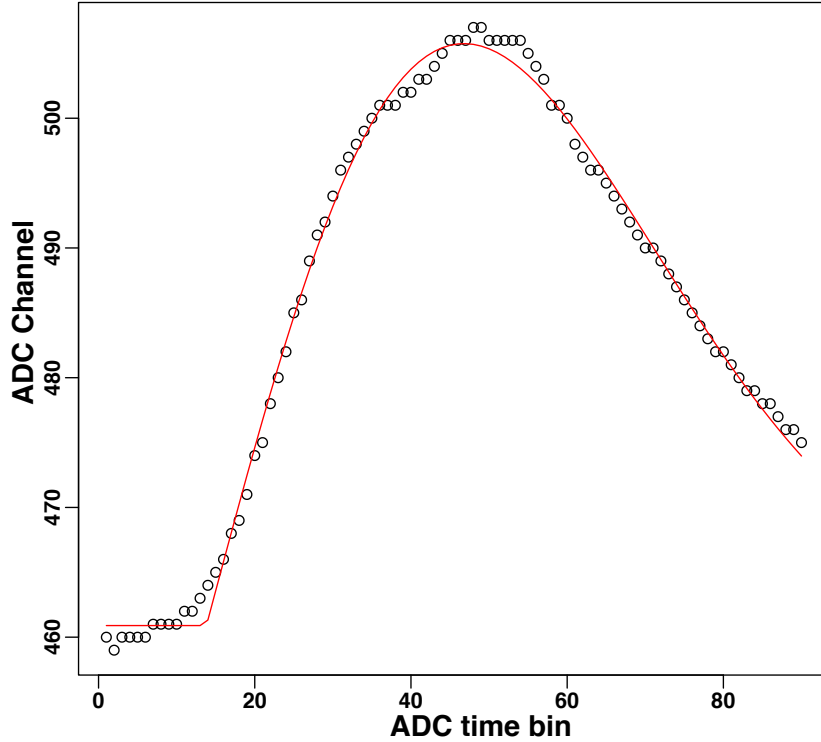


Figure 6.4: This is a typical waveform fit that was obtained using Eq. 6.1. The waveform fitting function worked extremely well except that the χ^2 was not correlated with the presence of a peak because if there was no peak the background would be flat and the algorithm could shrink all of the coefficients to zero except of the DC-offset and in such a case the $\chi^2/\text{d.o.f}$ would be very good.

function that we used was

$$f(x, \mu, \sigma, D, N, S) = \begin{cases} D & x \leq S \\ D + N \left(\frac{1}{2\pi\sigma^2} e^{-\frac{(x-\mu)^2}{2\sigma^2}} \text{erf} \left(\frac{x-\mu}{\sqrt{2\sigma^2}} \right) \right) & x > S \end{cases} \quad (6.1)$$

where μ is the mean of the gaussian and σ is the width, D is the DC-offset and S is a cutoff below which we assumed that the background was flat and had a value of D , N is the overall normalization. A typical fit using this function is shown in Fig. 6.4.

There were a couple of major drawbacks to fitting each waveform. First, because the fitting function fit a flat background just as well as a true peak, the χ^2 did not help us to determine if a peak was present or not. The determination step had to come after the fit from the parameters obtained, such as the N parameter. Since N is essentially the peak area no new information is gained over simply summing up all of the bins. The only benefit from fitting was to smooth the noise and derive analytic expressions for the peak height and timing. The second drawback was that the fitting operation was computationally expensive and a speed test on a subset of the data led to the conclusion that it would take 190 processor years to fit all of the waveforms.

The solution to the problem was to allow a fast algorithm to extract things like the peak area or height without the benefit of noise smoothing. One such algorithm sums all of the data in the peak and waveform-by-waveform subtracts off the DC-offset. Another tries and find the largest deviation from the DC-offset level. A schematic of these two algorithms is shown in Fig. 6.5. The decision about if it was an event or background was then based on this much more easily obtained information. The algorithm chosen for this experiment uses the average DC-offset that is subtracted from all points, and the resulting points are summed. This algorithm can operate on all of the data in 120 processor hours, which is ≈ 10000 times faster than fitting. Running the same experimental data through both algorithms gives energy spectra that are very similar. A comparison between the spectrum for lower X strip 20 can be seen in Fig. 6.6

Both of these methods are good at extracting the energy from the waveforms. To classify each event as background or not, an energy threshold has to be applied above the noise peak. The energy threshold was applied after the strips had been calibrated by fitting them to a β energy spectrum produced by our **GEANT4** simulation. The β

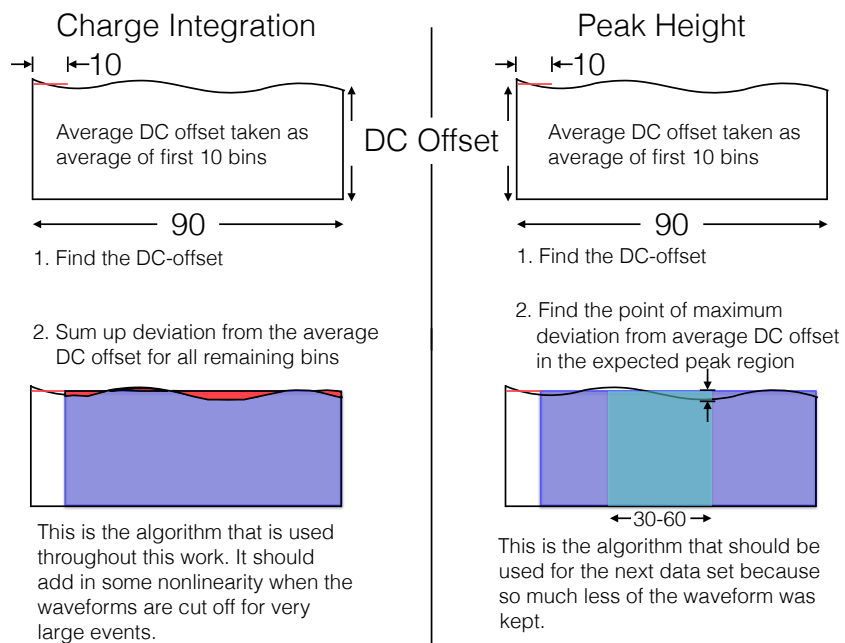
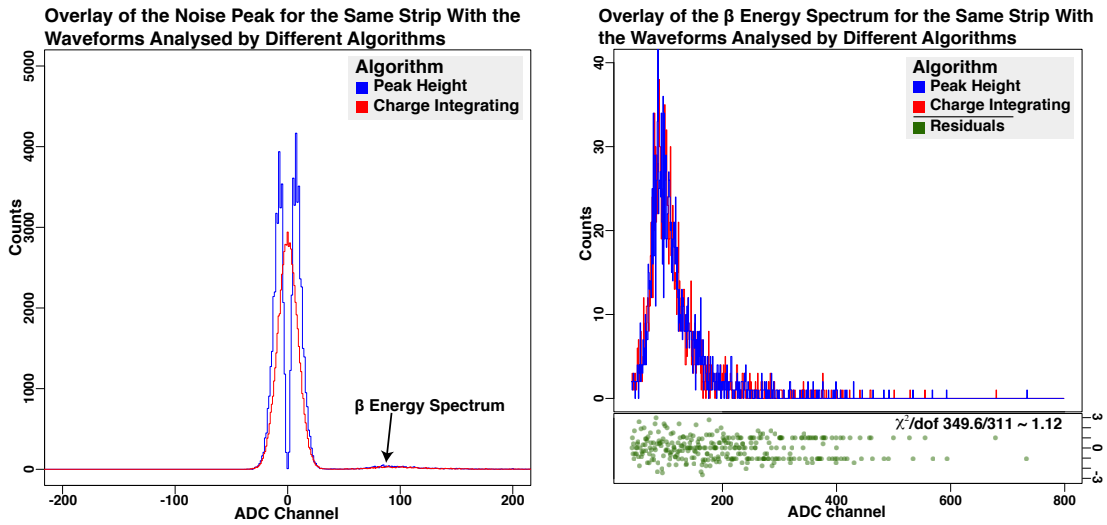


Figure 6.5: A schematic view of different waveform energy extraction algorithms. The two algorithms run very fast compared to the peak fitting that was tried earlier and all of the waveform data can be analyzed in 120 cpu hours. When compared head-on there is virtually no difference between the two in terms of speed.



(a) The noise peaks produced by the digital charge integrating and peak sensing algorithms

(b) A zoomed in view of the β energy spectrum

Figure 6.6: Spectrum differences between the digital charge integrating and peak sensing algorithms. The structure of the noise peak changes dramatically between the two algorithms see Fig. 6.6a. The large dip at zero in the peak height algorithm is due to the fact that the algorithm deliberately chooses the value that differs from zero by as much as possible as shown in Fig. 6.5. As shown in Fig. 6.6b the β energy spectrum returned by both algorithms are very similar.

spectrum was averaged over the whole detector. Something that could be done in the future to improve upon this would be to fit each strip to its own simulated spectrum. This would help the edge strips where deviations were observed. The calibrations for each strip and the calibration procedure are shown in Appendix A. As a check of the thresholds that we applied, we can look at the distribution of strips above threshold as a percent of all events and compare this with `GEANT4` data. This comparison is shown in Fig. 6.7. Looking to the future for ways to improve the system, we found that VF48 readout is the bottleneck of the data acquisition system. If we want to go to higher event rates we need to find an algorithm to classify events quickly and run it on the FPGA of the VF48 and then only read out the waveforms of interest or just the energy and timing. The FPGAs on the VF48 modules might not be up to the task and modules with more capable FPGAs might be needed to replace them.

6.1.3 *Timestamp Mismatch*

Online during the experiment we only looked at total energy spectra for the strip detectors like those shown Fig. 6.6b. These appeared to match well with previous test I had done with the strip detectors and with `GEANT4`. It was not until after arriving back in Texas and trying to apply coincidence conditions with the strip detector was there an indication that something was wrong. The perplexing results of trying to apply such a condition are shown in Fig. 6.8. Applying a condition that any of the silicon strips had an ADC reading above threshold wiped out the β spectrum.

To try to make sense of this non-intuitive behavior I plotted energy in the the strip detector gated on scintillator energy (Fig. 6.9a). I broke the PMT energy spectrum into rough energy bins and then looked at the energy spectrum in the strips for those same bins that I had defined on the PMT spectrum. Doing this should tell us if the peak that we have been calling the β energy distribution in the

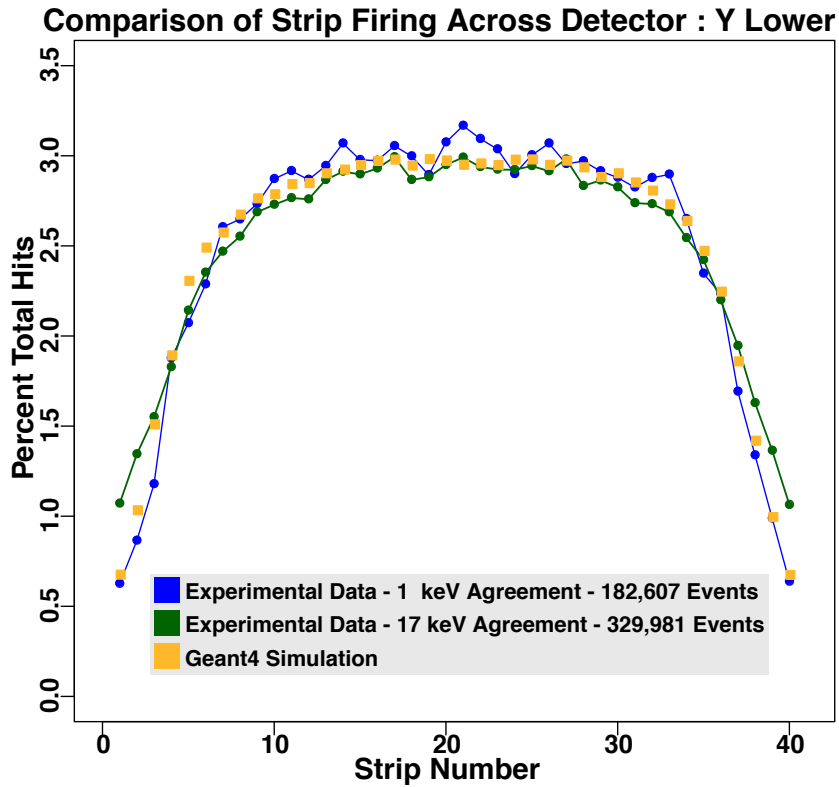


Figure 6.7: Comparison of strip firing across detector. This is a consistency check of the detector calibrations and the applied thresholds. Overall things look good except in the edge strips (1, 2, 39, 40). The calibration in these strips is suspect and in the final analysis they were excluded. The experimental data is shown after applying two different energy agreement values for the front and back planes of the detector. The energy agreement algorithm is described in Section 6.1.4. As shown tightening the energy agreement condition from 17 keV, the average value of the noise from the calibration fits, to 1 keV reduces the number of accepted events by 45%

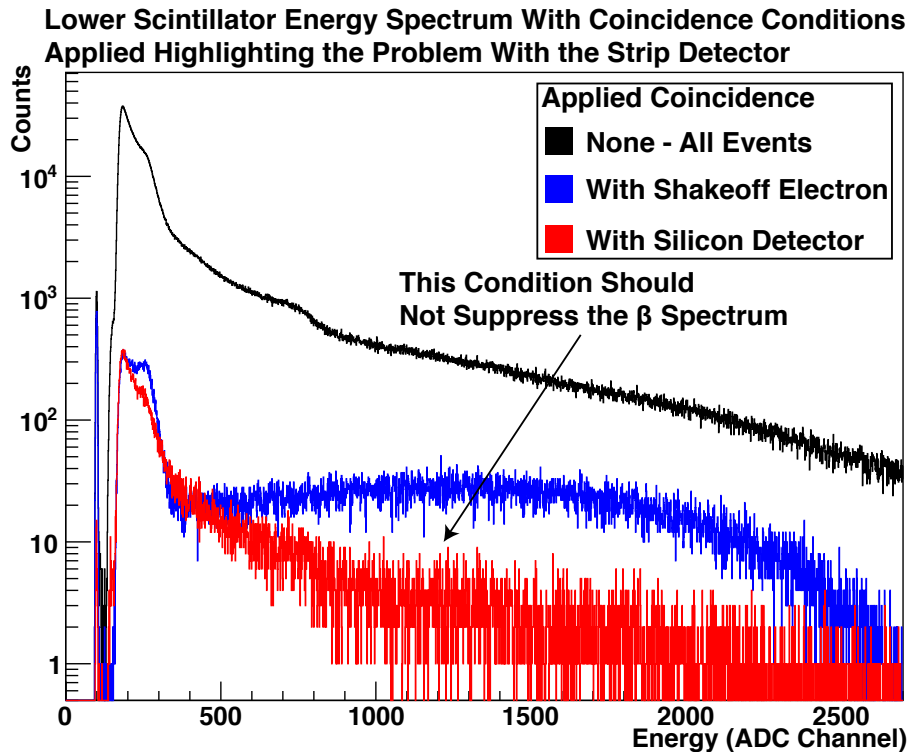
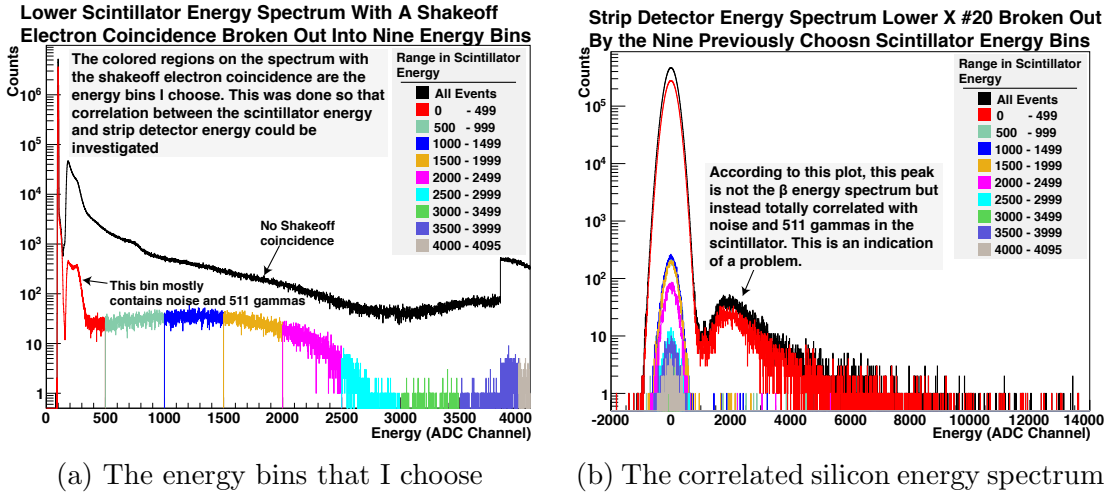


Figure 6.8: The effect of silicon detector coincidence condition on the scintillator energy spectrum before fixing the data stream mismatch. Applying the coincidence condition that the shakeoff electron MCP fired at least once reveals the β energy spectrum (blue). Unfortunately, independent of the shake off electron cut, if we apply a condition that any of the silicon strips had an ADC reading above threshold the beta spectrum is wiped out (red). This was our first clue that something was wrong with the strip detector signal.

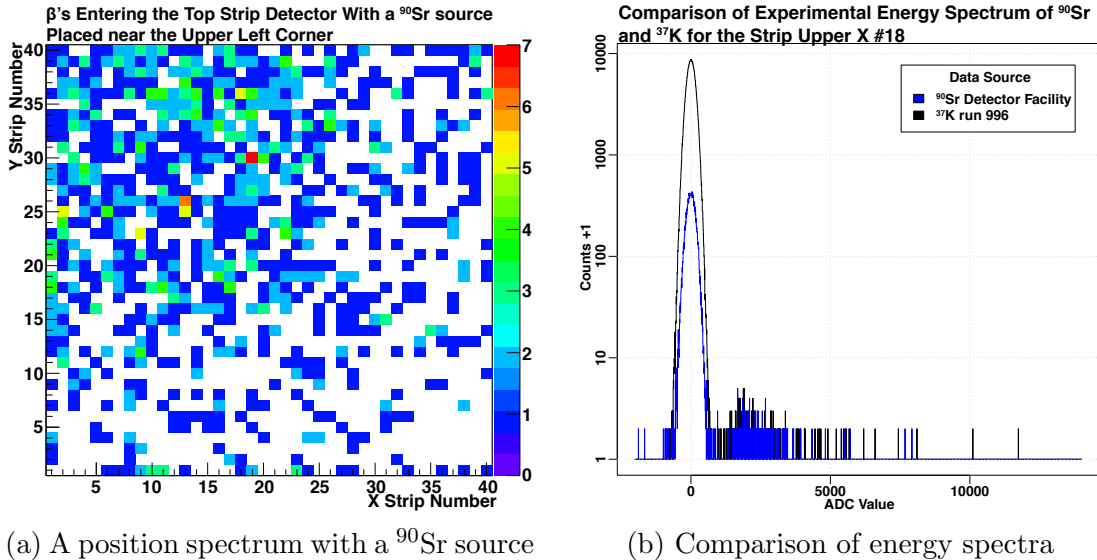


(a) The energy bins that I choose (b) The correlated silicon energy spectrum

Figure 6.9: Silicon energy gated on scintillator energy before fixing the data stream mismatch. In Fig. 6.9a scintillator energy bins are chosen. In Fig. 6.9b the silicon energy spectrum for each of the chosen bins is shown. It is strange to note that almost all of what we see above threshold in the silicon detector, \gtrsim channel 1000 in Fig. 6.9b, is what we label as a gamma, $<$ channel 500 in Fig. 6.9a. This plot caused us to rethink what the problem was because taken at face value this plot says that the strip detectors did nothing at all.

strip energy spectrum is correlated correctly with the energy spectrum that we see in the PMTs. I was surprised to see in the results from this procedure shown in Fig. 6.9. It appeared that what we were calling the β energy peak in the silicon spectrum was coming almost exclusively from what looks like 511 keV gamma events in the PMT energy spectrum. After seeing these results we began to reconsider the problem and to attack it from a different angle.

Before the run I had done many tests with the strip detector while implementing the data acquisition system for the experiment. These tests were much less complex than the full experiment, especially from the standpoint of the event trigger. I did a comparison with some of the earlier test data to try to narrow in on the problem. For the comparison I chose some data that was taken while I moved a ^{90}Sr source around between the different corners of the detector and recorded the β position



(a) A position spectrum with a ⁹⁰Sr source (b) Comparison of energy spectra

Figure 6.10: Comparison of the energy spectrum of ³⁷K with that of ⁹⁰Sr. In Fig. 6.18a because we know that the source was located at $\approx (X = 0, Y = 40)$ we are confident that our waveform analysis algorithm is working because that is where we see the β s bunched. Comparing strips with what we had in the online experiment with ³⁷K Fig. 6.18b we see that the energy spectrum are almost identical.

information to make sure that the strip numbering scheme in software matched the physical layout on the detector. These were good data for comparison because I knew I was detecting betas just by looking at the position data and, since the position data relied on the energy information being right, I had confidence that everything was working correctly in these simple test runs. The result of the energy comparison is shown in Fig. 6.18b.

After seeing the results of the comparison it became clear that the strip detector energy signals were still working the same way that they had previously been working in the pre-run setup. This meant that the summed run information was correct but the event-by-event information was wrong. This led us to examine the timestamps that are attached by both the NIMIO32 modules and the VF48 modules to each triggered event. If I plotted the time difference between these two timestamps for

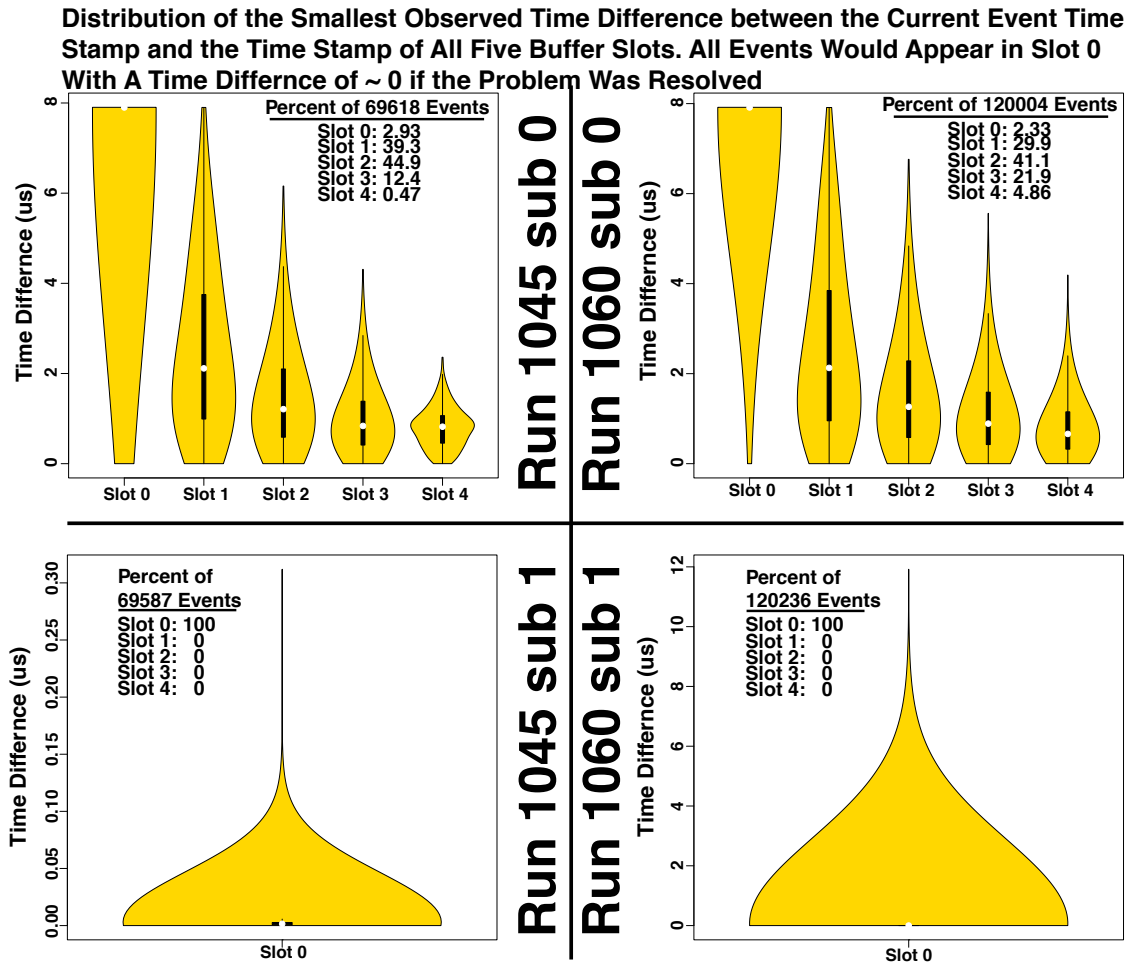


Figure 6.11: Diagnosis of the time stamp mismatch. These violin plots show the probability distribution of timestamp differences for each of the buffer slots. The probability distribution for each slot is mirrored left-right across the slot number to make it more attractive to look at. Overlaid on each probability distribution is the 5 number summary describing the distribution. It was discovered that, for a given event being read out, the corresponding VF48 signals with a matching timestamp would be read out 5 events later. I added in a buffer that kept the last 5 events in memory. These slots are listed on the X axis with the most recent event being placed in slot 4 and the previous events being placed in slots 3 through 0 with the event in slot 0 being the oldest. I then took the time difference of the buffered time stamps with the current global timestamps in all the slots and incremented the distribution of the slot where the smallest difference was found. It is clear that the off-by-5 rule was true for sub run > 0 because the smallest difference was always found in slot 0, where it was expected, but something more subtle was happening in sub run $= 0$.

each triggered event, then I would expect a delta function a few nanoseconds wide. When I did this operation however I did not get a delta function and this was the clear evidence that something was wrong with the way that the events were organized in the data files. Fig. 6.11 shows the distribution of time stamp time differences after a partial solution to the problem had been developed for all sub runs greater than sub run 0.

After examining the code that controls the modules, I found that a run-by-run header was added to the beginning of the data file in sub run zero but not subsequent sub runs. This header meant that the VF48 events got shifted by five events with respect to the rest of the event structure. This problem was corrected by marshalling all of the events into a five slot buffer and after the 5th event synchronize the global timestamp clock to the VF48 clock. After this, all subsequent events obey the same off-by-5 rule with the time stamps computed from the new base time. A flowchart showing the algorithm used to correct the time stamp mismatch is shown in Fig. 6.12. Even with this fix in place there are still timing glitches. Notice that the distribution for run 1060 sub run 1 in Fig. 6.11 extends out to $12 \mu\text{s}$. These timing glitches still need to be guarded against by checking for error flags in the module readout but they arise from a different type of problem than the offset in the data files. Not all of these timing glitches are understood. To check their effect on the final answer all cycles where timing irregularities were observed were eliminated from the data set and the difference in A_β including them or not is included in the error budget.

The major rewrite of the Analyzer code that was necessary to handle this event marshaling and time stamp syncing was what led to the creation of the software architecture plan shown in Fig. 3.11 and the creation of the Aggregator class that was mentioned in Sec. 3.9.

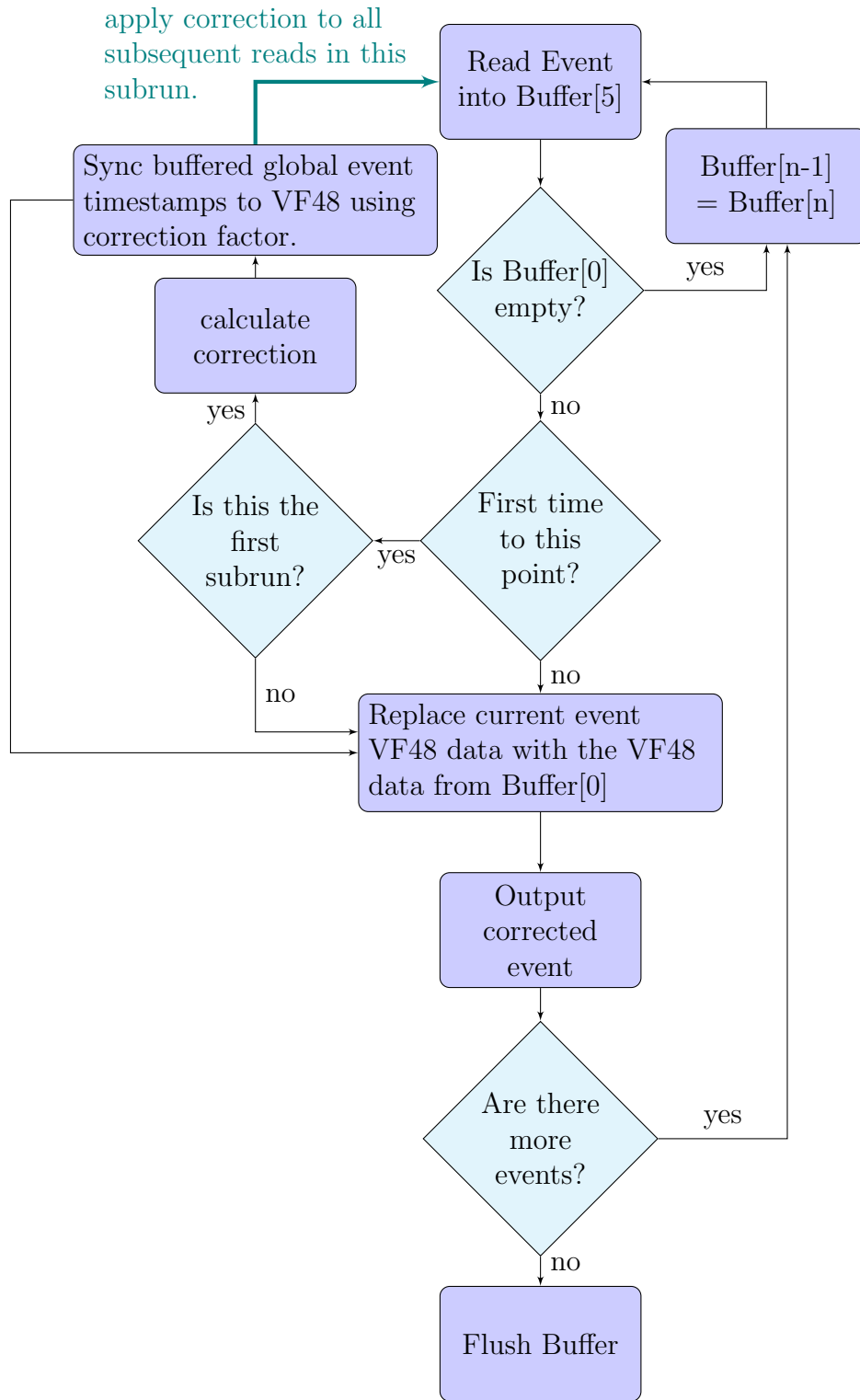


Figure 6.12: A schematic of the algorithm to correct the timestamp mismatch.

6.1.4 Energy Agreement Algorithm

A last step to making the silicon detector truly work is the implementation of an energy agreement algorithm. Each detector is double sided and β passing through will ionize atoms and the liberated electrons will migrate to one face of the detector and the holes to the other where they they will be collected and readout independently. After the energy spectrum for all of the strips have been calibrated by fitting each spectrum to a simulated spectrum from the **GEANT4** simulation then the energy agreement algorithm is run on the set of calibrated energies event-by-event. The first step of the algorithms is to search across each plane of the detector and look for strips that have an energy reading above threshold. The second step is to add the energy of each adjacent strip and see if that value is above threshold. For each instance that is found above threshold the strip number or combination is added to a potential list of events for that plane. The algorithms then compares the two list of potentials and tries to form matches. In trying to form matches each value is assigned an uncertainty because imperfect agreement could be cause by noise in the spectrum. The uncertainty value used is 17 keV, this being the average noise for all the strips from the calibration fitting. See Appendix A for all of the strip detector values. As can be seen in Fig. 6.7 imposing a tighter coincidence conditions does bring the edge strips closer into agreement with the **GEANT4** simulation but it also cuts away many events. The effect of tightening up the energy agreement between the detector planes is included in the error budget.

6.1.5 Cleaning the MCP Time Signals

Both MCP detectors in the experiment served the purpose of providing timing signals for the arrival of events. Coming out of the TDC we do not have absolute times. The relative timings between signals is what is important. For this reason we

always look at the timing from one signal and subtract the timing from another. For example a signal that we were intensely interested in was the arrival of photoions after a pulse of the UV photoionization laser because we use these events to measure the polarization of the atoms, as discussed in Sec. 5.3. The procedure for finding these events should work in the following manner. We should look through the data and look for events that have a TDC hit recorded for the photodiode, telling us when the laser fired, and a TDC hit for the anode of the ion MCP. In the ideal case all events should have at most 1 TDC hit for both of these detectors. Once we have found these events we can subtract the ion TDC signal from the photodiode TDC signal and find a relative timing of $1.5 \mu\text{s}$. This time corresponds to the time that a $1+$ ion would take to accelerate in the electric field from the trap and arrive at the ion MCP.

The reality of the situation is much different than the idealized case that was just described. In reality, both the electron MCP and the ion MCP timing spectrum had many peaks whose origin we do not understand. The signals feeding the CFDs were both extremely noisy, and we know that there were often multiple CFD triggers for a given event when the CFD would re-trigger off ringing from impedance mismatch. For a view of the relative timing between the ion MCP anode and the photodiode of the photoionization laser see Fig. 6.13. After trying some different algorithms in an attempt to extract information from the extra peaks, we decided that it was too complicated a problem and, for the analysis, we would limit ourselves to the use of the first hit timing signal. This timing most closely matches the simulated timing signals from GEANT4. This problem with multiple hits was not just a problem with the ion MCP but also with the electron MCP, though not as extreme in that case. Knowing a little about these timing signals, we are now in a position to appreciate why we require a coincidence with the electron MCP. What is required is at least

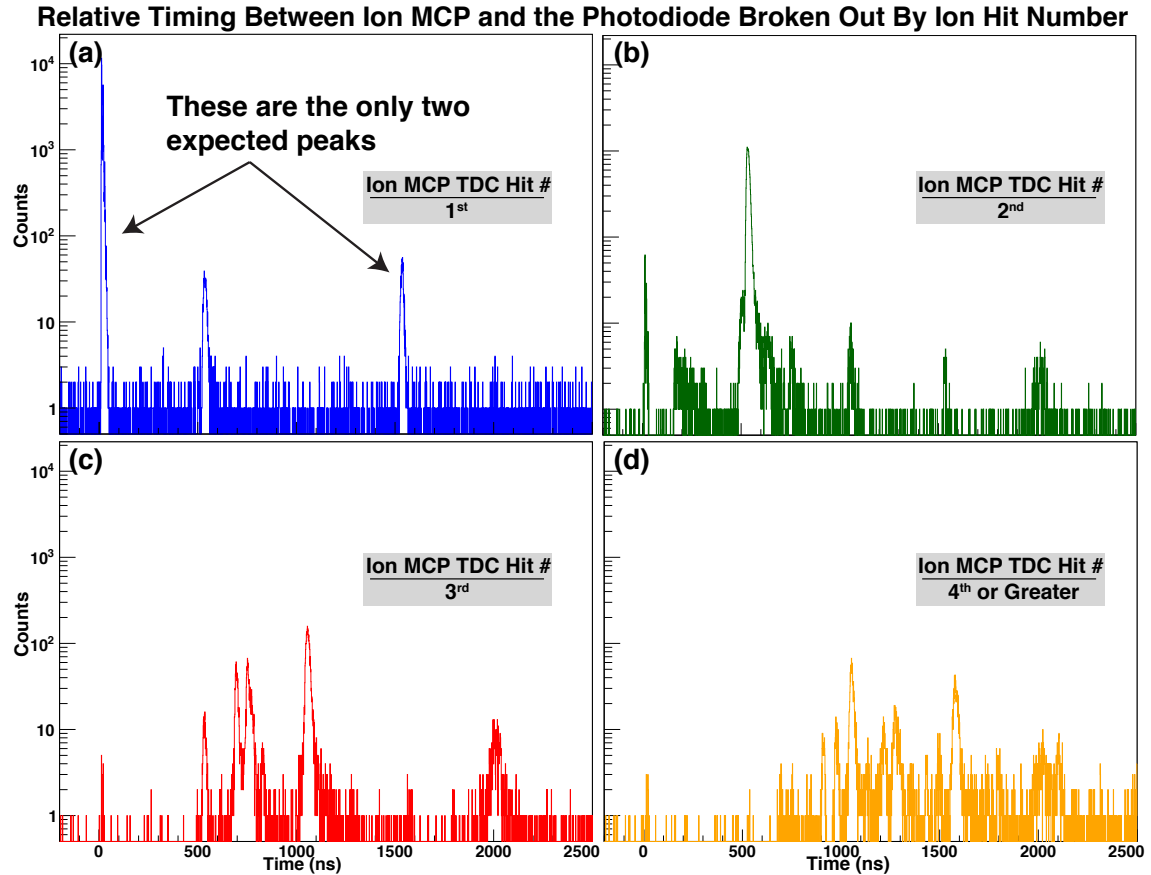


Figure 6.13: Ion – photodiode timing spectrum showing many poorly understood peaks broken out by hit number. The ion detector was the noisiest signal that we dealt with in the experiment. There were often four or more hits recorded by the TDC for a given event when we would have only expected one or two. The maximum that we observed was 18. As seen in the different panels, there are peaks in the relative timing that depend on the number of hits in the TDC; the source of these peaks is not understood. The only peaks shown here that were expected were the two peaks shown in Fig. 6.13a at zero and 1500 ns. In contrast to the ion MCP signal the photodiode signal was the cleanest in the experiment. It was observed to have only double triggered once in the 3 billion recorded events.

one hit on the electron MCP; no attempt is made to extract anything meaningful from any hit in addition to the first.

6.2 Asymmetries

In this section I will lay out the steps to reduce the ≈ 10 Tb of data that were collected into a single physics result. To start with, we will first examine the super-ratio and how it will be used to analyze the data. We will then check on the asymmetry as a function of time to make sure that we understand what is going on. This will lead us into discussion about the importance of the relative timing between the electron MCP and the scintillators. We will also briefly look at the asymmetry as a function of $\cos \theta$ and this will lead us into discussion about the strip detectors and how they were used in the final analysis. Last, we will examine the asymmetry as a function of energy and fit this asymmetry to extract, A_β .

6.2.1 The Super-Ratio

At the heart of our analysis scheme is the so-called “super-ratio” used in the evaluation of many asymmetry experiments, in particular the ultra-cold neutron A_β experiment (UCNA) [98, 99]. Why is it called the super-ratio and what makes it so super? Referring back to Eq. 1.6, the observed asymmetry can be defined in terms of the observed number of counts in the positive/negative directions, N^+/N^- according to:

$$A(E_e) = \frac{N^- - N^+}{N^- + N^+} \frac{c}{v} \frac{1}{P}. \quad (6.2)$$

Where A is the observed asymmetry and is related to A_β , and N is the number of events detected in the positive and negative Z directions for a given positron energy bin E_e . The N s are not shown with the explicit E_e notation because it will make the

later equations hard to read but it is still implied. This is straightforward and we will now show that the super-ratio collapses to this expression under a certain set of conditions that we will outline here.

To begin we will start with the expression that is given as an inline equation on page 4 column 1 in [99]

$$\begin{aligned}
 S(E_e) &= \frac{r(E_e)_1^\uparrow r(E_e)_2^\downarrow}{r(E_e)_1^\downarrow r(E_e)_2^\uparrow}, \\
 A(E_e) &= \frac{1 - \sqrt{S(E_e)}}{1 + \sqrt{S(E_e)}}.
 \end{aligned}
 \tag{6.3}$$

Here the $r(E_e)$ is the rate in detector 1 or 2. The arrows represent the two polarization states the \uparrow is when the nuclear spin is pointing at detector 1 and \downarrow is when it is pointing at detector 2. Now we will insert the value of $S(E_e)$ into $A(E_e)$,

$$A(E_e) = \frac{1 - \sqrt{(r(E_e)_1^\uparrow r(E_e)_2^\downarrow)/(r(E_e)_1^\downarrow r(E_e)_2^\uparrow)}}{1 + \sqrt{(r(E_e)_1^\uparrow r(E_e)_2^\downarrow)/(r(E_e)_1^\downarrow r(E_e)_2^\uparrow)}}.
 \tag{6.4}$$

Eq. 6.4 is what we will refer to as the super-ratio. Now to show that the super-ratio can simplify to the naive asymmetry we will need to make some assumptions about the problem. The assumptions that we make here are related to the design choices that were made when setting up the experiment. For example the experimental chamber was designed to be symmetric across the XY plane so that scattering in the two β -detectors would be the same. The assumptions that we will make are that we have a perfectly symmetric system with a perfectly centered trap, in this case the backscatter is the same in both directions. Additionally, if the efficiencies of both detectors are exactly the same, including any energy dependent efficiencies, then the rate in a given detector would be exactly the same as the rate in the other detector if

the polarization was flipped. If we then also assume that there are no rate dependent deadtime effects, we can sum over all collection time and we can come up with the following relations, $r(E_e)_2^\uparrow = r(E_e)_1^\downarrow = N^-$ and $r(E_e)_1^\uparrow = r(E_e)_2^\downarrow = N^+$. We will now insert this into Eq. 6.4. Since count rates are always positive there is no ambiguity over signs and we come to our final result,

$$\begin{aligned}
A(E_e) &= \frac{1 - \sqrt{(N^+)^2/(N^-)^2}}{1 + \sqrt{(N^+)^2/(N^-)^2}}, \\
A(E_e) &= \frac{\sqrt{(N^-)^2} - \sqrt{(N^+)^2}}{\sqrt{(N^-)^2} + \sqrt{(N^+)^2}}, \\
A(E_e) &= \frac{N^- - N^+}{N^- + N^+}.
\end{aligned} \tag{6.5}$$

We have now shown that the super-ratio is equivalent to our naive asymmetry under a certain set of circumstances. In the next section we will look at the uncertainty associated with these equations.

6.2.2 Super-Ratio Uncertainty

To use the super-ratio we will need to understand the uncertainties and how they will propagate into the final result of A_β . In general, for any computed quantity, F , with independent inputs (meaning we neglect cross terms), X_i the associated error is given by,

$$\sigma_{F(X_i)}^2 = \sum_{i=1}^n \left(\frac{\partial F}{\partial X_i} \right)^2 \sigma_{X_i}^2. \tag{6.6}$$

Let us look at the two cases of calculating the asymmetry from experimental measurements. We will start with the simple naive case given in Eq. 6.5. The partial

derivatives are straight forward to calculate and are

$$\begin{aligned}\frac{\partial A}{\partial N^+} &= \frac{2N^-}{(N^+ + N^-)^2}, \\ \frac{\partial A}{\partial N^-} &= \frac{-2N^+}{(N^+ + N^-)^2}.\end{aligned}\tag{6.7}$$

These partial derivatives can be inserted into Eq. 6.5 to obtain the final result,

$$\sigma_A = \frac{2}{(N^- + N^+)^2} \sqrt{N^{-2}\sigma_{N^+}^2 + N^{+2}\sigma_{N^-}^2}.\tag{6.8}$$

The case of the super-ratio is only slightly more complicated. The partial derivatives are

$$\begin{aligned}\frac{\partial A}{\partial r(E_e)_1^\uparrow} &= \frac{-\sqrt{\frac{r(E_e)_1^\uparrow r(E_e)_2^\downarrow}{r(E_e)_1^\downarrow r(E_e)_2^\uparrow}}}{r(E_e)_1^\uparrow \left(\sqrt{\frac{r(E_e)_1^\uparrow r(E_e)_2^\downarrow}{r(E_e)_1^\downarrow r(E_e)_2^\uparrow}} + 1 \right)^2}, \\ \frac{\partial A}{\partial r(E_e)_2^\downarrow} &= \frac{-\sqrt{\frac{r(E_e)_1^\uparrow r(E_e)_2^\downarrow}{r(E_e)_1^\downarrow r(E_e)_2^\uparrow}}}{r(E_e)_2^\downarrow \left(\sqrt{\frac{r(E_e)_1^\uparrow r(E_e)_2^\downarrow}{r(E_e)_1^\downarrow r(E_e)_2^\uparrow}} + 1 \right)^2}, \\ \frac{\partial A}{\partial r(E_e)_1^\downarrow} &= \frac{\sqrt{\frac{r(E_e)_1^\uparrow r(E_e)_2^\downarrow}{r(E_e)_1^\downarrow r(E_e)_2^\uparrow}}}{r(E_e)_1^\downarrow \left(\sqrt{\frac{r(E_e)_1^\uparrow r(E_e)_2^\downarrow}{r(E_e)_1^\downarrow r(E_e)_2^\uparrow}} + 1 \right)^2}, \\ \frac{\partial A}{\partial r(E_e)_2^\uparrow} &= \frac{\sqrt{\frac{r(E_e)_1^\uparrow r(E_e)_2^\downarrow}{r(E_e)_1^\downarrow r(E_e)_2^\uparrow}}}{r(E_e)_2^\uparrow \left(\sqrt{\frac{r(E_e)_1^\uparrow r(E_e)_2^\downarrow}{r(E_e)_1^\downarrow r(E_e)_2^\uparrow}} + 1 \right)^2}.\end{aligned}\tag{6.9}$$

Inserting the partial derivatives into Eq. 6.6 and dropping the energy dependence for

simplicity we arrive at the final result,

$$\sigma_A = \frac{\sqrt{\frac{r_1^\uparrow r_2^\downarrow}{r_1^\downarrow r_2^\uparrow}}}{\left(\sqrt{\frac{r_1^\uparrow r_2^\downarrow}{r_1^\downarrow r_2^\uparrow}} + 1\right)^2} \sqrt{\frac{\sigma_{r_1^\uparrow}^2}{(r_1^\uparrow)^2} + \frac{\sigma_{r_1^\downarrow}^2}{(r_1^\downarrow)^2} + \frac{\sigma_{r_2^\uparrow}^2}{(r_2^\uparrow)^2} + \frac{\sigma_{r_2^\downarrow}^2}{(r_2^\downarrow)^2}}. \quad (6.10)$$

6.2.3 Why the Super-Ratio is Super

It is hard just by looking at equation Eq. 6.8 and Eq. 6.10 to get a feel for how they behave. To help develop our sense will insert some numbers to see how the errors come out. The first test that I will do is insert numbers so that $r_1^\downarrow = r_2^\uparrow = N^-/2$ and $r_1^\uparrow = r_2^\downarrow = N^+/2$ and the sigmas are just taken to be the square root of the number of counts. The number that I put in were $N^- = 2000000$ and $N^+ = 1000000$. If the same total number of events is input into the naive formula and the super-ratio formula then they both give the same central value and error. For the input values given above both formulas give $A = -0.33333 \pm 0.00054$. It should be kept in mind that the super ratio requires more input and it is easy to forget to halve the number of events in each detector, half for each polarization state, to come up with the same overall count rate as the naive case. If an asymmetric error is introduced by multiplying the acceptance of one of the detectors by some attenuation then, in the case of the naive approach, the central value for the asymmetry changes and, depending if the attenuation is applied to N^+ or N^- , the error will change by a little or a lot. Using the numbers from above we will introduce an 80% efficiency to one of the detectors and compute the naive asymmetry so that we have $N^- = 2000000(0.8)$ and $N^+ = 1000000$, this gives $A = -0.23077 \pm 0.00060$. If we apply the efficiency to the other detectors we get $N^- = 2000000$ and $N^+ = 1000000(0.8)$ and $A = -0.42857 \pm 0.00054$.

The super-ratio does much better in this situation. For one case we have, $r_1^\downarrow = 1000000(0.8)$, $r_1^\uparrow = 500000(0.8)$, $r_2^\downarrow = 500000$, $r_2^\uparrow = 1000000$, and in the other case $r_1^\downarrow = 1000000$, $r_1^\uparrow = 500000$, $r_2^\downarrow = 500000(0.8)$, $r_2^\uparrow = 1000000(0.8)$. Both case give the same asymmetry -0.33333 ± 0.00058 . The central value remains unchanged from what we had previously. The only effect is to enlarge the uncertainty. The whole reason for doing this exercise was to find out what happens to symmetric errors: by that I mean errors that change sign with a spin flip. An examples of such an error is the trigger bias introduced through missing shakoff electrons due to Ar^- flight times. Such errors are neither cancelled well by the super-ratio nor the naive approach. In these cases the problems need to be corrected for through modeling or by only fitting the parts of the spectrum where these things are not important.

6.3 Asymmetry as a Function of Cycle Time

To start off our discussion about asymmetries, let us start by looking at the asymmetry as a function of cycle time (see Fig. 6.14). Each point on the plot is an asymmetry computed with Eq. 6.4, with the error bars representing the statistical error as computed with Eq. 6.10. An interesting thing that we see in the figure is that, during the optical pumping time, we see an asymmetry and we do not see a statistically significant asymmetry during the rest of the cycle ($\text{Asym} = -0.0005 \pm 0.0005$) as we expect. We also see that using the strip detectors as a coincidence condition is effective and the file offset mentioned previously has been corrected. Additionally notice the large effect that including the electron detector coincidence has on the observed asymmetry. Clearly the inclusion of this detector in the experiment was a good choice. For the fitting that we will do later with the energy spectrum, we will need to make a cut on polarized times. The cut that we will use is $300 \mu\text{s} \leq t \leq 1960 \mu\text{s}$, as shown in Fig. 6.14d.

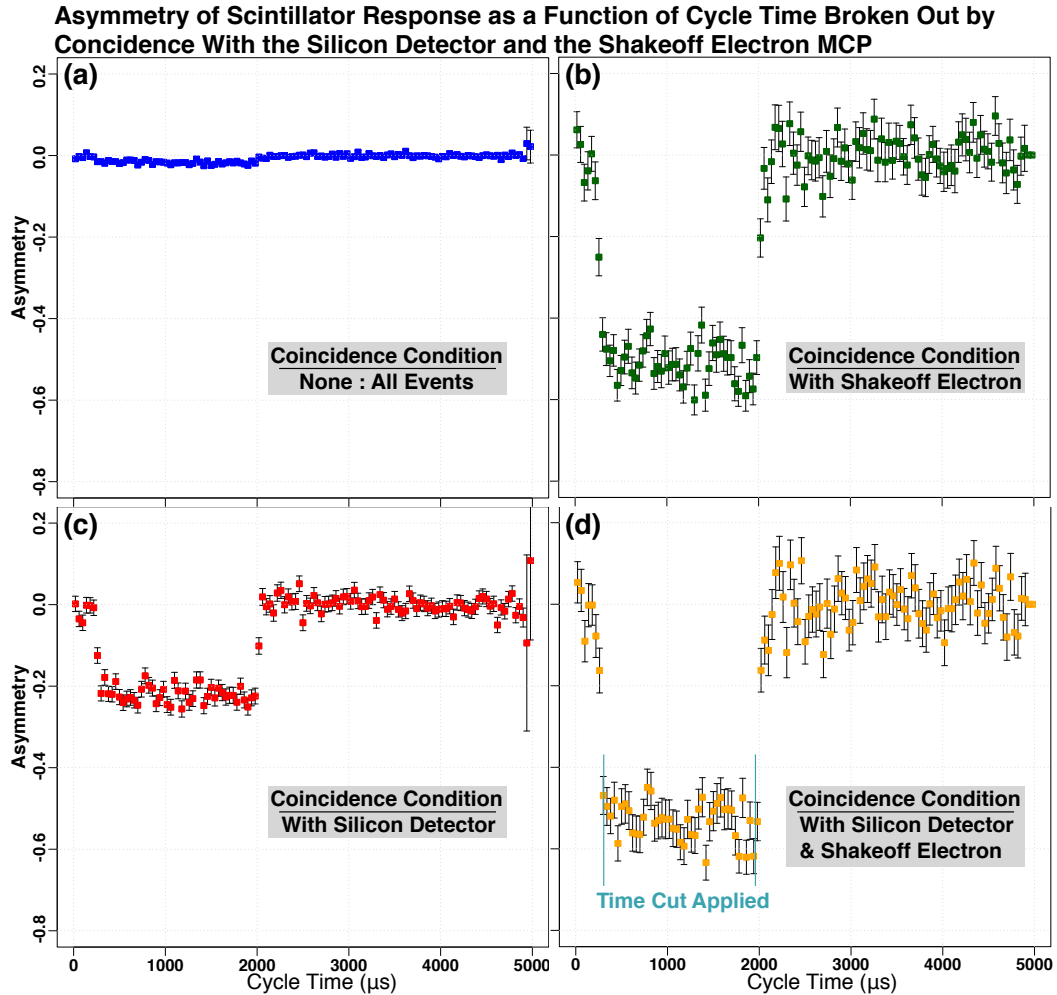


Figure 6.14: Asymmetry between the scintillators as a function of cycle time. In Fig. 6.14a we see that taking an asymmetry of the scintillator signal without a coincidence produces almost not asymmetry. We see in Fig. 6.14b - 6.14d, between the polarized time $250 \mu\text{s}$ and $2000 \mu\text{s}$, the asymmetry grows. By comparing Fig. 6.14b with Fig. 6.14c we can see that relative importance of the shakeoff electron coincidence is greater than the strip detector coincidence. To see the energy spectrum that went into these asymmetry plots see Fig. 6.19b. Shown in Fig. 6.14d are the timing cuts that were used to select events during polarized times.

6.4 Timing Coincidence Between the Scintillators and the Electron MCP

In the last section it was mentioned that the coincidence between the electron MCP and the the scintillators was the condition that has the largest impact on the observed asymmetry. To investigate this a little further we looked at the relative timing spectrum between these two detectors. A 2D histogram of the relative timing of these two detectors versus the energy left in the scintillator is shown in Fig. 6.15. The figure shows a number of stripes on along the timing axis. We recognize some of these stripes as β s by looking at the energy distribution of the events in each stripe. We also see in the figure a stipe that contains a large number of ADC overflows that that come from cosmic rays. These events need to be removed from the analysis of A_β because the analysis relies on fitting to GEANT4 simulations that have not included any background coming from cosmic rays. The cuts that were made to remove these events are $62 \text{ ns} \leq t_{scintillator}^{lower} \leq 68.5 \text{ ns}$ and $58.5 \text{ ns} \leq t_{scintillator}^{upper} \leq 65 \text{ ns}$. The decision was made to only use the strongest β peak in the spectrum because the amount that we would gain in statistics by including the others would be offset by increasing the uncertainty arising from the introduction of more cuts.

6.5 Asymmetry as a Function of Angle

One potential way that we could use the position information from the strip detector is to look at the decay rate as a function of angle. The reader will recall Eq. 1.1 where we see that the observed decay rate is not just dependent only on the value of A_β but also on $\cos\theta$. If we could look at the asymmetry as a function of $\cos\theta$ then we would be able to gain a greater handle on our systematic uncertainties. It would also be possible to vary the polarization and observe a change in the decay rate in this way but, as shown in Chapter 5, knowing the polarization in any state is a hard problem and changing it would add to that difficulty.

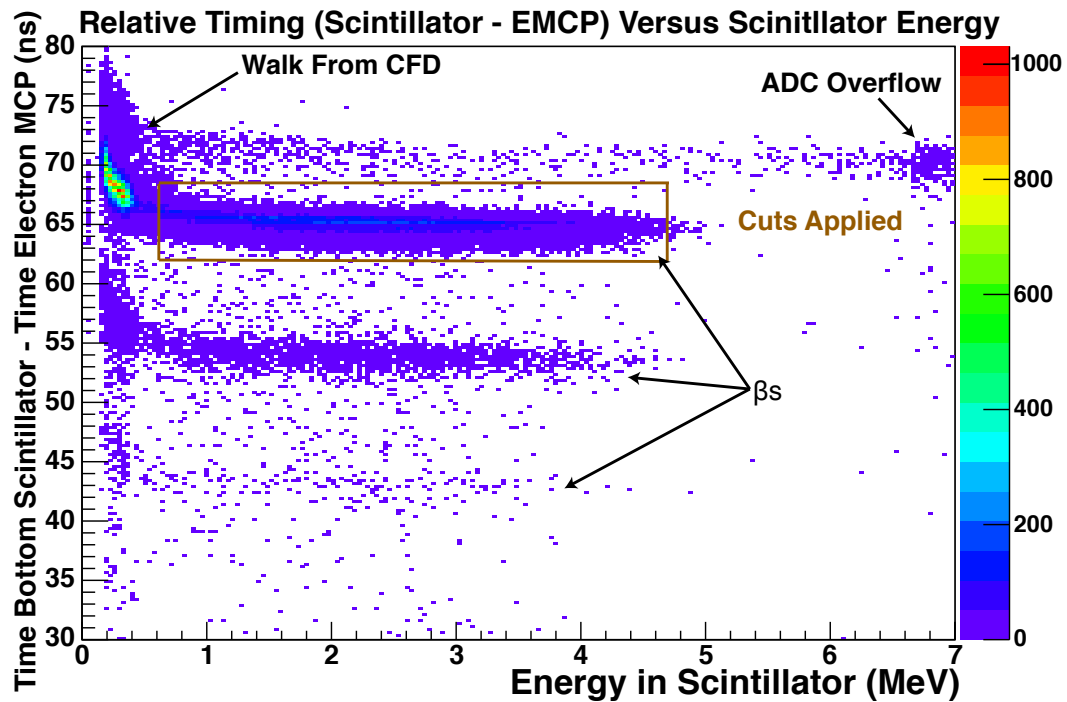
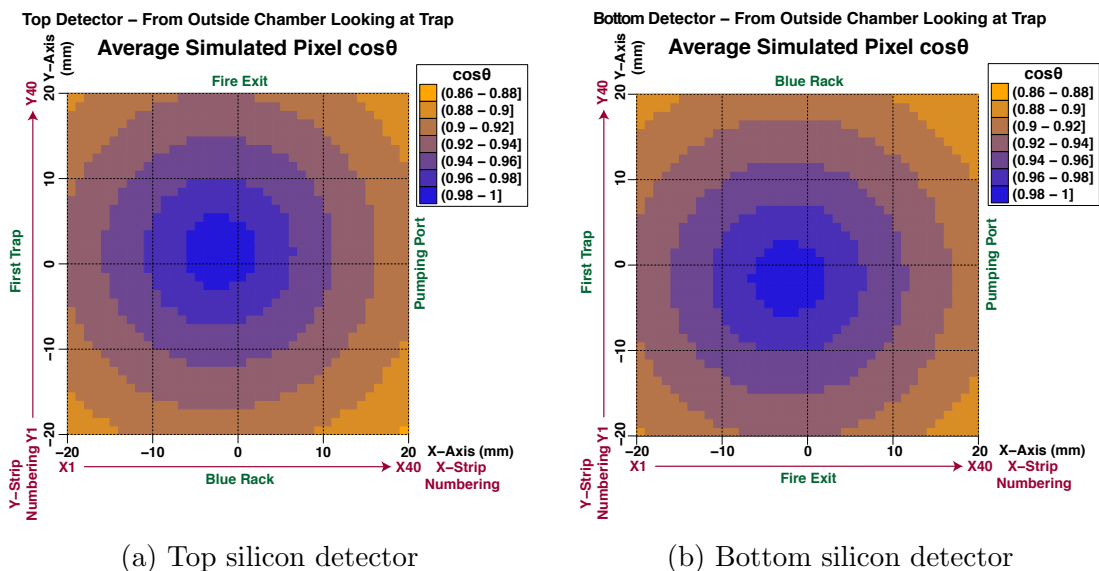


Figure 6.15: Relative timing between the scintillator and the electron MCP. The relative timing between the scintillators, top and bottom, and the electron MCP are almost exactly the same except for a few nanosecond constant offset that is probably due to a slightly longer signal cable. There are some stripes, separated by ≈ 10 ns, in this plot that originate from shakeoff electrons that bounce off of the plate without firing it and are then reaccelerated by the field and hit it again. This phenomenon is also observed in the GEANT4 simulation. The part of this spectrum that is worrisome is the stripe at 74 ns that does not have a β energy distribution and has a peak at high energy. This high energy peak is from cosmic muons and needs to be cut out of the asymmetry analysis.



(a) Top silicon detector

(b) Bottom silicon detector

Figure 6.16: Simulated $\cos\theta$ distribution for silicon detectors. These are contours of equal $\cos\theta$ that I found through Monte Carlo. The two distributions are not perfectly symmetric because the trap is not perfectly centered in the chamber.

The strip detectors have forty individual strip readouts per plane and the strip arrangement of the two planes front and back is perpendicular. So a typical β particle as it passes through the detector will deposit energy in one strip of the front plane and one strip of the back plane. In this way it is possible to identify to the accuracy of a 1 mm box the place that the β passed through the silicon detector.

In order to measure the asymmetry as a function of $\cos\theta$ using the position information provided by the strip detectors, it is necessary first to define areas of constant $\cos\theta$ projected onto the silicon. In order to find these $\cos\theta$ contours I wrote a small Monte Carlo program that would take the coordinates of the trap center and find the average $\cos\theta$ for each of the 1600 pixels and group them into contour levels that I would later use in computing the asymmetry. The results of this Monte Carlo simulation can be seen in Fig. 6.16. One of the limitations that I faced when trying to analyze the data in this way was that we only have pixel information for the

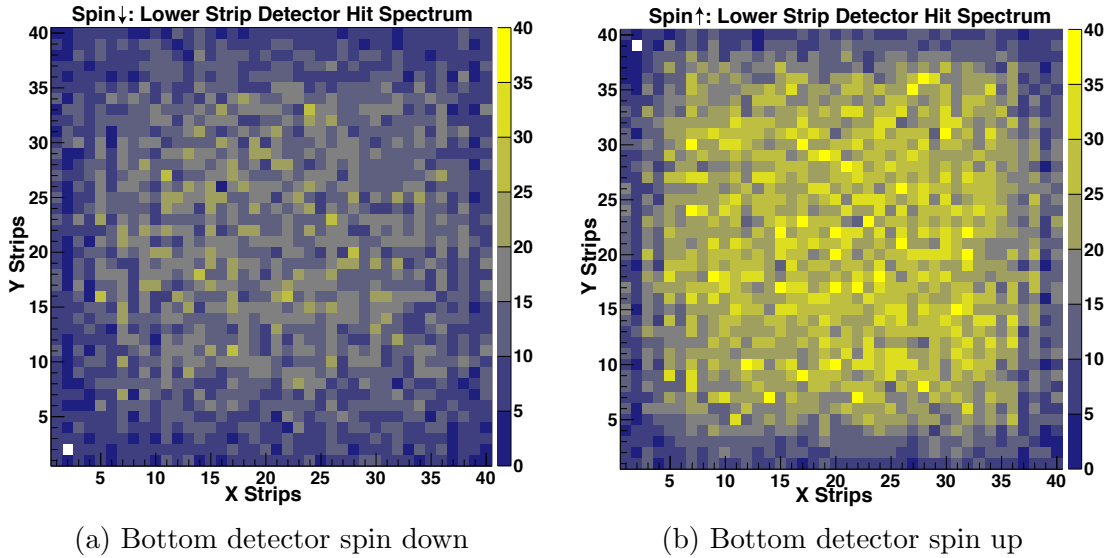


Figure 6.17: These are heatmaps of β hits on the bottom silicon detectors during polarized time. They would look the same as those shown in Fig. 6.16b if we had ~ 10000 times more data and there was no β scattering. A large asymmetry between the two polarization states Fig. 6.17a and Fig. 6.17b is clearly visible by eye. The magnitude of this asymmetry is shown in the lower left panel of Fig. 6.14.

bottom detector because of the faulty X-odd preamp on the top detector. That means that any analysis will exclude about half of the total data set. It quickly became apparent that, because of the lack of statistics, we were not going to be able to extract anything meaningful from the asymmetry as a function of angle. A heat map of β hits on the lower detector can be seen in Fig. 6.17b

One other thing that is possible to try is to use every other pixel. The upper-X even strips did work so we can use them in the analysis. If I impose a coincidence condition between the Y strips on both detectors and the even X strips on both detectors then I come up with a set that I can use in the super-ratio. This process, even though it throws away events, might still succeed because the overall data might be cleaner. With the position information that we have from using every other pixel it might be possible to see some angular effects. Using just the Y plane of the

detectors, we have in the whole data set 36,837 events that pass all of the other cuts. Applying the every-other strip condition for both detectors gives us a set of 11,051, spread into 1600 pixels over the two polarization states. This condition removes more than half of the data because energy agreement between the two planes of the detectors is enforced.

We can look now at the asymmetry for two areas of equal $\cos \theta$. The asymmetry is shown in Fig. 6.20b. The lack of statistics in the two spectra makes comparison meaningless. However, this comparison should be possible with the next data set because so much more data was collected and faulty preamp was replaced so that all of the strips on both detectors were working. In the next section we will begin to look more closely at the asymmetry as a function of the energy that the β left in the scintillator. To do that we will want to use both silicon detectors to increase our statistics. The way that I did this was to use the full detector on the bottom and on the top to use every other strip. In this way I could use the energy agreement algorithm. The effect of using the strip detector in this way should be taken into account by the super-ratio because it is just an efficiency that is applied to one detector the same as the example shown earlier. However, instead of relying on cancelation from the super ratio we remove the problem by fitting the data with GEANT4 simulation data that has been filtered to remove its upper X odd strips.

6.6 Asymmetry as a Function of β Energy

More fruitful than looking at the asymmetry as a function of $\cos \theta$ is to look at it as a function of kinetic energy of the β . In order to do this we will need to have a calibrated, clean β energy spectrum to work with. The data were calibrated by fitting to GEANT4 and the procedure is outlined in Appendices A and B. Shown in Fig. 6.19a is a view of the calibrated energy spectrum with all events collected in the experiment

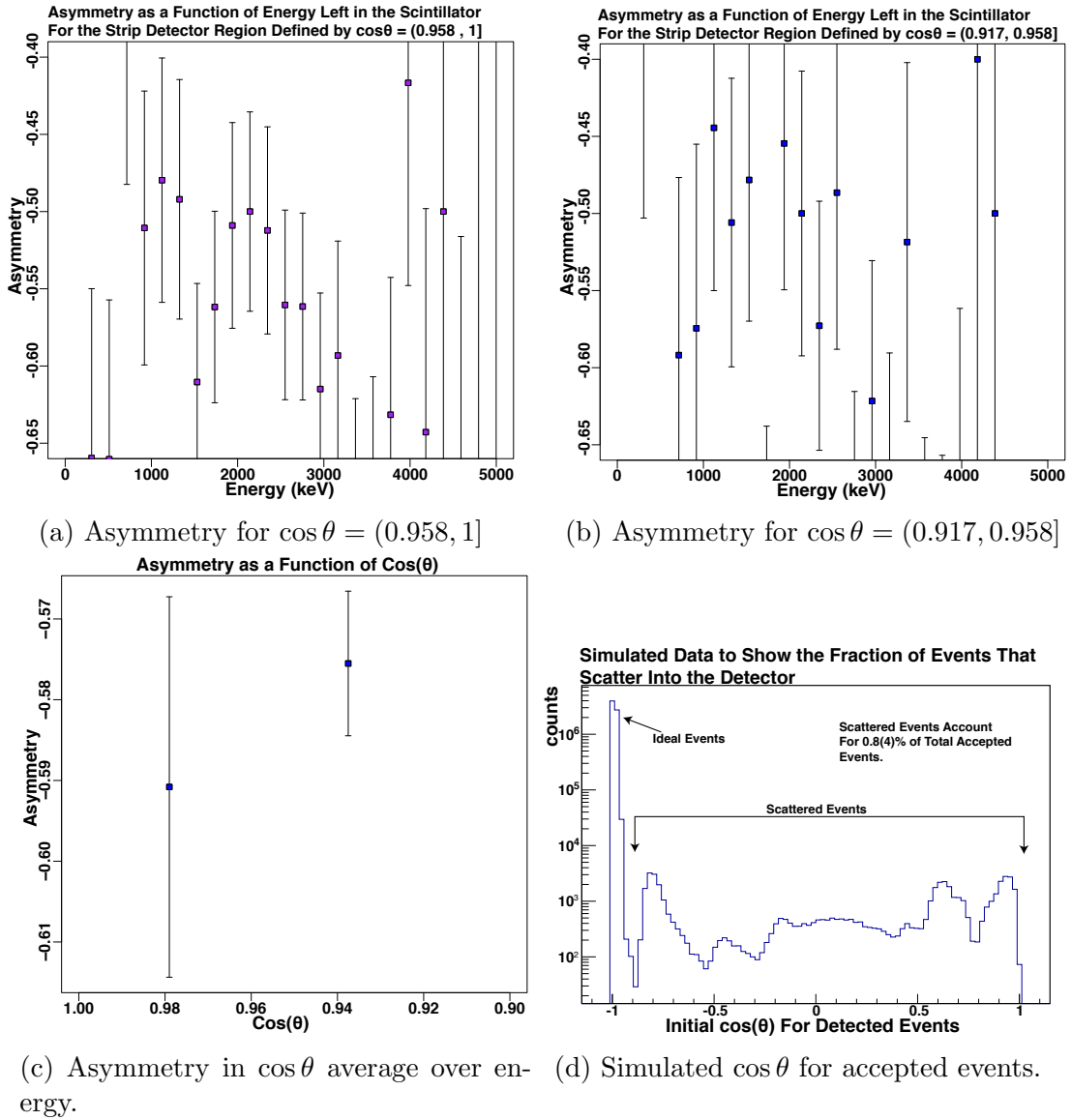
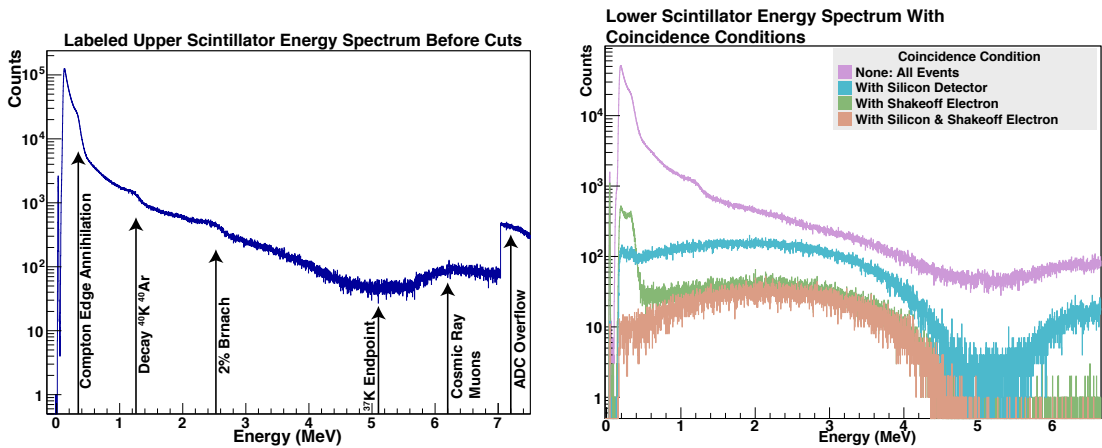
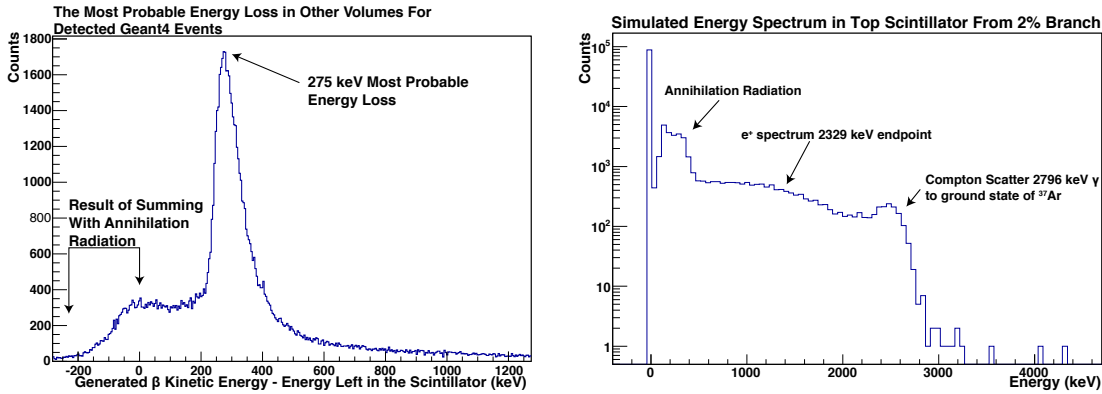


Figure 6.18: Asymmetry for two slices in $\cos\theta$. The strip detector was divided into three sections in $\cos\theta$. The innermost section $\cos\theta = (0.958, 1]$ is circular and the second section $\cos\theta = (0.917, 0.958]$ is an annulus. The third section is everything else on the strip detector and is oddly shaped. These regions were chosen because the inner two regions are the largest possible sections that are fully contained on the strip detector that have equal $\cos\theta$. The two top panels show the asymmetry signal from these two regions. The axes were intentionally made the same as Fig. 6.20b for comparison. If we average over the energy spectrum then we can come up with asymmetry as a function of $\cos\theta$ shown in Fig. 6.18c. When looking at asymmetry with bins in $\cos\theta$ it will be important to understand how many of the detected events have a different $\cos\theta$ than they started off with. We can simulate this in GEANT4 and the result is shown in Fig. 6.18d.



(a) Raw scintillator energy spectrum with labels

(b) The effect on the scintillator energy spectrum of introducing coincidence conditions



(c) The most probable energy lost in volumes other than the scintillator for detected events.

(d) Simulated energy spectrum of the 2% branch.

Figure 6.19: The scintillator energy spectrum. Fig. 6.19a shows the raw upper scintillator spectrum with labels of prominent features. It should be noted that the endpoint for the β spectrum will be shifted lower in energy from its nominal value of 5.12 MeV because a typical β will lose 275 keV of energy in the mirror, beryllium, and strip detector before coming to rest in the scintillator. As shown in Fig. 6.19c. Another visible feature is the Compton edge of the γ ray from the excited state of ^{37}Ar populated by the 2% pure Gamow-Teller branch. A simulated energy spectrum from our GEANT4 simulation for this branch is shown in Fig. 6.19d. The effect of introducing coincidence conditions on the scintillator energy spectrum is shown in Fig. 6.19b. As can be seen the the coincidence with the silicon detector greatly reduces the 511 keV annihilation background but leaves the cosmic rays at high energy. The coincidence with the shakeoff electron MCP eliminates the cosmic rays but leaves the 511s. In the final analysis we require them both.

from the upper scintillator. The figure is labeled with key features. Something important to note is that there are background gamma peaks. The background from these unpolarized gammas will need to be removed if we are going to be able to fit for A_β .

The cleaning of the energy spectrum in preparation for fitting was done by introducing the following coincidence conditions between the various detectors:

1. There should be at least one hit in the TDC for one and only one of the scintillators.
2. There should be at least one hit in the TDC for the shakeoff electron MCP.
3. The event had to have occurred within the time window $300 \mu\text{s} < t < 1960 \mu\text{s}$ after the start of the optical pumping signal.
4. The event had to have exactly one strip in the Y plane and exactly one strip in the X plane of the silicon detector in front of the scintillator register an energy above 20 keV. A summed pair of adjacent strips will also work in this case. Both of the planes had to be above 20 keV and agree within 17 keV. Strip numbers 1, 2, 39, 40 were excluded from all planes.
5. The event had to have a relative timing between the firsts hits on the TDC for the lower scintillator and the electron MCP of $62 \text{ ns} \leq t_{scintillator}^{lower} \leq 68.5 \text{ ns}$ or for the upper scintillator $58.5 \text{ ns} \leq t_{scintillator}^{upper} \leq 65 \text{ ns}$.

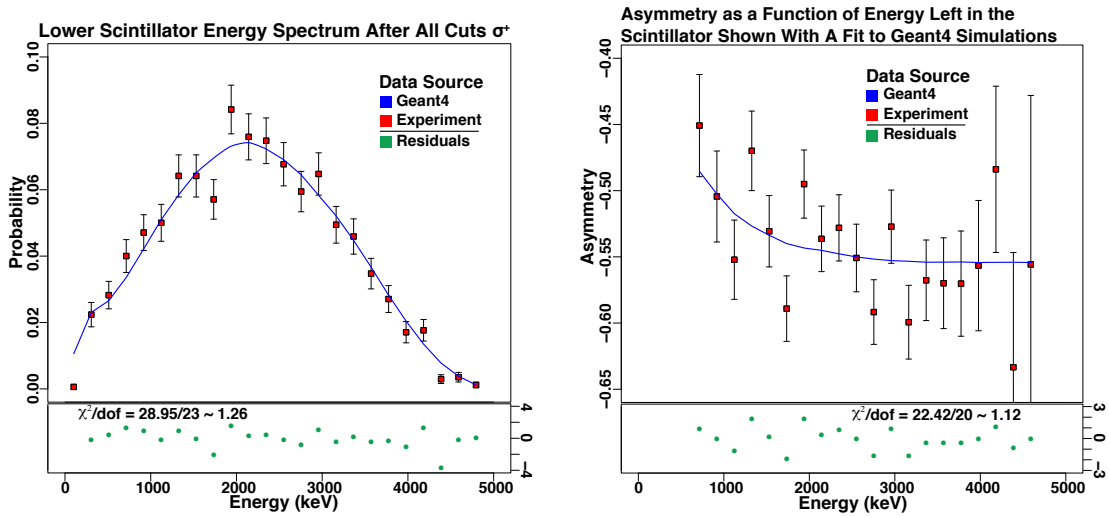
The effect of applying the previously listed coincidence conditions on one of the the β energy spectrum needed for the super-ratio can be seen in Fig. 6.20a along with a GEANT4 energy spectrum that has been put through the same filter. Now that we have applied the cuts necessary to clean up the β spectrum. We will apply the super

ratio bin-by-bin to the four β energy spectra. This will leave us with an asymmetry signal. Which is shown in Fig. 6.20b. We need to remember that the asymmetry will not be the same as A_β because of the v/c term in the decay rate, the polarization is not 100% and there is β scattering.

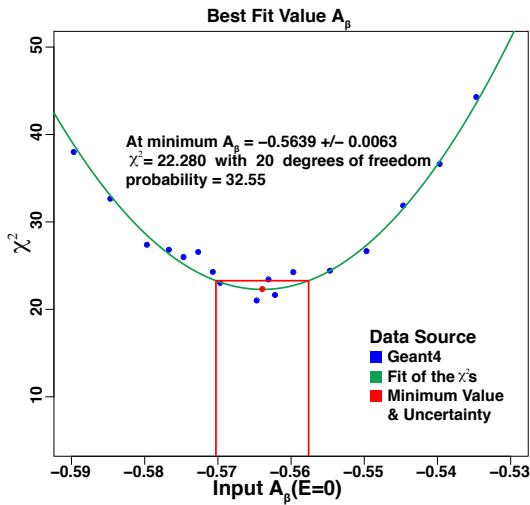
In the next step of the analysis we will fit the spectrum shown in Fig. 6.20b with multiple GEANT4 spectra corresponding to different values of A_β . In this step we need the central value for the polarization of the atoms; 0.99 was used as explained in Sec. 5.6. Using this number for the polarization you can either make a correction to the data or run all of your GEANT4 simulations with the measured polarization. The second method has the downside that if you want to try a different polarization that you need to run a new set of simulations and this becomes time prohibitive very quickly.

The other topic that we need to consider before we can make a fit of A_β is the fitting range. In the fit I choose to omit the first two bins because they are below or partially below 511 keV. This region is hard to get a handle on because the strip detectors are not perfect at vetoing 511 γ s, and β scattering at low energies is large. Also as shown in Fig. 6.15 because of the walk in the constant fraction for the scintillators the low energy gammas get spread out and some will be cut by the timing coincidence that we put on the relative timing between electron MCP and scintillators. Since this effect is not simulated in GEANT4 it is hard to know what effect it will have.

Now that we have established our spectrum and decided on a fitting region we will fit our experimental results to simulated spectrum that were generated by varying the input value of ρ that corresponds to different values of A_β . This was done so that a consistent set of all of the correlation parameters was obtained. For each spectrum we will calculate a χ^2 value. If we are sufficiently close to the minimum then the



(a) The lower scintillator spectrum fit to GEANT4 (b) Observed asymmetry after all time cuts fit with GEANT4.



(c) Fitting the value of A_β using GEANT4 simulations with different values of input A_β

Figure 6.20: Summary of A_β fitting procedure. First, the experimental and GEANT4 spectrum are passed through the same filter of conditions resulting in spectrum shown in Fig. 6.20a. There are four such spectrum produced one for each polarization state and detector. Second, the the super ratio is computed bin-by-bin using these four spectrum. The result is shown in Fig. 6.20b. Third, this spectrum is fit to multiple GEANT4 spectrum that have been run with different starting values for $A_\beta(0)$ and the result is shown in Fig. 6.20c.

distribution of χ^2 values will be parabolic and we could fit this distribution to find the minimum. The minimum corresponds to our best estimate of the central value of A_β . To calculate the error from this fit we look to find which $A_\beta(0)$ values would produce a $\chi^2 = \min(\chi^2) + 1$ and these are our 1σ limits. The result of this operation is shown in Fig. 6.20c. The result from our fit is $A_\beta(0) = -0.5639 \pm 0.0063$, assuming $P = 0.99$.

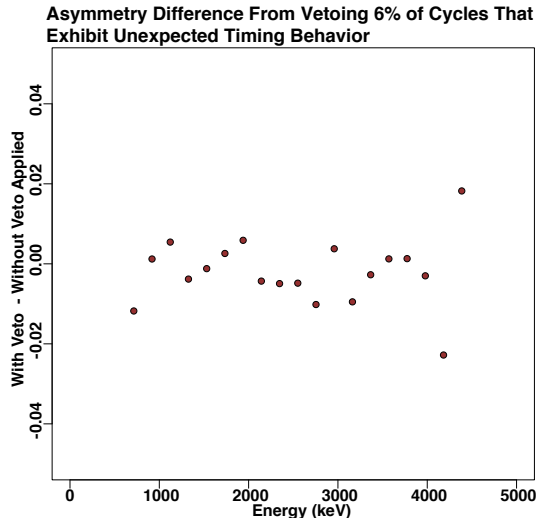
6.6.1 Systematic Uncertainties

There are of course systematic errors that we will also need to estimate and add into the total uncertainty that we will quote for our value of A_β . The first major systematic uncertainty is knowledge of the polarization of the atoms. This was discussed in detail in Chapter 5. It is worth summarizing here that during the experiment we made a measurement of the polarization of the atoms using photoions during the optical pumping time. In fitting this data it was revealed that there exist a large difference in the way that the two polarization models being used behave in the presence of misaligned magnetic fields. The value for the polarization that we have been using ($P = 0.99 \pm 0.01$) was measured using ^{41}K offline and has known problems. Depending on what is determined about the polarization and misaligned magnetic fields the final number for the polarization could have error bars larger or smaller than what is shown here. Additionally, if the central value changes then the central value of our fit value for A_β will also change. It needs to also be determined if the polarization was different between the two states. As it stands right now the systematic uncertainty associated with our knowledge of the polarization for our value of A_β is 0.0056. In a follow up ^{37}K A_β experiment performed by the TRINAT collaboration because so much more data was collected it will be possible to make measurements of the polarization of the atoms in both polarization states instead of

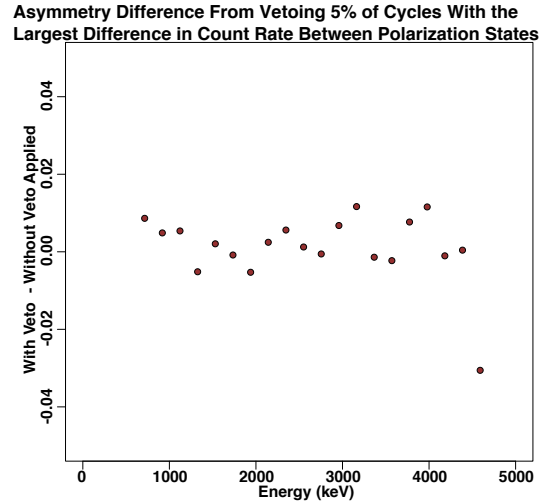
having to average of the two states as was done with this data set.

Some of the systematic errors that we considered have roots in the physical mechanics of the experiment. One such example is the number of atoms in the trap. If more atoms were in the trap in one polarization state than the other then this would lead to a fake asymmetry in the same way that unequal time in each polarization state would. The number of atoms in the trap does deviate but over the course of the experiment we expect the trap fluctuations will average out. Two ways of trying to get a handle on the number of atoms in the trap are the sum of the number of counts in the PMTs and the number of hits on the electron MCP. These two measures were summed for each 16 s polarization period and the difference between the two polarization states for a 32 s cycle was taken as an indication of an unequal number of atoms in the two polarization states. We wondered about the effect of the most extreme cases of these asymmetric cycles. The data was analyzed including all cycles and then excluding the 5% of cycles where this count asymmetry was highest. The asymmetry difference between these two fits is shown in Fig. 6.21b. It has a small effect on the fit value of A_β . The half difference between the central values of the two fits for A_β is what we will take to be our systematic uncertainty and is 0.001.

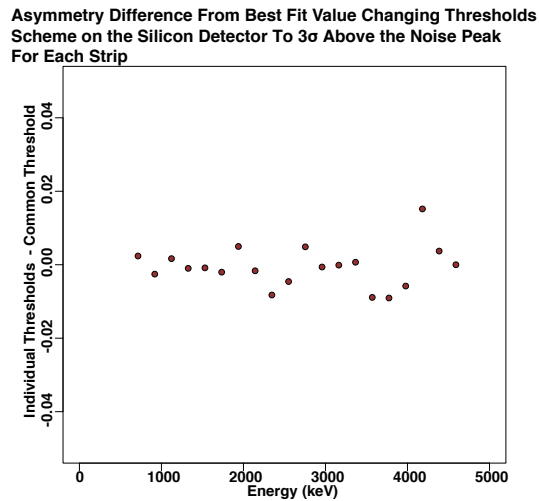
In the discussion about timestamp mismatch in Sec. 6.1.3 it was mentioned that besides the file offset timestamp problem there could be other deviations arising from other sources. The mechanisms that causes all of these problems are not well understood. If we were to take the difference in the timestamps between the first event in a cycle and the last timestamp in the event and do it cycle-by-cycle we should get a narrow gaussian distribution. This is what we get for 94% of the cycles. For the other 6% we see large quantized deviations. Since we do not know the source of these timing discrepancies or their consequences we calculated A_β using all of the cycles and then vetoing the 6% where these timestamp deviations occurred. A plot



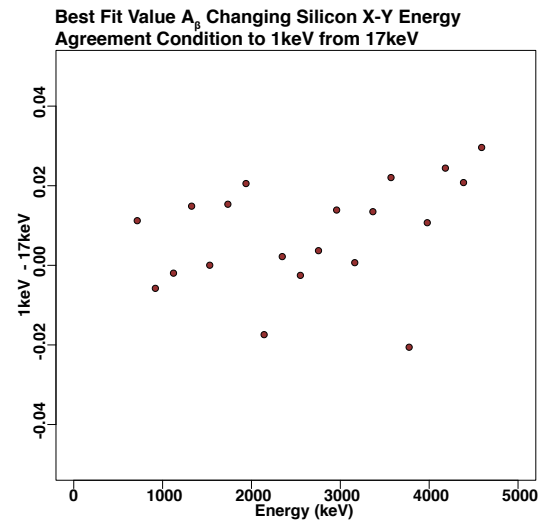
(a) Veto the 6% of cycles with observed timestamp deviations



(b) Veto the 5% of cycles with the highest deviations in the number of electron hits and summed scintillator hits between the polarization states



(c) Changing the threshold scheme on the strip detector from a common threshold to individual thresholds.



(d) Changing the energy agreement threshold between the X and Y planes of the silicon detectors.

Figure 6.21: Some asymmetry difference plots showing the effect of different systematic uncertainties considered.

of the asymmetry difference is shown in Fig. 6.21a. The half difference between the central values of the two fits for A_β is 0.0005.

We also know that not all of the strips used in the analysis were exactly the same. Some were noisier than others and others had worse calibrations. To this end we fit the noise peak of all of the strips with a gaussian and then set the threshold for each strip to be 3σ above the mean of the noise peak. We compared this with the with setting the threshold to a global value of 20 keV. The asymmetry difference resulting from this change is shown in Fig. 6.21c. The half difference between the central values of the two fits for A_β is 0.0005.

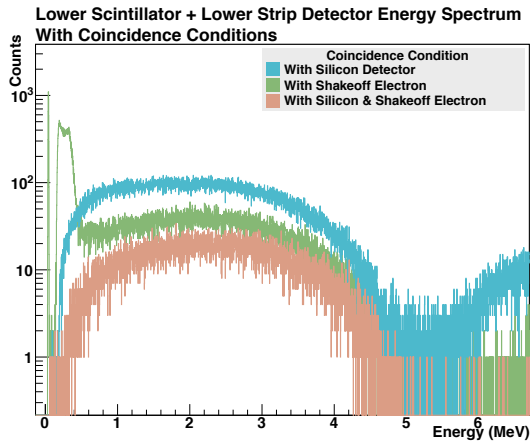
Another source of uncertainty associated with the use of the strip detectors is the energy agreement condition that we applied between the X and Y planes of the detector. Our choice of how tight to make the energy agreement was informed by the calibration fit done for each strip. In an ideal world this energy agreement condition would just reduce events where noise in the detector caused a disagreement between the X and Y planes. That being the case we should be able to tighten this condition to produce the same answer with larger error bars from the suppression of some of these real events. We do not live in a perfect world and tightening this condition slightly shifts our retuned value of A_β . The asymmetry difference that results from applying this condition is shown in Fig. 6.21d. This shift could be an indication that our algorithm comes with some bias such as working better for events that left lots of energy in the silicon detector. If that were the case the shape of the scintillator spectrum that we are fitting would change and hence our fit value. The half difference between the central values of A_β of the two fits with different energy agreement conditions is 0.0034.

The low energy threshold for the scintillator is another potential source of potential uncertainty in our experiment. This is because on the low energy side of the

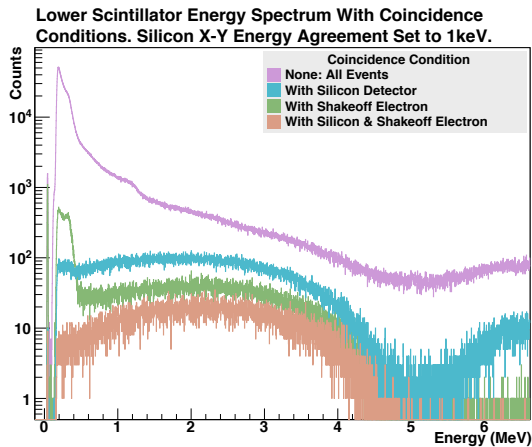
spectrum events will be cut out by the timing coincidence that was applied because of the walk on the constant fraction discriminator (see Fig. 6.15). For this reason a fit was made with the threshold raised. The half difference between the central values of the two fits for A_β is 0.0005.

Until this point in doing these fits we have always always the scintillator energy spectrum. This works because we fit the experimental scintillator spectrum with those generated by our GEANT4 model. Since we require a coincidence between the scintillator and silicon detector it is possible to sum these spectrum and to fit this spectrum with summed spectra from GEANT4. The energy spectrum and a fit with GEANT4 data is shown in Fig. 6.22. Fitting the data in this way gave a $\chi^2/\text{dof} = 26.575/20 \approx 1.33$ with a probability of 14.77. Comparing this to the reduced χ^2 from fitting the scintillator spectrum alone of $22.916/20 \approx 1.15$ with a probability of 29.29 it can be seen that the scintillator only spectrum fits better with the data. The half difference between the central values of A_β doing the fit with the scintillator spectrum and summed spectrum is 0.0011.

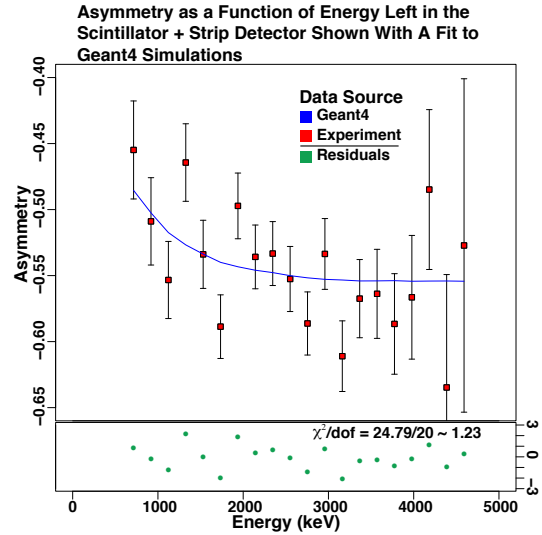
Another source of systematic uncertainty that we need to understand is the trap displacements and movement that could be different during the two different polarization states. If the trap is in the same off center position during the two states then this will cancel out in the super-ratio. If it moves positions depending on the polarization state then it will not cancel out and will lead to a fake asymmetry. The numbers that we will need to calculate the effect of the trap movement between the two polarization states is given in Table. 3.2. The variable that matters the most to the asymmetry is the Z position along the polarization axis. Two simulations were run one with the trap at the average Z position of 1.11 mm and the other with the trap at 1.059 in the σ^- state and 1.186 in the σ^+ This is a worst case scenario as the number in both states was moved by its uncertainty in opposite directions so that



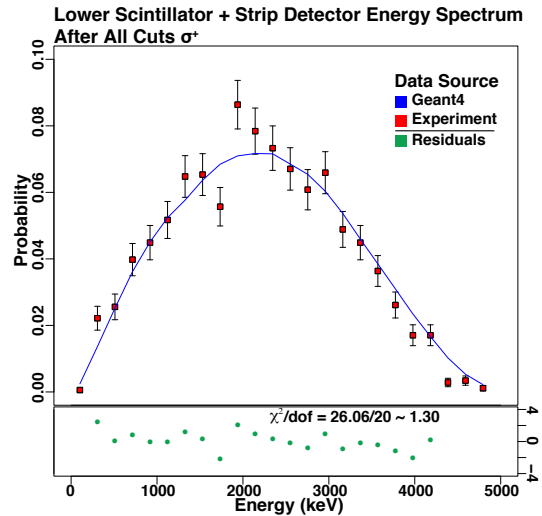
(a) The effect on the summed scintillator + strip detector energy spectrum of introducing coincidence conditions.



(c) The effect on the scintillator energy spectrum with a 1 keV agreement condition between the X and Y planes of the silicon detector.



(b) Fit of the asymmetry using the summed scintillator + strip detector spectrum.



(d) The lower summed scintillator + strip detector spectrum fit to GEANT4.

Figure 6.22: The effect of different conditions on the energy spectra and fits. The energy spectrum with coincidence shown in Fig. 6.22a and Fig. 6.22c look similar to that shown in Fig. 6.19b. The differences are that Fig. 6.22a is pushed to higher energy by the inclusion of the strip detector energy and Fig. 6.22c has less counts because of the tighter energy condition between the X and Y planes. The fit of the energy spectrum and asymmetry with GEANT4 shown in Fig. 6.22b and Fig. 6.22d are a little worse than the fits using only on the scintillator spectrum shown in Fig. 6.20.

the maximum difference between the two states was achieved. The half difference between the central values of the two fits for A_β is 0.001. The same procedure was used to vary the Z sail velocity but the difference was at the 10^{-5} level and neglected here.

There are also geometry effects that we are able to evaluate with **GEANT4**. One of these is evaluating the effects of machine tolerance on the mirror thickness. These mirrors come from the manufacture with a specification for optical quality flatness. This flatness is obtained by continually polishing the original mirror substrate. This means that the thickness cannot be guaranteed and indeed the thickness is quoted by the manufacture as $10 \pm 1 \mu\text{m}$. This thickness is simple to change in **GEANT4**. The way that this was done was by turning the trap position, temperature, and movement all to zero. Also the detector resolution and polarization were set to perfect. The reason for this is so that we could isolate the effect from just the mirror. I ran four total simulations with one in each polarization state for mirrors at 11 microns another set at 9 microns. I did this because there needs to be a fake asymmetry inducing mechanism. If the mirrors were both increased or decreased together then the effect was observed to be canceled out. I then took the half difference in the asymmetry returned from the simulations. The effect was small 0.0001.

The last systematic uncertainty that we need to consider is the **GEANT4** model itself. One of the largest questions regarding the **GEANT4** simulation is how well it reproduces β scattering. Studies have been done to try and quantify how well **GEANT4** reproduces scattering data and report that the deviations could be as large as 25% [100]. To quantify scattering effects on our measurement of A_β , all **GEANT4** events where a β scattered into the detectors as determined by the generated $\cos\theta$ of the β were vetoed in the **GEANT4** simulation. The experimental asymmetry spectrum

Source	Uncertainty
Statistical	0.0063
Systematics:	
Polarization	0.0056
Energy Agreement X-Y of Silicon Detectors	0.0034
Uncertainty in GEANT4 Model	0.0015
Asymmetric Number of Atoms in Trap	0.0014
Scintillator versus Summed Energy	0.0011
Trap Movement	0.0010
Scintillator Threshold	0.0005
Silicon Threshold	0.0005
Timing Errors	0.0005
Machine Tolerance Mirror Thickness	0.0001
Total systematic	0.0071
Total uncertainty	0.0095

Table 6.1: Error budget. A breakdown of the contribution of the systematic uncertainties to the overall error budget.

was then fit with this filtered set of **GEANT4** simulations. Assuming that **GEANT4** was off, in scattering, by 25% then our systematic uncertainty would be 25% of the difference in A_β from the fit using the filtered data and the best fit value, and the uncertainty is 0.0015.

6.6.2 The Final Result

Putting it all together now we come to our final answer $PA_\beta = -0.5583 \pm 0.0109$. If the polarization of the atoms is $P = 0.990 \pm 0.010$ then $A_\beta(0) = -0.5639 \pm 0.0094$ a 1.7% measurement. The contribution of the different systematic uncertainties were added together in quadrature due to our belief that large correlations do not exist between them. An error budget summarizing what we discussed in the last section is shown in Table. 6.1.

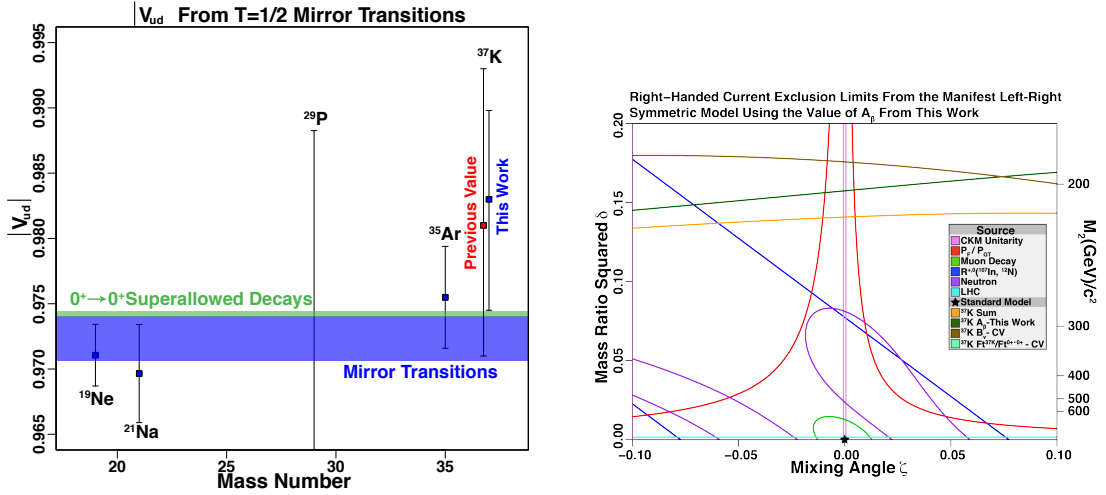
Let us examine some of the implications of this measurement in the two contexts that were discussed in Chapter 2, namely calculating V_{ud} using a set of $T = 1/2$ mirror

nuclei, and exclusion limits on parameters from right-handed current models. The value of A_β that was measured corresponds to a ρ value of $\rho = 0.553_{-0.021}^{+0.034}$ taking into account recoil order corrections at the average β energy. The previous measurement of B_ν that gave a ρ value of $\rho = 0.560_{-0.024}^{+0.029}$ [16]. These two measurements of ρ were combined by finding the peak of the probability density function,

$$\exp \left[-\frac{1}{2} \frac{\left(\frac{B_\nu^{calc}(\rho) - B_\nu^{experiment}}{dB_\nu} \right)^2 + \left(\frac{A_\beta^{calc}(\rho) - A_\beta^{experiment}}{dA_\beta} \right)^2}{\sqrt{2\pi(dB_\nu^2 + dA_\beta^2)}} \right]. \quad (6.11)$$

The result is $\langle \rho \rangle = 0.557_{-0.016}^{+0.021}$. This value for ρ can then be used in Eq. 2.17 along with the values of the statistical rate function given by Naviliat-Cuncic in [16] and the $\mathcal{F}t$ given in Ref. [23] to calculate $\mathcal{F}t_0 = (6.04_{-0.11}^{+0.09}) \times 10^3$ s. On its own, ^{37}K 's $|V_{ud}| = 0.983_{-0.009}^{+0.007}$. This value can be combined with the other isotopes listed by Naviliat-Cuncic yielding a value of $|V_{ud}|$ from $T = 1/2$ mirror transitions of 0.9723(17). When compared with the value reported by Naviliat-Cuncic 0.9719(17) it can be seen that the central value moves into better agreement with the value calculated from superallowed $0^+ \rightarrow 0^+$ decays but the increase in precision is not significant. A graphical representation of this comparison is shown in Fig. 6.23a.

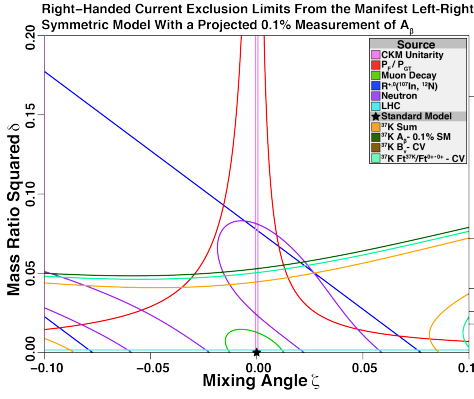
The other context that was developed in Chapter 2 that we could use to interpret our measurement of A_β was to limit the parameters of models that extended the SM by allowing for the presence of right-handed currents. As shown in Section 2.4.1 the algorithm for constructing the exclusion intervals can take as input experimental measurements of observables such as A_β , B_ν , and the ratio $\mathcal{F}t/\mathcal{F}t^{0^+ \rightarrow 0^+}$. These parameters depend on the value of ρ . Since the ρ dependence will also change in the presence of right-handed currents it is treated as a fitting parameter and is allowed to vary to minimize the χ^2 at each point where a new set of right-handed current model



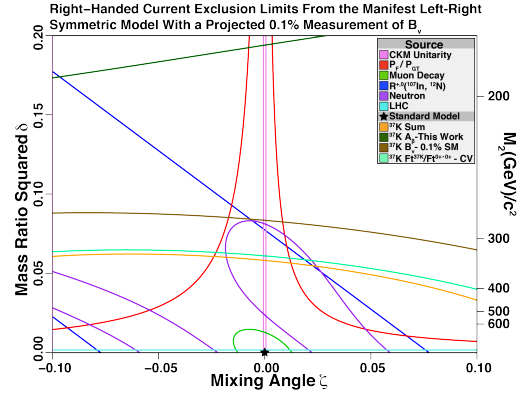
(a) The value of V_{ud} calculated from a set of $T = 1/2$ mirror transitions [16]. The value for ^{37}K had been updated because of a new lifetime measurement and what is labeled as “previous value” was taken from [23]. For comparison the most precise determination of V_{ud} calculated from superallowed $0^+ \rightarrow 0^+$ transitions [17] is also shown.

(b) Exclusion of right-handed current model parameters using the the value of A_β for ^{37}K from this work. See Chapter 2 for the references pertaining to the different limits. The abbreviation CV in the legend stands for current measured value.

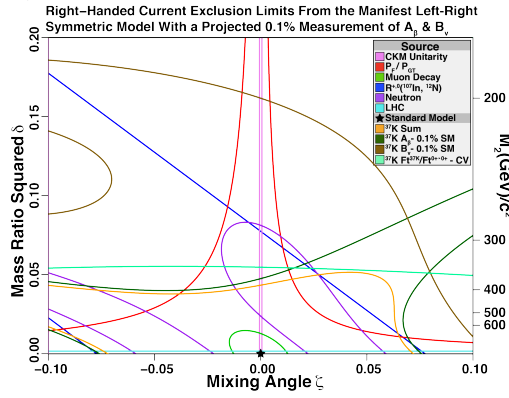
Figure 6.23: Interpretation of our measurement of A_β in the framework of the standard model and in the framework of the manifest left-right symmetric right-handed current model.



(a) Projected A_β 0.1%



(b) Projected B_ν 0.1%



(c) Projected A_β and B_ν 0.1%

Figure 6.24: Projected limits from future experiments measuring the correlation parameters A_β and B_ν at the 0.1% level of precision. The abbreviation CV in the legend stands for current measured value. It can be seen that a 0.1% measurement of either A_β or B_ν with the current $\mathcal{F}t$ is sufficient to place a limit that is competitive with the current neutron limit.

parameters are tried. A visualization of the achieved 90% exclusion limits achieved using just the present measured observables by themselves and the summed limit from all ^{37}K observables is shown in Fig. 6.23b. To see projected limits for future work at the 0.1% level of precision see Fig. 6.24.

7. FUTURE PROSPECTS AND SUMMARY OF RESULTS

7.1 Future Prospects

This experiment was never meant to be the stopping point in terms of the TRI-NAT collaborations measurement of A_β but rather a jumping off point for the program to really push the boundaries of precision measurements in this area. Seen in this light it is prudent to use the insight gained in the current analysis to make suggestions for upgrades to the experiment to help reduce systematic uncertainties. In this section I will outline some possible improvements.

7.1.1 Size and Position Sensitivity of Electron MCP

Early on in this project a question was raised about potential bias that could be introduced by populating a short lived $^{37}\text{Ar}^-$ state instead of the neutral ground state. Through the use of **GEANT4** simulations the possible bias was investigated, see Fig 4.9, and was determined to be small. Along these same lines a similar bias could arise if the shakeoff electron energy is higher than current theoretical predictions. In both cases the bias comes from the limited size of the detector. If we lose electrons off of the edge of the detector, preferentially in one polarization state versus the other, then this will lead to a fake asymmetry. The way to eliminate this bias is to use a higher electric field or a larger MCP.

In order to eliminate the bias mentioned in the previous paragraph it is desirable to use a larger shakeoff electron MCP. The one caveat is that increasing the size also increases the noise. In order to keep the noise under control. It is desirable to add position sensitivity to this detector also. In addition to helping clean up the noise, position sensitivity would offer two exciting capabilities. First it would allow for the first time a measurement of the shakeoff electron energy distribution and give us the

ability to test if we were missing high energy shakeoff electrons off of the edge of the detector. The second advantage that would be given by position sensitivity would be the ability to measure trap position and temperature. This information would be complementary with the information currently provided by the ion MCP and the cross check who allow us to reduce the systematic uncertainty associated with the trap position.

7.1.2 Increase Polarization Diagnostics

The largest systematic uncertainty is currently our knowledge of the polarization. There exist a few possibilities to improve this that can be achieved on reasonable time scales. The first thing is to install a triggerable photoionization laser. The current laser fires at 10 kHz but its clock is not synced to any of the other clocks in the experiment. This is pertinent to the polarization measurement because the photoions produced by this random firing only help us to make a polarization measurement if they come during the optical pumping time which is a small portion of the total cycle time. If we were able to trigger the laser on demand we could raster the continuous fluorescence curve into distinct time bins that we control. A triggerable laser has been delivered to TRIUMF and is awaiting someone to set it up and develop the trigger pattern that would allow us to sample from the time region that we are interested in. The linewidth of the current laser has been measured to be 10 MHz [101]. The natural linewidth of excited state is 6 MHz. It is unlikely that linewidth of the new triggerable laser will be sufficiently narrow to probe the sublevel populations directly.

The second action that would help, even if we do not have total control over it, is that we need to have more atoms in the trap. The photionization technique that we used to measure the polarization in this experiment works better with higher statistics. It was found after the experiment was over that the push beam was

not well aligned between the first and second traps. Correcting this alignment lead to a factor of 4 increase in the number of atoms in the second trap. In addition to correcting the problem with the push beam, the vacuum pressure in the main chamber needs to be reduced. Atoms in the trap can escape through collisions with residual gas in the chamber. The main contribution to residual gas in this experiment was from hydrogen. This was due to the failure of a non-evaporable getter pump that is specifically designed to pump hydrogen. The replacement of this pump did significantly reduce the total residual gas in the system and hence increase the number of atoms in the trap. The better vacuum meant that physical trap lifetime went from 1.5 s in the current experiment to 3.8 s. This increase in trap population was demonstrated in a subsequent experiment. In the present experiment TRIUMF used a low power target to produce the ^{37}K at a rate of 3.8×10^7 [26]. It was speculated that using a high power target could produce more ^{37}K and it would be worth it to work with TRIUMF to develop a high power TiC target to test this speculation. A high power target has been developed and it was confirmed during that it did produce more ^{37}K , 8.14×10^7 [26].

The third action that should be taken to improve polarization diagnostics is to enhance the direct optical imaging capabilities of the experiment. There is currently a camera installed to view the fluorescence from the trap and it works when there are millions of atoms in the trap but does not work with the low number of ^{37}K . A much more sensitive camera with a much faster frame rate has been delivered to TRIUMF for the purpose of replacing the old camera. It is awaiting someone to set it up, calibrate it, and develop the trigger pattern for it. It would be beneficial if the data from this camera was integrated into the nuclear acquisition system directly. Doing this would mean that the only job left for the Windows 98 computer would be timing and it could easily be replaced by a waveform generator or FPGA module

greatly reducing the timing uncertainties on the push beam signal.

7.1.3 Higher Electric Field

The position of the trap along the MCP axis is best located by the rising edge of the neutral ^{37}Ar hitting the ion MCP. In this experiment the 350 V/cm applied electric field was insufficient to provide separation of the rising edge of the fastest neutral Ar from the slowest $^{37}\text{Ar}^{1+}$, see Fig. 4.8. The knowledge of the trap position is tied up with knowledge of the applied electric field that can be determined by the separation between the high charge states 1^+ , 2^+ , *etc.* and this separation grows with the electric field. The exact position of the trap is not critical for the asymmetry analysis as long as it does not change during the two polarizations states. Applying a stronger field would allow the separation of charge states and the increased precision could allow us to quantify better the movement of the trap along this axis between the two polarizations states better. Additionally a higher electric field would allow for complete collection of the Ar^{1+} ions. Measurements of the other correlation parameters $a_{\beta\nu}$ and B_ν rely on knowing the ion spectrum very well and incomplete collection of these ions makes that a very difficult task.

7.1.4 Improved GEANT4 Simulations

The GEANT4 simulations of any experiment can never be 100% complete. In the short term the things that could be reasonably done that would have the biggest positive impact are first, to have a geometry review and implement missing parts or redefine simplified parts to be more realistic. For example even though I defined the copper coils with the correct wall thickness and filled the interior with cooling water, I did not implement the ceramic support structure that holds these coils in place. There are a number of small geometry elements like this that could benefit from a review. The second thing that would help would be to design and implement specific

tests of the GEANT4 simulations. These tests should be both software and physics tests. On the software side the implementation of unit tests with a goal of 100% code coverage is the standard that most large software companies operate under [102]. Where a “unit test” supplies input to a function and tests the returned value against a known correct answer. Unit tests should test the smallest division of code possible in C++ this is just a single function, and enough cases should be supplied that all of the logical branch points contained in the function can be evaluated. There are a number of reasons to do unit testing. First, it helps a programmer to find logical errors because 100% code coverage means that tests need to be designed for all of the branch points where it is easy to miss edge cases. Second, unit tests are generally integrated into the build process automatically so that a programmer is immediately alerted if the current change broke some part of the code that was already working. Third, because unit tests are often written by a programmer other than author of the original code and it is an opportunity for code review. Currently no unit tests are implemented in this project.

On the physics side the response of the detectors compared to GEANT4 should be done for different isotopes with different β and γ energies. The comparisons that we have seen with the ^{37}K experimental data, such as Fig. 6.20a, Fig. 6.20b, Fig. A.1, and Fig. B.1 have been favorable but more cases would help to increase our confidence that everything is right. Also our GEANT4 model should be tested against independent simulations built using EGS4 [103] and PENELOPE [104].

7.1.5 *Blind Analysis*

The current analysis was not done with myself being blinded to the final answer along the way. The reason for this was that we knew the time and manpower needed to implement a blinding scheme would be better spent elsewhere. The justification

for this being that with the statistics that we have we would not be able to see any deviation due to physics.

Having worked through the analysis once I can suggest a plausible blinding scheme for the next experiment. One way to do this would be to set up the **GEANT4** simulation so that in one polarization state, for a given amount of events requested, it would simulate some unknown amount less. This would create a fake time asymmetry in the **GEANT4** data as described in Sec. 6.1.1. The advantage of doing this versus other blinding schemes would be that it would be simple to implement and would not disturb any of the physics of the spectrum. Also at the time of unblinding, new simulations do not need to be run. The only correction that would need to be applied would be to veto the right amount of events from the other polarization state. Additionally the implementation of the scheme would entail the creation of a C++ blinding library that would not need to expose how many events it will veto just one public method that would veto an event or not. Since the number of accepted events coming out of **GEANT4** is a stochastic amount compared to the the number of requested events, the veto amount cannot be accidentally discovered.

7.2 Summary

The first experiment to make a measurement of the beta asymmetry parameter in ^{37}K is described. The online isotope separator of the TRIUMF ISAC facility provided the ^{37}K . By confining the ^{37}K in a magneto-optical trap, we prepared it in a point-like, cold, backing free source.

The positrons emitted from the decay of ^{37}K to the ground state of ^{37}Ar were detected using silicon strip detectors backed by plastic scintillators. In order to cancel out potential systematic errors we used two beta telescopes arranged along the direction of the nuclear polarization axis and evaluated the asymmetry using

information from both detectors and both polarization states using a super-ratio technique.

The energy calibration of the detectors was done by comparing the positron spectrum from the decay of ^{37}K with a detailed **GEANT4** Monte Carlo simulation. This simulation included the full detector geometry and the dynamics of the cloud movement during the optical pumping cycle. Calibrating the data in this way avoids potential differences that can arise from changes in experimental conditions from calibration to measurement phase.

To enhance the signal-to-noise ratio of the polarized decays an electric field was used to accelerate shakeoff electrons from the β -decay onto an MCP detector. This suppressed the unpolarized background of ^{37}K that had escaped from the trap and adhered to geometry elements inside of the chamber.

The same electric field that was used to accelerate shakeoff electrons in one direction also accelerated charged recoiling ^{37}Ar in the other direction towards an MCP equipped with a position sensitive readout. The position sensitivity of this detector enabled the characterization of the cloud position and movement during the trapping cycle.

The angular correlation between the positron (e) and the nuclear polarization vector (P) is defined in terms of the parameter A_β :

$$d\omega \sim 1 + A_\beta P \frac{v_e}{c} \cos \theta \quad (7.1)$$

In this experiment we integrated θ over the solid angle coverage of our detectors and used the energy spectrum of the scintillators to determine v_e/c . The polarization of the ^{37}K was explored in depth. Due to the ongoing work to fully understand depolarizing mechanisms the number used here for the polarization was taken from

optical measurements done with ^{37}Ar directly following the experiment, and has a value of 0.99 ± 0.01 . This number is known to be a place holder and will be superseded in the future with the fit value from the photoion spectrum.

We recorded about 41,702 events with a scintillator-silicon-electron MCP coincidence. Fitting the data to **GEANT4** simulations with our assumed value for the polarization yields a result of $A_\beta(0) = -0.5635 \pm 0.0094$ a 1.7% measurement. This measurement can be combined with others from a set of $T = 1/2$ mirror transitions to calculate $|V_{ud}| = 0.9723 \pm 0.0017$. Also this measurement being interpreted in the context of the manifest left-right symmetric model allows us to exclude masses of M_2 above 230 GeV at the 90% confidence level at $\zeta = 0$.

Using the insight that was gained in the analysis of the current experiment recommendations were made on how the systematic uncertainties in the measurement could be reduced paving the way for a truly precision measurement. In a follow up experiment data has already been collected that will allow for a measurement of a statistical precision of 0.3%. In that experiment due to much higher count rate a much clearer photoion spectrum has been seen that will allow a much more precise fit of the polarization than the current experiment. Additionally, because of the fixed Upper X odd preamp both strip detectors will be able to utilize all of their pixels.

REFERENCES

- [1] T. Lee and C. Yang. Question of Parity Conservation in Weak Interactions. *Physical Review*, 104(1):254–258, October 1956.
- [2] C. S. Wu. Experimental Test of Parity Conservation in Beta Decay. *Physical Review*, 105(4):1413–1415, February 1957.
- [3] Richard Garwin, Leon Lederman, and Marcel Weinrich. Observations of the Failure of Conservation of Parity and Charge Conjugation in Meson Decays: the Magnetic Moment of the Free Muon. *Physical Review*, 105(4):1415–1417, February 1957.
- [4] G. Soti, F. Wauters, M. Breitenfeldt, P. Finlay, P. Herzog, A. Knecht, U. Koster, I. S. Kraev, T. Porobic, P. N. Prashanth, I. S. Towner, C. Tramm, D. Zakoucky, and N. Severijns. Measurement of the β -asymmetry Parameter of ^{67}Cu in Search for Tensor-type Currents in the Weak Interaction. *Phys. Rev. C*, 90:035502, Sep 2014.
- [5] F. Wauters, I. Kraev, D. Zákoucký, M. Beck, M. Breitenfeldt, V. De Leebeeck, V. V. Golovko, V. Yu. Kozlov, T. Phalet, S. Roccia, G. Soti, M. Tandecki, I. S. Towner, E. Traykov, S. Van Gorp, and N. Severijns. Precision Measurements of the ^{60}Co β -asymmetry Parameter in Search for Tensor Currents in Weak Interactions. *Physical Review C*, 82(5):055502, November 2010.
- [6] F. Wauters, V. De Leebeeck, I. Kraev, M. Tandecki, E. Traykov, S. Van Gorp, and N. Severijns. β -asymmetry Parameter in the Decay of ^{114}In . *Physical Review C*, 80(6):062501, December 2009.

- [7] G. Masson and P. Quin. Measurement of the Asymmetry Parameter for ^{29}P β -decay. *Physical Review C*, 42(3):1110–1119, September 1990.
- [8] J. Garnett, E. Commins, K. Lesko, and E. Norman. β -decay Asymmetry Parameter for ^{35}Ar : An Anomaly Resolved. *Physical Review Letters*, 60(6):499–502, February 1988.
- [9] A. Converse, M. Allet, W. Haeberli, W. Hajdas, J. Lang, J. Liechti, H. Lüscher, M.A. Miller, R. Müller, O. Naviliat-Cuncic, P.A. Quin, and J. Sromicki. Measurement of the Asymmetry Parameter for ^{35}Ar β -decay as a Test of the CVC Hypothesis. *Physics Letters B*, 304(1-2):60–64, April 1993.
- [10] N. Severijns, J. Wouters, J. Vanhaverbeke, and L. Vanneste. β -decay Anisotropies of the Mirror Nuclei ^{15}O and ^{17}F . *Physical Review Letters*, 63(10):1050–1053, September 1989.
- [11] N. Severijns, J. Wouters, J. Vanhaverbeke, W. Vanderpoorten, and L. Vanneste. First Online β -decay Asymmetry Measurements of Oriented Nuclei. *Hyperfine Interactions*, 43(1-4):415–421, December 1988.
- [12] S. Hung, K. Krane, and D. Shirley. Beta-decay Asymmetry From the Decays of Oriented ^{52}Mn and ^{60}Co . *Physical Review C*, 14(3):1162–1173, September 1976.
- [13] Leo M. Chirovsky, Wen-Piao Lee, Albert M. Sabbas, Arthur J. Becker, Joel L. Groves, and C.S. Wu. Nuclear Orientation Facility for the Study of the Angular Distribution of γ Radiation and β Particles Emitted by Polarized Nuclei. *Nuclear Instruments and Methods in Physics Research*, 219(1):103–110, January 1984.

- [14] F. Calaprice, S. Freedman, W. Mead, and H. Vantine. Experimental Study of Weak Magnetism and Second-Class Interaction Effects in the β Decay of Polarized ^{19}Ne . *Physical Review Letters*, 35(23):1566–1570, December 1975.
- [15] D. Melconian, J. Behr, D. Ashery, O. Aviv, P. Bricault, M. Dombisky, S. Foster, A. Gorelov, S. Gu, and V. Hanemaayer. Measurement of the Neutrino Asymmetry in the β -decay of Laser-Cooled, Polarized ^{37}K . *Physics Letters B*, 649(5-6):370–375, June 2007.
- [16] O. Naviliat-Cuncic and N. Severijns. Test of the Conserved Vector Current Hypothesis in $T = 1/2$ Mirror Transitions and New Determination of $|V_{ud}|$. *Physical Review Letters*, 102(14):1–4, 2009.
- [17] J. Hardy and I. Towner. Superallowed $0^+ \rightarrow 0^+$ Nuclear β Decays: A New Survey With Precision Tests of the Conserved Vector Current Hypothesis and the Standard Model. *Physical Review C*, 79(5), 2009.
- [18] Carlos A. Bertulani. *Nuclear Physics in a Nutshell*. Princeton University Press, 1st edition, 2007.
- [19] Brian Martin. *Nuclear and Particle Physics: An Introduction*. Wiley, 2nd edition, 2009.
- [20] David Griffiths. *Introduction to Elementary Particles*. Wiley-VCH, 2nd edition, 2008.
- [21] Stanley G. Prussin. *Nuclear Physics for Applications*. Wiley-VCH, 1st. edition, 2007.
- [22] E. Hagberg, I. Towner, T. Alexander, G. Ball, J. Forster, J. Hardy, J. Hykawy, V. Koslowsky, J. Leslie, H.-B. Mak, I. Neeson, and G. Savard. Measurement

- of the l -forbidden Gamow-Teller Branch of ^{37}K . *Physical Review C*, 56(1):135–141, July 1997.
- [23] P. D. Shidling, D. Melconian, S. Behling, B. Fenker, J. C. Hardy, V. E. Iacob, E. McCleskey, M. McCleskey, M. Mehlman, H. I. Park, and B. T. Roeder. Precision Half-Life Measurement of the β^+ -decay of ^{37}K . *Phys. Rev. C*, 90:032501, Sep 2014.
- [24] F. Della Vedova, S. M. Lenzi, M. Ionescu-Bujor, N. Marginean, M. Axiotis, D. Bazzacco, A. M. Bizzeti-Sona, P. G. Bizzeti, A. Bracco, F. Brandolini, D. Bucurescu, E. Farnea, A. Iordachescu, S. Lunardi, T. Martinez, P. Mason, R. Menegazzo, B. Million, D. R. Napoli, M. Nespolo, P. Pavan, C. Rossi Alvarez, C. A. Ur, R. Venturelli, and A. P. Zuker. Isospin Symmetry Breaking at High Spin in the Mirror Nuclei ^{35}Ar and ^{35}Cl . *Phys. Rev. C*, 75:034317, Mar 2007.
- [25] N. Severijns, M. Tandecki, T. Phalet, and I. Towner. $\mathcal{F}t$ Values of the $T = 1/2$ Mirror β Transitions. *Physical Review C*, 78(5):055501, November 2008.
- [26] ISAC Potassium Beam Yields. <http://mis.triumf.ca/science/planning/yield/beam/K>. Accessed: 01-10-2015.
- [27] T. B. Swanson, D. Asgeirsson, J. a. Behr, A. Gorelov, and D. Melconian. Efficient transfer in a double magneto-optical trap system. *Journal of the Optical Society of America B*, 15(11):2641, November 1998.
- [28] Matthew Harvey and Andrew Murray. Cold Atom Trap with Zero Residual Magnetic Field: The AC Magneto-Optical Trap. *Physical Review Letters*, 101(17), October 2008.

- [29] P. A. Vetter, J. R. Abo-Shaeer, S. J. Freedman, and R. Maruyama. Measurement of the $\beta - \nu$ Correlation of ^{21}Na Using Shakeoff Electrons. *Physical Review C*, 77(3):20, May 2008.
- [30] J. Liu, M. Mendenhall, A. Holley, H. Back, T. Bowles, L. Broussard, R. Carr, S. Clayton, S. Currie, B. Filippone, A. García, P. Geltenbort, K. Hickerson, J. Hoagland, G. Hogan, B. Hona, T. Ito, C.-Y. Liu, M. Makela, R. Mammei, J. Martin, D. Melconian, C. Morris, R. Pattie, A. Pérez Galván, M. Pitt, B. Plaster, J. Ramsey, R. Rios, R. Russell, A. Saunders, S. Seestrom, W. Sondheim, E. Tatar, R. Vogelaar, B. VornDick, C. Wrede, H. Yan, and A. Young. Determination of the Axial-Vector Weak Coupling Constant with Ultracold Neutrons. *Physical Review Letters*, 105(18), October 2010.
- [31] J. D. Jackson, S. B. Treiman, and H. W. Wyld. Possible Tests of Time Reversal Invariance in Beta Decay. *Physical Review*, 106(3):517–521, 1957.
- [32] J. Govaerts, M. Kokkoris, and J. Deutsch. Polarization-asymmetry Correlation in Allowed β -decay: A Probe for Right-Handed Currents. *Journal of Physics G: Nuclear and Particle Physics*, 21(12):1675–1699, December 1995.
- [33] T. Lee and C. Yang. Question of Parity Conservation in Weak Interactions. *Physical Review*, 106(6):1371–1371, June 1957.
- [34] E. Sudarshan and R. Marshak. Chirality Invariance and the Universal Fermi Interaction. *Physical Review*, 109(5):1860–1862, March 1958.
- [35] R. Feynman and M. Gell-Mann. Theory of the Fermi Interaction. *Physical Review*, 109(1):193–198, January 1958.
- [36] C. S. Wu and S. A. Moszkowski. *Beta Decay*. John Wiley & Sons, Inc., 1966.

- [37] Nathal Severijns, Marcus Beck, and Oscar Naviliat-Cuncic. Tests of the Standard Electroweak Model in Nuclear Beta Decay. *Reviews of Modern Physics*, 78(3):991–1040, September 2006.
- [38] James D. Bjorken and Sidney D. Drell. *Relativistic Quantum Mechanics*. Mcgraw-Hill College, 1965.
- [39] J.D. Jackson, S.B. Treiman, and H.W. Wyld. Coulomb Corrections in Allowed Beta Transitions. *Nuclear Physics*, 4:206–212, August 1957.
- [40] I. S. Towner and J. C. Hardy. The evaluation of V_{ud} and its impact on the unitarity of the Cabibbo-Kobayashi-Maskawa quark-mixing matrix. *Reports on Progress in Physics*, 73(4):046301, April 2010.
- [41] D. Chitwood, T. Banks, M. Barnes, S. Battu, R. Carey, S. Cheekatmalla, S. Clayton, J. Crnkovic, K. Crowe, P. Debevec, S. Dhamija, W. Earle, A. Gararov, K. Giovanetti, T. Gorringer, F. Gray, M. Hance, D. Hertzog, M. Hare, P. Kammel, B. Kiburg, J. Kunkle, B. Lauss, I. Logashenko, K. Lynch, R. McNabb, J. Miller, F. Mulhauser, C. Onderwater, C. Özben, Q. Peng, C. Polly, S. Rath, B. Roberts, V. Tishchenko, G. Wait, J. Wasserman, D. Webber, P. Winter, and P. ?o?nierzuk. Improved Measurement of the Positive-Muon Lifetime and Determination of the Fermi Constant. *Physical Review Letters*, 99(3):032001, July 2007.
- [42] P. Herczeg. On the Mohapatra-Pati Model of CP violation. *Physical Review D*, 28(1):200–208, July 1983.
- [43] Paul Langacker and S. Sankar. Bounds on the Mass of W_R and the $W_L - W_R$ Mixing Angle ζ in General $SU(2)_L \times SU(2)_R \times U(1)$ Models. *Physical Review D*, 40(5):1569–1585, September 1989.

- [44] Jogesh Pati and Abdus Salam. Lepton Number as the Fourth “color”. *Physical Review D*, 10(1):275–289, July 1974.
- [45] P. Herczeg. On Muon Decay in Left-Right-Symmetric Electroweak Models. *Physical Review D*, 34(11):3449–3456, December 1986.
- [46] H. Abele. The Standard Model and the Neutron β -decay. *Nuclear Instruments and Methods in Physics Research Section A: Accelerators, Spectrometers, Detectors and Associated Equipment*, 440(3):499–510, February 2000.
- [47] M. Bég, R. Budny, R. Mohapatra, and A. Sirlin. Manifest Left-Right Symmetry and its Experimental Consequences. *Physical Review Letters*, 38(22):1252–1255, May 1977.
- [48] Barry Holstein and S. Treiman. Tests of Spontaneous Left-Right-Symmetry Breaking. *Physical Review D*, 16(7):2369–2372, October 1977.
- [49] P Herczeg. Beta Decay Beyond the Standard Model. *Progress in Particle and Nuclear Physics*, 46(2):413–457, 2001.
- [50] O. Naviliat-Cuncic. Left-Right Symmetry Breaking Sensitivity of Beta-Asymmetry Measurements. *Journal of Physics G: Nuclear and Particle Physics*, 17(6):919, 1991.
- [51] Dan Melconian. *Measurement of the Neutrino Asymmetry in the β -decay of Laser-cooled, Polarized ^{37}K* . Phd thesis, Simon Fraser University, 2005.
- [52] N. Severijns. Tests of P-violation in Neutron and Nuclear Beta Decay. *Hyperfine Interactions*, 201(1-3):47–55, April 2011.
- [53] K Nakamura. Review of Particle Physics. *Journal of Physics G: Nuclear and Particle Physics*, 37(7A):075021, July 2010.

- [54] V. Wichers, T. Hageman, J. van Klinken, H. Wilschut, and D. Atkinson. Bounds on Right-Handed Currents From Nuclear Beta Decay. *Physical Review Letters*, 58(18):1821–1824, May 1987.
- [55] A. Carnoy, J. Deutsch, T. Girard, and R. Prieels. Limits on Nonstandard Weak Currents From the Positron Decays of ^{14}O and ^{10}C . *Physical Review Letters*, 65(26):3249–3252, December 1990.
- [56] A. Carnoy, J. Deutsch, T. Girard, and R. Prieels. Limits on Nonstandard Weak Currents From the Positron Decays of ^{14}O and ^{10}C . *Physical Review C*, 43(6):2825–2834, June 1991.
- [57] P.A. Quin and T.A. Girard. Sensitivity of the Polarized Nucleus-Beta Polarization Correlation to Right-Handed Currents in the Weak Interaction. *Physics Letters B*, 229(1-2):29–32, October 1989.
- [58] N. Severijns, M. Allet, K. Bodek, B.A. Brown, J. Camps, P. De Moor, J. Deutsch, M. Ferro-Luzzi, F. Gimeno-Nogues, J. Govaerts, B.R. Holstein, R. Kirchner, J. Lang, R. Müller, S. Navert, O. Naviliat-Cuncic, T. Otto, I. Pepe, R. Prieels, P.A. Quin, P. Schuurmans, J. Sromicki, E. Stephan, E. Thomas, A. Van Geert, L. Vanneste, B. Vereecke, and J. Zejma. Helicity Structure in Low and Intermediate Energy Weak Interaction. *Nuclear Physics A*, 629(1-2):423–432, February 1998.
- [59] M. Allet, K. Bodek, J. Camps, J. Deutsch, M. Ferro-Luzzi, F. Gimeno-Nogues, J. Govaerts, J. Lang, R. Müller, S. Navert, O. Naviliat-Cuncic, I. Pepe, R. Prieels, P. Quin, N. Severijns, J. Sromicki, E. Stephan, E. Thomas, and J. Zejma. Search for Right-Handed Weak Currents in the β -asymmetry Polarization Correlation from ^{12}N Decay. *Physics Letters B*, 383(2):139–144, August 1996.

- [60] N. Severijns, J. Deutsch, F. Gimeno-Nogues, B. King, I. Pepe, R. Prieels, P. Quin, J. Camps, P. De Moor, P. Schuurmans, W. Vanderpoorten, L. Vanneste, J. Wouters, M. Allet, O. Navilliat-Cuncic, and B. Holstein. Limits on Right-Handed Charged Weak Currents From a Polarization-Asymmetry Correlation Experiment with ^{107}In . *Physical Review Letters*, 70(26):4047–4050, June 1993.
- [61] A. Gaponenko, R. Bayes, Yu. Davydov, P. Depommier, J. Doornbos, W. Faszer, M. Fujiwara, C. Gagliardi, D. Gill, P. Green, P. Gumplinger, M. Hasinoff, R. Henderson, J. Hu, B. Jamieson, P. Kitching, D. Koetke, A. Krushinsky, Yu. Lachin, J. Macdonald, R. MacDonald, G. Marshall, E. Mathie, L. Mia-soedov, R. Mischke, J. Musser, P. Nord, M. Nozar, K. Olchanski, A. Olin, R. Openshaw, T. Porcelli, J.-M. Poutissou, R. Poutissou, M. Quraan, N. Rodning, V. Selivanov, G. Sheffer, B. Shin, F. Sobratee, T. Stanislaus, R. Tacik, V. Torokhov, R. Tribble, M. Vasiliev, and D. Wright. Measurement of the Muon Decay Parameter δ . *Physical Review D*, 71(7):071101, April 2005.
- [62] J. F. Bueno, R. Bayes, Yu. I. Davydov, P. Depommier, W. Faszer, C. A. Gagliardi, A. Gaponenko, D. R. Gill, A. Grossheim, P. Gumplinger, M. D. Hasinoff, R. S. Henderson, A. Hillairet, J. Hu, D. D. Koetke, R. P. MacDonald, G. M. Marshall, E. L. Mathie, R. E. Mischke, K. Olchanski, A. Olin, R. Openshaw, J.-M. Poutissou, R. Poutissou, V. Selivanov, G. Sheffer, B. Shin, T. D. S. Stanislaus, R. Tacik, and R. E. Tribble. Precise measurement of parity violation in polarized muon decay. *Physical Review D*, 84(3):032005, August 2011.
- [63] Matti Heikinheimo, Martti Raidal, and Christian Spethmann. Testing right-handed currents at the LHC. *The European Physical Journal C*, 74(10):3107,

October 2014.

- [64] S. Mandelstam. Determination of the Pion-Nucleon Scattering Amplitude from Dispersion Relations and Unitarity. General Theory. *Physical Review*, 112(4):1344–1360, November 1958.
- [65] Barry Holstein. Recoil Effects in Allowed Beta Decay: The Elementary Particle Approach. *Reviews of Modern Physics*, 46(4):789–814, October 1974.
- [66] H. Behrens, H. Genz, M. Conze, H. Feldmeier, W. Stock, and A. Richter. Allowed β -transitions, Weak Magnetism and Nuclear Structure in Light Nuclei. *Annals of Physics*, 115(2):276–324, October 1978.
- [67] Behrens, Heinrich and Bühring, Wolfgang. *Electron Radial Wave Functions and Nuclear Beta-Decay*. Oxford Oxfordshire, 1982.
- [68] Ch Von Platen, J. Bonn, U. Köpf, R. Neugart, and E. W. Otten. Spin Exchange Polarization and HFS Anomaly Measurement of β -active ^{37}K . *Zeitschrift für Physik*, 244(1):44–69, February 1971.
- [69] M.L. Pitt, M. Jozoff, F.P. Calaprice, G. Wang, and E.K. Warburton. *Bull. Am. Phys. Soc.*, 33(8):1564, 1988.
- [70] K. Minamisono, P.F. Mantica, H.L. Crawford, J.S. Pinter, J.B. Stoker, Y. Utsuno, and R.R. Weerasiri. Quadrupole Moment of ^{37}K . *Physics Letters B*, 662(5):389–395, May 2008.
- [71] A. Klein, B.A. Brown, U. Georg, M. Keim, P. Lievens, R. Neugart, M. Neuroth, R.E. Silverans, and L. Vermeeren. Moments and Mean Square Charge Radii of Short-lived Argon Isotopes. *Nuclear Physics A*, 607(1):1–22, September 1996.

- [72] M. Wang, G. Audi, A.H. Wapstra, F.G. Kondev, M. MacCormick, X. Xu, and B. Pfeiffer. The AME2012 Atomic Mass Evaluation. *Chinese Physics C*, 36(12):1603–2014, December 2012.
- [73] Ian Towner. Reduced Matrix Elements and Quenched Correlation Coefficients Calculations for ^{37}K . Personal Communication, 2013.
- [74] D.H. Wilkinson. Evaluation of the Fermi Function; EO Competition. *Nuclear Instruments and Methods*, 82(0):122–124, May 1970.
- [75] D.H. Wilkinson. Evaluation of Beta-Decay. *Nuclear Instruments and Methods in Physics Research Section A: Accelerators, Spectrometers, Detectors and Associated Equipment*, 275(2):378–386, February 1989.
- [76] D.H. Wilkinson. Evaluation of Beta-Decay. *Nuclear Instruments and Methods in Physics Research Section A: Accelerators, Spectrometers, Detectors and Associated Equipment*, 290(2-3):509–515, May 1990.
- [77] Ian Towner. Fermi Function Calculation. Personal Communication, 2010.
- [78] Brian Gough, editor. *GNU Scientific Library Reference Manual*. Network Theory Ltd., 3rd edition, 2009.
- [79] I. Angeli. A Consistent Set of Nuclear RMS Charge Radii: Properties of the Radius Surface $R(N, Z)$. *Atomic Data and Nuclear Data Tables*, 87(2):185–206, 2004.
- [80] J. Behr, A. Gorelov, T. Swanson, O. Häusser, K. Jackson, M. Trinczek, U. Giesen, J. D’Auria, R. Hardy, T. Wilson, P. Choboter, F. Leblond, L. Buchmann, M. Dombisky, C. Levy, G. Roy, B. Brown, and J. Dilling. Magneto-optic Trapping of β -Decaying $^{38}\text{K}^m$, ^{37}K From an Online Isotope Separator. *Physical Review Letters*, 79(3):375–378, July 1997.

- [81] H. Wohlfahrt, E. Shera, M. Hoehn, Y. Yamazaki, and R. Steffen. Nuclear Charge Distributions in $1f_{7/2}$ -shell Nuclei From Muonic X-ray Measurements. *Physical Review C*, 23(1):533–548, January 1981.
- [82] T. Kong, A. Gorelov, C. Höhr, T. Wiebe, A. Chatwin-Davies, A. Berman, S. Behling, D. Ashery, G. Gwinner, M. R. Pearson, and J. A. Behr. Specific Mass Shift Measurements in Rubidium by Doppler-Free Two-Photon Transitions. *Journal of Physics B: Atomic, Molecular and Optical Physics*, 44(21):215004, November 2011.
- [83] A. Gorelov, D. Melconian, W. Alford, D. Ashery, G. Ball, J. Behr, P. Bricault, J. D’Auria, J. Deutsch, J. Dilling, M. Dombisky, P. Dubé, J. Fingler, U. Giesen, F. Glück, S. Gu, O. Häusser, K. Jackson, B. Jennings, M. Pearson, T. Stocki, T. Swanson, and M. Trinczek. Scalar Interaction Limits from the β - ν Correlation of Trapped Radioactive Atoms. *Physical Review Letters*, 94(14), April 2005.
- [84] N. Scielzo, S. Freedman, B. Fujikawa, and P. Vetter. Recoil-ion Charge-state Distribution Following the β^+ decay of ^{21}Na . *Physical Review A*, 68(2):022716, August 2003.
- [85] N. Scielzo, S. Freedman, B. Fujikawa, and P. Vetter. Measurement of the β - ν Correlation Using Magneto-optically Trapped ^{21}Na . *Physical Review Letters*, 93(10):102501, August 2004.
- [86] M. Landini, S. Roy, L. Carcagní, D. Trypogeorgos, M. Fattori, M. Inguscio, and G. Modugno. Sub-Doppler Laser Cooling of Potassium Atoms. *Physical Review A*, 84(4):043432, October 2011.
- [87] W. H. Lippincott, K. J. Coakley, D. Gastler, E. Kearns, D. N. McKinsey, and J. A. Nikkel. Scintillation Yield and Time Dependence From Electronic and

- Nuclear Recoils in Liquid Neon. *Physical Review C*, 86(1):015807, July 2012.
- [88] S. O. Flyckt and Carole Marmonier, editors. *Photomultiplier Tubes Principles and Applications*. Phillips, Brive, France, 2002.
- [89] VF48 - DAQ Wiki. <http://www.triumf.info/wiki/DAQwiki/index.php/VF48>. Accessed: 11-28-2014.
- [90] VME-NIMIO32 - DAQ Wiki. <https://www.triumf.info/wiki/DAQwiki/index.php/VME-NIMIO32>. Accessed: 11-28-2014.
- [91] Daniel G. Roberge. *Polarization Diagnostics for Rubidium-80 in a Spin-Polarized Beta Decay Experiment*. Master thesis, The University of British Columbia, 2006.
- [92] E. de Clercq, M. de Labachellerie, G. Avila, P. Cerez, and M. Tetu. Laser Diode Optically Pumped Caesium Beam. *Journal de Physique*, 45(2):239–247, February 1984.
- [93] P. Tremblay and C. Jacques. Optical Pumping With Two Finite Linewidth Lasers. *Phys. Rev. A*, 41:4989–4999, May 1990.
- [94] H. Wang, P. L. Gould, and W. C. Stwalley. Long-range interaction of the $^{39}\text{K}(4s)+^{39}\text{K}(4p)$ asymptote by photoassociative spectroscopy. I. The 0_g^- pure long-range state and the long-range potential constants. *The Journal of Chemical Physics*, 106(19):7899, May 1997.
- [95] B.J. Dalton, R. McDuff, and P.L. Knight. Coherent Population Trapping. *Optica Acta: International Journal of Optics*, 32(1):61–70, December 2010.
- [96] F. Renzoni, S. Cartaleva, G. Alzetta, and E. Arimondo. Enhanced Absorption Hanle Effect in the Configuration of Crossed Laser Beam and Magnetic Field. *Phys. Rev. A*, 63:065401, May 2001.

- [97] Ioana Craiciu. *Work Term Report*. Co-op term report, TRIUMF, 2013.
- [98] M. P. Mendenhall, R. W. Pattie, Y. Bagdasarova, D. B. Berguno, L. J. Broussard, R. Carr, S. Currie, X. Ding, B. W. Filippone, A. García, P. Geltenbort, K. P. Hickerson, J. Hoagland, A. T. Holley, R. Hong, T. M. Ito, A. Knecht, C.-Y. Liu, J. L. Liu, M. Makela, R. R. Mammei, J. W. Martin, D. Melconian, S. D. Moore, C. L. Morris, A. Pérez Galván, R. Picker, M. L. Pitt, B. Plaster, J. C. Ramsey, R. Rios, A. Saunders, S. J. Seestrom, E. I. Sharapov, W. E. Sondheim, E. Tatar, R. B. Vogelaar, B. VornDick, C. Wrede, A. R. Young, and B. A. Zeck. Precision Measurement of the Neutron β -decay Asymmetry. *Physical Review C*, 87(3):032501, March 2013.
- [99] R. Pattie, J. Anaya, H. Back, J. Boissevain, T. Bowles, L. Broussard, R. Carr, D. Clark, S. Currie, S. Du, B. Filippone, P. Geltenbort, A. García, A. Hawari, K. Hickerson, R. Hill, M. Hino, S. Hoedl, G. Hogan, A. Holley, T. Ito, T. Kawai, K. Kirch, S. Kitagaki, S. Lamoreaux, C.-Y. Liu, J. Liu, M. Makela, R. Mammei, J. Martin, D. Melconian, N. Meier, M. Mendenhall, C. Morris, R. Mortensen, A. Pichlmaier, M. Pitt, B. Plaster, J. Ramsey, R. Rios, K. Sabourov, A. Sallaska, A. Saunders, R. Schmid, S. Seestrom, C. Servicky, S. Sjue, D. Smith, W. Sondheim, E. Tatar, W. Teasdale, C. Terai, B. Tipton, M. Utsuro, R. Vogelaar, B. Wehring, Y. Xu, A. Young, and J. Yuan. First Measurement of the Neutron β Asymmetry with Ultracold Neutrons. *Physical Review Letters*, 102(1):012301, January 2009.
- [100] J. Martin, J. Yuan, M. Betancourt, B. Filippone, S. Hoedl, T. Ito, B. Plaster, and A. Young. New measurements and quantitative analysis of electron backscattering in the energy range of neutron β -decay. *Physical Review C*, 73(1):015501, January 2006.

- [101] John Behr. Laser Linewidths. Personal Communication, 2015.
- [102] Martin Reddy. *API Design for C++*. Elsevier, Burlington, 2011.
- [103] Alex F. Bielajew, Hideo Hirayama, Yoshihito Namito, Nelson W. R., and Dave W. O. Rogers. EGS4. http://rcwww.kek.jp/research/egs/egs4_source.html. Accessed: 01-19-2015.
- [104] Francesc Salvat, Jose Maria Fernandez-Varea, and Josep Sempau. PENELOPE. <http://www.oecd-nea.org/tools/abstract/detail/nea-1525>. Accessed: 01-19-2015.

APPENDIX A

STRIP DETECTOR CALIBRATIONS

The silicon strip detectors were calibrated by fitting the observed spectrum to a simulated spectrum obtained from `GEANT4`. The algorithm that I used to integrate the waveforms made output that was too large for the fortran fitting routine to deal with so as a first step all of the input values were divided by 20. Making this modification it was possible to fit almost the entire set of spectrum with the same set of starting parameters. The two exceptions were the strips closest to the edge of the detectors and the upper X odd strips. In the case of the edge strips the fitting routine could be rerun with a smaller normalization to the `GEANT4` spectrum and would complete having found acceptable values for all parameters. There are less counts in these edge spectrum but the shapes remain the same. In the case of the upper X odd strips the situation is different. The preamps that were used to read out those strips were damaged and were much noisier than the other preamps. In this case the β -spectrum is on top of a large non-Gaussian noise background. In the case of the analysis they were excluded because they could not be handled in a consistent way. Even though it is unlikely that this calibration will be applied to these detectors again in future experiments it is good that the information will be preserved so that calibrations in subsequent experiments can be compared in an effort to detect breakdown due to age or radiation damage.

In order to use the calibration to plot an energy spectrum like that shown in Fig. A.1 the value stored in the TTree for each strip should be put into the following

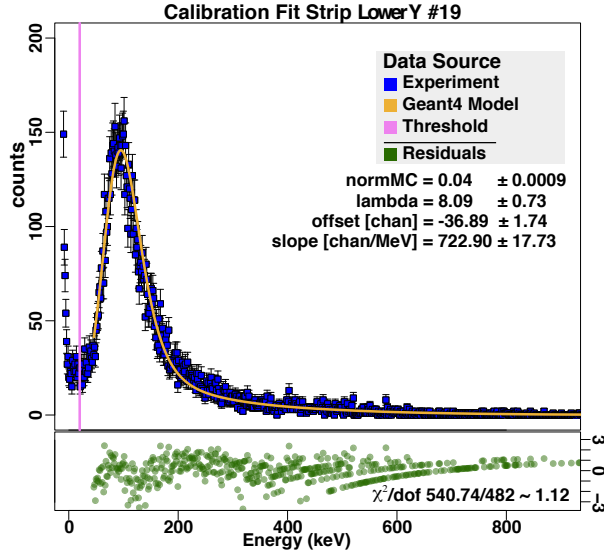


Figure A.1: This is a typical GEANT4 fit to a silicon strip spectrum.

formula.

$$\text{Silicon Energy (MeV)} = \frac{\left(\left(\frac{\text{TTree value}}{20}\right) - \text{offset (chan)}\right)}{\text{slope (chan/MeV)}} \quad (\text{A.1})$$

The value λ reported here for each strip is an energy dependent noise parameter where the total standard deviation of the noise for a strip is

$$\sigma_{total} = \sqrt{\sigma_0^2 + \lambda E}. \quad (\text{A.2})$$

Where σ_0 is the intrinsic noise of the strip. Due to the high correlation between σ_0 and λ , σ_0 was fixed to 0 and only λ was allowed to vary. The values of slope and offset for all available strips are listed in the following tables. The units of tables that follow are slope (chan/MeV), the units on offset are (chan), and the units of λ are (keV).

Strip Detector Calibrations Lower Y							
Name	χ^2/dof	slope	Δslope	offset	Δoffset	λ	$\Delta\lambda$
LY_01	0.99	8.03E+2	3.53E+1	3.40E+1	3.57	2.39E+1	3.52E+0
LY_02	0.97	7.47E+2	2.85E+1	2.49E+1	2.71	1.48E+1	2.26E+0
LY_03	0.98	7.51E+2	2.65E+1	2.89E+1	2.56	1.34E+1	1.82E+0
LY_04	0.97	6.23E+2	2.00E+1	2.86E+1	2.00	2.63E+1	3.56E+0
LY_05	1.09	6.60E+2	1.85E+1	2.90E+1	1.76	1.23E+1	1.49E+0
LY_06	1.04	7.18E+2	1.91E+1	3.31E+1	1.86	9.59E+0	9.95E-1
LY_07	1.06	6.15E+2	1.55E+1	2.84E+1	1.49	1.68E+1	1.93E+0
LY_08	1.03	6.31E+2	1.52E+1	3.33E+1	1.49	1.49E+1	1.50E+0
LY_09	1.18	7.11E+2	1.77E+1	3.42E+1	1.74	9.85E+0	9.45E-1
LY_10	1.08	5.91E+2	1.40E+1	3.30E+1	1.36	1.50E+1	1.56E+0
LY_11	1.12	6.45E+2	1.52E+1	3.28E+1	1.47	1.29E+1	1.26E+0
LY_12	0.99	5.89E+2	1.37E+1	3.37E+1	1.35	1.76E+1	1.76E+0
LY_13	1.08	6.97E+2	1.66E+1	3.79E+1	1.64	1.00E+1	8.80E-1
LY_14	1.08	6.61E+2	1.59E+1	3.71E+1	1.56	1.34E+1	1.21E+0
LY_15	1.08	6.64E+2	1.57E+1	3.57E+1	1.54	1.23E+1	1.12E+0
LY_16	1.13	7.07E+2	1.69E+1	3.82E+1	1.67	9.46E+0	8.19E-1
LY_17	1.02	6.97E+2	1.63E+1	3.73E+1	1.61	8.94E+0	7.81E-1
LY_18	1.03	5.93E+2	1.40E+1	3.33E+1	1.35	1.63E+1	1.65E+0
LY_19	1.12	7.22E+2	1.77E+1	3.68E+1	1.74	8.08E+0	7.28E-1
LY_20	1.00	6.46E+2	1.50E+1	3.65E+1	1.47	1.31E+1	1.17E+0
LY_21	1.02	6.22E+2	1.45E+1	3.37E+1	1.40	1.41E+1	1.36E+0
LY_22	1.11	6.23E+2	1.44E+1	3.49E+1	1.41	1.45E+1	1.36E+0
LY_23	1.00	5.96E+2	1.36E+1	3.50E+1	1.33	1.57E+1	1.50E+0
LY_24	1.27	7.17E+2	1.77E+1	3.77E+1	1.75	1.01E+1	9.00E-1
LY_25	1.08	6.71E+2	1.57E+1	4.00E+1	1.56	1.06E+1	9.03E-1
LY_26	1.07	6.20E+2	1.43E+1	3.43E+1	1.40	1.37E+1	1.31E+0
LY_27	1.15	7.18E+2	1.71E+1	3.53E+1	1.68	9.29E+0	8.32E-1
LY_28	0.95	6.17E+2	1.46E+1	3.57E+1	1.42	1.27E+1	1.22E+0
LY_29	0.96	5.79E+2	1.37E+1	3.41E+1	1.34	1.77E+1	1.78E+0
LY_30	1.11	6.87E+2	1.58E+1	3.28E+1	1.54	9.37E+0	8.83E-1
LY_31	0.98	5.89E+2	1.43E+1	3.26E+1	1.38	1.63E+1	1.72E+0
LY_32	1.09	6.36E+2	1.57E+1	3.43E+1	1.52	1.25E+1	1.24E+0
LY_33	1.05	6.24E+2	1.56E+1	3.45E+1	1.52	1.55E+1	1.56E+0
LY_34	1.09	6.39E+2	1.59E+1	3.35E+1	1.54	1.23E+1	1.27E+0
LY_35	1.05	6.91E+2	1.83E+1	3.08E+1	1.76	1.12E+1	1.21E+0
LY_36	1.09	6.78E+2	1.79E+1	3.40E+1	1.76	1.33E+1	1.38E+0
LY_37	1.08	7.19E+2	2.18E+1	3.30E+1	2.13	1.23E+1	1.41E+0
LY_38	0.93	6.87E+2	2.22E+1	3.23E+1	2.16	1.33E+1	1.67E+0
LY_39	1.08	7.50E+2	2.65E+1	3.22E+1	2.62	1.46E+1	1.90E+0
LY_40	0.93	7.16E+2	2.84E+1	3.40E+1	2.83	2.03E+1	2.92E+0

Table A.1: Strip detector calibration lower Y.

Strip Detector Calibrations Lower X							
Name	χ^2/dof	slope	Δslope	offset	Δoffset	λ	$\Delta\lambda$
LX_01	0.93	6.31E+2	2.25E+1	3.63E+1	2.27	2.34E+1	3.16E+0
LX_02	0.95	7.56E+2	3.49E+1	3.23E+1	3.47	2.07E+1	3.38E+0
LX_03	0.97	6.67E+2	2.06E+1	3.33E+1	2.04	2.14E+1	2.53E+0
LX_04	0.97	6.61E+2	2.31E+1	3.16E+1	2.27	2.00E+1	2.77E+0
LX_05	0.92	6.07E+2	1.59E+1	3.13E+1	1.55	1.98E+1	2.20E+0
LX_06	0.99	5.99E+2	1.75E+1	2.82E+1	1.69	1.80E+1	2.40E+0
LX_07	1.07	5.92E+2	1.36E+1	3.32E+1	1.34	1.79E+1	1.80E+0
LX_08	1.00	6.62E+2	1.74E+1	3.31E+1	1.69	1.18E+1	1.26E+0
LX_09	0.99	5.65E+2	1.34E+1	3.27E+1	1.33	2.08E+1	2.16E+0
LX_10	1.03	5.95E+2	1.49E+1	3.13E+1	1.43	1.56E+1	1.75E+0
LX_11	0.99	5.89E+2	1.37E+1	3.35E+1	1.33	1.73E+1	1.71E+0
LX_12	1.08	6.56E+2	1.59E+1	3.45E+1	1.56	1.23E+1	1.19E+0
LX_13	0.97	5.66E+2	1.32E+1	3.45E+1	1.30	1.87E+1	1.87E+0
LX_14	0.98	6.04E+2	1.47E+1	3.48E+1	1.44	1.68E+1	1.67E+0
LX_15	0.98	5.74E+2	1.32E+1	3.30E+1	1.27	1.62E+1	1.64E+0
LX_16	1.02	6.66E+2	1.61E+1	3.39E+1	1.57	1.27E+1	1.21E+0
LX_17	1.07	5.75E+2	1.31E+1	3.68E+1	1.31	1.99E+1	1.86E+0
LX_18	1.05	6.13E+2	1.39E+1	3.27E+1	1.36	1.55E+1	1.52E+0
LX_19	1.08	6.14E+2	1.41E+1	3.48E+1	1.38	1.52E+1	1.44E+0
LX_20	1.11	6.32E+2	1.44E+1	3.67E+1	1.42	1.40E+1	1.26E+0
LX_21	1.01	5.78E+2	1.33E+1	3.38E+1	1.31	1.83E+1	1.81E+0
LX_22	1.11	6.18E+2	1.43E+1	3.52E+1	1.40	1.44E+1	1.35E+0
LX_23	1.11	6.22E+2	1.48E+1	3.55E+1	1.45	1.57E+1	1.49E+0
LX_24	1.03	5.98E+2	1.37E+1	3.37E+1	1.33	1.61E+1	1.57E+0
LX_25	1.07	6.61E+2	1.58E+1	3.11E+1	1.52	1.20E+1	1.21E+0
LX_26	1.12	5.82E+2	1.33E+1	3.41E+1	1.32	2.02E+1	1.95E+0
LX_27	1.03	6.06E+2	1.46E+1	3.52E+1	1.43	1.48E+1	1.47E+0
LX_28	1.03	6.05E+2	1.42E+1	3.80E+1	1.41	1.81E+1	1.64E+0
LX_29	1.08	6.65E+2	1.66E+1	3.36E+1	1.62	1.37E+1	1.35E+0
LX_30	0.99	5.46E+2	1.29E+1	3.25E+1	1.27	2.11E+1	2.22E+0
LX_31	1.06	6.09E+2	1.51E+1	3.12E+1	1.46	1.56E+1	1.70E+0
LX_32	0.97	5.76E+2	1.35E+1	3.32E+1	1.33	1.94E+1	1.96E+0
LX_33	0.96	6.15E+2	1.56E+1	3.29E+1	1.50	1.28E+1	1.41E+0
LX_34	1.04	6.19E+2	1.51E+1	3.71E+1	1.49	1.68E+1	1.57E+0
LX_35	1.09	6.19E+2	1.77E+1	3.08E+1	1.74	2.01E+1	2.41E+0
LX_36	0.97	6.39E+2	1.62E+1	3.50E+1	1.59	1.51E+1	1.50E+0
LX_37	0.93	6.05E+2	2.10E+1	2.66E+1	2.07	2.58E+1	3.87E+0
LX_38	1.02	6.55E+2	1.79E+1	3.36E+1	1.77	1.86E+1	1.99E+0
LX_39	0.98	6.99E+2	2.65E+1	3.29E+1	2.66	2.16E+1	3.12E+0
LX_40	0.92	5.89E+2	2.00E+1	3.19E+1	2.05	3.10E+1	4.33E+0

Table A.2: Strip detector calibration lower X.

Strip Detector Calibrations Upper Y							
Name	χ^2/dof	slope	Δslope	offset	Δoffset	λ	$\Delta\lambda$
UY_01	1.01	7.28E+2	2.79E+1	2.93E+1	2.79	2.67E+1	3.81E+0
UY_02	0.93	6.93E+2	2.45E+1	3.47E+1	2.45	2.07E+1	2.65E+0
UY_03	0.90	6.83E+2	2.32E+1	3.45E+1	2.31	2.56E+1	3.14E+0
UY_04	1.10	7.08E+2	2.21E+1	3.04E+1	2.14	1.66E+1	1.98E+0
UY_05	0.96	6.49E+2	1.86E+1	3.54E+1	1.86	2.37E+1	2.56E+0
UY_06	1.12	7.21E+2	1.91E+1	3.41E+1	1.88	1.21E+1	1.19E+0
UY_07	1.01	6.98E+2	1.92E+1	3.76E+1	1.92	1.81E+1	1.74E+0
UY_08	1.17	7.41E+2	1.89E+1	3.42E+1	1.86	1.16E+1	1.08E+0
UY_09	1.01	6.20E+2	1.56E+1	3.53E+1	1.57	2.38E+1	2.34E+0
UY_10	1.05	7.29E+2	1.79E+1	3.34E+1	1.76	1.15E+1	1.06E+0
UY_11	1.04	6.25E+2	1.53E+1	3.46E+1	1.52	2.12E+1	2.05E+0
UY_12	1.09	6.63E+2	1.62E+1	3.75E+1	1.61	1.67E+1	1.50E+0
UY_13	1.04	7.01E+2	1.72E+1	3.95E+1	1.74	1.79E+1	1.51E+0
UY_14	1.10	6.53E+2	1.52E+1	3.58E+1	1.50	1.52E+1	1.36E+0
UY_15	1.01	6.63E+2	1.54E+1	3.79E+1	1.53	1.56E+1	1.34E+0
UY_16	1.09	6.63E+2	1.53E+1	3.60E+1	1.51	1.44E+1	1.27E+0
UY_17	1.15	7.03E+2	1.60E+1	3.58E+1	1.59	1.38E+1	1.17E+0
UY_18	1.12	6.87E+2	1.66E+1	3.78E+1	1.65	1.30E+1	1.13E+0
UY_19	1.02	6.81E+2	1.62E+1	3.52E+1	1.60	1.51E+1	1.35E+0
UY_20	1.03	6.50E+2	1.56E+1	3.59E+1	1.54	1.68E+1	1.52E+0
UY_21	1.02	6.57E+2	1.54E+1	3.95E+1	1.56	1.97E+1	1.66E+0
UY_22	1.06	6.50E+2	1.50E+1	3.87E+1	1.49	1.38E+1	1.18E+0
UY_23	1.10	6.69E+2	1.55E+1	3.97E+1	1.57	1.80E+1	1.49E+0
UY_24	1.12	7.22E+2	1.76E+1	4.13E+1	1.77	1.24E+1	1.02E+0
UY_25	0.96	6.05E+2	1.47E+1	3.91E+1	1.48	2.22E+1	2.02E+0
UY_26	1.13	6.97E+2	1.63E+1	3.84E+1	1.62	1.12E+1	9.49E-1
UY_27	1.09	6.35E+2	1.48E+1	3.42E+1	1.45	1.59E+1	1.47E+0
UY_28	1.08	6.91E+2	1.63E+1	3.71E+1	1.62	1.23E+1	1.07E+0
UY_29	1.07	6.61E+2	1.55E+1	4.04E+1	1.56	1.55E+1	1.29E+0
UY_30	1.06	7.10E+2	1.71E+1	3.67E+1	1.69	1.11E+1	9.81E-1
UY_31	1.09	6.06E+2	1.43E+1	3.94E+1	1.45	2.02E+1	1.80E+0
UY_32	1.09	6.83E+2	1.68E+1	3.92E+1	1.68	1.39E+1	1.21E+0
UY_33	1.03	6.30E+2	1.55E+1	3.93E+1	1.56	1.99E+1	1.81E+0
UY_34	1.01	6.72E+2	1.73E+1	3.49E+1	1.70	1.38E+1	1.35E+0
UY_35	1.00	6.16E+2	1.61E+1	3.41E+1	1.59	2.00E+1	2.11E+0
UY_36	1.02	6.57E+2	1.88E+1	3.58E+1	1.87	2.01E+1	2.16E+0
UY_37	1.02	6.93E+2	2.15E+1	3.45E+1	2.15	2.32E+1	2.62E+0
UY_38	0.99	7.35E+2	2.50E+1	3.19E+1	2.46	1.68E+1	2.09E+0
UY_39	0.99	7.13E+2	2.67E+1	3.34E+1	2.72	3.06E+1	4.09E+0
UY_40	0.96	8.02E+2	3.19E+1	3.34E+1	3.22	2.10E+1	2.83E+0

Table A.3: Strip detector calibration upper Y.

Strip Detector Calibrations Upper X Even							
Name	χ^2/dof	slope	Δslope	offset	Δoffset	λ	$\Delta\lambda$
UX_02	0.90	6.64E+2	2.30E+1	3.87E+1	2.35	2.86E+1	3.50E+0
UX_04	1.01	6.66E+2	1.94E+1	3.88E+1	1.96	2.08E+1	2.17E+0
UX_06	1.03	6.06E+2	1.58E+1	3.40E+1	1.57	2.18E+1	2.30E+0
UX_08	1.00	5.85E+2	1.54E+1	3.55E+1	1.55	2.79E+1	2.89E+0
UX_10	0.99	5.91E+2	1.45E+1	3.39E+1	1.44	2.33E+1	2.33E+0
UX_12	0.93	5.93E+2	1.41E+1	3.71E+1	1.41	2.09E+1	1.95E+0
UX_14	1.01	6.24E+2	1.51E+1	3.62E+1	1.50	1.97E+1	1.84E+0
UX_16	1.09	6.03E+2	1.40E+1	3.35E+1	1.40	2.17E+1	2.10E+0
UX_18	0.97	5.86E+2	1.46E+1	3.42E+1	1.44	2.20E+1	2.23E+0
UX_20	1.14	6.85E+2	1.64E+1	3.57E+1	1.62	1.54E+1	1.38E+0
UX_22	1.02	6.15E+2	1.48E+1	3.37E+1	1.46	1.92E+1	1.89E+0
UX_24	1.03	6.37E+2	1.57E+1	3.52E+1	1.55	1.90E+1	1.81E+0
UX_26	0.98	6.20E+2	1.56E+1	3.15E+1	1.52	1.83E+1	1.92E+0
UX_28	1.08	6.25E+2	1.60E+1	3.61E+1	1.59	2.10E+1	2.06E+0
UX_30	0.90	6.17E+2	1.58E+1	3.38E+1	1.55	1.97E+1	2.03E+0
UX_32	0.99	6.09E+2	1.59E+1	3.44E+1	1.58	2.28E+1	2.37E+0
UX_34	0.94	5.90E+2	1.61E+1	3.38E+1	1.60	2.26E+1	2.53E+0
UX_36	0.95	6.34E+2	1.90E+1	3.04E+1	1.84	2.10E+1	2.59E+0
UX_38	0.99	6.69E+2	2.37E+1	3.18E+1	2.33	2.19E+1	2.97E+0
UX_40	0.92	6.82E+2	3.29E+1	2.86E+1	3.28	3.61E+1	6.57E+0

Table A.4: Strip detector calibration upper X.

APPENDIX B

SCINTILLATOR CALIBRATIONS

The scintillator detectors were calibrated by fitting the observed spectrum to a simulated spectrum obtained from `GEANT4`. The procedure used was similar to that used to fit the silicon detectors as described in Appendix A. The one difference is that it was necessary to add together two `GEANT4` simulations in order to match the experimental spectrum. The reason for this is that we do not explicitly model the background in `GEANT4` from sources other than the 2% branch of the decay. To model the background in `GEANT4` I had to track the β^+ in the chamber and let them annihilate. Then I filtered the energy left in the scintillators to ensure that none of it was left by the β s and added this to the total observed spectrum with the same conditions that we apply to accept asymmetry events. This model works well enough and the fit values are shown in Table B.1. A graphical representation of the fit is shown in Fig. B.1. To convert the scintillator spectrum in the TTrees to energy in MeV the following formula should be used

$$\text{Scintillator Energy (MeV)} = \frac{\text{TTree value} - \text{offset (chan)}}{\text{slope (chan/MeV)}}. \quad (\text{B.1})$$

Scintillator Calibrations							
Name	χ^2/dof	offset	Δoffset	slope	Δslope	λ	$\Delta\lambda$
Upper	1.35	8.11E+1	5.92E-1	5.34E+2	1.07	7.62	5.23E-2
Lower	1.57	7.55E+1	5.81E-1	5.66E+2	1.09	7.36	5.61E-2

Table B.1: Scintillator calibrations. The units of slope are (chan/MeV), the units on offset are (chan), and the units of λ are (keV).

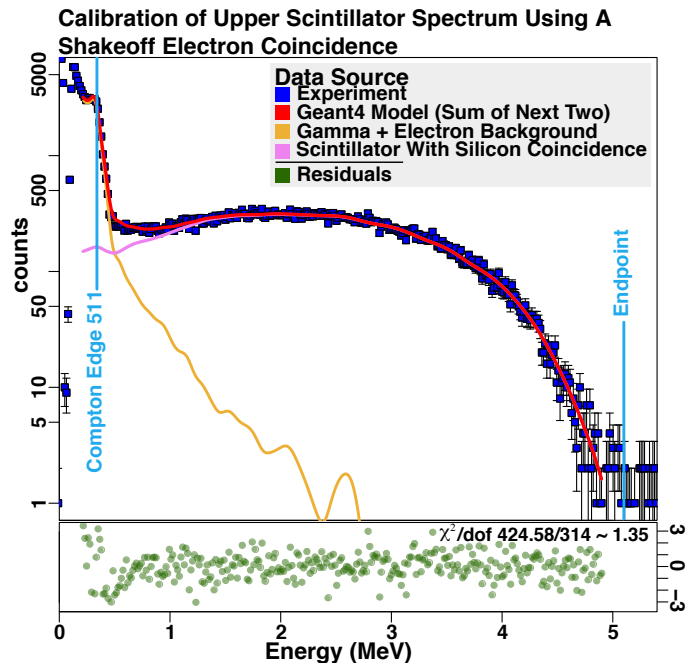


Figure B.1: Upper scintillator calibration fit with GEANT4. The set of starting parameters for the fit of both the upper and lower spectrum are the same. The red line is the fit and it is the sum of the pink and orange lines. The light blue lines are the known reference points for the spectrum. The data being fit is the scintillator spectrum requiring a hit on the electron MCP. The reason for using this is so that the Compton edge of the 511 γ s would be very prominent as opposed to a spectrum with a strip detector coincidence were the peak is suppressed to the point that it becomes very hard to fit to properly.

The value λ reported here for the scintillators is an energy dependent noise parameter where the total standard deviation of the noise for a strip is

$$\sigma_{total} = \sqrt{\sigma_0^2 + \lambda E}. \quad (\text{B.2})$$

Where σ_0 is the intrinsic noise of the detector. Due to the high correlation between σ_0 and λ , σ_0 was fixed to 0 and only λ was allowed to vary. In the future the scintillators will be gain stabilized with a flash from a temperature controlled LED and an analog feedback loop. This stabilization will reduce the noise term. Another idea is to lower the gain so that the whole peak from the minimally ionizing cosmic muons is visible and use it in the fitting routine with the endpoint and 511 Compton edge as another reference point.

APPENDIX C

MIRROR SPECIFICATION

The mirrors that we have in the vacuum are very specialized. The diameter is very large and the mirror had to be very thin for for the β s to pass through it. Here is the information that we have about the mirrors. There are very few materials that have a sufficiently high Young's modulus to produce an optically flat large thin mirror.

Mirror Attributes

Substrate Material SiC

Diameter 61 mm.

Thickness 0.010" \pm 0.001".

Smoothness polished both sides to surface roughness \lesssim 125 Å

Flatness 10 waves/inch.

Reflectivity 99.5+0.25-0.5% 770 nm at 9°.

Coating Same coating on front and back for stress reduction. Each coating has a total thickness of 1140 nm SiO₂ and 870 nm Nb₂O₅ (alternating high and low index of refraction materials).

We measured the S_3 of the mirror as a function of incident light angle to try to quantify the effect of poor mechanical mounting. Scott Smale did these measurements and they are documented in his co-op report. It was found that even for very poor alignment that the mirrors preserved the $S_3 > 0.9997$ which was the design specification.